Imperial College London

Department of Mechanical Engineering

Bulk viscosity effects in compressible turbulent Couette flow

Teddy Szemberg O'Connor

Abstract

This work investigates the effect of bulk viscosity in one-, two-, and three–dimensional compressible flows via direct numerical simulation.

The role of bulk viscosity in compressible turbulence is of increasing importance due to three applications: spacecraft descending through the Martian atmosphere, the thermodynamic cycle of solar–thermal power plant, and carbon capture and storage compressors. All three rely on the accurate description of turbulence in carbon dioxide, a gas with a bulk–to–shear viscosity ratio three orders of magnitude larger than for air. In these applications, invoking Stokes's hypothesis is questioned as the divergence of velocity is non–zero, implying a significant difference between mechanical and thermodynamic pressures.

Results of a constantly forced velocity perturbation follow the same trend as that predicted by Landau's acoustic absorption coefficient for sufficiently high Reynolds numbers. Below an optimum Reynolds number, the damping effectiveness reduces by a different mechanism to that of Landau. Maximum damping is achieved at an acoustic Reynolds number equal to unity. Two–dimensional decaying turbulence at the bulk-to-shear viscosity ratio of carbon dioxide demonstrates that the magnitude of the dilatational production term is greatly enhanced and is strongly biased to negative values, reducing the generation of velocity dilatation compared to the zero bulk viscosity case. Compressible Couette flow at two Reynolds numbers and two bulk–to–shear viscosity ratios show minimal changes to mean flow quantities and the main terms of interest in the turbulence kinetic energy budget. Instantaneous views of the dilatational velocity field show that an intermediate range of scales are damped in accordance with Landau's acoustic damping coefficient. At small scales, however, damping reduces and turbulent patterns are preserved.

Acknowledgements

Declaration of Authorship

I, Teddy Szemberg O'Connor, declare that this thesis and the work it contains is my own work and is based on results generated by me during my time as a PhD candidate at Imperial College London. Any work that is not my own has been referenced appropriately.

Copyright Declaration

Symbols

Roman

$\mathbf{A}$	Matrix of coefficients for finite difference stencil coefficients
$\mathcal{A}$	amplitude factor for dissipation
B	DRP solution vector term
a_j	finite difference stencil coefficients
$\boldsymbol{b}$	finite difference stencil coefficients
b_j^{ik}, c_j^{ik}, d_j^{ik}	Fourier coefficients
C_p	specific heat capacity at constant pressure
C_v	specific heat capacity at constant volume
e	specific internal energy, Euler's number
e_t	specific total energy
$\boldsymbol{e}_r$	radial unit vector in cylindrical coordinates
$\boldsymbol{e}_z$	axial unit vector in cylindrical coordinates
D	DRP matrix term, material derivative
$\mathbf{D}$	strain rate tensor
$\mathbf{D}^{\bullet}$	$\mathbf{D} - \Theta/3\mathbf{I}$
d_j	filter stencil coefficients
$\mathrm{d}t$	time step

E	kinetic energy
$\mathbf{I}$	identity matrix
i	$\sqrt{-1}$
k	wavenumber
k^*	modified wavenumber
l	grid point at which derivative is evaluated
M, N	numer of stencil points to the right, and left of derivative point; limits for summation.
Ma	Mach number $u_\mathrm{w}/c_\mathrm{w}$
Ma_∞	Mach number based on free–stream conditions
nx, ny, nz	number of grid points in physical domain in the streamwise, wall–normal and spanwise directions
$n\xi$	number of grid points in computational grid in wall–normal direction
p	thermodynamic pressure, order of derivative
p_m	mechanical pressure
$\boldsymbol{q}$	heat flux vector
Pr	Prandtl number $\mu c_p/\kappa$
Re	Reynolds number based on channel height $\rho_\mathrm{w} u_\mathrm{w} h/\mu$
Re_{Λ_0}	Reynolds number based on acoustic wavelength and sounds speed
Re_L	Reynolds number based on maximum velocity fluctuation and box length
Re_τ	Reynolds number based on friction velocity and half channel height
T	temperature
T_w	wall temperature
t	time

$\boldsymbol{u}$	velocity vector with streamwise, wall-normal and spanwise components (u, v, w)
$\boldsymbol{v}$	vector of finite difference stencil coefficients
u_w	streamwise velocity at the wall
u_τ	friction velocity
u_ad	advection speed
$\boldsymbol{x}$	position vector with streamwise, wall-normal and spanwise components (x, y, z)
y_1	parameter used in grid stretching function

Greek

α	Landau acoustic damping coefficient
α_Stokes	Stokes acoustic damping coefficient
β	stretching parameter for non–uniform grid
γ	ratio of specific heats c_p/c_v
$\Delta x, \Delta y, \Delta z$	local grid spacing
δ	half channel height
$\varepsilon_\mathrm{dispersion}$	integral dispersion error
$\varepsilon_\mathrm{dissipation}$	integral dissipation error
Θ	divergence of velocity
κ	thermal conductivity
Λ	wavelength
Λ_0	reference wavelength
λ	second viscosity
μ	dynamic shear viscosity
μ_b	bulk viscosity

ν	kinematic shear viscosity
ξ	computation grid coordinate, order of convergence for finite difference, and for filter schemes
$\boldsymbol{\Sigma}$	viscous stress tensor
$\boldsymbol{\sigma}$	stress tensor
τ	shear stress
$\overline{\tau}_{\mathrm{w}}$	wall shear stress
π	ratio of a circle's circumference to its diameter (3.141592...)
ρ	fluid density
ρ_{w}	fluid density at the wall
χ	ratio of bulk viscosity to shear viscosity μ_{b}/μ
Φ,ϕ	velocity scalar potential, phase shift due to dispersion
ω	wave frequency

Operators

$\boldsymbol{\nabla}$	gradient operator
$\boldsymbol{\nabla}\cdot,\nabla\cdot$	divergence operator
$\otimes$	diadic product

Subscripts/ superscripts

i,j,k	indices for streamwise, wall–normal and spanwise directions, or for summation terms.
w	quantity at the wall
$\widetilde{(\cdot)}$	Terms in Fourier space, Favre avereaged terms
$(\cdot)'$	Reynolds decomposition fluctuation
$(\cdot)''$	Favre decomposition fluctuation

Contents

List of Tables

List of Figures

Chapter 1

Introduction

1.1 Motivation

On August 6th 2012 the Mars Science Laboratory (MSL) spacecraft landed the Curiosity rover in the Gale crater on Mars. During its decent through the atmosphere, composed of about 97% carbon dioxide (CO_2) by volume, a 4.5 m diameter, high–drag aeroshell (see figure 1.1a), decelerated the craft from its entry speed of around 5.9 km/s to 0.47 km/s (after which a supersonic parachute took over) (Bose *et al.*, 2013). The MSL design was the first of its kind to incorporate pressure and temperature measurements on the surface of the heat–shield during entry. These measurements allowed the design team to compare their design predictions with data from the real event (the MEDLI project). During the development phase it became clear that the numerical predictions of the ablation rates of the heat shield were different from experimental tests. The heat flux boundary condition was found to have an uncertainty of about 20% and the experimental recession rate of the ablative layer of the heat–shield was 2.5 times larger than predicted (Beck *et al.*, 2014). In addition, a 50% margin was added to the heat flux value at the location of maximum heating from NASA's LAURA code in order to match experimental data (Edquist *et al.*, 2014). Given the range of environmental conditions experienced by the spacecraft during its descent (bow shock, hypersonic boundary layer flow, surface chemistry of ablative material, supersonic boundary layer flow, large Knudsen number conditions at high altitude) there is a long list of sources that could be responsible for the discrepancies in the computational fluid dynamics (CFD) predictions. One difference - which the work in thesis aims to clarify - is the way the gas is modelled in CFD simulations. Modelling the gas as a continuum brings with it a number of

assumptions, one of which is Stokes's hypothesis: the assumption that the divergence of velocity in a flow leads to no change in the stress tensor.

1.1.1   Bulk viscosity derivation

Following Thompson (1972), if a fluid is assumed isotropic and Newtonian with no net angular momentum, the number of coefficients that linearly relate the strain-rate tensor $\mathbf{D}$ to the viscous stress tensor $\boldsymbol{\Sigma}$ is two : the shear viscosity μ and second (or dilatational) viscosity λ. The total stress $\boldsymbol{\sigma}$ is the sum of the viscous stress and thermodynamic pressure p, where p is in local thermodynamic equilibrium in a closed system that has constant chemical composition. The state principle allows p to then be completely described by two independent thermodynamic variables, e.g. $p = p(\rho, T)$. A detailed derivation of the constitutive relations, see for example Aris (1989, p. 107), reveals mathematically that μ acts to resist both shearing motion and changes in velocity dilatation $\Theta \equiv \nabla \cdot \boldsymbol{u}$ (i.e. compression and expansion), and λ acts to resist changes only in velocity dilatation.

$$\boldsymbol{\sigma} = -p\mathbf{I} + \underbrace{2\mu\mathbf{D} + \lambda\Theta\mathbf{I}}_{\boldsymbol{\Sigma}} \tag{1.1.1}$$

where $\mathbf{D} \equiv (\boldsymbol{\nabla u} + (\boldsymbol{\nabla u})^{\mathrm{t}})/2$ and $\boldsymbol{u} = [u, v, w]^{\mathrm{t}}$ is the velocity vector and $\boldsymbol{\nabla u}$ is the gradient of the velocity vector. To fully describe the stress tensor both shear and second viscosities are required for any given fluid. Whilst the measurement of shear viscosity is easily achievable, direct measurement of the second viscosity is extremely difficult and still being developed (Cramer, 2012). One way around this problem is to relate λ to μ. To do so, the fluid deformation associated with shearing and with velocity dilatation are separated

$$\boldsymbol{\Sigma} = 2\mu\mathbf{D}^{\bullet} + \mu_{\mathrm{b}}\Theta\mathbf{I} \tag{1.1.2}$$

where $\mathbf{D}^{\bullet} \equiv \mathbf{D} - \Theta\mathbf{I}/3$ is the strain-rate tensor with the isotropic part removed and $\mu_{\mathrm{b}} \equiv 2\mu/3 + \lambda$ is the bulk viscosity. The complete stress tensor then becomes

$$\boldsymbol{\sigma} = -p\mathbf{I} + \mu_{\mathrm{b}}\Theta\mathbf{I} + 2\mu\mathbf{D}^{\bullet} \tag{1.1.3}$$

which has two isotropic terms, p and $\mu_{\mathrm{b}}\Theta$; the latter will be called the "dilatational pressure". Combining these two terms forms the mechanical pressure
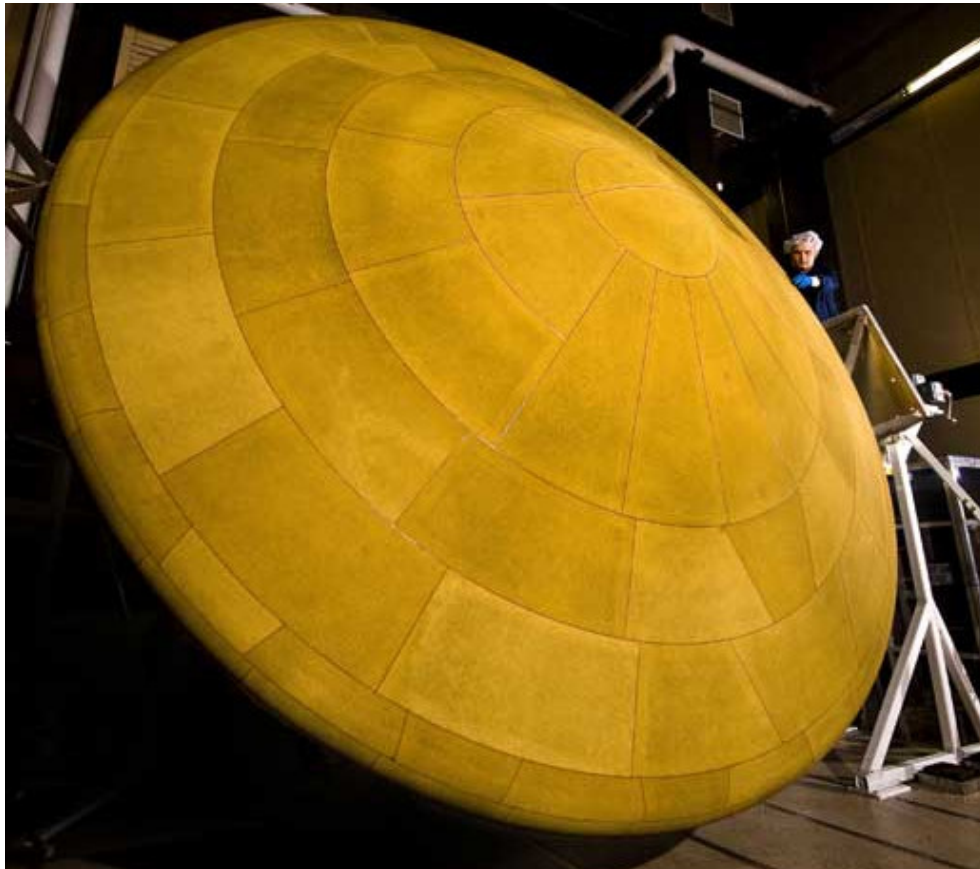
(a)

(b)

Figure 1.1: MSL protective heat shield (a) during production and (b) attached to the MSL spacecraft. *Images from nasa.com*

$$p_{\mathrm{m}} \equiv p - \mu_{\mathrm{b}}\Theta, \tag{1.1.4}$$

which is the negative of the average normal stress at a point. Whilst p is based on equilibrium thermodynamic conditions, the "dilatational pressure" is a viscous transport term which introduces a time lag to reach equilibrium. At a molecular level, the time lag is due to the longer time scales to reach equilibrium of rotational (slow) and vibrational (very slow) degrees of freedom compared with their translational counterparts.

Stokes (1845) hypothesised that setting μ_{b} to zero (and thereby assuming no time lag from the isotropic viscous term) could simplify making flow predictions as only the shear viscosity would need to be measured; λ is found through the relation $\lambda = -2\mu/3$. Due to computational constraints, it has often been too expensive to retain the bulk viscosity when using explicit codes. The diffusion CFL number $\mathrm{d}t\,\chi/(\rho\Delta x^2 \mathrm{Re})$ (t, χ, ρ Δx, and Re are the time, ratio of bulk viscosity to shear viscosity, grid spacing, and Reynolds number) is directly proportional to the bulk viscosity and hence an increase in the bulk viscosity requires a decrease in the time step by the same amount. Depending on the flow case, a judgement would be made on whether the error introduced by assuming Stokes's hypothesis was worth incurring.

Stokes's justification was based on the fact that the density of a fluid particle (and therefore the velocity dilatation) for "most cases [of interest]...is constant, or may without sensible error be regarded as constant, or else changes slowly with time. In the first two cases the results would be the same, and in the third case nearly the same whether [μ_{b}] were equal to zero or not. Consequentially, if theory and experiment in such cases agree, the experiments must not be regarded as confirming that part of the theory which relates to supposing [μ_{b}] be equal to zero."

In the Navier–Stokes equations (see chapter 2) the bulk viscosity appears as a product with the velocity dilatation. Comparing the magnitude of their product $\mu_{\mathrm{b}}\Theta$ to the thermodynamic pressure (Buresti, 2015) indicates whether Stoke's hypothesis can be assumed without introducing a significant error. In addition, it is the gradient of these terms that appear as forcing terms in the Navier–Stokes equations and as surface work done in the energy equation. Incompressible flows do not exist in nature but are a good approximation for many low-speed flow configurations and they are widely used for research and design (see Orszag and Israeli (1974); Fischer and Patera (1994) for an overview).

1.2   Bulk viscosity measurement

Measurements of bulk viscosity are difficult to perform experimentally and it is usually computed from attenuation measurements of acoustic waves. This method originated from the observation that sound absorption measurements far exceeded predictions based on the shear viscosity alone (Richards, 1939). Kinetic theory shows that $\mu_b = 0$ for monatomic gases, however Truesdell (1952) claims that the Maxwell–Boltzmann distribution (on which the kinetic theory of gases is based) inherently assume zero bulk viscosity. Tisza (1942) derived an expression for the zero-frequency bulk viscosity and used room temperature and pressure acoustic attenuation data from Kneser (1933) to estimate χ for CO_2 and nitrous oxide (N_2O) to be of the order of 10^3. Both substances are three atom molecules that are linear in shape. The dependence on frequency of the bulk viscosity when measured using acoustic attenuation has been questioned due to the fact that if μ and μ_b are not constants (of the gas in question) then the stress tensor fails to be a linear function of the deformation tensor, breaking the definition of the constitutive relations between $\boldsymbol{\sigma}$ and $\mathbf{D}$ (Truesdell, 1954). Karim and Rosenhead (1952) compiled direct estimations of χ for liquids. The fundamental disagreement as to whether the second viscosity is a fluid or flow property caused Rosenhead to organise a discussion at the Royal Society of Engineering in 1954. The conclusion was that whilst the bulk viscosity can be interpreted as a relaxation parameter at a macroscopic level, at a microscopic level, complicated effects start to operate for which more theoretical (and quantum) work is required (Andrade, 1954). Additional measurements of μ_b at ultrasonic frequencies were performed by Prangsma *et al.* (1973) for nitrogen, carbon monoxide, methane and deuterated methane. Through experimental experience they observed that a small discrepancy in measuring the absorption coefficient can lead to a large error in the calculation of μ_b.

An alternative method of inferring the bulk viscosity is by measuring the thickness of a shockwave. Emanuel and Argrow (1994) established from the shock jump conditions in one-dimension that the shock thickness is linearly dependent on χ. The results of Sherman (1955) agree with sound attenuation measurements that χ of nitrogen is approximately 2/3. Chikitkin *et al.* (2015) found from numerical simulation that the bow shock generated at the nose of a cooled sphere thickened when the bulk viscosity was included and better matched the results of Alsmeyer (1976). Additionally they reported an increase of 11% in the heat flux near the stagnation point of the sphere. The bulk viscosity used in their simulation was modelled by solving the Boltzmann equation using

the Chapman–Enskog expansion method for relatively rarefied gas ($Kn \approx 0.5$).

In practical applications, transonic and supersonic compressors suffer from pressure losses due to shocks present between blade rows (Miller and Lewis, 1961) and consequentially accurate prediction of the shock thickness can help improve compression efficiency. The effective compression of CO_2 is crucial to the economic viability of carbon capture and storage (CCS) and of solar thermal power stations in which supercritical CO_2 is the working fluid. In the former, the compression work accounts for approximately 10% of a coal-fired power station output (Goto *et al.*, 2013; Abu Zahra *et al.*, 2011). The latter makes use of the large variation in transport properties close to the thermodynamic critical point to reduce the compression work; supercritical fluids have the compressibility similar to a gas and the density similar to a liquid (Kim *et al.*, 2014; Wright *et al.*, 2010b).

More recently, numerical modelling of molecular interactions based on the Lennard–Jones potential (Cramer, 2012) and Green-Kubo correlation function (Hoover *et al.*, 1980) have been attempted to estimate the equilibrium and non-equilibrium bulk viscosity. The relaxation times of each mode is computed and converted into a single coefficient for use in continuum flow simulations. A molecular approach is taken in the chemistry community which has provided a large set of data of relaxation times for different substances from experiment (Andersen and Hornig, 1956; Dukhin and Goetz, 2009) and numerical modelling (Eu and Ohr, 2001).

1.2.1 Acoustic absorption

The calculation of the bulk viscosity mentioned above requires an understanding of the absorption of acoustic waves in a fluid. The fact that the absorption measurements are frequency dependent indicates that studying analytically the absorption of a one–dimensional wave will give a basis for what to expect in more complicated fluid motion such as three–dimensional turbulence. Stokes (1845) was the first to estimate the attenuation of a propagating wave as it travelled in time and produced an absorption coefficient

$$\alpha_{\text{Stokes}} = \frac{2\mu}{3\rho}\left(\frac{2\pi}{\Lambda}\right)^2 \tag{1.2.1}$$

which included the assumptions that $\mu_{\text{b}} = \kappa = 0$, where κ is the thermal conductivity. The density of the fluid is ρ through which a wave travels with wavelength Λ. It was Landau and Lifshitz (1959) who derived an expression for the acoustic absorption coefficient, α, based on the

shear and bulk viscosities, and thermal conductivity contributing to dissipation of the acoustic wave's kinetic energy to internal energy. It is reproduced here from Landau's book:

$$\alpha = \frac{\omega^2}{2\rho c^3}\left[\left(\frac{4}{3}\mu + \mu_{\mathrm{b}}\right) + \kappa\left(\frac{1}{C_v} - \frac{1}{C_p}\right)\right] \tag{1.2.2}$$

where c is the sound speed, C_v and C_p are the specific heats at constant volume and pressure, respectively. There is a dependence on the square of the wave frequency, ω, showing that the damping effectiveness of the bulk viscosity is much larger at small scales (for a given sound speed). This mechanism will be called "Landau acoustic damping" throughout the thesis. The damping of acoustic waves is relevant to the description of compressible turbulence. Miura and Kida (1995) found that acoustic waves act as the transfer mechanism between kinetic and internal energy and is effective at all flow scales. At small scales, the bulk viscosity acts as an additional dissipation term and hence an additional path for kinetic energy to be transferred to internal energy, via the propagation of acoustic waves.

1.2.2   Limitation of Stokes' hypothesis

There are particular cases in which the dilatational pressure may not be small compared to the thermodynamic pressure. In the context of re–entry vehicles entering Mars's atmosphere, the combination of large velocity dilatation rates during hypersonic and supersonic conditions and χ being of the order of 10^3 questions the validity of Stokes's hypothesis. NASA's LAURA code assumed Stokes's hypothesis for its continuum flow predictions but additional equations are solved to account for the dissociation of molecules in the high temperature region behind the bow-shock in which the relaxation of internal vibration and electronic degrees of freedom are accounted for (Wright *et al.*, 2010a). They also found that modelling the thermochemical non–equilibrium is crucial to accurately predicting the radiation heating behind the bow shock. Emanuel (1992) considered analytically a laminar flat-plate boundary layer using the extended, first-order boundary layer equations with the bulk viscosity term retained. They found that the heat transfer caused by the bulk viscosity varied as $\mathrm{Ma}_\infty^4/\mathrm{Re}$ and became significant for $\mathrm{Ma}_\infty \approx 9$ (typical during aerogravity-assisted maneuvers). In contrast to their Couette flow analysis (Gonzalez and Emanuel, 1993), the skin friction showed no dependence on the bulk viscosity. Recent work by Pan and Johnsen (2017) on the effect of bulk viscosity in compressible decaying homogeneous turbulence found that the bulk viscosity reduced the velocity dilatational

by two orders of magnitude (for $\chi = 10^3$).

1.2.3 Compressible Couette flow

The equation describing the evolution of turbulent kinetic energy (TKE) shares common terms with both the governing equation of mean internal energy (MIE), and mean kinetic energy (MKE). Terms common between two of the equations indicate a transfer term (see Lele (1994) for a map). Retaining the bulk viscosity introduces new transfer pathways which have the potential to modify the overall balance of energy conversion. The previous section shows that results have been reported of bulk viscosity affecting supersonic and hypersonic flows but little has been published on the effect on turbulence alone, i.e. removing the mean dilatation effect and mean pressure gradient. This work tackles this question by simulating plane Couette flow; the flow driven by the relative motion of two walls separated by a constant gap. A single source of kinetic energy (from the walls) which is distributed between the MKE, TKE and MIE reservoirs. In doing so, the effect of the bulk viscosity on turbulence generated velocity dilatation will become apparent. Channel flow is less suitable due to the driving pressure gradient which introduces an spatially constant forcing term. Early analytical work of compressible plane Couette flow was conducted by Korkegi and Briggs (1967) who used von Kármán's mixing length model and fitted constants to compare their results to incompressible experimental data. The stability analysis of Duck *et al.* (1994) showed that linear unstable modes exist in compressible Couette flow (unlike the incompressible equivalent) and the work of Hughes and Osterle (1957) found an analytical expression for the pressure and temperature distribution for adiabatic walls. From their one-dimensional analysis, Gonzalez and Emanuel (1993) found that the flow became almost incompressible for high μ_b in Couette flow that included mass injection at both plates, along with a doubling of the skin friction coefficient at the moving wall. The variation in skin friction led to the proposal of an alternative method of measuring the bulk viscosity. A Taylor-Couette configuration with porous cylinders would experience a difference in drag depending on the bulk viscosity.

The only results to analyse the turbulent structures and mean statistics of velocity correlations in compressible Couette flow were published by Buell (1991). The aim of his paper was to establish differences between incompressible and compressible wall-bounded turbulence with the aim of providing models for high Mach number boundary layer calculations. A correlation was found between areas of low shear and high velocity dilatation rates, and the shear stress (averaged

in time and the homogeneous directions) was only 13% lower in the Ma = 3 case compared to the Ma = 0.2 case. Couette flow generates very large streamwise vortices in the centre of the channel caused by a non-zero mean shear at the centreline (Lee, 1991) that can be as long as the domain. Buell (1991) calculated that 150-250 tu_{w}/h are required to achieve a constant total shear stress with less than 2% variation across the channel. Many authors have investigated the large coherent and long–persisting structures in incompressible Couette flow. This structure was believed to have little dependence on time and along the streamwise direction. This behaviour was demonstrated by Spalart *et al.* (2014) who successfully generated large streamwise vortices from a two-dimensional (in the wall-normal and spanwise directions) Reynolds–Averaged–Navier–Stokes (RANS) simulation. Komminaho *et al.* (1996) calculated the streamwise integral length scale (the area under the curve of the longitudinal correlation function) to be eight times larger than in channel flow at Re = 750 and that the break-up regeneration process for large structures occurred over a time–scale of about 20-25 tu_{w}/h . They also reported that the large streamwise vortices contain only approximately 10% of the kinetic energy in the flow field despite their dominating presence when visualising the flow field. Turbulent patches are stretched in the streamwise direction and spread more rapidly than those in boundary layers (Lundbladh and Johansson, 1991).

1.2.4   Thesis aims

This thesis aims to address the question of the bulk viscosity effect on turbulence due to turbulence induced velocity dilatation. Simplified two–dimensional flows are used to clarify the solenoidal to dilatational energy transfers followed by the effect in three–dimensional compressible Couette flow. The latter is the simplest wall-bounded configuration to investigate this effect. Turbulence statistics for compressible Couette flow are presented, an area that is underrepresented in the literature. Similarities between channel flow and Couette flow near the wall have been reported by Orlandi *et al.* (2015) who found that the friction coefficient is very similar in both cases when scaled by centreline properties. Hamilton *et al.* (1995) summarised the near-wall streak characteristics of Couette flow establishing that the minimum spacing between streaks is about 100 ν/u_τ units in width (ν is the kinematic viscosity, $u_\tau \equiv \sqrt{\overline{\tau}_{\mathrm{w}}/\rho}$, $\overline{\tau}_{\mathrm{w}}$ is the wall shear stress and ρ is the density). Because near–wall streaks are essential to maintaining turbulence, this spacing indicates a minimum width required for Couette flow. Despite the finite-domain effects and long time series required to converge statistics, the Couette flow configuration is a convenient choice

to make a comparison between zero and non-zero bulk viscosity cases.

Chapter 2 outlines the governing equations and numerical method used to generate the data. Chapter 3 shows results to validate the numerical method. Chapter 4 investigates the bulk viscosity in the context of 1D temporal forcing cases and 2D test cases including an ideal vortex and decaying isotropic turbulence. Chapter 5 discusses the effect in three–dimensional Couette flow. Conclusions are made in chapter 6.

Chapter 2

Governing equations and numerical method

2.1 Instantaneous equations

The governing equations of mass, momentum and energy are written for a Newtonian fluid with bulk viscosity $\mu_{\mathrm{b}} \equiv 2\mu/3 + \lambda$ retained. The shear viscosity is μ and the second viscosity is λ. The term $\mu_{\mathrm{b}}\Theta$, where $\Theta \equiv \nabla \cdot \boldsymbol{u}$, has the dimensions of pressure and will be referred to as the "dilatational pressure". It is combined with the thermodynamic pressure p to form the mechanical pressure (in dimensionless units) $p_{\mathrm{m}} \equiv p - \chi\Theta/\mathrm{Re}$. The density, time, temperature, and viscous stress tensor are represented by ρ, t, T, and $\boldsymbol{\Sigma}$. The streamwise, wall-normal, and spanwise directions are x, y, z, respectively. The components of the velocity vector field $\boldsymbol{u}$ are u, v, w (or u_i for $i \in \{1, 2, 3\}$), for each direction (see A for details on the non-dimensionalisation). The equations are

$$
\begin{aligned}
\frac{\partial \rho}{\partial t} + \nabla \cdot (\rho \boldsymbol{u}) &= 0 \\
\frac{\partial \rho \boldsymbol{u}}{\partial t} + \boldsymbol{\nabla} \cdot (\rho \boldsymbol{u} \otimes \boldsymbol{u}) &= -\boldsymbol{\nabla} p_{\mathrm{m}} + \frac{1}{\mathrm{Re}} \boldsymbol{\nabla} \cdot \boldsymbol{\Sigma} \\
\frac{\partial \rho e_{\mathrm{t}}}{\partial t} + \nabla \cdot (\rho e_{\mathrm{t}} \boldsymbol{u}) &= -\nabla \cdot (p_{\mathrm{m}} \boldsymbol{u}) + \frac{1}{\mathrm{Re}} \nabla \cdot (\boldsymbol{\Sigma} \boldsymbol{u}) - \frac{1}{\mathrm{PrReMa}^2(\gamma - 1)} \nabla \cdot \boldsymbol{q},
\end{aligned}
\tag{2.1.1}
$$

where

$$\boldsymbol{\Sigma} \equiv 2\mu \mathbf{D}^\bullet, \tag{2.1.2}$$

$$\mathbf{D}^\bullet \equiv \mathbf{D} - \frac{1}{3}\Theta\mathbf{I}, \tag{2.1.3}$$

$$\mathbf{D} \equiv \frac{1}{2}\left(\boldsymbol{\nabla}\boldsymbol{u} + (\boldsymbol{\nabla}\boldsymbol{u})^{\mathrm{t}}\right). \tag{2.1.4}$$

The reference velocity, temperature and density are taken as the wall values: u_{w}, T_{w}, and ρ_{w}, respectively. A subscript "w" indicates wall values. The reference pressure is $\rho_{\mathrm{w}}u_{\mathrm{w}}^2$ and the reference time is found from the channel height and reference velocity h/u_{w}. The ratio of the bulk to shear viscosity is

$$\chi \equiv \frac{\mu_{\mathrm{b}}}{\mu}, \tag{2.1.5}$$

and heat flux $\boldsymbol{q}$ is defined by the Fourier heat conduction law

$$\boldsymbol{q} = -\kappa\boldsymbol{\nabla}T, \tag{2.1.6}$$

where κ is the thermal conductivity of the fluid. The gas is ideal and perfect leading to the thermal and caloric equations of state,

$$p = \frac{\rho T}{\gamma \mathrm{Ma}^2}, \tag{2.1.7}$$

$$e = \frac{T}{\gamma(\gamma - 1)\mathrm{Ma}^2}, \tag{2.1.8}$$

in which e is the specific internal energy, and $\gamma \equiv C_p/C_V$ is the ratio of specific heats at constant pressure and volume, respectively. The dimensionless numbers are defined with respect to reference values taken at the wall (indicated by the subscript "w"), i.e. $u_{\mathrm{w}} = 1$, $\rho_{\mathrm{w}} = 1$, $h = 1$:

$$\mathrm{Re} = \frac{\rho_{\mathrm{w}}u_{\mathrm{w}}h}{\mu}, \quad \mathrm{Ma} = \frac{u_{\mathrm{w}}}{c_{\mathrm{w}}}, \quad \mathrm{Pr} = \frac{\mu C_p}{\kappa} \tag{2.1.9}$$

Throughout the thesis the shear and bulk viscosities (and hence χ), and the thermal conductivity, are constants.

2.2   Numerical scheme

A direct numerical simulation (DNS) was performed using the group's fully explicit, in-house code (CompReal). Cartesian grids were used with constant spacing in homogeneous directions (x and y for the 2D configuration, and x and z for the Couette configuration) and hyperbolic-tangent stretching in the wall-normal direction, refining the near–wall region. Derivatives were evaluated by finite-difference and the governing equations integrated in time using a third-order accurate low storage Runge-Kutta method. Spatial gradients are performed using centred finite differences which are stabilised by explicit filtering. This section details each of these methods. The implementation and development of the dispersion relation preserving finite difference schemes, optimised filtering, and boundary conditions was conducted by Dr. Nicolas Alferez and Dr. Emile Touber.

2.2.1   Grid arrangement

The physical domain is discretised with a shifted Cartesian grid that in homogeneous directions has constant spacing between grid points. Figure 2.1 shows a sketch of the relationship between physical domain and computational domain.
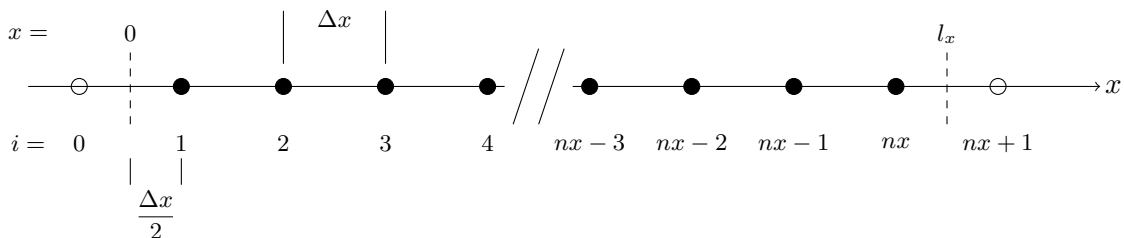
Figure 2.1: Shifted grid arrangement for periodic (x and z) directions.

For the Couette configuration, the grid in the wall-normal direction is not shifted to allow the direct application of Dirichlet boundary conditions at the wall. Figure 2.2 shows this arrangement.
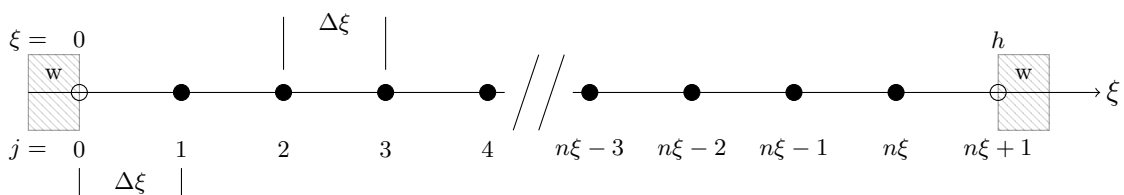
Figure 2.2: Non-shifted grid arrangement for wall direction.

2.2.2 Grid stretching

To improve resolution in the near–wall region in the wall-normal (y) direction, an analytical hyperbolic–tangent stretching function is applied to the physical grid coordinate $y \in [0,1]$

$$y = \frac{1}{2y_1} \tanh^2 \left(\beta \left(\xi - \frac{1}{2} \right) \right) + \frac{1}{2}, \tag{2.2.1}$$

where $y_1 \equiv \tanh(\beta/2)$. To increase the clustering of points in the near wall region, the parameter β is increased. The computational grid coordinate ξ (i.e. the one used for finite-differencing) has constant spacing. The finite differences are performed in the computational domain and the results are multiplied by the metric term $\mathrm{d}\xi/\mathrm{d}y$ to produce the derivatives in the physical domain, i.e.

$$\frac{\mathrm{d}f}{\mathrm{d}y} = \frac{\mathrm{d}f}{\mathrm{d}\xi} \frac{\mathrm{d}\xi}{\mathrm{d}y} \tag{2.2.2}$$

where

$$\frac{\mathrm{d}\xi}{\mathrm{d}y} = \frac{2y_1}{\beta} \cosh^2 \left(\beta \left(\xi - \frac{1}{2} \right) \right). \tag{2.2.3}$$

For all Couette cases, $\beta = 4.5$, giving a ratio of grid spacing at the centreline to wall of approximately 23.

2.3 Dispersion relation-preserving finite difference schemes

2.3.1 Taylor constraints

This section details the method used to construct a finite difference stencil and its coefficients for any order derivative to any order of accuracy and follows the description given in Leveque (2007). As an example, a centred first-order derivative is derived with constant grid spacing. The pth derivative of a continuous function $f(x)$ can be approximated at a point x_0 as a weighted sum of f evaluated at $x_{-N}, x_{-N+1}, ..., x_0, ..., x_{M-1}, x_M$, with N values to the left of x_0 and M values to the right. This requires that the pth derivative is smooth for $x \in [x_{-N}, x_M]$, and that $N + M + 1 \geq p + 1$. The approximation of the first derivative ($p = 1$) can be written as

$$\frac{\mathrm{d}f}{\mathrm{d}x}(x_0) \approx \frac{1}{\Delta x} \sum_{j=-N}^{M} a_j f(x + j\Delta x) \tag{2.3.1}$$

where a_j are the weighting coefficients to be determined. The same can be applied to a discrete function f, the derivative of which is taken at x_l. There are N points to the left of x_l and M points to the right. Equation (2.3.1) can be rewritten as

$$\frac{\mathrm{d}f_l}{\mathrm{d}x} \approx \frac{1}{\Delta x} \sum_{j=-N}^{M} a_j f_{l+j}. \tag{2.3.2}$$

In order to compute the stencil coefficients a_j, a Taylor series expansion of f about x_l can be written at each x_{l+j} in the stencil as

$$f_{l+j} = f_l + f_l'(x_{l+j} - x_l) + \frac{1}{2}f_l''(x_{l+j} - x_l)^2 + ... + \frac{1}{n!}f_l^n(x_{l+j} - x_l)^n + \mathcal{O}(\Delta x^{n+1}), \tag{2.3.3}$$

where $n = M + N + 1$ and $j \in \{-N, -N+1, -N+2, ..., M\}$. This forms n relations for $j \in \{-N, -N+1, -N+2, ..., M\}$ from which the derivative f_l' can be extracted. Each equation is premultiplied by a_j, forming a linear system in a_j equal to the desired derivative and the residual error:

$$a_{l-N}f_{l-N} + a_{l-N+1}f_{l-N+1} + ... + a_l f_l + ... + a_{l+M}f_{l+M} = \frac{df^{(p)}}{dx}(x_0) + \mathcal{O}(\Delta x^{n-p}). \tag{2.3.4}$$

The a_j can be solved for by constraining all extra terms except for the residual error to vanish and hence the desired approximation is found. To do so, each f_{l+j} in (2.3.4) is substituted for the Taylor series expansion from (2.3.3):

$$a_{l-N}(f_l + f_l'(x_{l-N} - x_l) + ...) + a_{l-N+1}(f_l + f_l'(x_{l-N+1} - x_l) + ...) + a_l f_l + ...$$
$$+ a_{l+M}(f_l + f_l'(x_{l+M} - x_l) + ...) = \frac{df^{(p)}}{dx}(x_0) + \mathcal{O}(\Delta x^{n-p}). \tag{2.3.5}$$

Equation (2.3.5) is split by terms of the same order of derivative. For this example of a first derivative, only terms in f_l' are set equal to unity, the rest are set equal to zero. In summation form this can be represented as:

$$\frac{1}{(i-1)!} \sum_{j=-N}^{M} a_j (x_j - x_l)^{(i-1)} = \begin{cases} 1, \text{if } i-1 = p \\ 0, \text{otherwise} \end{cases} \tag{2.3.6}$$

for $i \in \{1, ..., n\}$. Note that if $M = N$ the stencil is centred (i.e. symmetric about the derivative point). For such a case, the linear system of equations in matrix form is $\boldsymbol{Av} = \boldsymbol{b}$:

$$\begin{bmatrix} 1 & \dots & 1 & \dots & 1 \\ x_{-N} - x_l & \dots & x_j - x_l & \dots & x_N - x_l \\ \frac{(x_{-N} - x_l)^2}{2} & \dots & \frac{(x_j - x_0)^2}{2} & \dots & \frac{(x_N - x_0)^2}{2} \\ \frac{(x_{-N} - x_l)^{i-1}}{(i-1)!} & \dots & \frac{(x_j - x_0)^{i-1}}{(i-1)!} & \dots & \frac{(x_N - x_0)^{i-1}}{(i-1)!} \\ \vdots & & \vdots & & \vdots \\ \frac{(x_{-N} - x_0)^{N-1}}{(N-1)!} & \dots & \frac{(x_j - x_0)^{N-1}}{(N-1)!} & \dots & \frac{(x_N - x_0)^{N-1}}{(N-1)!} \end{bmatrix} \begin{bmatrix} a_{-N} \\ a_{-N+1} \\ a_{-N+2} \\ a_j \\ \vdots \\ a_N \end{bmatrix} = \begin{bmatrix} 0 \\ 1 \\ 0 \\ 0 \\ \vdots \\ 0 \end{bmatrix} \tag{2.3.7}$$

where i and j are the row and column indices, respectively. The resulting Vandermonde matrix $\boldsymbol{A}$ is ill–conditioned (Pan, 2016). As a consequence, only the matrix corresponding to the half–stencil is inverted (noting that $a_{-j} = -a_j$) and the matrix size is kept small ($N < 6$), minimising numerical errors. In addition, the inversion is performed at quadruple precision to ensure that the sum of the stencil coefficients is zero to double precision (the working precision chosen for the code).

2.3.1.1 Modified wavenumber

For the derivative approximation to converge at order ξ, the minimum number of stencil points required is $N + M + 1 = \xi + 1$; a relation found from the Taylor constraints (Tannehill *et al.*, 1997, p. 61). Dispersion-relation preserving schemes use additional stencil points ($N + M + 1 > \xi + 1$) to control the dispersion properties of the discrete differential operator. The following section outlines the methods developed by Tam and Webb (1993); Bogey and Bailly (2004). The hyperbolic equations governing compressible flows result in the presence of acoustic modes and the relationship between their propagation is described by the dispersion relation. In addition to its

order of grid convergence, the accuracy of a finite difference scheme can be evaluated by computing its dissipation and dispersion errors in wavenumber space. This section presents this analysis for a centred scheme. The Fourier transform is defined as

$$\widetilde{f}(k) \equiv \frac{1}{2\pi} \int_{-\infty}^{\infty} f(x)e^{-\mathrm{i}kx}\,\mathrm{d}x, \tag{2.3.8}$$

where $\mathrm{i} = \sqrt{-1}$ and k is the wavenumber, which when applied to (2.3.1) gives

$$\mathrm{i}k\widetilde{f} \approx \left(\frac{1}{\Delta x} \sum_{j=-N}^{M} a_j e^{\mathrm{i}kj\Delta x} \right) \widetilde{f} \equiv \mathrm{i}k^*\widetilde{f} \tag{2.3.9}$$

By inspection, the right-hand side contains the Fourier transform of the finite difference approximation and can be called the "modified wavenumber"

$$k^* \equiv \frac{-\mathrm{i}}{\Delta x} \sum_{j=-N}^{M} a_j e^{\mathrm{i}kj\Delta x}. \tag{2.3.10}$$

In general k^* is complex and is used to express the dispersion and dissipation errors of the finite difference scheme.

2.3.1.2   Dispersion and dissipation of finite difference operator

A common way of illustrating the properties of the finite difference scheme is to consider its application to the one–dimensional advection problem. Following the presentation in Berland *et al.* (2007), the governing equation is

$$\frac{\partial u}{\partial t} + u_{\mathrm{ad}} \frac{\partial u}{\partial x} = 0 \tag{2.3.11}$$

where u_{ad} is the constant advection speed and $\partial/\partial x$ is approximated by the finite difference approximation (2.3.1). Equation (2.3.11) has the dispersion relation

$$\omega = k^* u_{\mathrm{ad}} \tag{2.3.12}$$

where ω is the angular frequency. The initial condition is prescribed to be an harmonic wave of the form $u(x, t = 0) = \exp[\mathrm{i}kx]$, and the approximate solution of the right–running (positive x direction) wave takes the form

$$u(x,t) = \exp\left[\mathrm{i}(kx - \omega t)\right]. \tag{2.3.13}$$

Substituting for the dispersion relation (2.3.12) gives

$$u(x,t) = \exp\left[\mathrm{i}(kx - k^* u_{\mathrm{ad}}t)\right], \tag{2.3.14}$$

in which k^* can be split into real ($\Re$) and imaginary ($\Im$) parts to give

$$u(x,t) = \underbrace{\exp\left[\mathrm{i}\left\{k - \Re(k^*)\right\}u_{\mathrm{ad}}t\right]}_{\text{dispersion}} \underbrace{\exp\left[\Im(k^*)u_{\mathrm{ad}}t\right]}_{\text{dissipation}} \underbrace{\exp\left[\mathrm{i}k(x - u_{\mathrm{ad}}t)\right]}_{\text{exact solution}}. \tag{2.3.15}$$

The solution (2.3.15) is the analytical solution modified by two terms that emerge as a result of using an approximation for the finite difference. Consider when the wave travels one grid spacing, i.e. $\Delta x = u_{\mathrm{ad}}t$, the dissipation error modifies the wave amplitude of the analytical solution by the factor $\mathcal{A}$ and the dispersion error introduces a phase shift ϕ, where

$$\mathcal{A} = \Im(k^*\Delta x)$$

$$\phi = k\Delta x - \Re(k^*\Delta x). \tag{2.3.16}$$

Centred schemes, for which $M = N$ and $a_j = -a_{-j}$, have zero dissipation by construction. This can be seen by taking the imaginary part of (2.3.10) to give

$$\Im(k^*) = -\frac{1}{\Delta x}\sum_{j=-N}^{N} a_j\left[\cos(kj\Delta x)\right] = 0. \tag{2.3.17}$$

The Taylor constraints ensure a high–order convergence rate as the mesh is refined but can lead to large errors when differentiating a function resolved with only a few points per wavelength. This undesired phenomenon can be improved by the use of dispersion–relation–preserving (DRP) schemes as outlined in the next section.

2.3.2 Dispersion-relation preserving constraints

Comparing k^* and k indicates how well a finite–difference scheme preserves the dispersion properties of the differential operator. Figure 2.3 plots curves for all the centred schemes used in this
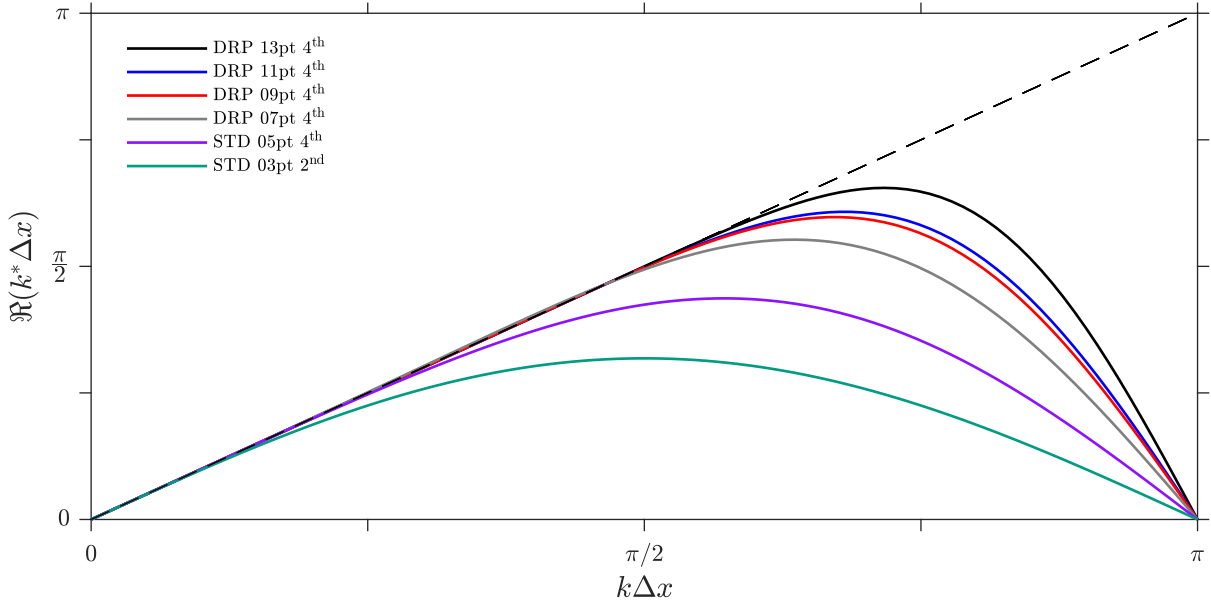
Figure 2.3: Modified wavenumber vs. wavenumber plot for the finite difference schemes used in this work.

thesis. The axes plotted are in terms of a dimensionless wavenumber $k\Delta x$ and $k^*\Delta x$, defined by taking the relationship between the wavenumber and wavelength Λ

$$k = \frac{2\pi}{\Lambda} \tag{2.3.18}$$

and multiplying by Δx to give

$$k\Delta x = \frac{2\pi\Delta x}{\Lambda}. \tag{2.3.19}$$

Note that all schemes fail to preserve the dispersion (no longer follow the line $k\Delta x = k^*\Delta x$) at $k\Delta x = \pi$; which if substituted into (2.3.19) corresponds to a wave with only two points per wavelength, $\Lambda/\Delta x = 2$. Integrating the difference between the actual and numerical wavenumber gives the integral error $\varepsilon_{\text{dispersion}}$ between k^* and k within the wavenumber range of interest $(0 < k\Delta x < \pi)$ is defined as

$$\varepsilon_{\text{dispersion}} = \int_0^\pi \left| k\Delta x - k^*\Delta x \right|^2 \mathrm{d}(k\Delta x). \tag{2.3.20}$$

Substituting (2.3.10) into (2.3.20) and assuming a centred stencil where N now includes the additional points for the DRP optimisation

$$\varepsilon_{\text{dispersion}} = \int_0^\pi \left| k\Delta x - \sum_{j=-N}^{N} a_j[\sin(jk\Delta x) - \mathrm{i}\cos(j\Delta x)] \right|^2 \mathrm{d}(k\Delta x) \tag{2.3.21}$$

shows that $\varepsilon_{\text{dispersion}}$ is a function of the coefficients a_j. To minimise the error, the condition

$$\frac{\partial \varepsilon_{\text{dispersion}}}{\partial a_j} = 0 \tag{2.3.22}$$

must be satisfied. This system of equations adds relations that use the extra degrees of freedom introduced by adding additional points to the stencil. Any number of additional coefficients may be used as free parameters for DRP optimisation. As an example, one coefficient (on each side of the stencil) is included to the end (and therefore beginning) of the system $\boldsymbol{A}$ from (2.3.7)

$$\begin{bmatrix}
D_{1,-N} & \dots & D_{1,j} & \dots & D_{1,N} \\
1 & \dots & 1 & \dots & 1 \\
x_{-N} - x_l & \dots & x_j - x_l & \dots & x_N - x_l \\
\dfrac{(x_{-N} - x_l)^2}{2} & \dots & \dfrac{(x_j - x_0)^2}{2} & \dots & \dfrac{(x_N - x_0)^2}{2} \\
\dfrac{(x_{-N} - x_l)^{i-1}}{(i-1)!} & \dots & \dfrac{(x_j - x_0)^{i-1}}{(i-1)!} & \dots & \dfrac{(x_N - x_0)^{i-1}}{(i-1)!} \\
\vdots & & \vdots & & \vdots \\
\dfrac{(x_{-N} - x_0)^{N-1}}{(N-1)!} & \dots & \dfrac{(x_j - x_0)^{N-1}}{(N-1)!} & \dots & \dfrac{(x_N - x_0)^{N-1}}{(N-1)!} \\
D_{N+1,1} & \dots & D_{N+1,j} & \dots & D_{N+1,N+1}
\end{bmatrix}
\begin{bmatrix}
a_{-N} \\ a_{-N+1} \\ a_{-N+2} \\ a_{-N+3} \\ a_j \\ \vdots \\ a_{N-1} \\ a_N
\end{bmatrix}
=
\begin{bmatrix}
B_{-N} \\ 0 \\ 1 \\ 0 \\ 0 \\ \vdots \\ 0 \\ B_N
\end{bmatrix}. \tag{2.3.23}$$

The solution to (2.3.22) has been included in the matrix $\boldsymbol{A}$ and solution vector $\boldsymbol{b}$, where

$$D_{ij} = \begin{cases} \sin\left(\dfrac{\pi}{2}(j-i)\right)\dfrac{1}{j-i} - \sin\left(\dfrac{\pi}{2}(j+1)\right)\dfrac{1}{j+i}, & \text{for } i \neq j \\ \dfrac{\pi}{2}, & \text{for } i = j, \end{cases} \tag{2.3.24}$$

and
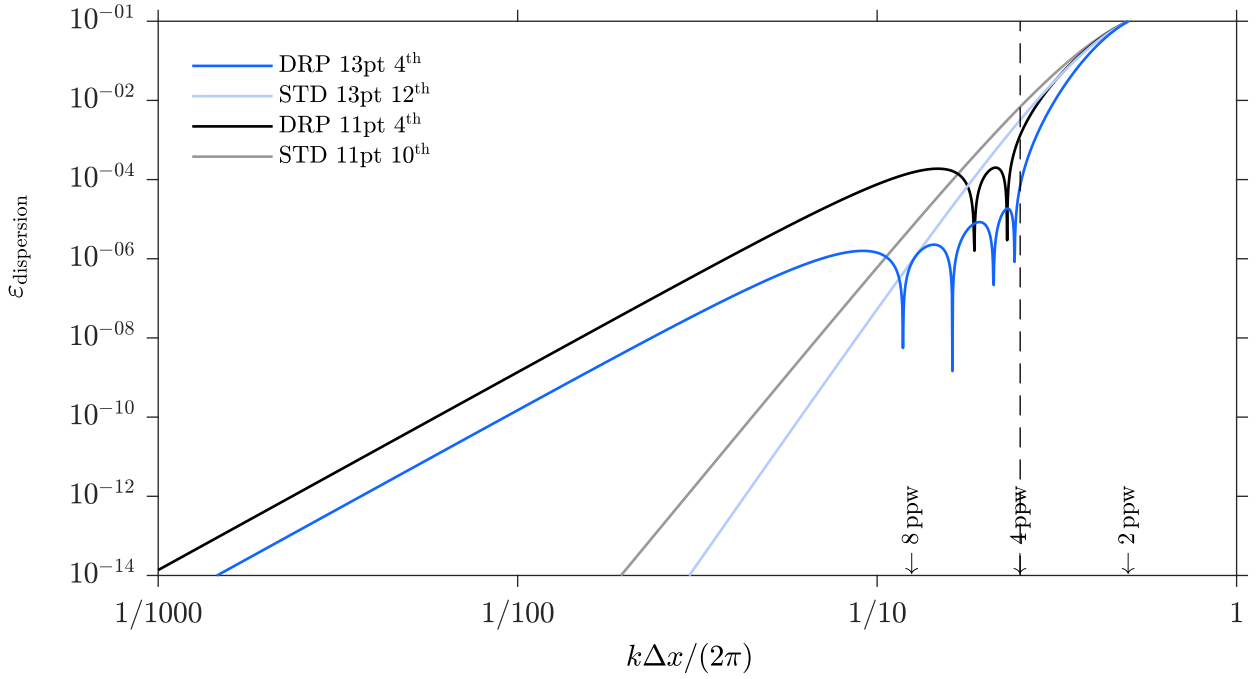
Figure 2.4: Dispersion error comparison between DRP schemes and their standard counterparts.

$$B_i = \frac{1}{i^2}\sin\left(i\frac{\pi}{2}\right) - \frac{\pi}{2i}\cos\left(i\frac{\pi}{2}\right). \qquad (2.3.25)$$

Equation (2.3.23) can be solved by Gaussian elimination. Appendix D shows the routine written by Dr. Nicolas Alferez used to generate the coefficients. The main stencil used (away from the walls, if present) to compute Euler fluxes is a 13 point, 4th order DRP scheme (*DRP 13pt 4*$^{\text{th}}$) for which a four point–per–wavelength cutoff was chosen for the optimisation. The additional eight points in the stencil are used to satisfy the constraints given in (2.3.22) and its characteristics are shown in figure 2.4. The range $1/8 < k\Delta x/(2\pi) < 1/2$ shows the greatest reduction in $\varepsilon_{\text{dispersion}}$ for the *DRP 13pt 4*$^{\text{th}}$ scheme. At the wavenumber cut–off of four points–per–wavelength the ratio of dispersion errors is $\varepsilon_{\text{dispersion}}^{DRP,13}/\varepsilon_{\text{dispersion}}^{STD,13} = 0.022$. At larger wavelengths the optimised schemes show more dispersion but the absolute magnitude is lower at those scales. Similar behaviour is seen for the *DRP 11pt 4*$^{\text{th}}$ scheme, used in the near wall region, but shows less advantage due to two fewer stencil points available for optimisation. Note that the derivative of viscous fluxes uses a 5 point, 4th order stencil throughout the domain, until $j = 2$ (and the equivalent at the upper wall, $j = ny - 1$) when the near wall schemes take over.

2.3.3 Wall treatment

The problem of implementing a wall boundary condition in compressible flows has been tackled by many different approaches. As described by Roache (1982), implementing a boundary condition on the density at the wall is best achieved using a staggered grid (a grid point either side of the wall), whereas implementing the other boundary conditions - the velocity and temperature - favours a point at the wall. These competing requirements make it inherently difficult to implement a wall that is robust to all kinds of flow conditions. If the non–staggered mesh is used and a mesh point coincides with the wall, then a one–sided derivative is required to compute fluxes at the wall. For continuity, this leads to an unstable scheme under certain conditions, such as separation at the wall. Gloerfelt (2001) expands on Roache's work to describe different ways of stabilising the wall implementation. One option is to fix the wall–normal pressure gradient to zero, by setting the pressure at the wall, and first grid point off the wall, to the same value. This allows the density to be computed from the equation of state (given the temperature wall boundary condition). The next section outlines the approach taken in CompReal. In terms of the finite difference stencils used in the near wall region, two approaches are possible. Either the stencil length can be kept the same and made progressively off centred (e.g. $N = 1$ and $M = 11$ at $j = 1$), or the stencil length is reduced and kept centred. The latter approach has the advantage that the scheme retains zero dissipation and all stencil points surplus to those used for the Taylor constraints are available for DRP optimisation. It is the latter approach that is implemented in this work. For the wall derivative, a one-sided 3 point, 2nd order scheme is used. Figure 2.5 shows a schematic of the derivative schemes used and includes the wall treatment. Table 2.1 lists the coefficients for the schemes used.
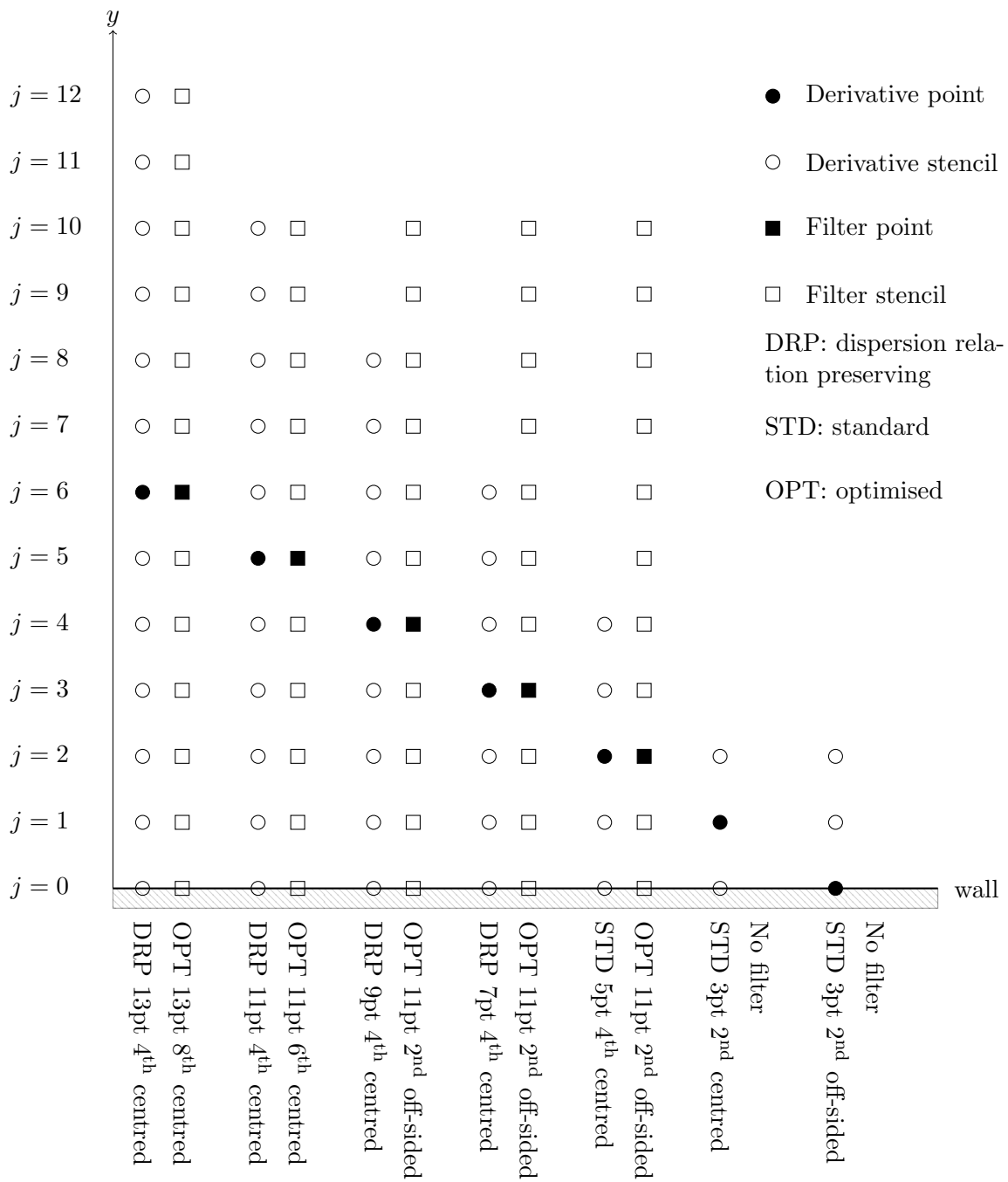
Figure 2.5: Sketch of finite difference and filtering stencils used. Lower wall shown (same procedure at upper wall). Further from the wall (i.e. at $j > 6$), the finite difference stencil – DRP 13pt 4th centred – and filter stencil – OPT 13pt 8th centred – are used.

i	DRP 13pt 4th	DRP 11pt 4th	DRP 9pt 4th	DRP 7pt 4th	5pt 4th	3pt 2nd	3pt 2nd
	$j \geq 6$	$j = 5$	$j = 4$	$j = 3$	$j = 2$	$j = 1$	$j = 0$
a_0	0.0000000000000000	0.0000000000000000	0.0000000000000000	0.0000000000000000	0	0	-3/2
$a_{+1} = -a_{-1}$	0.8910608923461686	0.8532797593597380	0.8437330226474239	0.8306659553971226	2/3	1/2	2
$a_{+2} = -a_{-2}$	-0.3128958166199386	-0.2603562460025875	-0.2475592505234550	-0.1924527643176981	-1/12		-1/2
$a_{+3} = -a_{-3}$	0.1126517314083857	0.0707590048837207	0.0612107939453125	0.0272798577460912			
$a_{+4} = -a_{-4}$	-0.0333125681563120	-0.0122273368595452	-0.0080617258591128				
$a_{+5} = -a_{-5}$	0.00688002952724707	0.0008130130864912					
$a_{+6} = -a_{-6}$	-0.0007292761780923						

Table 2.1: Finite difference coefficients. In periodic directions, the scheme *DRP 13pt* 4th *order* is used for the entire domain. If walls are present, the y direction stencil size is reduced on approach to the wall (here shown for the lower wall) from $j = 5$ to $j = 0$. Note: wall stencil at $j = 0$ is one sided. All coefficients have been computed.

2.4   Boundary conditions

For initial–value problems like freely–decaying isotropic turbulence simulations, periodic bound-ary conditions are applied in all directions. In practice, all runs were conducted using the Message Passing Interface (MPI) with edge cores connected to their neighbouring cores at the other end of the domain (in a Taurus shape). As a consequence, periodicity was achieved directly by inter-core communication and the use of extra (ghost) cells at the boundary of each processor's domain. In the x direction, taking f as an example function, this translates to

$$f_{i=0} = f_{i=nx}$$

$$f_{i=1} = f_{i=nx+1},$$

(2.4.1)

which assumes a periodic length l_x. The same is done in the y and z directions.

For the Couette flow simulations, periodic boundary conditions are applied in the homogeneous (streamwise and spanwise) directions and Dirichlet boundary conditions for velocity and temper-ature are applied at the walls at each (sub-step) iteration according to

$$
\begin{aligned}
u(y = 0) &= -u_{\mathrm{w}} & u(y = h) &= u_{\mathrm{w}} \\
v(y = 0) &= 0 & v(y = h) &= 0 \\
w(y = 0) &= 0 & w(y = h) &= 0 \\
T(y = 0) &= T_{\mathrm{w}} & T(y = h) &= T_{\mathrm{w}}.
\end{aligned}
$$

(2.4.2)

The remaining terms to calculate are the wall values of ρ, e_t and p. It is common to prescribe the wall boundary condition by setting the wall-normal gradient of pressure to zero in order to represent the physical condition of the wall exerting a force on the flow to obtain $v(y = 0) = 0$ and $v(y = h) = 0$. In fact the choice of pressure at the point outside of the physical domain is chosen such that $\partial p/\partial y = 0$ and $v(y = 0) = v(y = h) = 0$ (Tam and Dong, 1994). In CompReal, the wall boundary condition, developed by Dr. Nicolas Alferez and Dr. Emile Touber, does not prescribe the wall-normal pressure gradient. Instead the wall is assumed isothermal and ρ and e_t are computed at either wall by evaluating mass conservation and specific total energy,

respectively, that have been simplified by the Dirichlet boundary conditions. The pressure is computed at each (sub-step) iteration via the thermal equation of state recast in terms of the specific internal energy e

$$p = (\gamma - 1)\rho e. \qquad (2.4.3)$$

Note that the temperature field in the domain is computed from the caloric equation of state (2.1.8). The following process is applied at each time sub-step:

1. Set boundary conditions from (2.4.2)

2. Compute the derivatives of the Euler fluxes that have been simplified by the application of the Dirichlet boundary conditions: $\partial \mathcal{F}_{E,x}/\partial x$, $\partial \mathcal{F}_{E,y}/\partial y$ and $\partial \mathcal{F}_{E,z}/\partial z$. Away from the wall the *DRP 13pt 4*th scheme is used. Approaching the wall the stencil length is reduced to compute $\partial \mathcal{F}_{E,y}/\partial y$.

3. To compute ρ at the wall, continuity is solved at the wall point where ρ is from the previous sub-step (here shown for the lower wall, the upper wall is the same but the velocities are evaluated at $y = h$). *RHS* is used to indicate all terms other than the unsteady term and has the subscript of the variable it refers to:

$$\nabla \cdot (RHS_\rho) = \left.\frac{\partial \rho u(y=0)}{\partial x}\right|_{\mathrm{w}} + \left.\frac{\partial \rho v(y=0)}{\partial y}\right|_{\mathrm{w}} + \left.\frac{\partial \rho w(y=0)}{\partial z}\right|_{\mathrm{w}} \qquad (2.4.4)$$

4. The same approach is taken for the specific total energy, which is simplified using the Dirichlet boundary conditions:

$$\nabla \cdot (RHS_{e_t}) = -\left.\frac{\partial}{\partial x_j}\right|_{\mathrm{w}} \left(\rho[e + u_k^2(y=0)/2]\, u_j(y=0)\right) - \left.\frac{\partial}{\partial x_j}\right|_{\mathrm{w}} \left(pu_j(y=0)\right)$$
$$+ \frac{1}{\mathrm{Re}}\left.\frac{\partial}{\partial x_j}\right|_{\mathrm{w}} \left(\Sigma_{ij}(y=0)u_j(y=0)\right) - \frac{1}{\mathrm{RePrMa}^2(\gamma-1)}\left.\frac{\partial}{\partial x_j}\right|_{\mathrm{w}} \left(\kappa\left.\frac{\partial T(y=0)}{\partial x_j}\right|_{\mathrm{w}}\right). \qquad (2.4.5)$$

5. Once the divergence of the RHS of mass, momentum and specific total energy have been computed, the time integration scheme updates all primitive variables. At this point, the

equation of state can be used to compute the pressure field throughout the domain, including the walls.

2.5   Optimised filters

To maintain numerical stability when using centred schemes, discrete explicit filters are used to add artificial dissipation at small scales. Centred filters are used throughout the domain due to their zero-dispersion property. Approaching either wall, filtering in the wall-normal direction retains the same stencil used at $j = 5$ - an optimised 11 point, 6th order filter - and becomes progressively off-centred (e.g. $j = 3$ at the lower wall, N=3 and M=7). The wall point and the first point off the wall are not filtered. Away from the walls ($j \geq 5$ at the lower wall) the filter stencils are the same length as the finite difference schemes. All filters are optimised in wavenumber space to ensure numerical dissipation occurs at small scales with fewer or equal to four points per wavelength. A summary of the filter coefficients used is shown in table 2.2.

2.5.1   Filtering operation

A filtered function $\hat{f}(\eta)$ results from the convolution of a filter kernel G and the original (one dimensional) function $f(\zeta)$, defined as

$$\hat{f}(\eta) = \frac{1}{\Delta\eta} \int_{-\infty}^{\infty} G\left(\frac{\eta - \zeta}{\Delta\eta}, \zeta\right) f(\zeta) \mathrm{d}\zeta. \tag{2.5.1}$$

Constraints on G derive from the type of filtering required. For computational purposes, it is more convenient to define the filtering operation in discrete form. Following Berland *et al.* (2007), in a computational domain with coordinate x, a centred filtering operation of f at grid point x_l can be written

$$\hat{f}(x_l) = f(x_l) - \alpha \sum_{j=-N}^{N} d_j f(x_{l+j}). \tag{2.5.2}$$

where d_j are the filter coefficients. The transfer function of the filter is found by taking the spatial Fourier transform of (2.5.2)

$$G(k\Delta x) = 1 - \sum_{j=-N}^{N} d_j e^{\mathrm{i}jk\Delta x}. \tag{2.5.3}$$

The filter coefficients are found by enforcing two criteria on the behaviour of G. The first is that as $k\Delta x \to 0$

$$G(k) = 1 + \mathcal{O}(k\Delta x^\xi) \tag{2.5.4}$$

which translates to

$$\sum_{j=-N}^{N} d_j j^m = 0 \tag{2.5.5}$$

where $m = 1, ..., 2N - 1$, ξ is the order of convergence that can be achieved as long as there are sufficient stencil points $\xi = 2N$. The second condition requires that as $k\Delta x \to \pi$

$$G(\pi) = 0 \tag{2.5.6}$$

which translates to

$$\sum_{j=-N}^{N} (-1)^j d_j = 1 \tag{2.5.7}$$

and represents full damping at two points–per–wavelength. An additional constraint is to ensure zero damping when filtering a constant function

$$\sum_{j=-N}^{N} d_j = 0. \tag{2.5.8}$$

The equations (2.5.5), (2.5.7), and (2.5.8) represent a system of equations that can be solved to determine the filter coefficients d_j.

If more points are included in the stencil $N > \xi/2$, the additional points in the stencil can be used for optimisation. The following section outlines this procedure.

2.5.1.1   Dissipation-optimised filters

Applying the same analysis as for the finite difference schemes (see Bogey and Bailly (2004) for background to the method) and assuming a centred scheme, i.e. $M = N$, the Fourier transform of (2.5.3) is

$$[D_p^*(f^*)](k) = \left(\sum_{j=-N}^{N} d_j e^{ikj\Delta x} \right) f^*, \tag{2.5.9}$$

which simplifies to

$$D_p^*(k) = d_0 + 2 \sum_{j=1}^{N} d_j \cos(kj\Delta x) \tag{2.5.10}$$

due to the (imaginary) sinusoidal component summing to zero for centred filters $d_j = d_{-j}$. Its integral dissipation is

$$\varepsilon_{\text{dissipation}} = \int_0^{\pi/2} D_p^*(k) \mathrm{d}(k\Delta x) \tag{2.5.11}$$

which can be used to optimise the filter behaviour; enhancing its filtering strength at unresolved scales and minimising its effect at small wavenumbers (large scales). This is achieved in a similar manner to the finite difference stencils, namely by increasing the stencil size. The additional coefficients are found by solving the linear system minimising the integral dissipation (Bogey and Bailly, 2004)

$$\frac{\partial \varepsilon_{\text{dissipation}}}{\partial d_j} = 0. \tag{2.5.12}$$

The limits of the integral define the range over which the integral dissipation is minimised. In (2.5.11) the range corresponds to 4 points per wavelength ($k\Delta x = \pi/2$) to infinitely many points per wavelength for the mean signal ($k\Delta x = 0$). The results are shown in figure 2.6. The dissipation is reduced for the range $1/6 < k\Delta x/(2\pi) < 1/4$. At small scales the filter is tuned to remove energy at physically unresolved scales. At larger scales the optimised filters show larger dissipation than the standard scheme, but the overall magnitude is less than at the smallest resolved scales (4 points per wavelength). The optimisation constraints are added to the Taylor constraints to form a linear system that can be solved in the same way as the finite difference coefficients described in section 2.3.

2.5.1.2   Non-centred filtering

For three points close to the wall ($j = 2, 3, 4$), optimised filters are used. Instead of reducing the stencil length as is done for the finite difference scheme, the stencils maintain 11 points but

	OPT 13pt 8th	OPT 11pt 6th	OPT 11pt 2nd	OPT 11pt 2nd	OPT 11pt 2nd
	$j \geq 6$	$j = 5$	$j = 4$	$j = 3$	$j = 2$
a_{-6}	a_{+6}				
a_{-5}	a_{+5}	a_{+5}			
a_{-4}	a_{+4}	a_{+4}	0.0083912351450000		
a_{-3}	a_{+3}	a_{+3}	-0.0474025064440000	-0.0000545960100000	
a_{-2}	a_{+2}	a_{+2}	0.1214385477250000	0.0421247724460000	0.0525239010120000
a_{-1}	a_{+1}	a_{+1}	-0.2000630428120000	-0.1731031078410000	-0.2062991338110000
a_0	0.2025290156983785	0.2245598717068986	0.2400690478360000	0.2996158713520000	0.3535279982500000
a_{+1}	-0.1794082631518038	-0.1935503564144711	-0.2072692001400000	-0.2765436129350000	-0.3481423948420000
a_{+2}	0.1238033248972423	0.1224705172963396	0.1222631078440000	0.1312235065710000	0.1814818036190000
a_{+3}	-0.0648197120657933	-0.0544322892039974	-0.0471210628190000	-0.0234249664180000	0.0094408043700000
a_{+4}	0.0242842514706709	0.0152495468502111	0.0090148914950000	0.0139375617790000	-0.0776751004520000
a_{+5}	-0.0057720247824029	-0.0020173543815316	0.0018558122160000	-0.0245650957060000	0.0448873648630000
a_{+6}	0.0006479157828976		-0.0011768300440000	0.0130982878520000	-0.0099719618490000
a_{+7}				-0.0023086210900000	0.0001133594200000
a_{+8}					0.0001133594200000

Table 2.2: Filter coefficients used to maintain numerical stability. In periodic directions, the filter *OPT 13pt 4th order* was used for the entire domain. If walls are present, the y direction stencil size is reduced on approach to the wall from $j = 5$ to $j = 2$. Note there is no filtering in the y direction at the wall point and first point off the wall ($j = 0$ and $j = 1$, respectively at the lower wall). Centred filtering is performed throughout the domain in the x and z direction. All centred filter coefficients are computed.
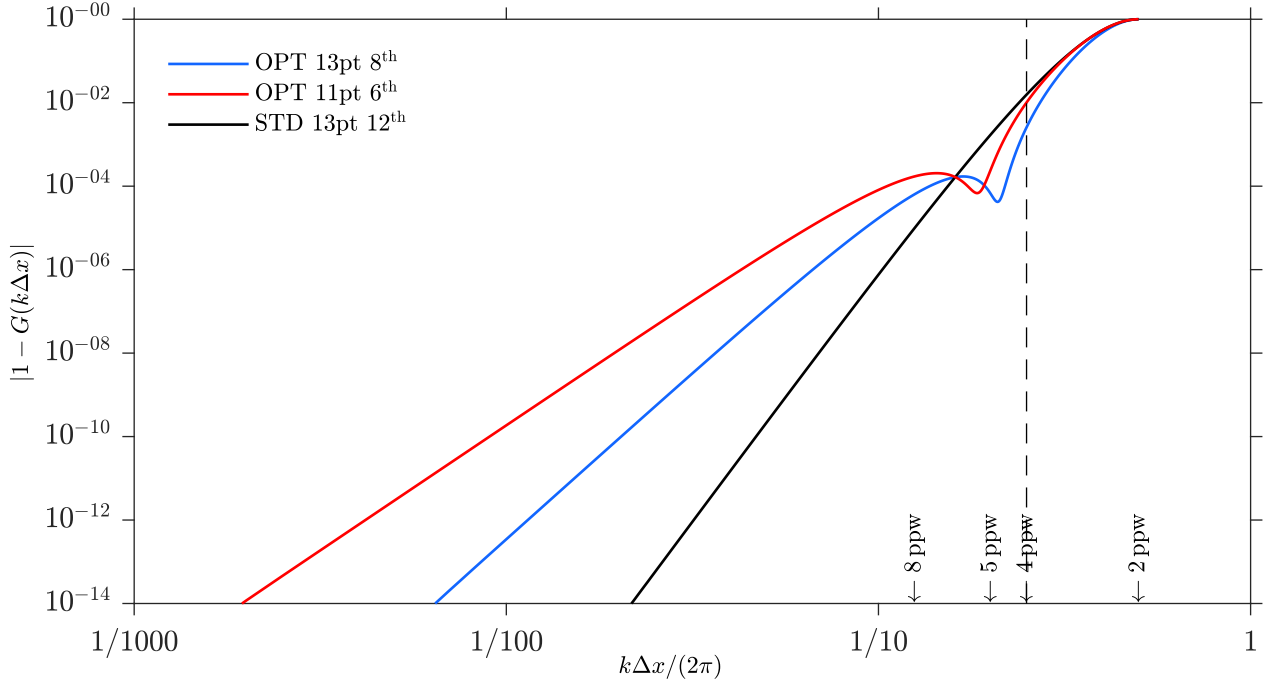
Figure 2.6: Integral dissipation for two optimised central filters used for majority of domain (away from walls). A standard filter is included for comparison. Dashed line at 4 points per wavelength indicates the cut-off scale used to optimise the filter.

become progressively off centred. The filtering operation now uses a non-centred filter where $M \neq N$. Following Berland *et al.* (2007)

$$\hat{f}(x_l) = f(x_l) - \alpha \sum_{j=-N}^{M} d_j f(x_{l+j}) \tag{2.5.13}$$

and its transfer function is (by taking the Fourier transform)

$$G(k\Delta x) = 1 - \sum_{j=-N}^{M} d_j e^{\mathrm{i}jk\Delta x}. \tag{2.5.14}$$

with both real part representing dissipation

$$\Re(G) = 1 - \sum_{j=-N}^{M} d_j \cos(kj\Delta x) \tag{2.5.15}$$

and imaginary part representing dispersion

$$\Im(G) = - \sum_{j=-N}^{M} d_j \sin(kj\Delta x). \tag{2.5.16}$$

The transfer function $G(k\Delta x)$ can be written in terms of a modulus $|G|$ (the dissipation being $1 - |G(k\Delta x)|$ and phase error $\phi_G(k\Delta x)$

$$G(k\Delta x) = |G|e^{i\phi_G}. \tag{2.5.17}$$

From this, similar to the centred filters, the integral error can be defined and includes both dissipation and dispersion errors

$$\varepsilon_{\text{diss+disper}} = \int_0^{\pi/2} \left[(1-\beta)|1 - G(k\Delta x)| + \beta|\phi_g(k\Delta x)| \right] \frac{\mathrm{d}(k\Delta x)}{k\Delta x}, \tag{2.5.18}$$

where β is a parameter that controls the relative importance of dissipation and dispersion errors for the optimisation process. In this work, three filters from Berland *et al.* (2007) were used in the near wall region and their coefficients are reproduced in table 2.2.

Chapter 3

Validation cases

This chapter presents six checks to ensure the code and post processing produces expected results. Taylor–Green vortex test results are shown to observe the effect that different strength filtering has on simulations with DRP and standard finite difference schemes. A three–dimensional laminar Couette case was run to check the implementation of the wall boundary conditions. A low Mach number turbulent Couette flow case was run to ensure that the mean streamwise velocity and root–mean–square profiles from the incompressible literature can be matched. The well-known streamwise rollers are visualised to ensure that the domain is sufficiently wide to sustain turbulence. The Helmholtz decomposition with walls is tested at the accuracy of the scheme. And finally the particle tracking algorithm is tested for convergence and, in two–dimensions, against an analytical solution.

3.1 Taylor–Green vortex

The use of dispersion–relation–preserving finite difference schemes and optimised filters is more expensive than standard schemes of the same order of convergence. The advantages are discussed in sections 2.3 and 2.5. This section presents results from a series of tests conducted by Dr. Nicolas Alferez and Dr. Emile Touber to demonstrate the importance of considering the filtering operation used to stabilise numerical schemes. For cases that are under–resolved, it is not just the order of convergence of the finite–difference scheme that should be considered but also the filtering strength. The ability to simulate the small scale physics depends not only on the type of filter, but also on the accompanying finite difference scheme. To show these effects, a three–dimensional low Mach number (set to 0.1) Taylor–Green vortex case was run at Reynolds number 1600; details
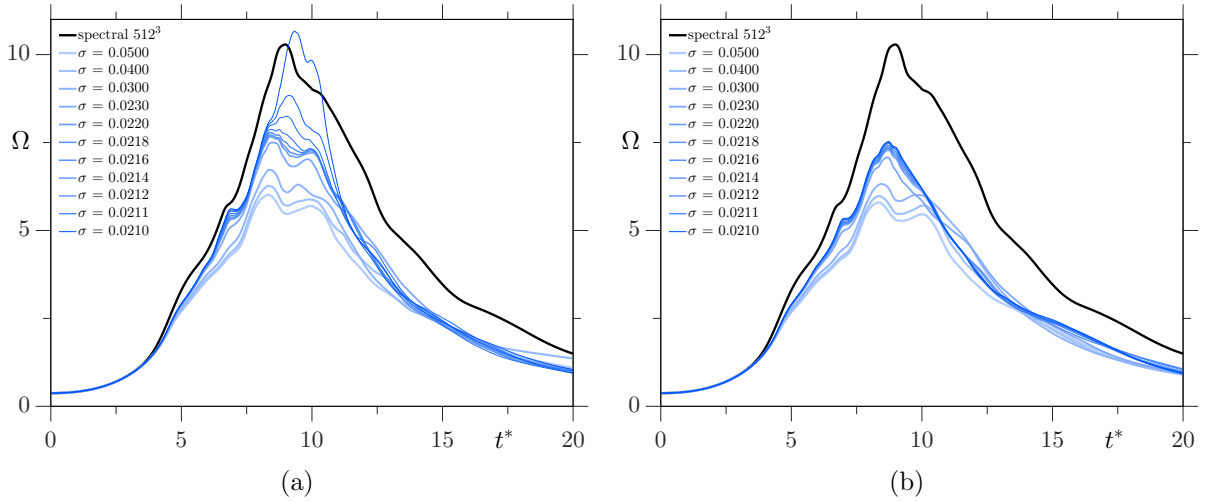
Figure 3.1: Time evolution of volume–averaged enstrophy. (a) 13 point, 4th order DRP scheme. (b) 13 point, 12th order standard scheme. $\sigma \in [0, 1]$ is the filter strength. (*Courtesy of Dr. N. Alferez and Dr. E. Touber.*)

can be found in DeBonis (2013). The grid was chosen to be under–resolved for the Reynolds number selected and had $nx = ny = nz = 64$ grid points. The mean enstrophy Ω

$$\Omega = \frac{1}{\rho_0 V} \int_V \rho \frac{\boldsymbol{\omega} \cdot \boldsymbol{\omega}}{2} \mathrm{d}V \tag{3.1.1}$$

where $\boldsymbol{\omega}$ is the vorticity, is compared for a 13 point, 4th order finite difference scheme, and a 13 point, 12th order standard equivalent. Both tests use an optimised 13 point, 8th order filter. The results were compared with the spectral results of van Rees *et al.* (2011). Figure 3.1 shows that peak enstrophy is lower for the standard scheme compared to the DRP scheme. The filter strength is $\sigma \in [0, 1]$, with $\sigma = 1$ representing maximum filtering. For the DRP scheme, as the filtering strength is reduced (darker blue color), it better matches the spectral result, recovering not only the enstrophy value but also the shape. The standard scheme struggles to achieve either and represents a larger amount of artificial damping than is needed for stabilisation.

3.2 Couette flow initialisation

To generate a statistically stationary turbulent flow, the simulations were initialised using the laminar Couette profile to which pseudo–random noise was added to initiate turbulence. The laminar solution assumes a steady, three–dimensional flow that is fully developed in the streamwise direction. The fluid is Newtonian and isotropic (linear relation between $\boldsymbol{\Sigma}$ and $\mathbf{D}$, and a linear dependence on only μ and λ, respectively). There is no streamwise pressure gradient and the flow is

maintained by the relative motion of two parallel plates, infinite in the homogeneous (streamwise and spanwise) directions and separated by the full channel gap h. The top plate moves at $+u_{\mathrm{w}}$, the bottom at $-u_{\mathrm{w}}$. The wall–normal coordinate origin is on the lower wall ($y = 0$). In addition, both walls are kept at constant temperature T_{w}. The viscosities and thermal conductivity are assumed to be constant. The laminar solution is (details found in A.2)

$$
\begin{aligned}
u &= u_{\mathrm{w}}(2y - 1), & \rho &= \frac{1}{T}, \\
v &= 0, & p &= \frac{\rho_{\mathrm{w}} T_{\mathrm{w}}}{\gamma \mathrm{Ma}^2}, \\
w &= 0, & T &= T_{\mathrm{w}} + 2u_{\mathrm{w}}^2(\gamma - 1)\mathrm{Pr}\mathrm{Ma}^2 y(1 - y), \\
& & e_{\mathrm{t}} &= \frac{p}{\rho(\gamma - 1)} + \frac{1}{2}(\boldsymbol{u} \cdot \boldsymbol{u}).
\end{aligned}
\tag{3.2.1}
$$

and figure 3.2 shows mean quantities (averaged over $10tu_{\mathrm{w}}/h$ time units and the homogeneous directions) of a three–dimensional laminar case to confirm that the correct implementation of the walls. In blue markers is a comparison with the analytical solution shown in (3.2.1). Pseudo–random noise is added to the laminar velocity field $\boldsymbol{u}$ and ρ. At each point in the domain, a number is generated such that rand $\in [0, 1]$. This is then modified to give the range -1 to 1, which produces a three–dimensional field of pseudo–random "fluctuations" that is added to the laminar profiles. The magnitude of the noise added to the velocity field follows a parabolic profile in the wall–normal direction to ensure that the boundary conditions are maintained, whilst producing maximum fluctuations in the centre of the channel. As an example, a noisy profile $u_n(t = 0)$ results from adding noise to a laminar profile $u_l(t = 0)$ according to

$$
u_n = u_l + \alpha(2\,\mathrm{rand} - 1)(y(1 - y)).
\tag{3.2.2}
$$

For ρ, no parabolic profile is used, i.e.

$$
\rho_n = \rho_l(1 + \alpha(2\,\mathrm{rand} - 1)).
\tag{3.2.3}
$$

For all cases, the coefficient $\alpha = 0.25$. The fluctuations introduced are then forced by the wall motion at a sufficiently high Reynolds number to generate a flow field that approximates a true turbulent flow field. The simulation is allowed to develop for a sufficiently long time before

collecting statistics that can be compared with the literature. Due to the small amount of available data for compressible Couette flow, this comparison was made with a low Mach number case, as outlined in the next section.
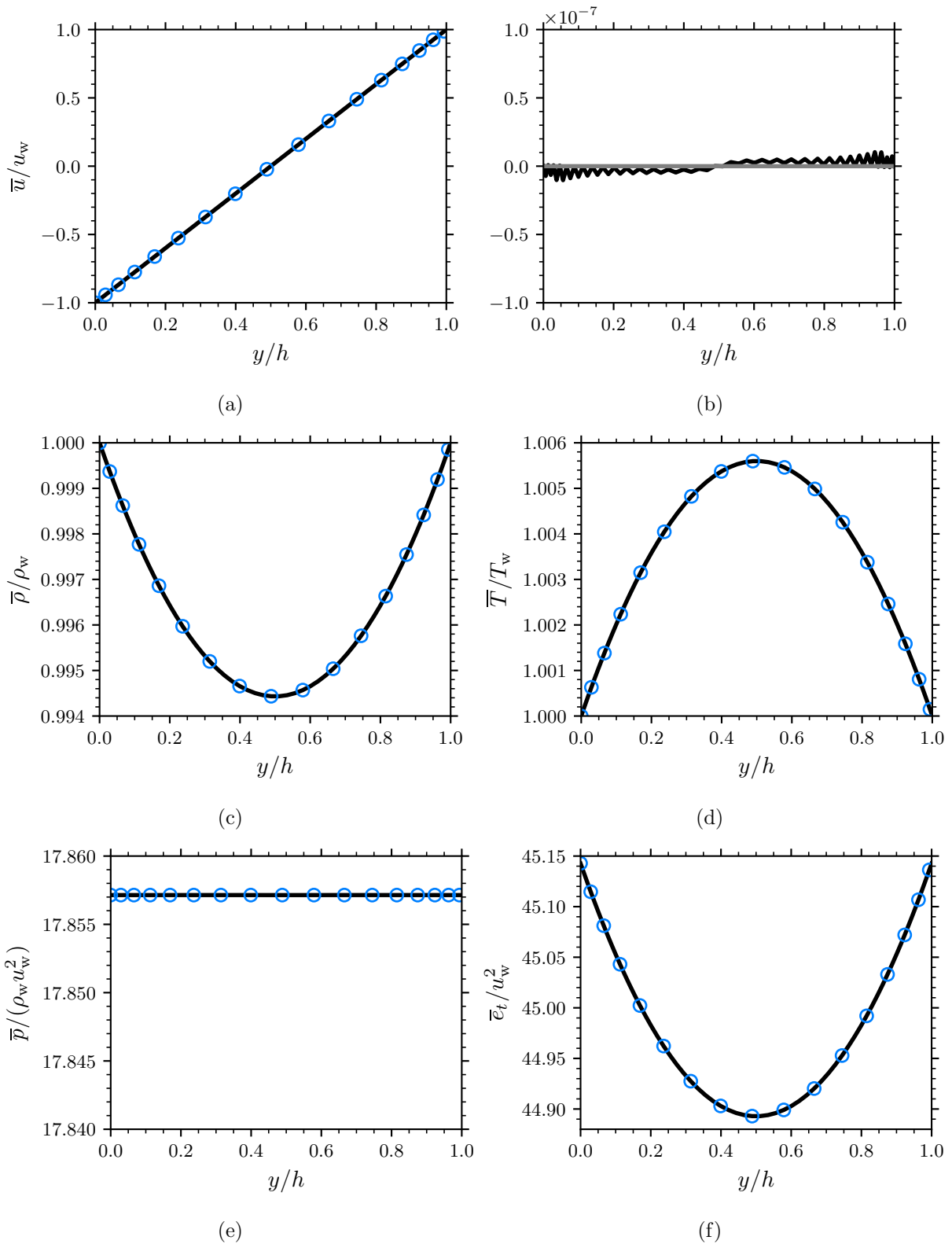
Figure 3.2: Mean profiles of three–dimensional laminar Couette flow. Black lines are simulation data, blue marker are the analytical solutions from (3.2.1). In (b) $\overline{v}/u_{\mathrm{w}}$ is shown in black and $\overline{w}/u_{\mathrm{w}}$ is shown in grey (note that data is saved to single precision).

3.3 Low Mach number Couette flow

To validate the numerical method for the main configuration used in this thesis, a $\mathrm{Ma} = 0.1$, $\mathrm{Re} = 10^4$ ($\mathrm{Re}_\tau \approx 270$) case was run to compare with incompressible Couette data. The simulation was started and managed in the same way as the high Mach number runs; the details of all runs are found in table 5.1. There is little published data for compressible plane Couette flow and of those available, the majority are about stability analysis (see for example Duck *et al.* (1994); Chagelishvili *et al.* (1994); Malik *et al.* (2008)). Figure 3.3a compares the mean velocity profile with Pirozzoli *et al.* (2014) and Avsarkisov *et al.* (2014) (log–law only). All the data collapse onto the log–law of the wall, with the von Kármán constant equal to 0.41 and constant of integration equal to 5. Buell (1991) conducted one of the first compressible Couette flow simulations at $\mathrm{Re} = 6 \times 10^3$ and $\mathrm{Ma} = 1.5$. His root–mean–square (rms) velocity profiles are included in figure 3.3c (grey line). In comparison, incompressible Couette flow has been studied in detail and the data of Pirozzoli *et al.* (2014) (blue line, $\mathrm{Re}_\tau = 260$) and Avsarkisov *et al.* (2014) (red markers, $\mathrm{Re}_\tau = 250$) are shown for comparison. There is good agreement in the viscous sub layer and peak $u_\mathrm{r.m.s.}$ and $v_\mathrm{r.m.s.}$ except for the data from Buell (1991) (which was digitised from his paper). Away from the wall at $y^+ > 50$, case V has reasonable agreement except for $u_\mathrm{r.m.s.}$, which is likely due to the long time series needed for full convergence. For Pirozzoli *et al.* (2014), the time window used for averaging is $t_\mathrm{av} u_\tau / h = 36.1$, whereas for case V it is 6.4. This is due to the requirement to resolve acoustic wave motion in time, which at $\mathrm{Ma} = 0.1$ results in a separation of wall and acoustic time scales by an order of magnitude. Figure 3.3d shows the total stress $\overline{\tau}_\mathrm{total}$ is within 3% of a constant value of unity at the centreline.

3.4 Streamwise rollers

Poiseuille and Couette flow share many similar turbulent structures in the region away from the wall. One key difference seen only in Couette flow are coherent structures that span the full length, and a substantial width, of the domain. They are long streamwise rollers that are associated with streamwise streaks. They can be seen visually from the averaged (in time and the streamwise direction) velocity field on a slice normal to the $z-y$ direction (front view). Plotting v and w shows large cells of counter–rotating vortices that are roughly circular in shape and span the full height of the channel (Hamilton *et al.*, 1995). These patterns have been seen experimentally by Dauchot

and Daviaud (1995) who found that after transition, the turbulence was self–sustaining, however the streamwise rollers would remain only if constantly excited by a wire placed in the flow. Kitoh and Umeki (2008) performed an experiment at $\mathrm{Re} = 7.5 \times 10^3$ in which long streamwise structures were observed without any disturbance, although they meandered in the spanwise direction due to experimental disturbances, making it difficult to define a streamwise length scale. With the addition of vortex generators, the streamwise vortices became much better defined and showed additional streaks at oblique angles branching from the main streamwise ones. Similar features have been demonstrated in numerical simulations. Figure 3.4 shows streamwise rollers from the $\mathrm{Ma} = 0.1$ and $\mathrm{Ma} = 3.0$, $\chi = 0$ cases and figure 3.5 shows the same for the $\mathrm{Ma} = 3.0$, $\chi = 0$, case A simulation. The length of the longest arrow on the plots represents the maximum speed in the flow; all other arrows are scaled accordingly. Both cases demonstrate that the small domain width, $z/h = 3$ is sufficiently large to contain two streamwise vortices; the minimum required to sustain the turbulence regeneration mechanism (Hamilton *et al.*, 1995).
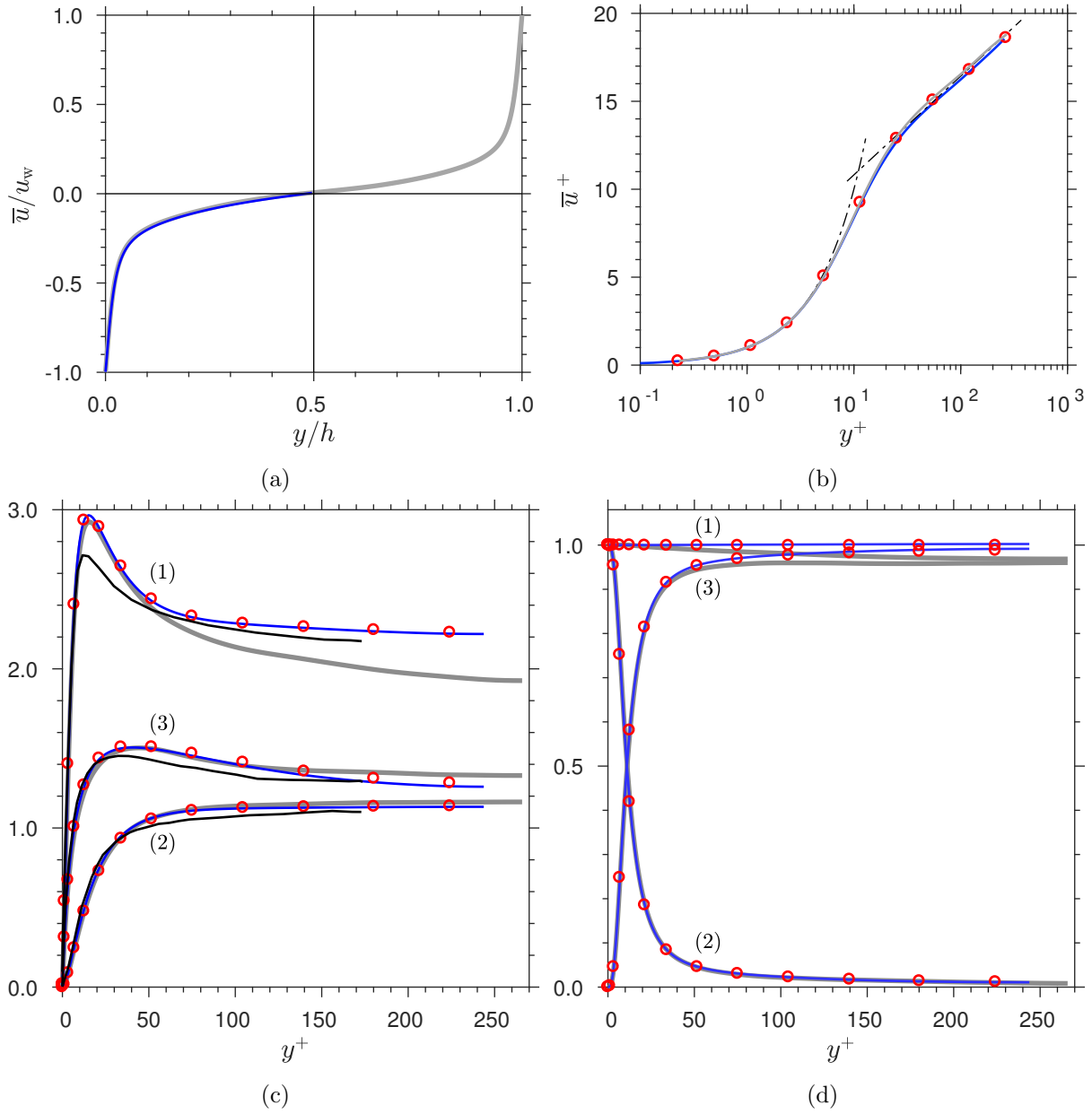
Figure 3.3: Mean streamwise velocity profile for Ma = 0.1 case (V): (a) full channel width; (b) in wall units and averaged about $y = h/2$, the von Kármán constant is 0.41 and the constant of integration is 5. The Ma = 0.1 case (V) is shown in grey, the incompressible Couette data of Pirozzoli *et al.* (2014) in blue and Avsarkisov *et al.* (2014) in red markers. (c) Root–mean–square velocity profiles: (1) is $u_{\text{r.m.s.}}$, (2) is $v_{\text{r.m.s.}}$ and (3) is $w_{\text{r.m.s.}}$. (d) Shear stress decomposition: (1) is $\overline{\tau}_{\text{total}}$, (2) is $-\overline{\rho}\,\widetilde{u''v''}/\overline{\tau}_{\text{w}}$, (3) is $(\mathrm{d}\overline{u}/\mathrm{d}y)/(\mathrm{Re}\,\overline{\tau}_{\text{w}})$. The Ma = 0.1 case (V) is shown in grey, the incompressible Couette data of Pirozzoli *et al.* (2014) in blue and Avsarkisov *et al.* (2014) in red markers, and in black is the data of Buell (1991). Both figures have been averaged about $y = h/2$.
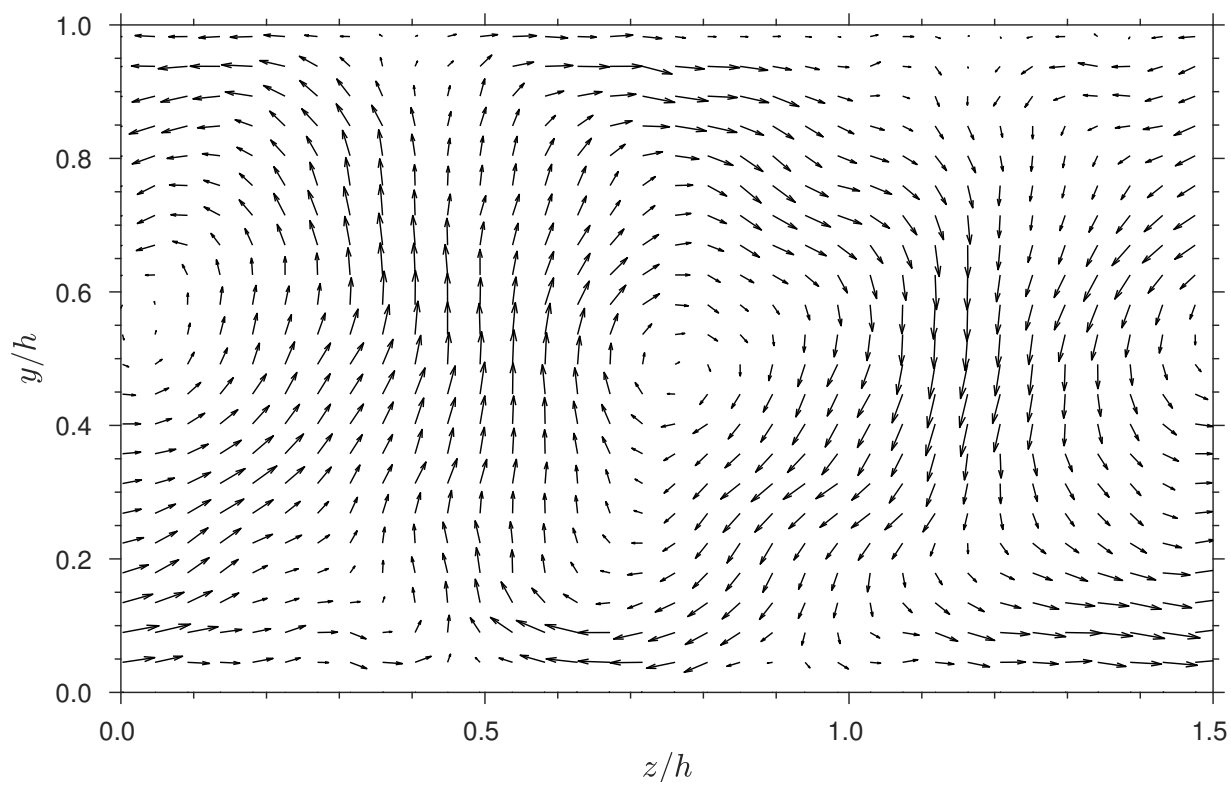
(a)
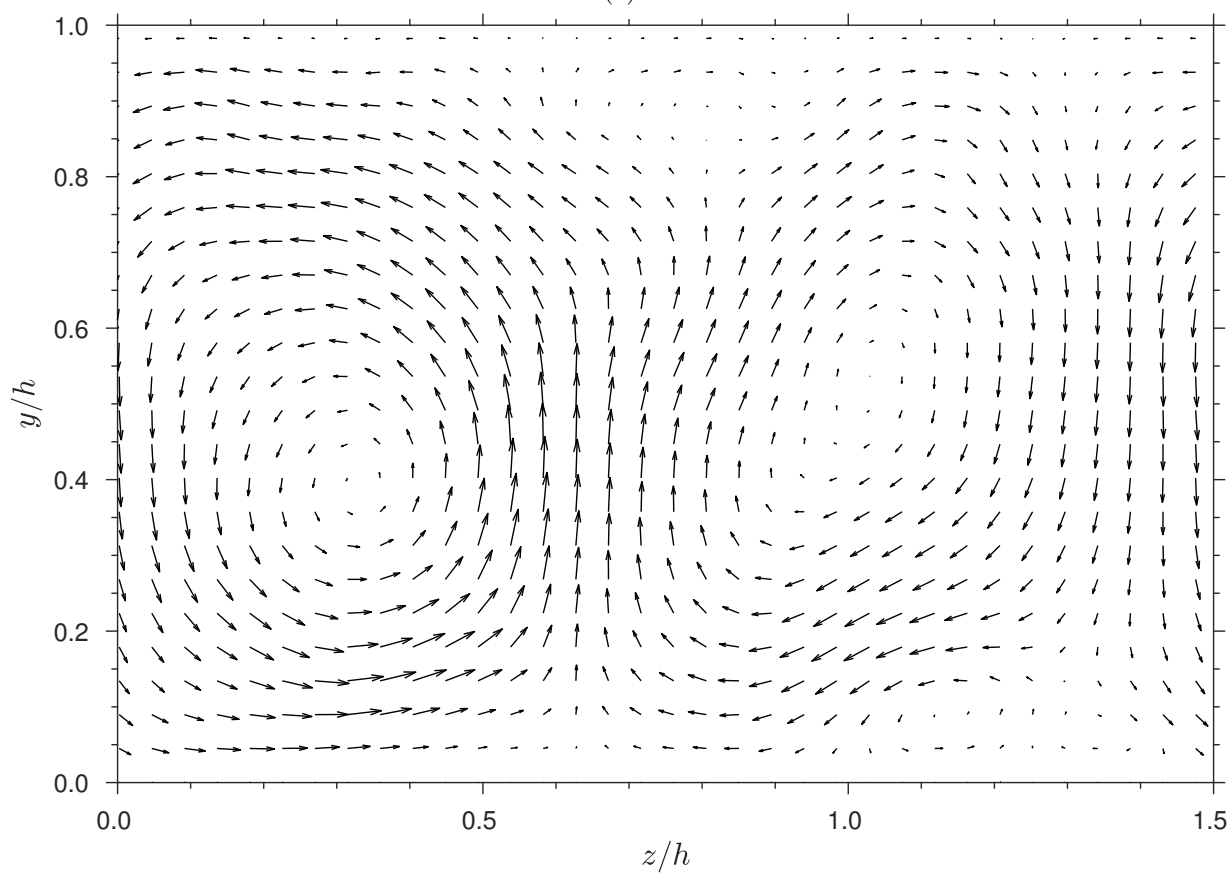
(b)

Figure 3.4: Streamwise vortices of (a) Ma = 0.1 case V; (b) Ma = 3.0, $\chi = 0$, case C.
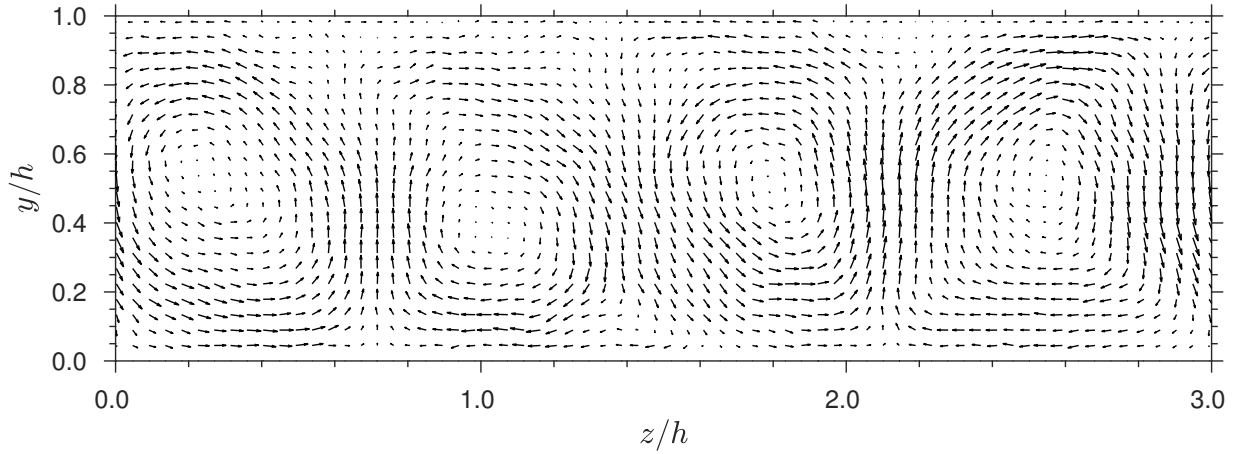
Figure 3.5: Streamwise vortices of Ma = 3.0, $\chi = 0$, case A.

3.5   Helmholtz decomposition with walls

In order to visualise and assess the influence of the bulk viscosity on the Couette flow fields, a Helmholtz decomposition can be used to separate the solenoidal and dilatational velocity fields. A continuously differentiable vector field $\boldsymbol{F}$ can be represented as the sum of an irrotational term $\boldsymbol{\nabla}\Phi$, a solenoidal term $\boldsymbol{\nabla} \times \boldsymbol{A}$, and a harmonic term $\boldsymbol{H}$, which is both irrotational and solenoidal,

$$\boldsymbol{F} = \boldsymbol{\nabla}\Phi + \boldsymbol{\nabla} \times \boldsymbol{A} + \boldsymbol{H}, \qquad (3.5.1)$$

where Φ is a scalar potential, the gradient of which is irrotational, and $\boldsymbol{A}$ is a vector potential, the curl of which is solenoidal. See Bhatia *et al.* (2014) for an in–depth summary of these definitions and the methods of performing the decomposition. The harmonic term represents the mean value of the vector field. To find Φ and $\boldsymbol{A}$ two approaches can be taken. The first is to use the Helmholtz decomposition that guarantees $\boldsymbol{F}$ is unique as long as its divergence and curl tend to zero faster than $1/x^2$ as $x \to \infty$ where $|\boldsymbol{x} - \boldsymbol{x}'| \approx x$ at the large x limit (Griffiths, 1999). While this works well for periodic domains, in the case of wall–bounded flows, the wall poses a problem as the domain is no longer infinite. If only Φ is required, an alternative approach is to take the divergence of (3.5.1) and solve the resulting Poisson equation

$$\nabla \cdot \boldsymbol{F} = \nabla \cdot (\boldsymbol{\nabla}\Phi). \qquad (3.5.2)$$

The existence of a solution to (3.5.2) requires the compatibility condition to be met (Strauss, 2007, p. 161), i.e.

$$\int\limits_V \nabla \cdot \boldsymbol{F} \, \mathrm{d}V = \int\limits_S \boldsymbol{\nabla}\Phi \cdot \boldsymbol{n} \, \mathrm{d}S, \tag{3.5.3}$$

where V is the volume of the domain and S is its surface.

3.5.1 Solving for Couette flow

Applying (3.5.2) to Couette flow results in

$$\nabla \cdot \boldsymbol{u} = \nabla \cdot (\boldsymbol{\nabla}\Phi), \tag{3.5.4}$$

where the dilatational and solenoidal velocity fields are $\boldsymbol{u}_{\mathrm{dil}} \equiv \boldsymbol{\nabla}\Phi$ and $\boldsymbol{u}_{\mathrm{sol}} \equiv \boldsymbol{u} - \boldsymbol{\nabla}\Phi$, respectively. The periodic boundary conditions in the streamwise and spanwise directions enable the derivatives in those directions to be computed in Fourier space. The fields $\nabla \cdot \boldsymbol{u}$ and Φ are dependent on all three coordinate directions, therefore the Fourier transform is taken in the x and z directions. This leaves only a dependence on y in real space, forming a one–dimensional Poisson equation for each k_x, k_z wavenumber pair, represented by the index i and k, respectively. This is achieved by writing (3.5.4) in terms of approximate Fourier series for Φ and $\nabla \cdot u$:

$$\Phi(x,y,z) = \sum_{i=-N}^{N} \sum_{k=-M}^{M} c^{ik}(y) \exp\left[\mathrm{i}\left(\frac{2\pi ix}{l_x} + \frac{2\pi kz}{l_z}\right)\right] \tag{3.5.5}$$

$$\nabla \cdot u(x,y,z) = \sum_{i=-N}^{N} \sum_{k=-M}^{M} d^{ik}(y) \exp\left[\mathrm{i}\left(\frac{2\pi ix}{l_x} + \frac{2\pi kz}{l_z}\right)\right]. \tag{3.5.6}$$

Note that $\mathrm{i} = \sqrt{-1}$ and i and k are indices for the x and z directions, respectively. The limits N and M are the terms in the Fourier series that represents the Nyquist wavenumber, a value that depends on the grid resolution. Equation (3.5.4) is then solved for each wavenumber pair according to

$$d^{ik}(y) = \left(-\left(\frac{2\pi ix}{l_x}\right)^2 - \left(\frac{2\pi kz}{l_z}\right)^2 + \frac{\mathrm{d}^2}{\mathrm{d}y^2}\right) c^{ik}(y). \tag{3.5.7}$$

The wall–normal derivative can be approximated by a centred second order finite difference scheme,

$$\left.\frac{\mathrm{d}^2 c^{ik}}{\mathrm{d}y^2}\right|_{y_j} = \frac{c_{j-1}^{ik} - 2c_j^{ik} + c_{j+1}^{ik}}{\Delta y^2} + O(\Delta y^2) \tag{3.5.8}$$

where c_j^{ik} is the value of $c^{ik}(y)$ evaluated at the y_j, where $y \in [0, h]$, $y_j = j\Delta y$, $j = 0, ..., ny, ny + 1$ and $\Delta y = h/(ny + 1)$. Equation (3.5.7) can be written as a linear system of equations in matrix form

$$\mathbf{A}x = r \tag{3.5.9}$$

where $x = c_0^{i,k}, ...c_{ny}^{i,k}, c_{ny+1}^{i,k}$ and $r = 0, d_1^{ik}, ..., d_{ny}^{ik}, 0$ and $\mathbf{A}$

$$\mathbf{A} = \begin{bmatrix} b_0 & a & 0 & \dots & & 0 \\ a & b_1 & \ddots & \ddots & & \vdots \\ 0 & \ddots & \ddots & \ddots & & 0 \\ \vdots & \ddots & \ddots & b_{ny} & & a \\ 0 & \dots & 0 & a & & b_{ny+1} \end{bmatrix} \tag{3.5.10}$$

$$a = \frac{1}{\Delta y^2}$$

$$b_j = -\left(\frac{2\pi i x}{l_x}\right)^2 - \left(\frac{2\pi k z}{l_z}\right)^2 - \frac{2}{\Delta y^2} \tag{3.5.11}$$

with $j = 0, ..., ny + 1$.

The boundary condition is found from the fact that there is no contribution from the dilatational velocity field to the wall motion, i.e. $u_{\text{dil}} = 0$ at $y = 0$ and $y = h$. Hence Φ obeys the von Neumann boundary condition

$$\frac{\mathrm{d}\Phi}{\mathrm{d}y} = 0 \quad \text{at} \quad y = 0 \quad \text{and} \quad y = h. \tag{3.5.12}$$

The compatibility condition (3.5.3) is satisfied due to the fact that there is no net velocity dilatation in the flow domain

$$\int_V \nabla \cdot u \, \mathrm{d}V = \int_S \boldsymbol{\nabla}\Phi \cdot n \, \mathrm{d}S = 0. \tag{3.5.13}$$

The von Neumann boundary condition is valid for every wavenumber pair and hence to each c_j^{ik}. The boundary conditions of the Poisson equation follow the implementation given in Pugh (2009). The wall–normal derivative is approximated using a second–order central difference scheme which introduces a ghost point at y_{-1} and at y_{ny+2}. Taking the lower wall as an example (the same

procedure applies at the upper wall):

$$\frac{\mathrm{d}c^{ik}}{\mathrm{d}y}\bigg|_{y=0} \approx \frac{c_1^{ik} - c_{-1}^{ik}}{2\Delta y} = 0. \tag{3.5.14}$$

This can be combined with a second–order accurate finite difference scheme for the second derivative at the wall point

$$\frac{\mathrm{d}^2 c_0^{ik}}{\mathrm{d}y^2} \approx \frac{c_1^{ik} - 2c_0^{ik} + c_{-1}^{ik}}{\Delta y^2} \tag{3.5.15}$$

to remove the term c_{-1}^{ik},

$$\frac{\mathrm{d}^2 c_j^{ik}}{\mathrm{d}y^2} \approx \frac{2c_1^{ik} - 2c_0^{ik}}{\Delta y^2}. \tag{3.5.16}$$

The matrix $\boldsymbol{A}$ with boundary conditions (labelled $\mathbf{A}_{bc}$) becomes

$$\mathbf{A}_{bc} = \begin{bmatrix} b_0 & 2a & 0 & \dots & & 0 \\ a & b_1 & \ddots & \ddots & & \vdots \\ 0 & \ddots & \ddots & \ddots & & 0 \\ \vdots & \ddots & \ddots & b_{ny} & & a \\ 0 & \dots & 0 & 2a & b_{ny+1} \end{bmatrix}, \tag{3.5.17}$$

3.5.2   Poisson solver

The Poisson solver used to extract the scalar potential of the velocity field (3.5.7) uses a second–order accurate finite difference scheme to compute the derivative in the y direction. Figure 3.6a demonstrates that the convergence accuracy for a range of grids is at second order. Figure 3.6b shows the result of solving an analytical test problem

$$-\frac{\mathrm{d}^2 \phi}{\mathrm{d}y^2} = f(y) \tag{3.5.18}$$

defined on $y \in [0, 2\pi] \subset \mathbb{R}$, where

$$f(y) = 2\sin(y) + y\cos(y) \tag{3.5.19}$$

with Dirichlet boundary conditions

$$\phi(0) = 0, \quad \phi(2\pi) = 2\pi. \tag{3.5.20}$$

The analytical solution is

$$\phi(y) = y\cos(y). \tag{3.5.21}$$

3.5.3   Full resolution test

For non–uniform grids, the original data is interpolated onto a constant spacing grid, ideally taken as the smallest of the original domain, i.e. the spacing between the wall point and first point off the wall. Figure 3.6c shows Θ of the extracted $\boldsymbol{u}_{\text{sol}}$ of case C in table 5.1, where the interpolated grid spacing is taken as the wall spacing of the physical grid. This is obtained by subtracting Θ of the dilatational field from the full field, i.e. $\Theta_{\text{sol}} \equiv \Theta - \Theta_{\text{com}}$. Analytically this is zero for Couette flow and the figure shows that Θ_{sol} is close to zero at the precision of the slice data (single precision).

3.5.4   Large domain assessment

The accuracy of the procedure to extract the solenoidal and dilatational velocity fields can be assessed by plotting the velocity dilatation of the solenoidal velocity field. The decomposition is memory–heavy to post–process and it was not possible to generate an interpolated grid with uniform grid spacing equal to the wall grid spacing of the original grid for the large domain (three hundred million point) cases. Instead, twice the grid spacing at the wall was used. This led to an inaccuracy in the near–wall region, which results in some velocity dilatation remaining in the solenoidal velocity field. At the first point off the wall, the value of Θ for the solenoidal field is approximately 10% of Θ for the dilatational field (shown in figure 3.7). By the second point it has reduced to 3% (shown in figure 3.8). The error is concentrated in areas of large gradients in Θ, indicating that the original profile of Θ is not well captured by the interpolated grid.

3.5.5   Wavenumber cut–off

A filter with a bandwidth of five wavenumbers was applied in Fourier space to wall-normal slices of the Couette data to indicate how well the selected grid resolves small–scale dilatational

(a)

(b)

(c)
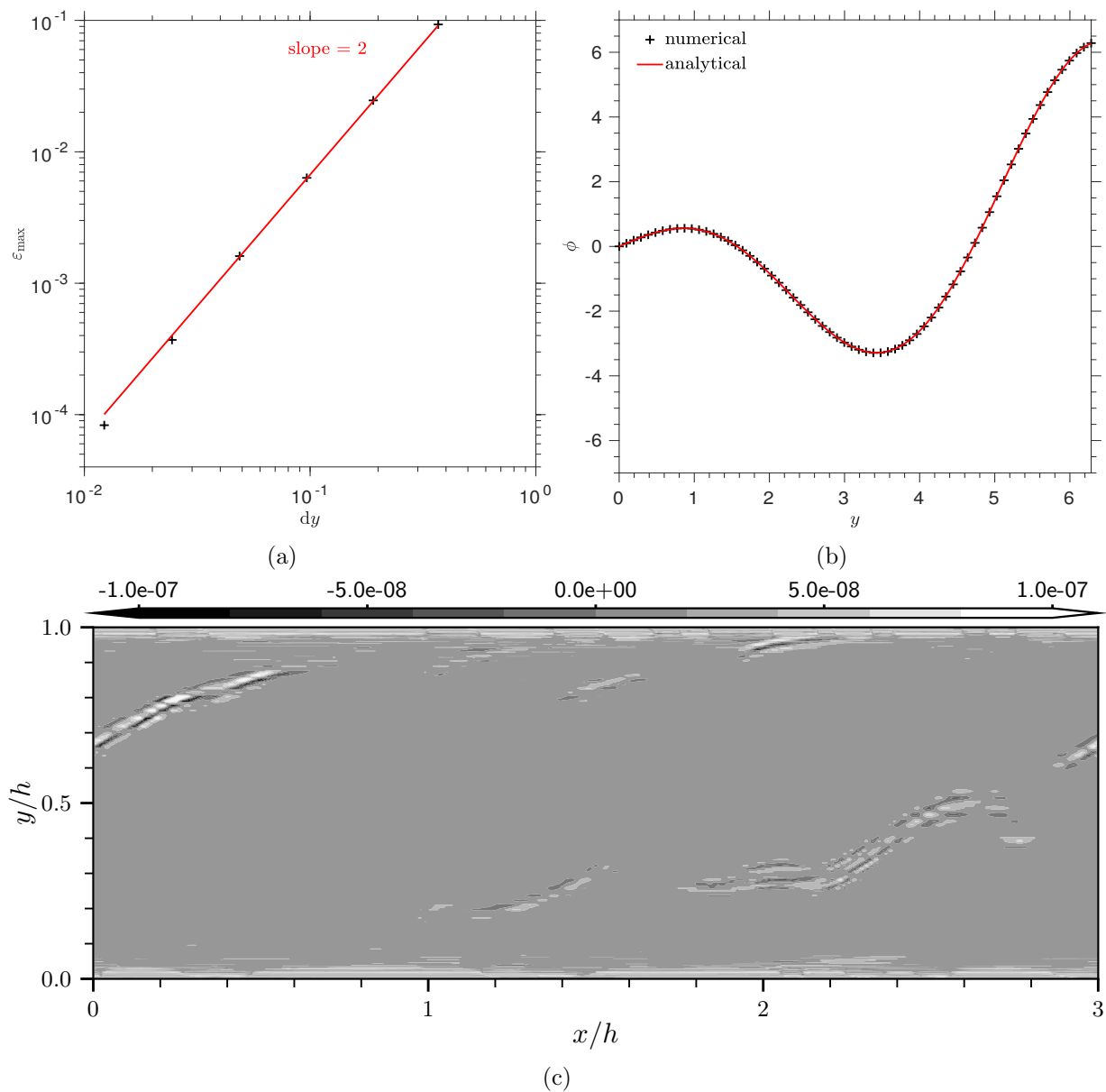
Figure 3.6: (a) convergence of maximum error of Poisson solver; (b) comparison of numerical (black crosses) and analytical (red line) solution of equation (3.5.21); (c) divergence of solenoidal velocity field. Small domain case, $\chi = 0$ case C.
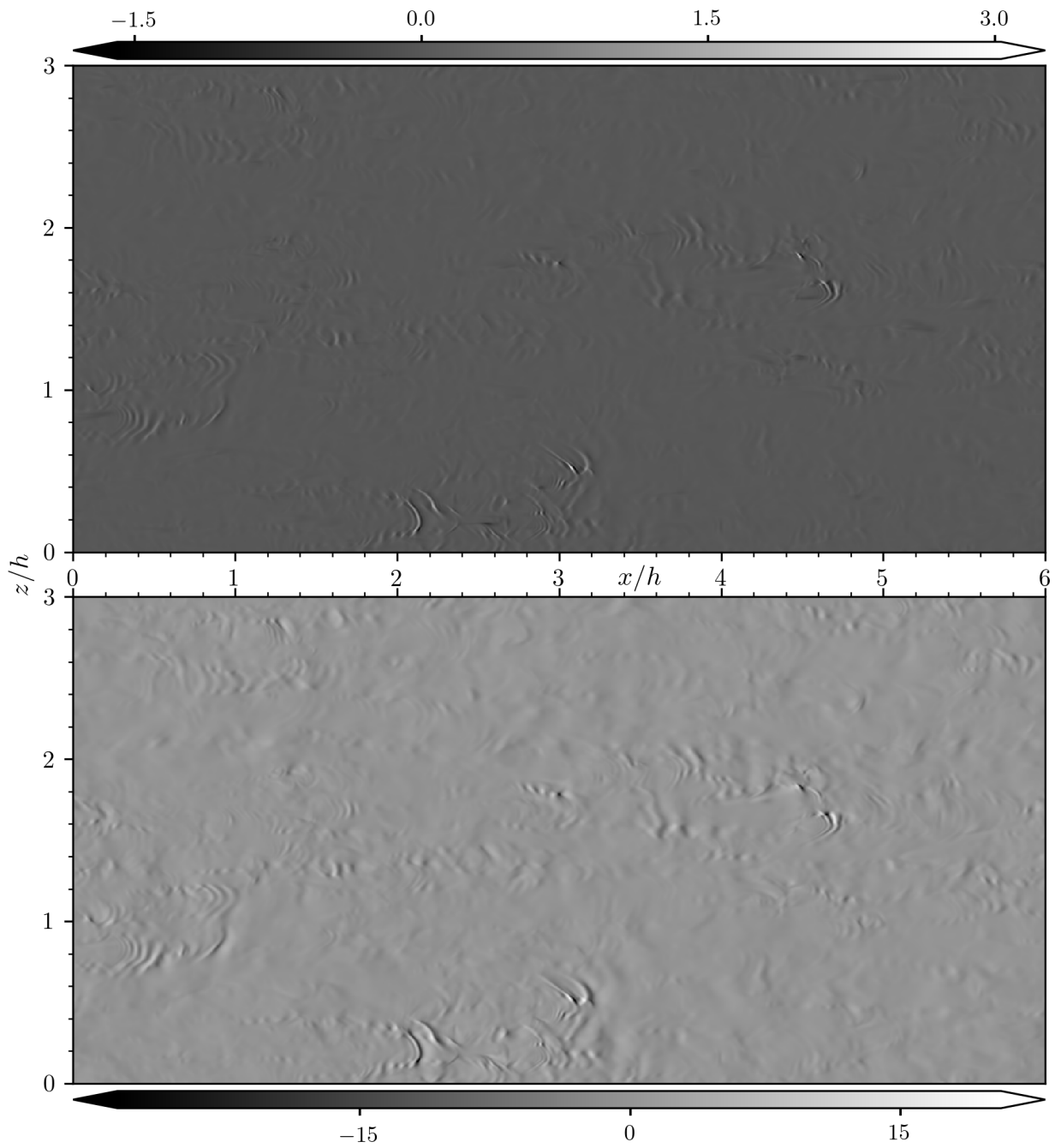
Figure 3.7: Top view of velocity dilatation of case A, $\chi = 0$, at $j = 1$ (first point off the wall). Top panel: Θ of solenoidal velocity field, bottom panel: Θ of dilatational velocity field.
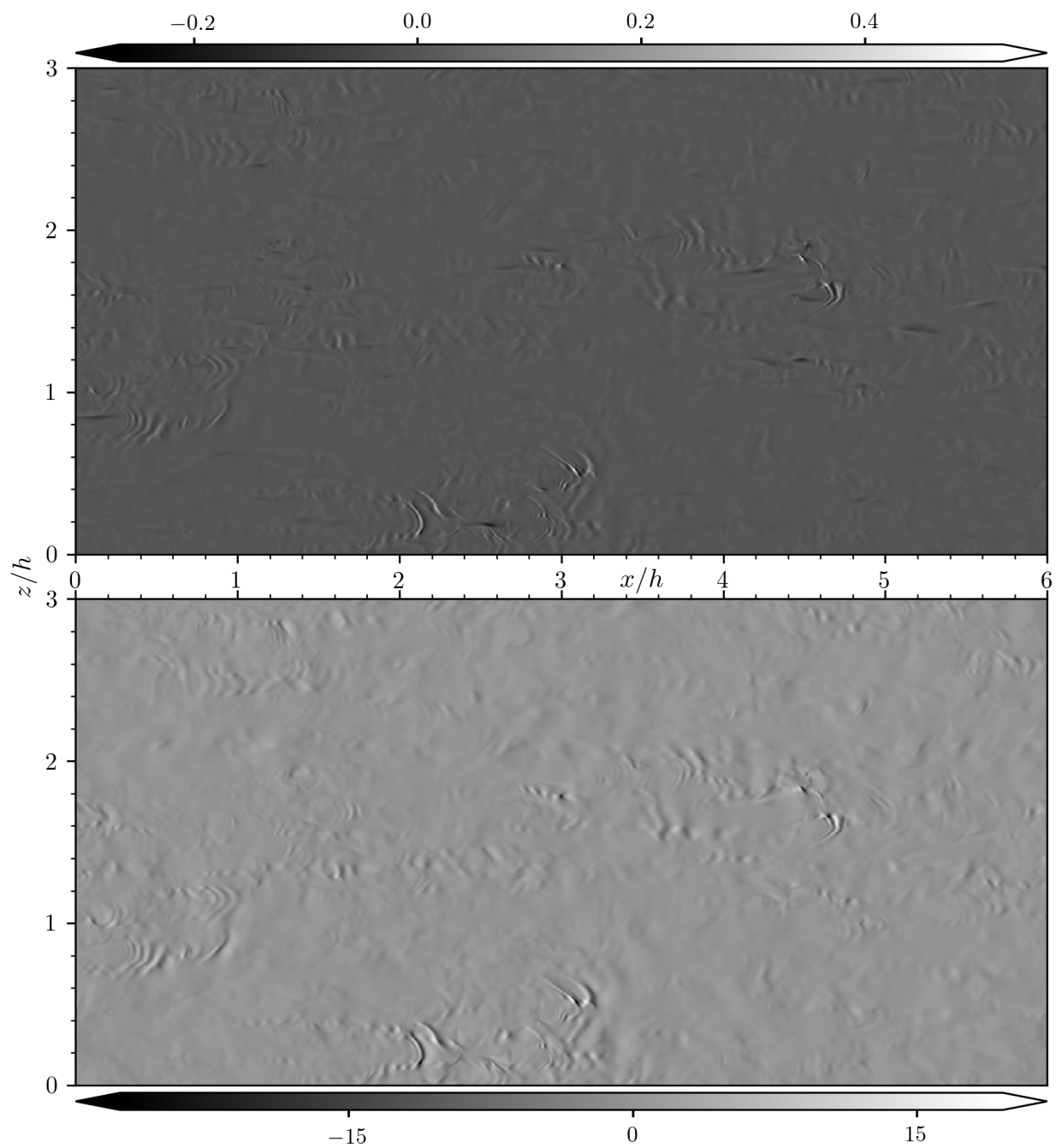
Figure 3.8: Top view of velocity dilatation of case A, $\chi = 0$, at $j = 2$ (second point off the wall). Top panel: computed solenoidal velocity dilatation, bottom panel: dilatational velocity dilatation.
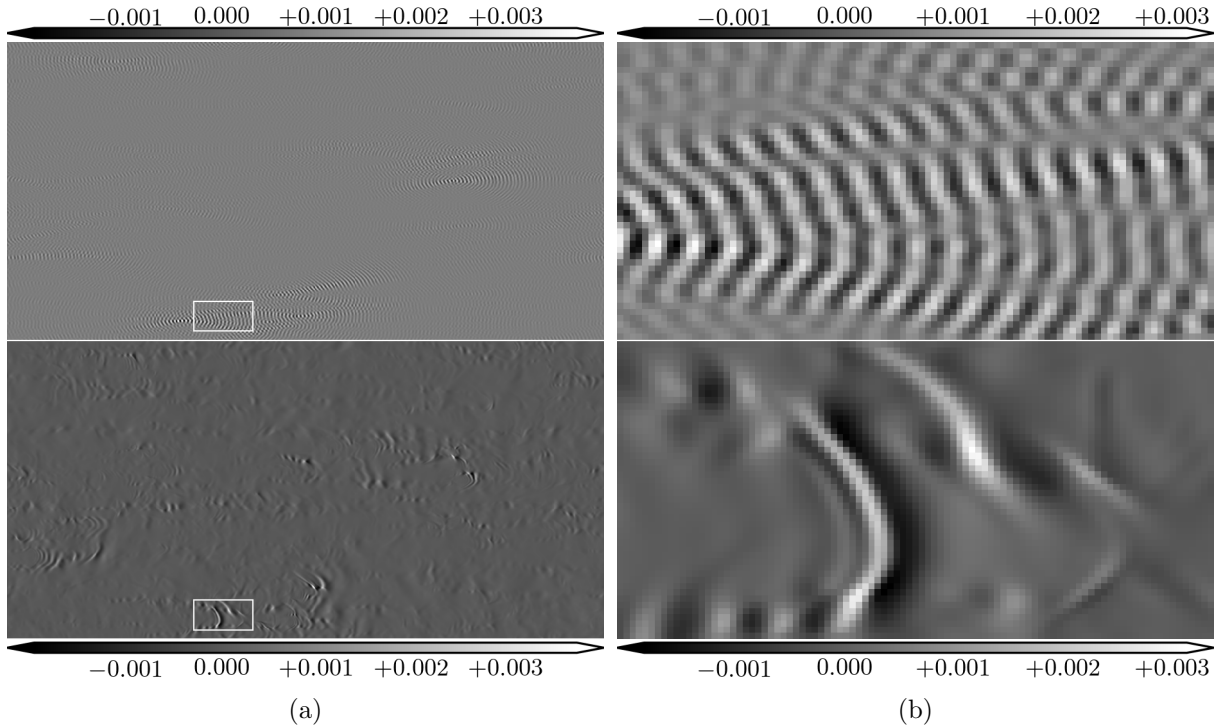
Figure 3.9: dilatational streamwise velocity field at $y^+ \approx 0.2$. Top panel: filtered field leaving only scales with wavenumber $\boldsymbol{k}_{x,z}$, such that $160 < |\boldsymbol{k}_{x,z}| < 165$. Bottom panel: unfiltered field. Left half: full field. Right half: subsection of field to show that this wavenumber band represents the maximum wavenumber that can be considered as scales are resolved (i.e. more than four points per wavelength).

structures. The absolute values of the band width limits were progressively reduced until the smallest structures showed more than five pixels (and therefore grid points) per wavelength. This occurred at an in–plane wavenumber magnitude of between 160 and 165, indicating the velocity field just outside of the stabilisation filter's cut-off limit (of four points per wavelength). Figure 3.9 shows a wall–normal plane at $y^+ \approx 0.2$ for both the full field and a close up view (the location of which is indicated in the full field by a white box).

3.6 Fluid–particle tracking algorithm

The particle–tracking algorithm used to assess the maximum length a particle can travel under isentropic conditions in the turbulent Couette flow is described here. Particles are seeded and released. Their position, velocity, thermodynamic pressure, and velocity dilatation are computed at every iteration using trilinear interpolation. The method was first validated using a two–dimensional vortex test problem and bilinear interpolation to compare the location of the fluid particle to the analytical solution computed from the analytical flow field. Figure 3.10c shows

the path of a single fluid particle starting close to the boundary and being convected by the steady flow field. Figures 3.10a and 3.10b shows that both the bilinear and trilinear interpolation schemes converge at second order accuracy when a uniform mesh is refined. Figure 3.10d shows the total error between the numerical and analytical solution, which includes the interpolation error and first–order accurate time integration error.
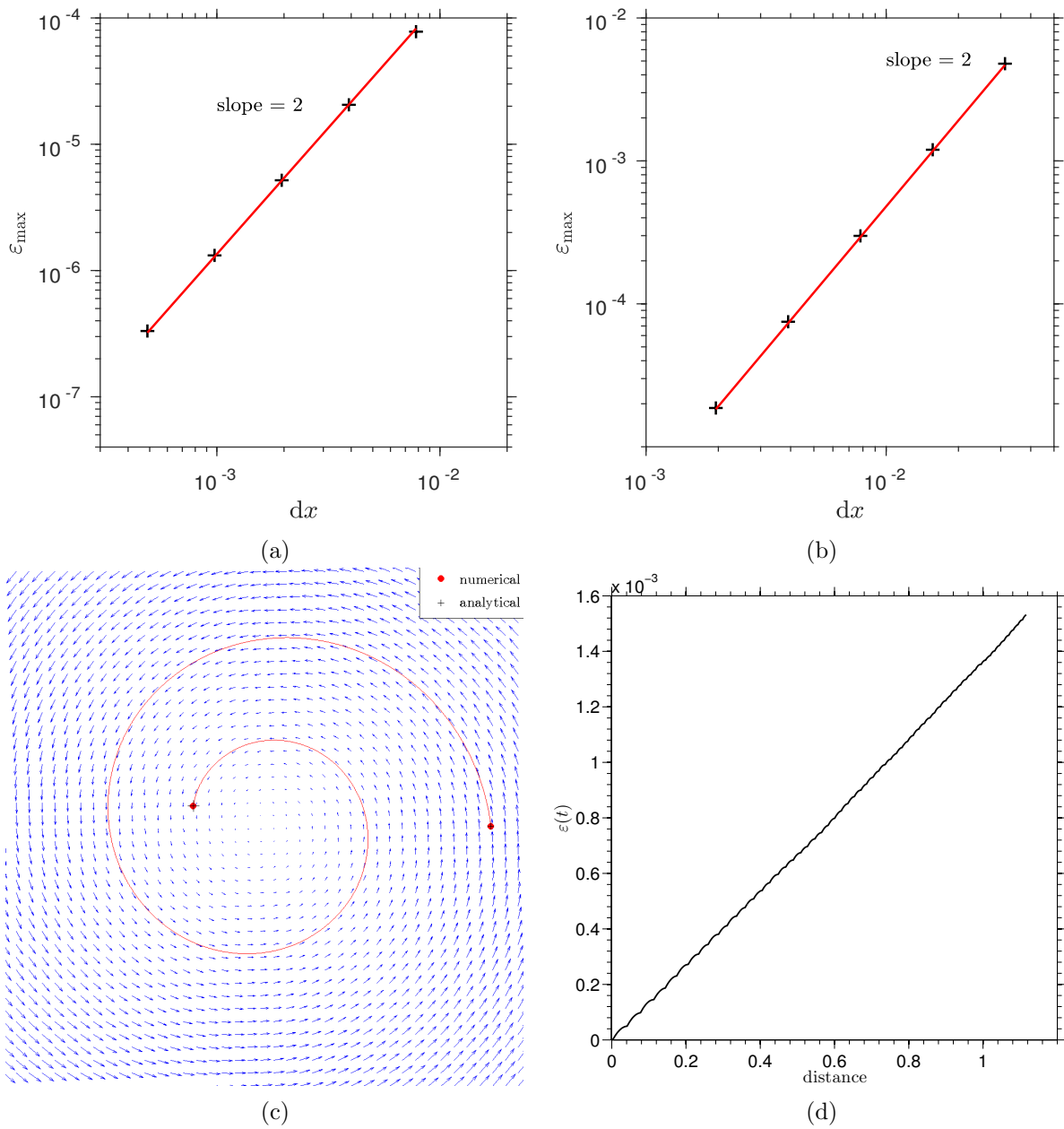
Figure 3.10: Maximum global error $e_{\max}$ of (a) bilinear interpolation scheme; (b) trilinear interpolation scheme; (c) single particle path comparison between numerical approximated trajectory (red line and red dot) and analytical position (black cross); (d) maximum global error in time $e(t)$ of combined bilinear interpolation and time–integration scheme.

Chapter 4

Simple flow cases

This chapter presents a one–dimensional perturbation case to test Landau's sound absorption theory; a two–dimensional ideal vortex case to show the generation of a dilatational field from a solenoidal one; and a two–dimensional freely decaying turbulence case to investigate the effect on the energy spectra and budget of velocity dilatation.

4.1   One dimensional perturbation damping

Both Stokes (1845) and Landau and Lifshitz (1959) investigated the absorption of a one–dimensional acoustic wave as it propagated through a gas. Whilst Stokes assumed zero bulk viscosity and thermal conductivity, Landau retained all three transport coefficients, μ, $\mu_{\rm b}$, and κ. To test the effect of increasing χ on the absorption of an acoustic wave in one–dimensional space, a perturbation to u with an amplitude of 5% of the mean flow value is applied via a Gaussian support spanning 20% of λ_0. It is located at $x/\Lambda_0 = 0$, where Λ_0 is the reference wavelength, and forced in time with frequency f_0. The Prandtl number is constant $\mathrm{Pr} = 0.7$ and $\gamma = 1.29$, the value for CO_2. The one–dimensional governing equations are solved, assuming a Newtonian fluid, Fourier's law, no body force, constant transport properties and an ideal gas:

$$\frac{\partial \rho}{\partial t} + u\frac{\partial \rho}{\partial x} = -\rho\frac{\partial u}{\partial x}$$

$$\frac{\partial u}{\partial t} + u\frac{\partial u}{\partial x} = -\frac{1}{\gamma\rho}\frac{\partial p}{\partial x} + \frac{1}{\text{Re}_{\Lambda_0}}\left[\frac{4}{3}+\chi\right]\frac{1}{\rho}\frac{\partial^2 u}{\partial x^2} \qquad (4.1.1)$$

$$\frac{\partial p}{\partial t} + u\frac{\partial p}{\partial x} = -\gamma p\frac{\partial u}{\partial x} + \frac{\gamma(\gamma-1)}{\text{Re}_{\Lambda_0}}\left[\frac{4}{3}+\chi\right]\left(\frac{\partial u}{\partial x}\right)^2 + \frac{\gamma}{\text{Re}_{\Lambda_0}\text{Pr}}\frac{\partial^2(p/\rho)}{\partial x^2}.$$

Terms have been non–dimensionalised using the reference scales $\rho^\star = \rho\rho_0^\star$, $u^\star = uc_0^\star$, $p^\star = pp_0^\star$, $t^\star = t/\omega_0^\star$, and $x^\star = x\Lambda_0^\star$. The Reynolds number is based on the sound speed and wavelength $\text{Re}_{\Lambda_0} \equiv \rho_0 c_0 \Lambda_0/\mu_0$, where $\Lambda_0 = c_0/\omega_0$ and the sound speed equation is $\rho_0 c_0^2 = \gamma p_0$. There is a mean flow travelling at $\text{Ma}_0 = u_0/c_0 = 0.5$, on which the forced perturbation propagates both downstream and upstream. Perturbations are generated in p and ρ as a result of the coupling between the governing equations. Due to the three transport coefficients, these are damped in space and figures 4.1 to 4.6 show six maps for ρ, u, and p for both $\chi = 0$ and $\chi = 10$. The mean flow travels from the bottom to the top of the figure and the greyscale intensity shows the amplitude of the perturbation as a percentage of the mean flow amplitude.

The maps show the effect of changing the Reynolds number on the amplitude of the flow perturbations after seven forcing periods. The general form for a one–dimensional wave damped in space takes the form

$$f(x,t) = Ae^{-\alpha x}\sin(kx - \omega t) \qquad (4.1.2)$$

where f represents ρ, u, or p. A is the amplitude and k is the wavenumber. The temporal damping coefficient of Landau and Lifshitz (1959, eq. 77.6)

$$\alpha = \frac{\omega^2}{2\rho c^3}\left[\left(\frac{4}{3}\mu + \mu_{\text{b}}\right) + \kappa\left(\frac{1}{c_v} - \frac{1}{c_p}\right)\right] \qquad (4.1.3)$$

can be converted to a spatial damping coefficient via the wave relations $\omega = 2\pi f$ and $c = f\Lambda$ to give

$$\alpha = \frac{1}{\Lambda}\frac{2\pi^2}{\text{Re}_{\Lambda_0}}\left[\frac{4}{3} + \chi + \frac{1}{\text{Pr}}(\gamma - 1)\right], \qquad (4.1.4)$$

where $\Lambda = \Lambda_0(1 \pm \text{Ma})$ to account for the mean flow speed.

All maps show a propagation of the perturbation both downstream and upstream of the forc-

ing location $x/\Lambda_0 = 0$, but due to the mean flow motion travelling at Ma $= 0.5$, the effective

length is shorter (by a factor of two for pure acoustic modes in an Euler flow) in the upstream

direction. Concentrating on figure 4.1 for ρ, at high Re$_{\Lambda_0}$ three modes propagate at three phase

velocities: two acoustic modes travelling at $u = u_0 \pm c_0$, which reach locations $x/\Lambda_0 = +10.5$ and

$x/\Lambda_0 = -3.5$, respectively, and an entropy mode travelling at u_0, reaching $x/\Lambda_0 = +3.5$. As Re$_{\Lambda_0}$

is reduced and friction forces increase in significance, all three modes are progressively damped

until maximum damping is achieved at approximately Re$_{\Lambda_0} = 10$. Figure 4.2 shows the same map

of ρ but for $\chi = 10$. The Reynolds number of maximum damping has shifted by approximately

one order of magnitude to Re$_{\Lambda_0} = 10^2$. The shift in the location of the point of strongest damping

can be explained by observing the behaviour of α from Landau's damping coefficient, shown in

the figures as white lines. They represent the contours that correspond to the x/Λ_0 location at

which the amplitude of the velocity perturbation is 95% of its original value at $x/\Lambda_0 = 0$. At

approximately Re$_{\Lambda_0} = 10$ the curve is almost at $x/\Lambda_0 = 0$. An acoustic Reynolds number, which

includes all three transport coefficients can be defined as

$$\mathrm{Re}_{\mathrm{ac.}} \equiv \frac{\rho_0 c_0 \Lambda_0}{\mu_0 \left[\dfrac{4}{3} + \chi + \dfrac{1}{\mathrm{Pr}}\left(\gamma - 1\right)\right]}. \tag{4.1.5}$$

Supposing that maximum damping occurs at Re$_{\mathrm{ac.}} \sim 1$, i.e. the friction forces balance the convec-

tion of an acoustic wave, it can be used to predict the value of Re$_{\Lambda_0}$ at which maximum damping

occurs. The relationship between Re$_{\Lambda_0}$ and Re$_{\mathrm{ac.}}$ is Re$_{\mathrm{ac.}} = $ Re$_{\Lambda_0}/(4/3 + \chi + (\gamma - 1)/\mathrm{Pr})$. There-

fore if $\gamma = 1.29$ and Pr $= 0.7$, the $\chi = 0$ case gives Re$_{\Lambda_0} \sim 2$. This value matches the location

where the Landau damping curve reaches $x/\Lambda_0 = 0$ reasonably well (see figure 4.1 for example).

The same can be done for the $\chi = 10$ case, which gives Re$_{\Lambda_0} \sim 12$, again corresponding to the

same order of magnitude as the Landau damping curve (see figure 4.2 for example). Measure-

ment data of acoustic absorption demonstrates that the bulk viscosity is more effective at damping

the amplitude of acoustic waves at higher frequencies (equivalent to smaller scales). From the

governing equation of internal energy

$$\frac{\partial \rho e}{\partial t} + \nabla \cdot (\rho e \boldsymbol{u}) = -(p - \mu_{\mathrm{b}}\Theta)\Theta + \frac{1}{\mathrm{Re}}\boldsymbol{\Sigma} : \frac{1}{2}(\boldsymbol{\nabla}\boldsymbol{u} + [\boldsymbol{\nabla}\boldsymbol{u}]^{\mathrm{t}}) - \frac{1}{\mathrm{Pr}\mathrm{Re}\mathrm{Ma}^2(\gamma - 1)}\nabla \cdot \boldsymbol{q} \tag{4.1.6}$$

there is a dissipation term $\mu_{\mathrm{b}}\Theta^2$, representing an irreversible transfer of kinetic energy to internal

energy. If the dilatational field has a similar amplitude at all scales, regions of the velocity field

at small scales will have a large gradient, leading to a larger Θ^2 and an increased effectiveness of μ_{b} at small scales. Consequentially, the magnitude of the dilatational velocity field at small scales is reduced and the transfer to internal energy occurs at progressively larger scales as χ is increased.

Landau's damping coefficient (4.1.4) is only valid in the context of damping acoustic waves, i.e. in the large Reynolds number regime. However the simulation results show a different behaviour at small Re_{Λ_0}. In both zero and non–zero χ cases, as Re_{Λ_0} is reduced below the value of strongest damping, the perturbation amplitude of ρ recovers and travels at the mean flow speed u_0. The velocity perturbation maps (figures 4.3 and 4.4) show a weak perturbation travelling at u_0 as well as a region of continuous pale grey (positive amplitude) that extends to the edge of the plotted domain, indicating the acoustic mode. At low Reynolds number the viscous term dominates and the flow obeys diffusion–like properties rather than hyperbolic ones. In the context of the two–dimensional and three–dimensional flows considered later in the thesis, it is the hyperbolic regime (high Reynolds number) that is of interest.
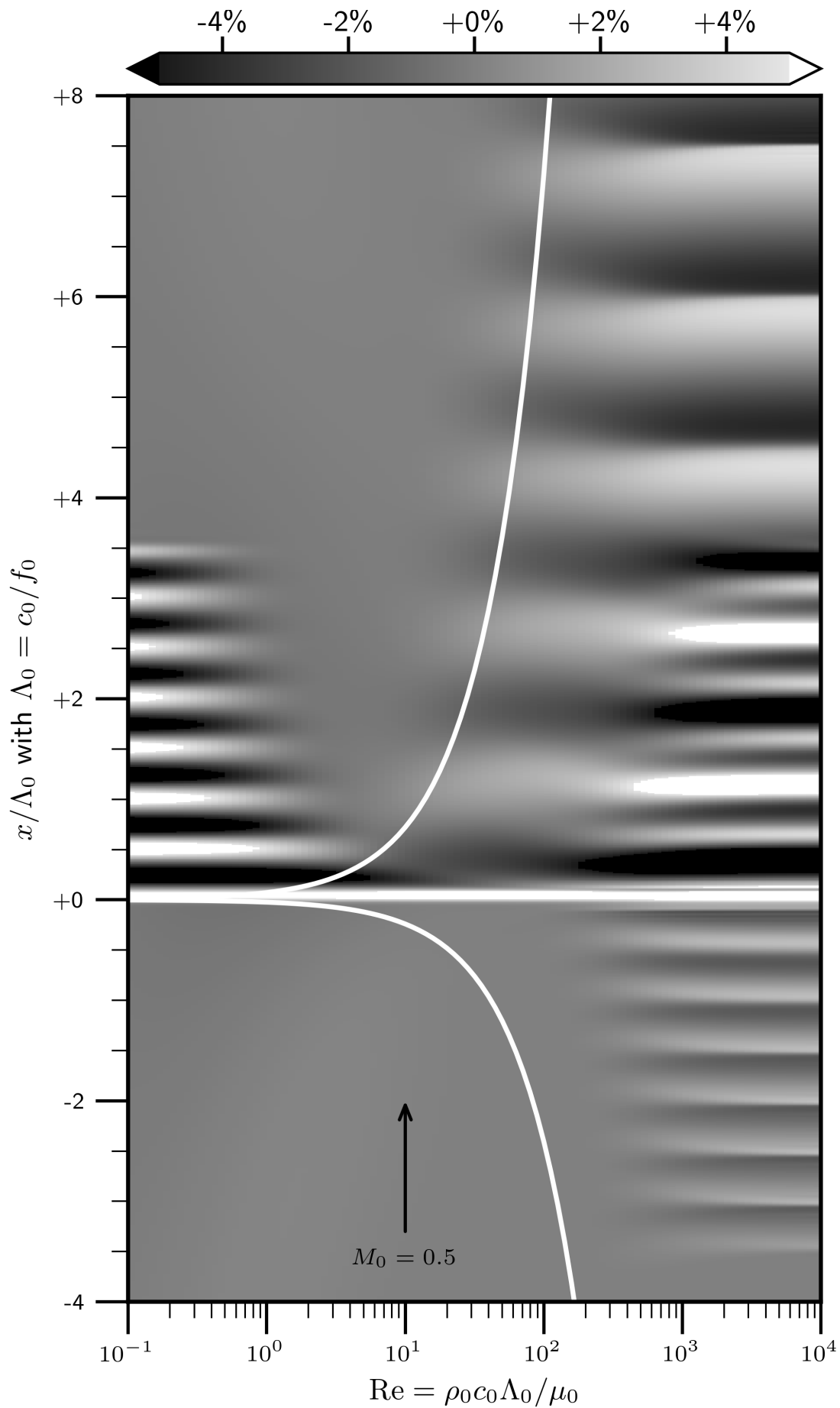
Figure 4.1: Perturbation map of ρ for $\chi = 0$. White line represents location where the velocity perturbation amplitude is 95% of its original value (at $x/\Lambda_0 = 0$). Ma = 0.5, Pr = 0.7, and $\gamma = 1.29$.
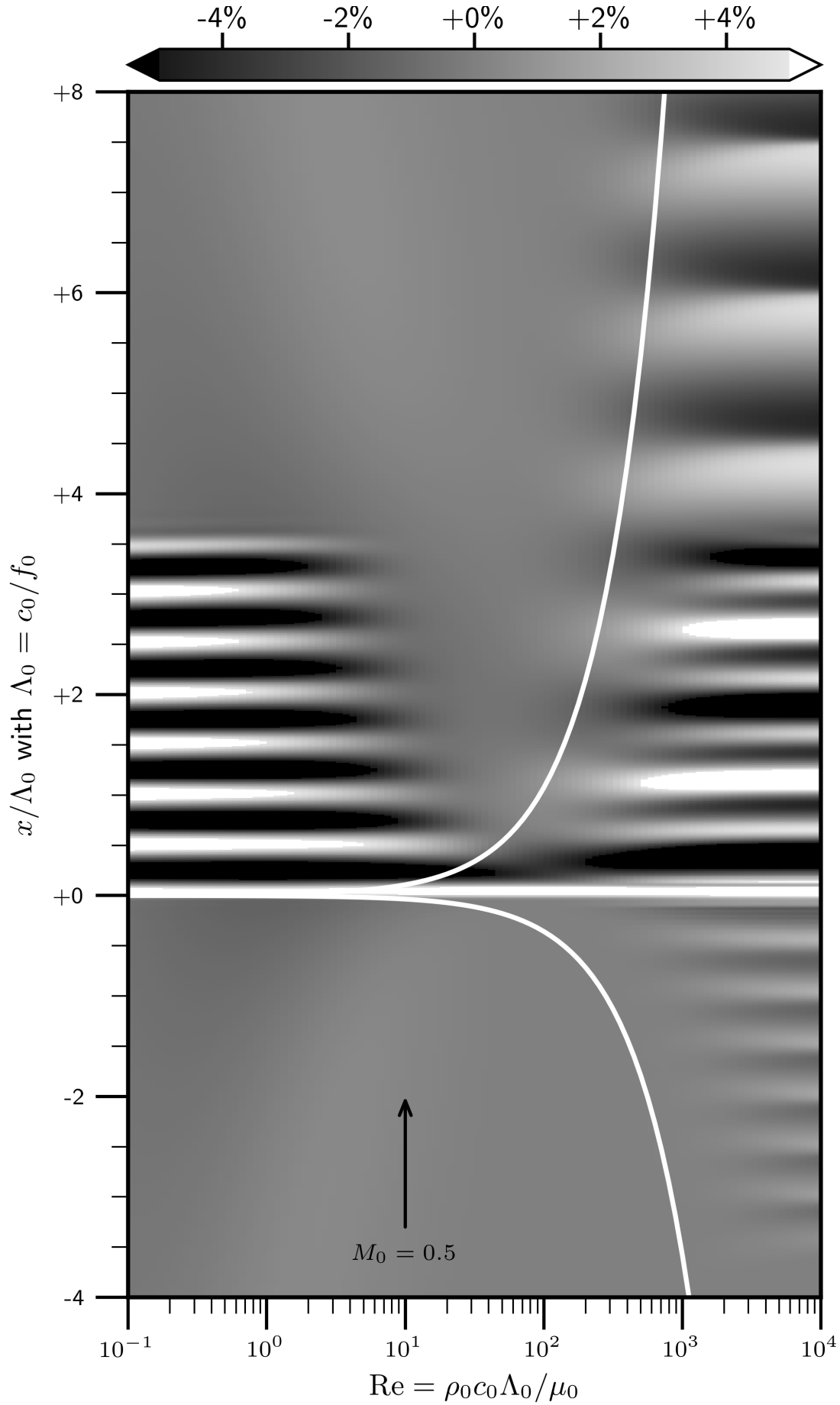
Figure 4.2: Perturbation map of ρ for $\chi = 10$. White line represents location where the velocity perturbation amplitude is 95% of its original value (at $x/\Lambda_0 = 0$). Ma = 0.5, Pr = 0.7, and $\gamma = 1.29$.
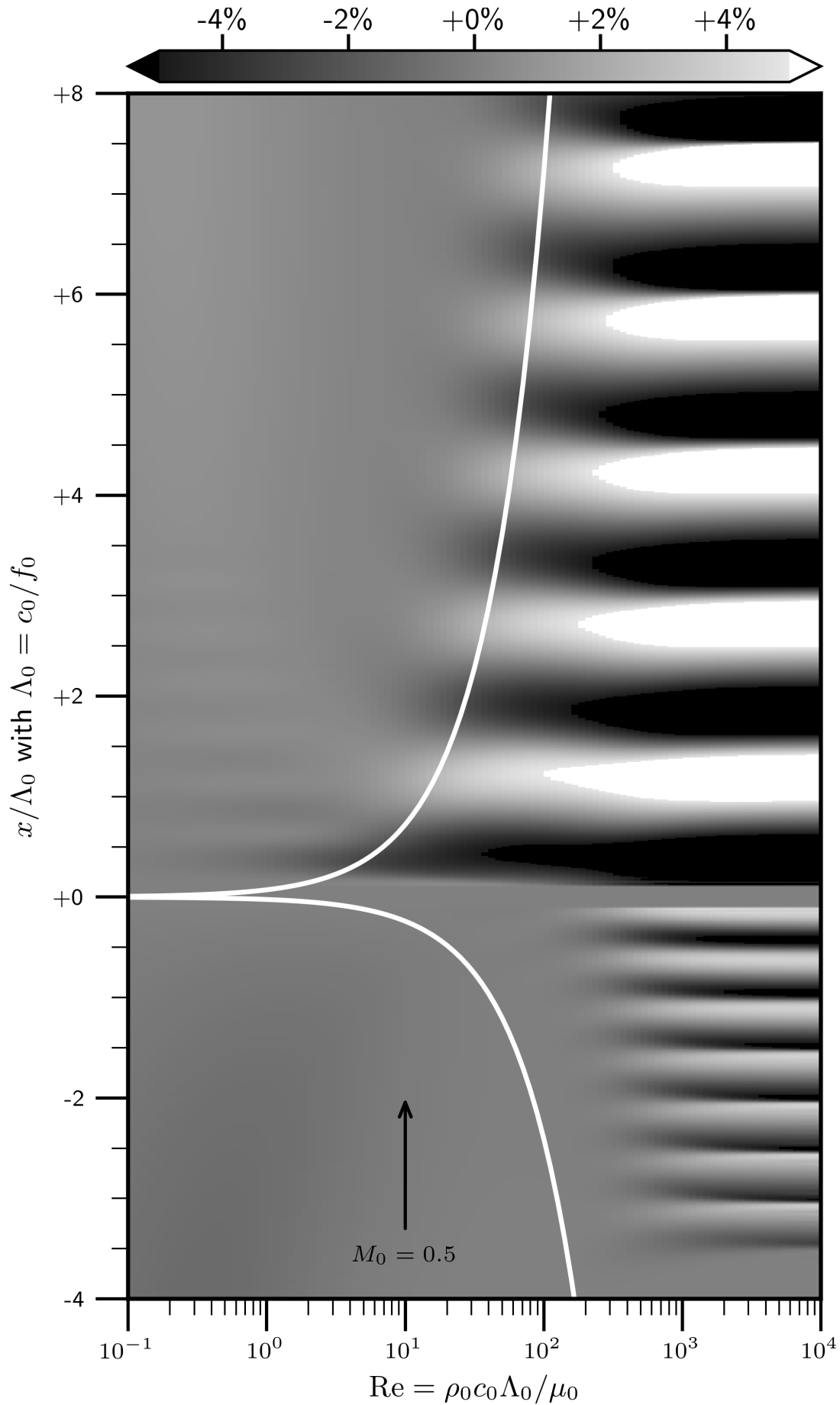
Figure 4.3: Perturbation map of u for $\chi = 0$. White line represents location where the velocity perturbation amplitude is 95% of its original value (at $x/\Lambda_0 = 0$). Ma $= 0.5$, Pr $= 0.7$, and $\gamma = 1.29$.
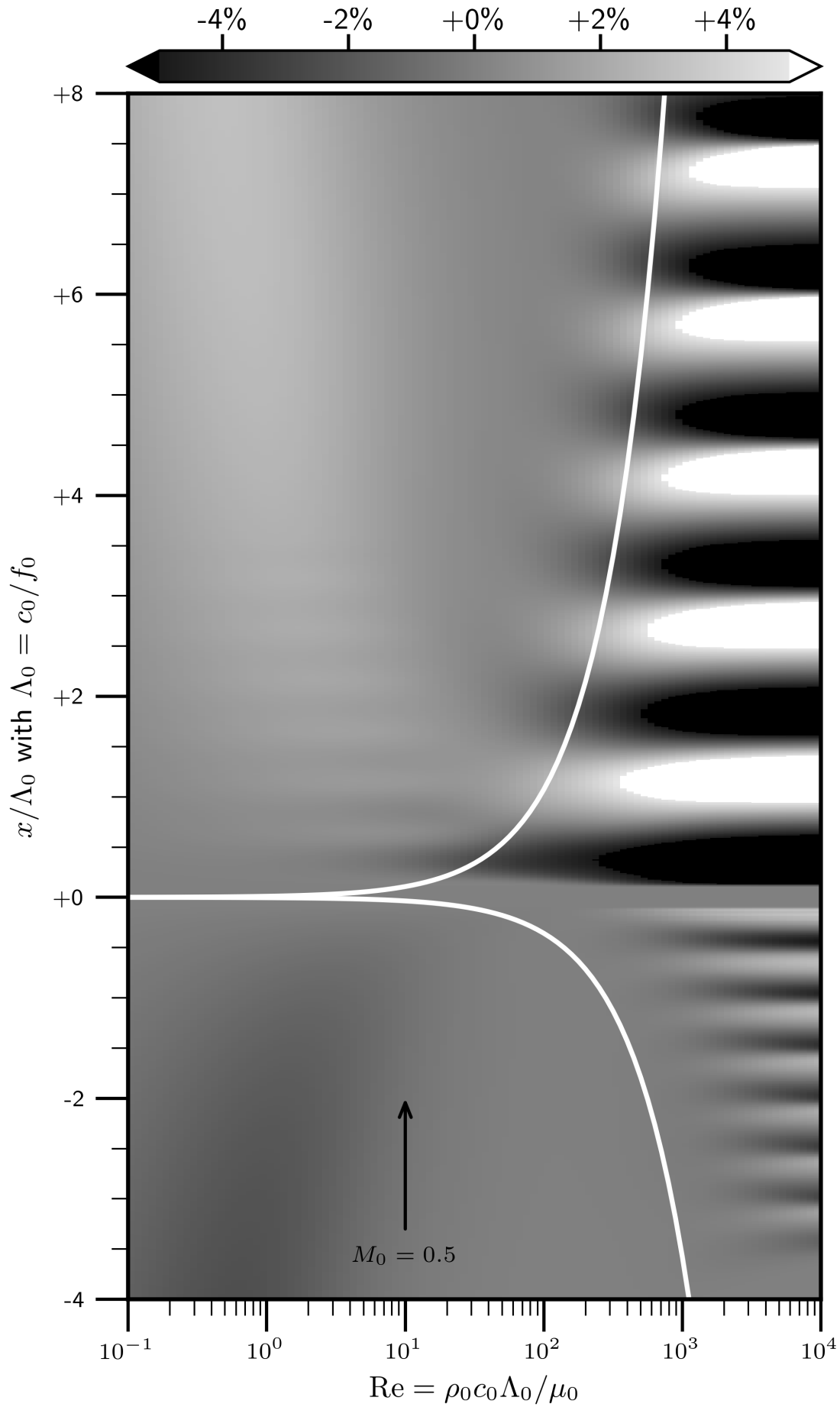
Figure 4.4: Perturbation map of u for $\chi = 10$. White line represents location where the velocity perturbation amplitude is 95% of its original value (at $x/\Lambda_0 = 0$). $\mathrm{Ma} = 0.5$, $\mathrm{Pr} = 0.7$, and $\gamma = 1.29$.
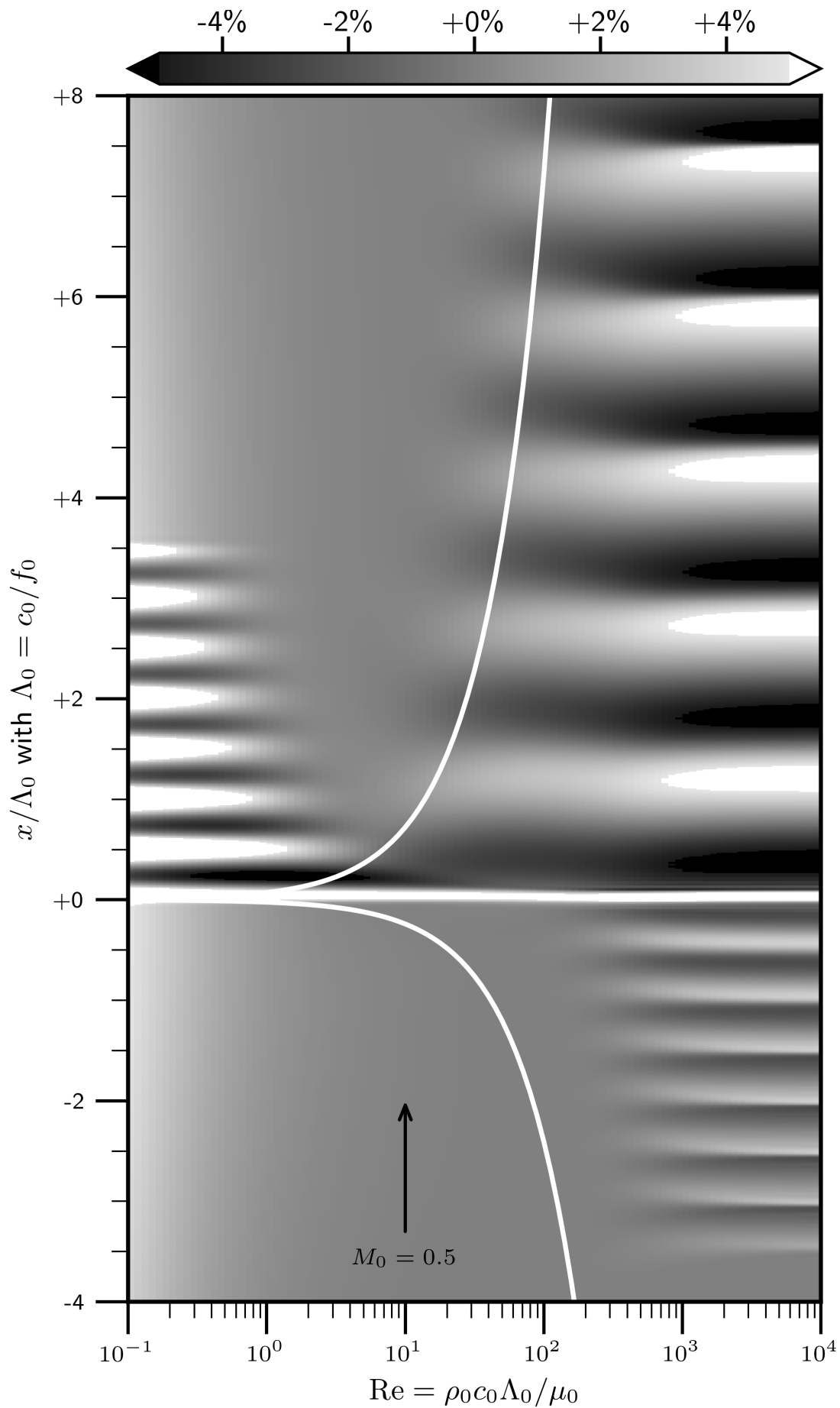
Figure 4.5: Perturbation map of p for $\chi = 0$. White line represents location where the velocity perturbation amplitude is 95% of its original value (at $x/\Lambda_0 = 0$). Ma = 0.5, Pr = 0.7, and $\gamma = 1.29$.
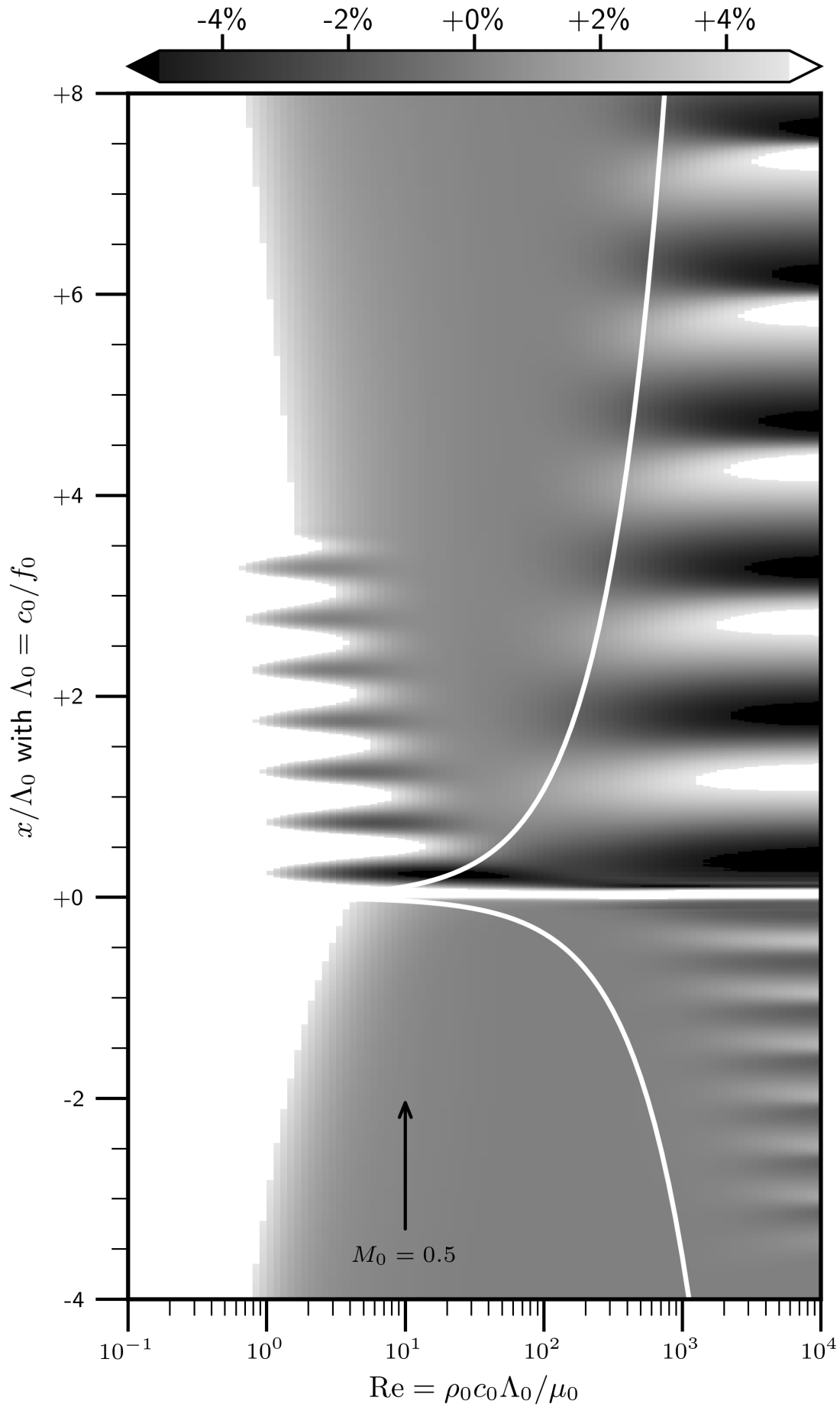
Figure 4.6: Perturbation map of p for $\chi = 10$. White line represents location where the velocity perturbation amplitude is 95% of its original value (at $x/\Lambda_0 = 0$). $\mathrm{Ma} = 0.5$, $\mathrm{Pr} = 0.7$, and $\gamma = 1.29$.

4.2   Solenoidal to dilatational kinetic energy transfers

To establish the mechanism by which energy is exchanged between solenoidal and dilatational velocity fields, terms from the governing equation of Θ are plotted for an ideal vortex and two–dimensional turbulence.

4.2.1   Governing equation of velocity dilatation

The time-evolution of the divergence of velocity is found by taking the divergence of the non-conservative form of the Navier–Stokes equations (see appendix B.6 for a derivation),

$$\frac{D\Theta}{Dt} + \boldsymbol{\nabla} \boldsymbol{u}^{\mathrm{t}} : \boldsymbol{\nabla} \boldsymbol{u} = -\boldsymbol{\nabla}\left(\frac{1}{\rho}\right) \cdot \boldsymbol{\nabla} p_m - \frac{1}{\rho}\nabla^2 p_m + \boldsymbol{\nabla} \cdot \left(\frac{1}{\rho}\boldsymbol{\nabla} \cdot \boldsymbol{\Sigma}\right), \tag{4.2.1}$$

where

$$\frac{D\Theta}{Dt} = \frac{\partial\Theta}{\partial t} + (\boldsymbol{u} \cdot \nabla)\Theta. \tag{4.2.2}$$

The viscous term, assuming constant viscosity, simplifies to

$$\boldsymbol{\nabla} \cdot \left(\frac{1}{\rho}\boldsymbol{\nabla} \cdot \boldsymbol{\Sigma}\right) = \frac{4}{3}\mu\nabla^2\Theta. \tag{4.2.3}$$

It is useful to isolate solenoidal and dilatational contributions in order to see which terms are responsible for the production and dissipation of Θ. Rewriting the convective acceleration and splitting the mechanical pressure allows (4.2.1) to be written

$$\overbrace{\frac{\partial\Theta}{\partial t} + \nabla \cdot (\boldsymbol{u}\Theta)}^{(1)} = \underbrace{\overbrace{\Theta^2 - \boldsymbol{\nabla}\boldsymbol{u}^{\mathrm{t}} : \boldsymbol{\nabla}\boldsymbol{u}}^{(2)} \overbrace{- \frac{1}{\rho}\nabla^2\left(p - \left(\frac{4}{3}\mu + \mu_{\mathrm{b}}\right)\Theta\right)}^{(3)}}_{\text{extended Poisson equation term}}$$

$$+ \underbrace{\overbrace{\boldsymbol{\nabla}\left(\frac{1}{\rho}\right) \cdot \rho_0\frac{D\boldsymbol{u}_{\mathrm{sol}}}{Dt}}^{(4)}}_{\text{solenoidal production term}} + \underbrace{\overbrace{\left(\frac{1}{3}\mu + \mu_{\mathrm{b}}\right)\boldsymbol{\nabla}\left(\frac{1}{\rho}\right) \cdot (\boldsymbol{\nabla}\Theta)}^{(5)}}_{\text{dilatational production term}}, \tag{4.2.4}$$

where the material acceleration of a solenoidal velocity field $\boldsymbol{u}_{\mathrm{sol}}$ based on the reference density ρ_0 has been substituted according to the momentum equation

$$\rho_0 \frac{D\boldsymbol{u}_{\text{sol}}}{Dt} = -\boldsymbol{\nabla}p + \mu_0 \nabla^2 \boldsymbol{u}. \tag{4.2.5}$$

If term (2) is balanced by term (3), then it is the solenoidal production term (4) that initially produces the velocity dilatation. This can be understood by observing that $\boldsymbol{\nabla}(1/\rho)$ is positive towards the centre of an ideal vortex (opposite to the radial unit vector $\boldsymbol{e}_r$) as illustrated in figure 4.7, along with the acceleration of a fluid element travelling at a finite radius from the vortex centre. The scalar product is non–zero and leads to a production of Θ. The next section shows this generation mechanism for an ideal vortex initial condition and what effect the bulk viscosity has on velocity dilatation.

4.2.2 Ideal vortex

To test how term (4) in (4.2.4) generates a dilatational velocity field, a two–dimensional simulation initialised with a solenoidal velocity field that contains a single vortex was prescribed. This is computed by prescribing a solenoidal pressure field

$$p = p_0 \left(1 - \alpha \exp\left\{ -\left(\frac{r}{\sigma}\right)^n \right\} \right), \tag{4.2.6}$$

where p_0 is a reference pressure, α is a parameter that controls the pressure at the centre of the vortex to ensure it is positive. The pressure varies in the radial direction $\boldsymbol{e}_r$ from the centre of the domain with magnitude $r = \sqrt{x^2 + y^2}$. The parameter n controls the symmetry of the function (a Gaussian distribution results when $n = 2$) and σ controls the spread of the function. Setting σ to a small value (0.1) ensures that the region $p < p_0$ is contained in the centre of the domain. The Poisson equation for pressure can be used to find the corresponding solenoidal velocity field

$$-\frac{1}{\rho_0} \nabla^2 p = \boldsymbol{\nabla}\boldsymbol{u}^{\text{t}} : \boldsymbol{\nabla}\boldsymbol{u}. \tag{4.2.7}$$

The azimuthal velocity component is u_Θ. Re–writing (4.2.7) as

$$n^2 \alpha \frac{p_0}{\rho_0} \frac{\mathrm{d}}{\mathrm{d}r} \left[\left(\frac{r}{\sigma}\right)^n \exp\left\{ -\left(\frac{r}{\sigma}^n\right) \right\} \right] = \frac{\mathrm{d}u_\Theta^2}{\mathrm{d}r} \tag{4.2.8}$$

and integrating with respect to r gives the azimuthal velocity profile

$$u_\Theta = n\sqrt{\alpha\frac{p_0}{\rho_0}}\left(\frac{r}{\sigma}\right)^{\frac{n}{2}}\exp\left[-\frac{1}{2}\left(\frac{r}{\sigma}\right)^n\right] + C_1 \tag{4.2.9}$$

where the constant of integration C_1 is zero due to the condition that $\lim\limits_{r\to+\infty} u_\Theta = 0$. Once released, the solenoidal motion generates a divergence of velocity field, shown in figure 4.9 for a viscous case where $\mathrm{Re}_L \equiv \rho_0 u_0 L/\mu = 10^4$ and $\chi = 0$. Figure 4.10 shows the equivalent for the $\chi = 10^3$ case. The initial divergence of velocity can be found analytically by taking (4.2.4) at the initial time t_0

$$\left.\frac{D\Theta}{Dt}\right|_{t_0} = \boldsymbol{\nabla}v \cdot \rho_0 \left.\frac{D\boldsymbol{u}_{\mathrm{sol}}}{Dt}\right|_{t_0} \tag{4.2.10}$$

where $v = 1/\rho_0$ at t_0 (the solenoidal initial condition). For $t > 0$ it is determined by the equation of state. Substituting the expression for u_Θ from (4.2.9) gives

$$\left.\frac{D\boldsymbol{u}_{\mathrm{sol}}}{Dt}\right|_{t_0} = -\frac{u_\Theta^2}{r}\boldsymbol{e}_r = -n^2\frac{p_0}{\rho_0}\frac{a}{r}\left(\frac{r}{\sigma}\right)^n\exp\left[-\left(\frac{r}{\sigma}\right)^n\right]\boldsymbol{e}_r. \tag{4.2.11}$$

The gradient of specific volume can be approximated to be initially isentropic and hence $pv^\gamma = p_0 v_0^\gamma$ and

$$\boldsymbol{\nabla}v = v_0\frac{\mathrm{d}}{\mathrm{d}r}\left(\left[\frac{p}{p_0}\right]^{-\frac{1}{\gamma}}\right) = -\frac{an}{\rho_0\gamma}\frac{1}{r}\left(\frac{r}{\sigma}\right)^n\left\{1 - a\exp\left[-\left(\frac{r}{\sigma}\right)^n\right]\right\}^{-\frac{\gamma+1}{\gamma}}\exp\left[-\left(\frac{r}{\sigma}\right)^n\right]\boldsymbol{e}_r. \tag{4.2.12}$$

Taking the scalar product gives

$$\left.\frac{D\Theta}{Dt}\right|_{t_0} = \frac{a^2 n^3}{\gamma}\frac{p_0}{\rho_0}\frac{1}{r^2}\left(\frac{r}{\sigma}\right)^{2n}\left\{1 - a\exp\left[-\left(\frac{r}{\sigma}\right)^n\right]\right\}^{-\frac{\gamma+1}{\gamma}}\exp\left[-2\left(\frac{r}{\sigma}\right)^n\right]. \tag{4.2.13}$$

Figure 4.8 shows (4.2.13) plotted as a function of radius from the centre of the vortex. The peak value lies at approximately $r/L = 0.1$, indicating that from the initial condition, term (1) in (4.2.4) is non–zero. Term (4) represents the production of Θ due to the ideal vortex which transfers kinetic energy from the solenoidal velocity field to the dilatational one. Term (5) is a transfer term from the dilatational field to the internal energy and depends on the sign of $\boldsymbol{\nabla}\Theta$ but also the magnitude of μ and μ_{b}. Increasing the bulk viscosity can increase the transfer to the internal energy reservoir via the dilatational production term, and hence reduces the magnitude of Θ. This is seen in the time evolution of the velocity dilatation field for $\chi = 0$ and $\chi = 10^3$ in

figures 4.9 and 4.10. The intensity of the ring of Θ is much weaker than the $\chi = 0$ case. The next section presents the same analysis for a freely decaying two–dimensional turbulence case.
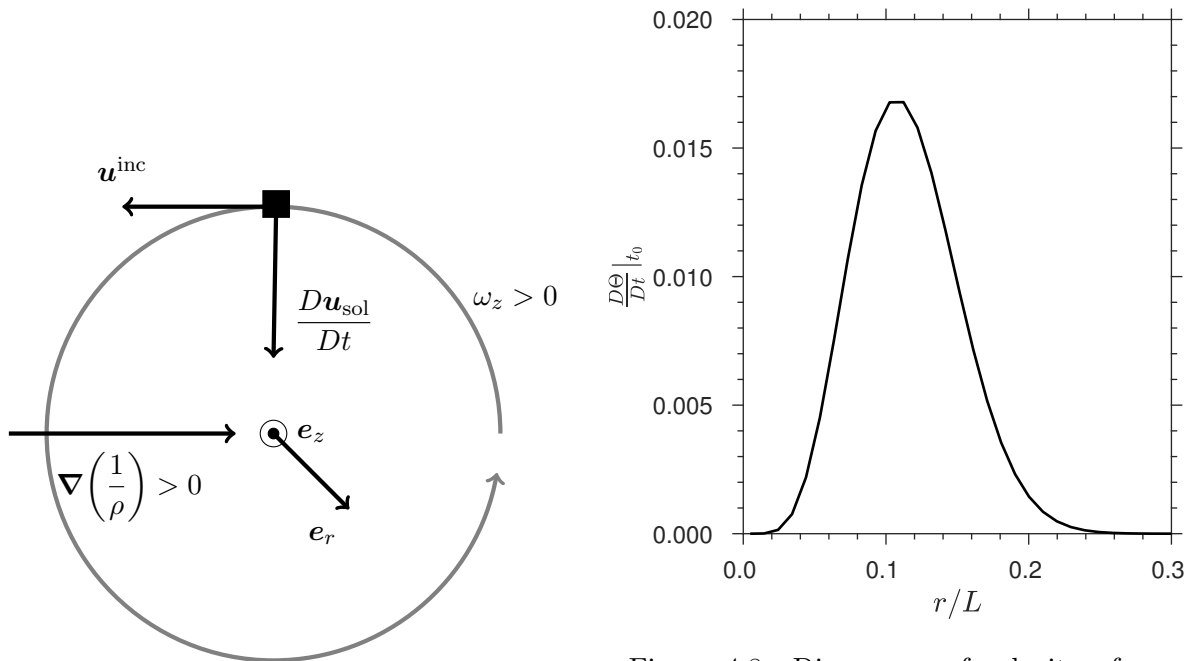
Figure 4.7: Diagram showing the mechanism by which a solenoidal vortex generates velocity dilatation.
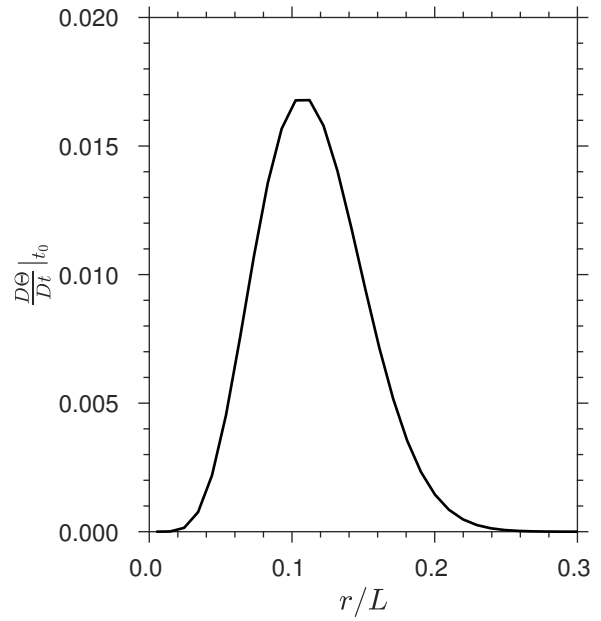
Figure 4.8: Divergence of velocity of an ideal vortex at advancing times. $\text{Re}_L = 10^4$, $\text{Ma}_t = 0.8$, $\chi = 0$. $\text{Pr} = 0.7$ and $\gamma = 1.29$.
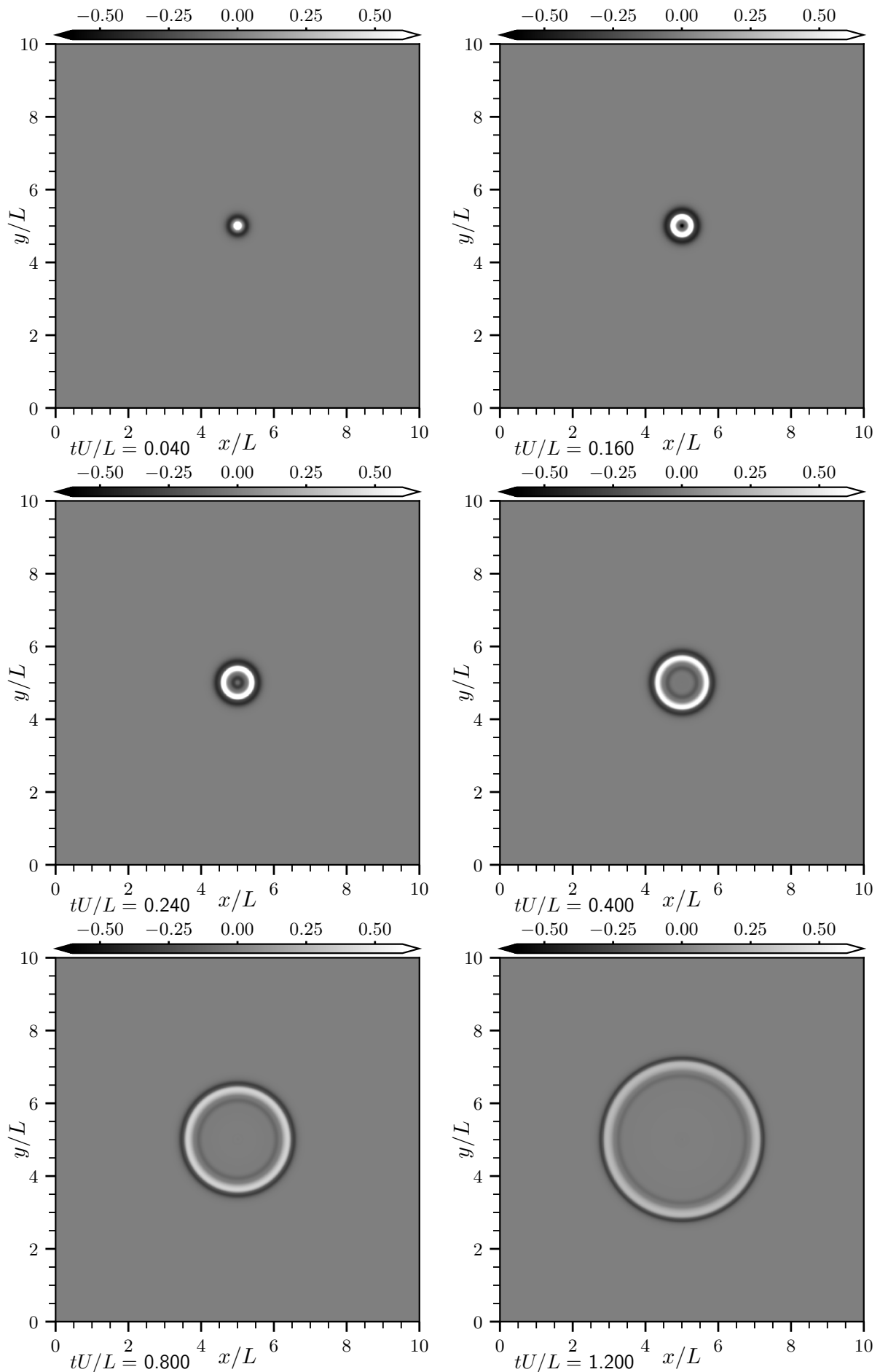
Figure 4.9: Divergence of velocity of an ideal vortex at advancing times. $\mathrm{Re}_L = 10^4$, $\mathrm{Ma}_t = 0.8$, $\chi = 0$. $\mathrm{Pr} = 0.7$ and $\gamma = 1.29$.
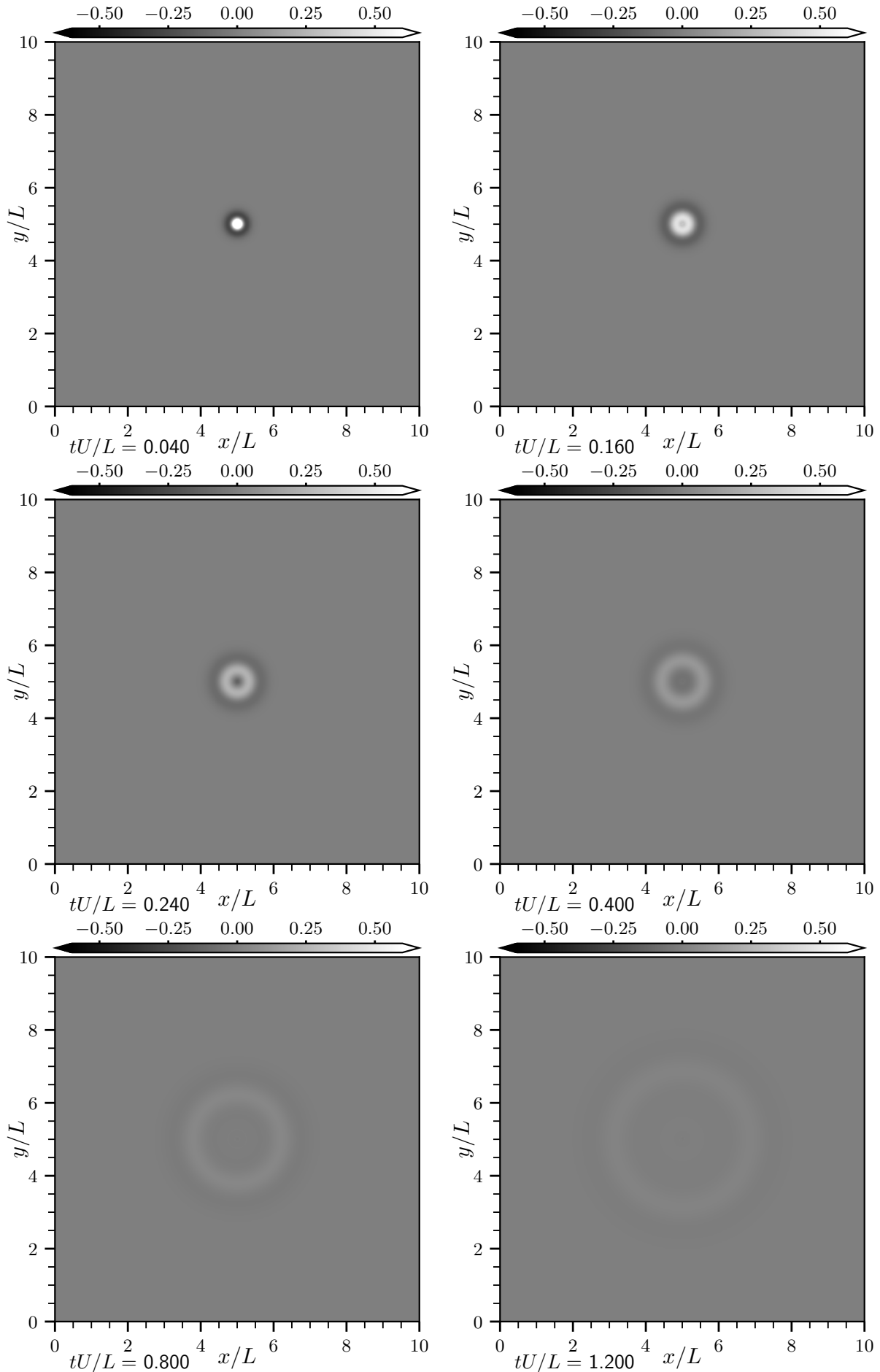
Figure 4.10: Divergence of velocity of an ideal vortex at advancing times. $\mathrm{Re}_L = 10^4$, $\mathrm{Ma}_t = 0.8$, $\chi = 10^3$. $\mathrm{Pr} = 0.7$ and $\gamma = 1.29$.

4.3   Two dimensional turbulence

Due to the computational cost scaling linearly with the value of χ, it was not possible to run a three-dimensional Couette case at a relatively high Reynolds number ($\mathrm{Re}_\tau \approx 490$) for $\chi = 10^3$, the value representative of CO_2. It was possible, however, to investigate high χ values in two-dimensional, freely decaying homogeneous turbulence. This section outlines the method of generating the initial condition and presents results of Navier–Stokes cases at $\chi = 0$ and $\chi = 10^3$, for a turbulence Mach number $\mathrm{Ma}_t = |\boldsymbol{u}|_{\max}/c_0$ of 0.8 and $\mathrm{Re}_L = 8 \times 10^4$. The run parameters are summarised in table 4.1.

4.3.1   Flow field initialisation

Freely decaying turbulence is an initial value problem that requires an initial state of turbulence. One way of achieving this is to generate a pseudo-random velocity field with certain characteristics. An analytical spectrum of kinetic energy is generated with maximum energy at the 'peak wavenumber' k_p. A pseudo-random flow is assumed to be solenoidal and is rescaled to the desired energy spectrum. The pressure is found by solving the Poisson equation for pressure and the density from the equation of state, assuming a constant temperature field. The following section explains this procedure in detail.

4.3.1.1   Pseudo-random velocity field

The kinetic energy $\widehat{\underline{E}}(k)$, a " $\widehat{(\cdot)}$ " denotes non-rescaled values and an underscore "$(\underline{\cdot})$" denotes the Fourier transformed function. The initial velocity field is defined in wavenumber space

$$\widehat{\underline{E}}(k) = k \exp\left\{ -\left(\frac{k}{\sqrt{2}k_p} \right)^2 \right\}, \qquad\qquad (4.3.1)$$

Case	l_x	l_y	nx	ny	γ	χ	Re_L	Ma_t	tu_0/L
A	1	1	1024	1024	1.29	0	8×10^4	3.0	12.8
B	1	1	1024	1024	1.29	10^3	8×10^4	3.0	12.8

Table 4.1: Table of parameters for two-dimensional results. $\mathrm{Pr} = 0.7$.

where k_p is the 'peak' wavenumber at which the maximum energy is located and $k \in [1, k_{\max}]$ is the magnitude of the wavenumber vector in the x and y directions, i.e. $k = |\boldsymbol{k}| = \sqrt{k_x^2 + k_y^2}$. Note that all wavenumbers have been rescaled according to $k = k^* L/(2\pi)$, where k^* is the unscaled wavenumber, so that all wavenumbers represent the number of wavelengths in the domain. It is rescaled by its sum to give

$$\underline{E}(k) = \frac{\widehat{\underline{E}}(k)}{\int_0^{k_{\max}} \widehat{\underline{E}}(k)\mathrm{d}k}. \tag{4.3.2}$$

The velocity-component fields are each defined by two pseudo-random number (from a uniform distribution) fields at each $\boldsymbol{x}$ location, $\mathcal{R}_n \in [0, 1]$ for $n \in \{1, 2, 3, 4\}$, to which the transformation of Box and Muller (1958) is applied to give two-dimensional normal distributions of pseudo-random numbers

$$\widehat{u}(\boldsymbol{x}) = \left(\sqrt{-2\ln(\mathcal{R}_1)} \right) \sin(2\pi \mathcal{R}_3)$$

$$\widehat{v}(\boldsymbol{x}) = \left(\sqrt{-2\ln(\mathcal{R}_2)} \right) \sin(2\pi \mathcal{R}_4). \tag{4.3.3}$$

To extract the solenoidal part of the velocity field, Helmholtz's decomposition is applied in Fourier space. Any vector field $\widehat{\boldsymbol{u}}$ (the velocity field, say) can be split into the sum of a solenoidal (incompressible) part, expressed as the curl of a vector potential $\boldsymbol{A}$, and an irrotational (compressible) part, expressed as the gradient of a scalar potential Φ, as well as a harmonic part representing the mean component of the vector field. For decaying turbulence the velocity field has no mean component, which simplifies the equation to

$$\widehat{\boldsymbol{u}}(\boldsymbol{x}) = \boldsymbol{\nabla}\Phi + \boldsymbol{\nabla} \times \boldsymbol{A}. \tag{4.3.4}$$

The vector field, $\widehat{\boldsymbol{u}}$, can be expressed in terms of its Fourier transform

$$\widehat{\boldsymbol{u}}(\boldsymbol{x}) = \frac{1}{2\pi} \int_{-\infty}^{\infty} \widehat{\underline{\boldsymbol{u}}}(\boldsymbol{k}) e^{i\boldsymbol{k}\cdot\boldsymbol{x}} d\boldsymbol{k}. \tag{4.3.5}$$

The solenoidal and irrotational components (see Griffiths (1999); Baierlein (1995) for details of the Helmholtz decomposition) are

$$
\begin{aligned}
\widehat{\underline{\boldsymbol{u}}}_\Phi(\boldsymbol{k}) &= \frac{\boldsymbol{k}(\boldsymbol{k} \cdot \widehat{\underline{\boldsymbol{u}}}(\boldsymbol{k}))}{||\boldsymbol{k}||^2} \\[2mm]
\widehat{\underline{\boldsymbol{u}}}_A(\boldsymbol{k}) &= \frac{\boldsymbol{k}(\boldsymbol{k} \times \widehat{\underline{\boldsymbol{u}}}(\boldsymbol{k}))}{||\boldsymbol{k}||^2},
\end{aligned}
\tag{4.3.6}
$$

respectively. The solenoidal component $\widehat{\underline{\boldsymbol{u}}}_\Phi$, depends on $\boldsymbol{k} = [k_x, k_y]^{\mathrm{t}}$ and is rescaled to the desired energy spectra (4.3.2) by first computing the energy $\underline{\mathcal{E}}(\boldsymbol{k})$ of $\underline{\boldsymbol{u}}_\Phi$

$$
\underline{\mathcal{E}}(\boldsymbol{k}) = \underline{\boldsymbol{u}}_\Phi(\boldsymbol{k})\underline{\boldsymbol{u}}_\Phi^\star(\boldsymbol{k})
\tag{4.3.7}
$$

The solenoidal part is then scaled according to

$$
\underline{\boldsymbol{u}}_\Phi(\boldsymbol{k}) = \widehat{\underline{\boldsymbol{u}}}_\Phi(\boldsymbol{k})\sqrt{\left(\frac{\mathcal{E}(\boldsymbol{k})}{\underline{E}(\boldsymbol{k})}\right)}.
\tag{4.3.8}
$$

The resulting spectra is transformed back to real space to give the desired divergence-free velocity field, which is rescaled by the maximum of the Eulerian norm to give a function of order unity

$$
\begin{aligned}
u(x,y) &= \frac{\widehat{u}}{\max\left[\sqrt{\widehat{u}^2 + \widehat{v}^2}\right]} \\[2mm]
v(x,y) &= \frac{\widehat{v}}{\max\left[\sqrt{\widehat{u}^2 + \widehat{v}^2}\right]}.
\end{aligned}
\tag{4.3.9}
$$

4.3.1.2   Pressure calculation

The non-dimensional Poisson equation for the pressure field of a two–dimensional solenoidal flow is

$$
\left(\frac{\partial u}{\partial x}\right)^2 + 2\frac{\partial u}{\partial y}\frac{\partial v}{\partial x} + \left(\frac{\partial v}{\partial y}\right)^2 = -\frac{1}{\rho_0}\left(\frac{\partial^2 p}{\partial x^2} + \frac{\partial^2 p}{\partial y^2}\right),
\tag{4.3.10}
$$

where the reference length, velocity and pressure scales are the box length $x_{\mathrm{ref}} = L$, the maximum fluctuation $u_0 = \max\left[\sqrt{u^2 + v^2}\right]$ and $p_{\mathrm{ref}} = \rho_0 u_0^2$, respectively. Equation (4.3.10) is used to compute the fluctuating pressure field based on the divergence-free fluctuating velocity field (defined in section 4.3.1.1). The Poisson equation can be solved by taking the Fourier transform of the left-hand-side of (4.3.10), integrating with respect to x and y, and taking the inverse Fourier transform to solve for the pressure. In order to produce an initial condition of a compressible

flow, the pressure must be given a thermodynamic meaning by rescaling it in accordance with a thermodynamic state, here chosen to be defined by a reference density and temperature

$$\rho_0 = 1, \quad T_0 = 1,$$
(4.3.11)

and the equation of state for an ideal gas

$$p_0 = \frac{\rho_0 T_0}{\gamma \mathrm{Ma}_t^2}.$$
(4.3.12)

The turbulent Mach number Ma_t is based on the maximum velocity magnitude

$$\mathrm{Ma}_t = \frac{|\boldsymbol{u}|_{\max}}{c_0}$$
(4.3.13)

and is set as an input parameter. The sound speed $c_0 = \sqrt{\gamma\, p_0/\rho_0}$ is then used to form a velocity scale $u_0 = \mathrm{Ma}_t\, c_0$. The rescaled velocity, pressure, and (constant) temperature fields are then

$$\widetilde{u} = u_0\, u, \quad \widetilde{p} = p_0 + \rho_0\, u_0^2\, p$$
$$\widetilde{v} = u_0\, v, \quad \widetilde{T} = T_0.$$
(4.3.14)

All that remains is to calculate the density and specific total energy fields from the equations of state

$$\widetilde{\rho} = \frac{\widetilde{p}\gamma \mathrm{Ma}_t^2}{T_0}$$
$$\widetilde{e}_t = \frac{T_0}{\gamma(\gamma - 1)\mathrm{Ma}_t^2} + \frac{1}{2}\left(\widetilde{u}^2 + \widetilde{v}^2\right).$$
(4.3.15)

4.3.2 Initial condition

The peak wavenumber for the initial condition was chosen to be $k_p = 2$, concentrating the majority of the kinetic energy at large scales. The initial condition spectrum is shown with a grey line in figure 4.11 and is compared with the desired analytical profile shown in red circles, calculated from (4.3.2).
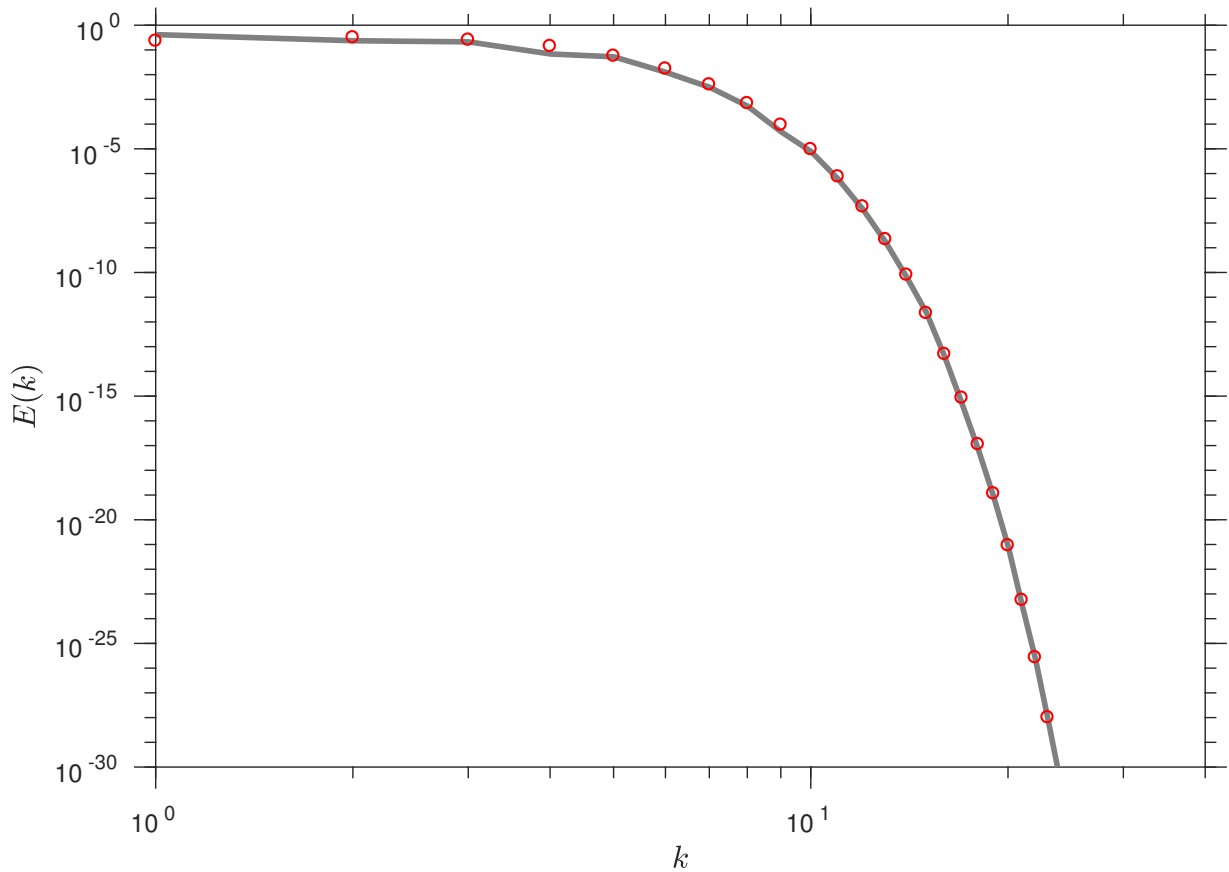
Figure 4.11: Energy spectrum of initial condition for freely evolving, two-dimensional homogeneous isotropic turbulence, $\mathrm{Ma}_t = 0.8$, $nx = ny = 1024$. Grey line shows computed spectrum, red markers shows prescribed analytical spectrum.

4.3.3   Bulk viscosity effect

The vorticity of both viscous cases, shown in figures 4.12 and 4.13 is similar in magnitude for both $\chi = 0$ and $\chi = 10^3$ throughout the simulation. However, the velocity dilatation fields show a large difference. Figure 4.14 shows fine structures emerging above $tu_0/L \sim 2$, creating regions of sharp contrast that represent acoustic wave fronts propagating through the domain. In figure 4.15, however, there is a fast decrease in the magnitude of the velocity dilatation after the initial time. By $tu_0/L \sim 12.80$ these blur into less well defined regions. The thread–like structures are regions of large dilatational production (term 5), as shown in figure 4.16d and 4.17d. The field is both positive and negative but the thread–like structures are predominantly negative, representing a transfer to internal energy. These regions can be produced by two counter–rotating vortices resulting in a compressed region between them that have large gradients in Θ and hence increase term 5. The largest magnitude of the negative value in the $\chi = 10^3$ case is three orders of magnitude larger than the $\chi = 0$ case, consistent with the linear dependence on μ_b in term 5.

However, for $\chi = 10^3$, term 5 is smaller than the solenoidal production (term 4) due to the fact that term 5 contains the factor $(1/3 + \chi)/\mathrm{Re}_L$ when non–dimensionalised. For the current simulation $\mathrm{Re}_L \sim 10^3$ and $\chi = 10^4$, hence term 5 is an order of magnitude smaller than term 4. The sum of the two production terms (4+5) is shown in figures 4.18c and 4.18d and is very similar for both cases, although slightly smaller for the $\chi = 10^3$ case, indicating that overall production has decreased. The two terms comprising the extended Poisson equation term (2 and 3) are shown in figures 4.16a and 4.16b for $\chi = 0$ and figures 4.17a and 4.17b for $\chi = 10^3$. Term 2 appears to have the inverse greyscale colouring of similar magnitude to term 3, indicating that these two terms balance each other. For $\chi = 0$, the only difference from the $\chi = 10^3$ case are the thread–like structures, which match the material derivative of Θ shown in figure 4.16e. Once this contribution is removed terms 2 and 3 balance almost perfectly, as shown in figure 4.16f by summing terms 2 and 3. For $\chi = 10^3$, the extended Poisson equation terms match well and the thread–like structures are not visible (figures 4.17a and 4.17b). This is due to the increased negative dilatational production reducing the magnitude of term 1 by two orders of magnitude.

Figures 4.19a and 4.19b show the maximum pressure and velocity dilatation in the domain as a function of time. Both show a decrease in the $\chi = 10^3$ case and the divergence of velocity shows a decrease by approximately a factor of six at late times. Whilst p_{max} of both cases are similar until $tu_0/L \sim 8$, Θ_{max} reduces almost immediately for the $\chi = 10^3$ case, due to the increased dilatational production term reducing the magnitude of term 1.

4.3.4 Energy Spectra

Once the cascade of enstrophy starts to generate "eddies" throughout the inertial range, the slope of the energy cascade follows the expected '-3' trend as predicted by the theory of Kraichnan (1967). At high wavenumbers ($k\,L/(2\pi) > 40$), the viscosity dissipates kinetic energy to internal energy. Any scales with fewer than four points per wavelength are filtered (see section 2.5) to prevent a build up of energy at sub-grid scales which lead to numerical instability.

Applying the idea from the one–dimensional perturbation simulations of maximum damping occurring at $\mathrm{Re}_{\mathrm{ac.}} \sim 1$ (see section 4.1), the current simulation can be checked to see if it is in the regime for maximum Landau acoustic damping. Taking the ratio of Re_L and Re_{Λ_0} and rearranging gives

$$\frac{\Lambda_0}{L} \sim \frac{\text{Re}_L}{\text{Re}_{\Lambda_0}} \text{Ma}_t. \tag{4.3.16}$$

For $\chi = 0$, taking $\text{Re}_{\Lambda_0} \sim 10$, $\text{Ma}_t = 0.8$ and $\text{Re}_L = 8 \times 10^4$, $\Lambda_0/L \sim 10^{-4}$, which indicates that 10^4 points would be needed per domain length L to capture the small scales at which the acoustic damping is strongest. In fact, due to the filter cut–off at four points–per–wavelength, at least 5×10^4 points would be needed. The current simulation has $nx = ny = 1024$ and therefore cannot resolve the scales at which maximum Landau acoustic damping would be observed. For $\chi = 10^3$, now taking $\text{Re}_{\Lambda_0} \sim 10^4$, $\Lambda_0/L \sim 10^{-1}$, which corresponds to 10 points in the domain size L (50 including the filter cut–off). The current simulation has of the order of 10^2 more points than this and suggests that Landau acoustic damping is present in the simulation. In the low Re_{Λ_0} regime, lower damping is likely to be observed at scales smaller than the one associated with maximum Landau damping. This lower damping regime could correspond to the production, by term 5 in (4.2.4), of fine thread–like structures that are sharply preserved in the $\chi = 10^3$ fields of Θ (figure 4.17e), whereas larger scales are blurred. The solenoidal energy spectra in figure 4.20a shows no impact from the bulk viscosity. The compressible spectra however (figure 4.20b) shows a wavenumber range $5 < k < 70$ in which the energy has been reduced. The prediction for the wavelength at which maximum damping occurs due to the Landau acoustic damping mechanism was at $\Lambda_0/L \sim 10^{-1}$ which corresponds to an acoustic wave with ten points per wavelength, corresponding to a wavenumber of 10^2 given that $nx = ny \sim 10^3$. At small Re_{Λ_0}, the Landau acoustic damping mechanism changes to a different mechanism (see figure 4.2 for example). In figure 4.20b, the curves for each χ value meet at approximately $k = 10^2$, possibly indicating the end of the Landau acoustic damping regime. The $\chi = 10^3$ curve recovers to match the zero bulk viscosity case, implying lower damping and therefore less transfer from dilatational kinetic energy to internal energy. The next chapter explores the same ideas in the context of a three–dimensional, wall driven turbulent flow.
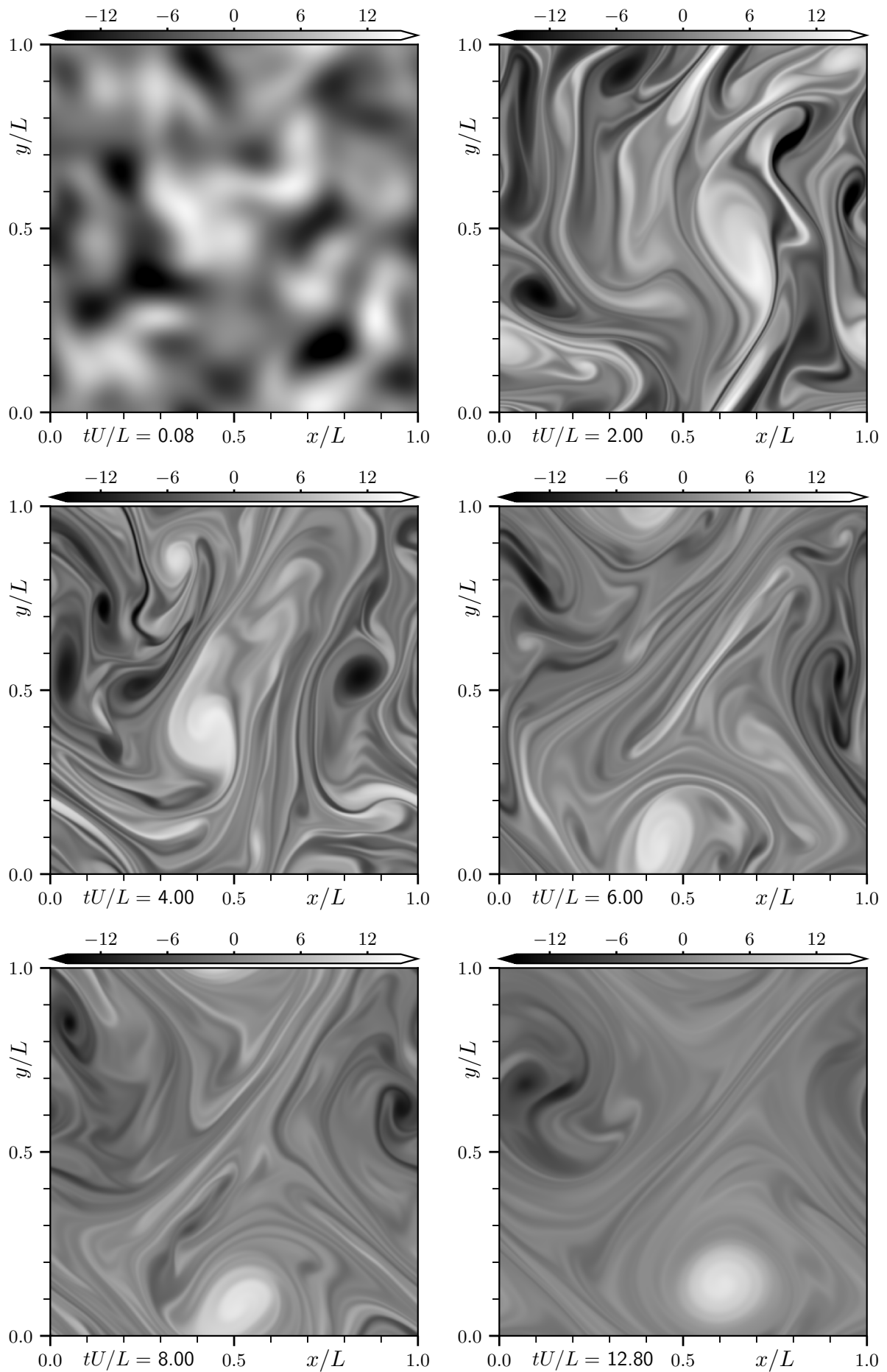
Figure 4.12: Vorticity at advancing times. $\text{Ma}_t = 0.8$, $\text{Re}_L = 8 \times 10^4$. $\chi = 0$.
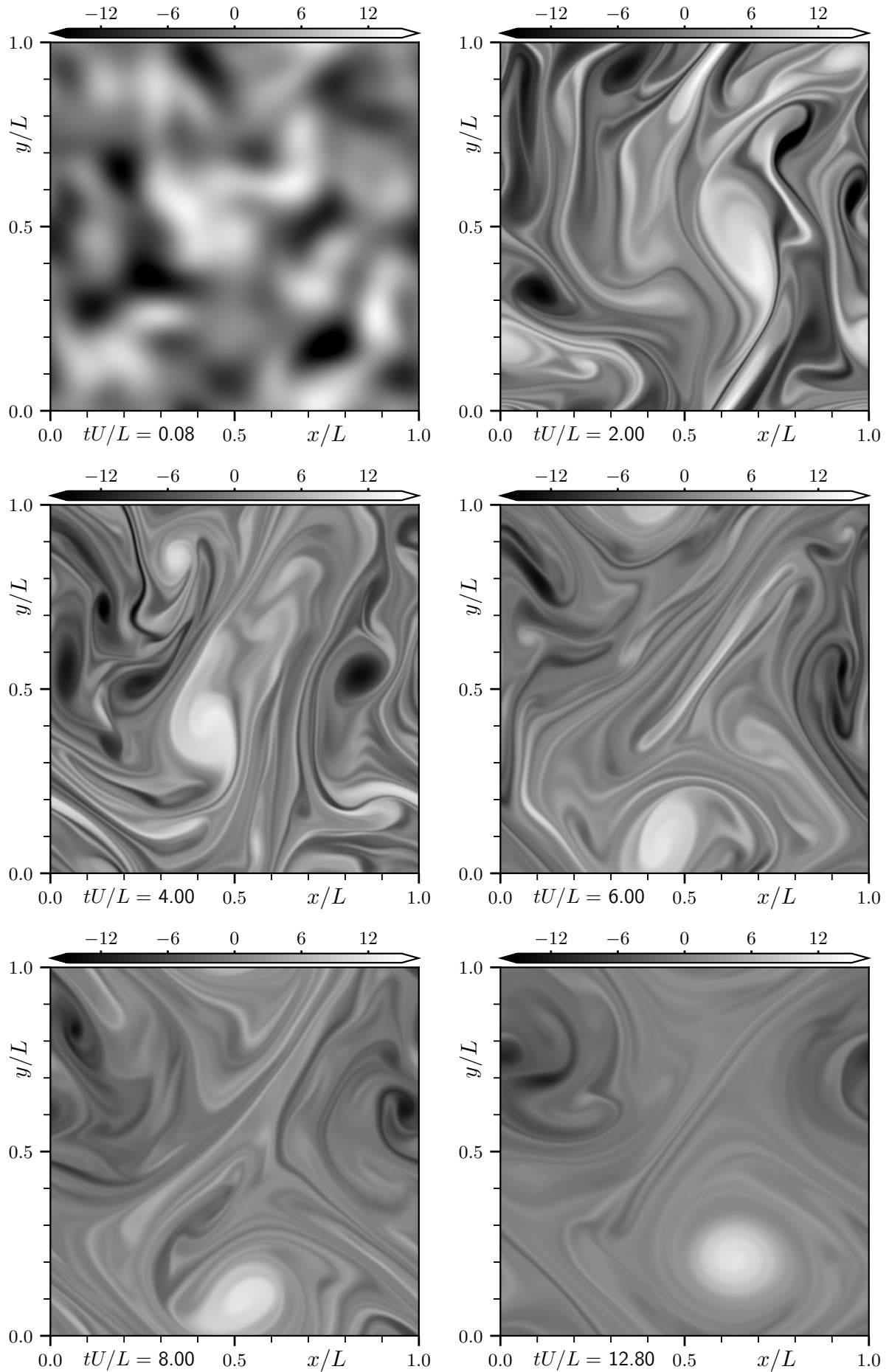
Figure 4.13: Vorticity at advancing times. $\mathrm{Ma}_t = 0.8$, $\mathrm{Re}_L = 8 \times 10^4$, $\chi = 10^3$.
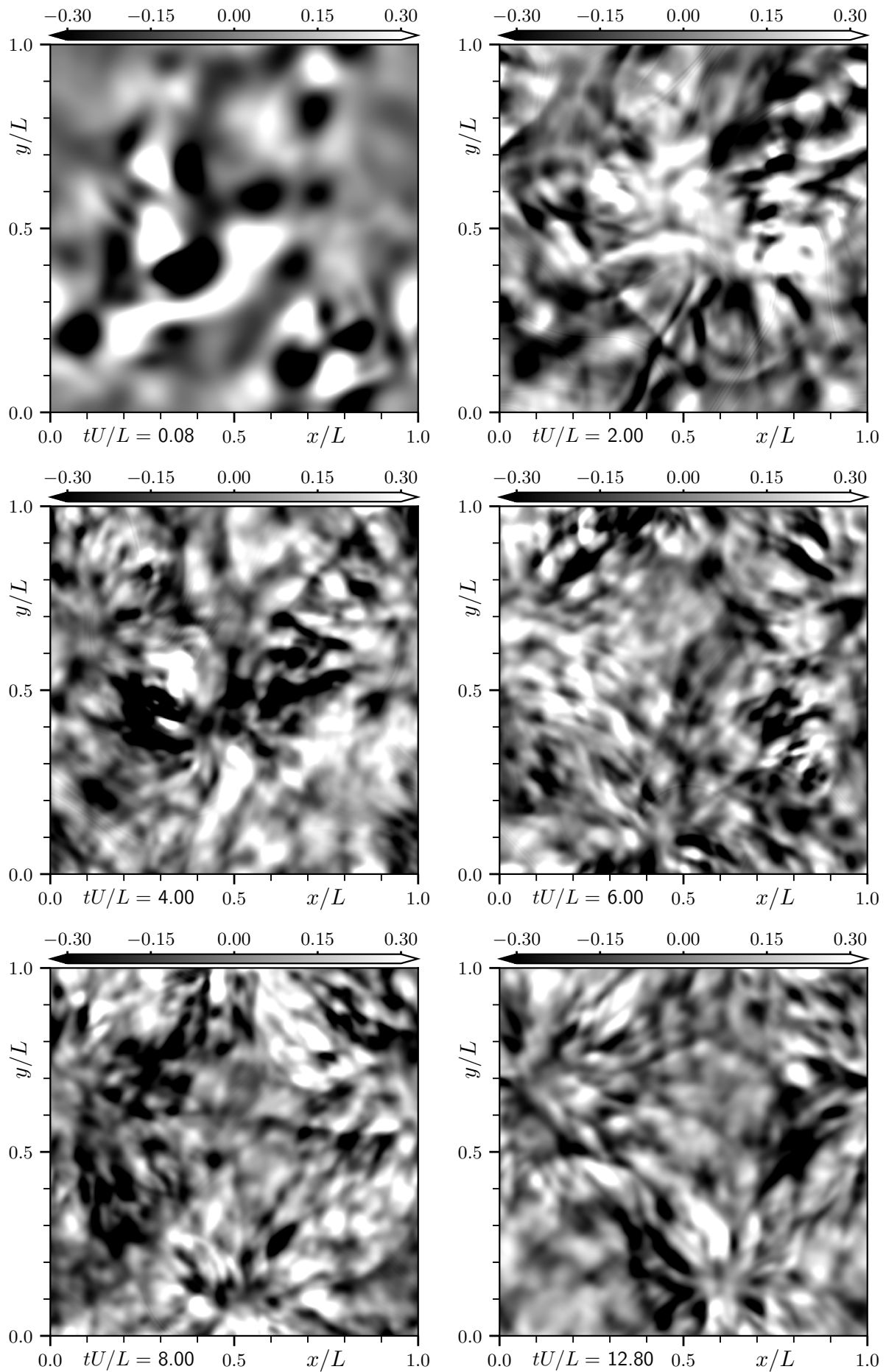
Figure 4.14: Divergence of velocity at advancing times. $\text{Ma}_t = 0.8$, $\text{Re}_L = 8 \times 10^4$. $\chi = 0$.
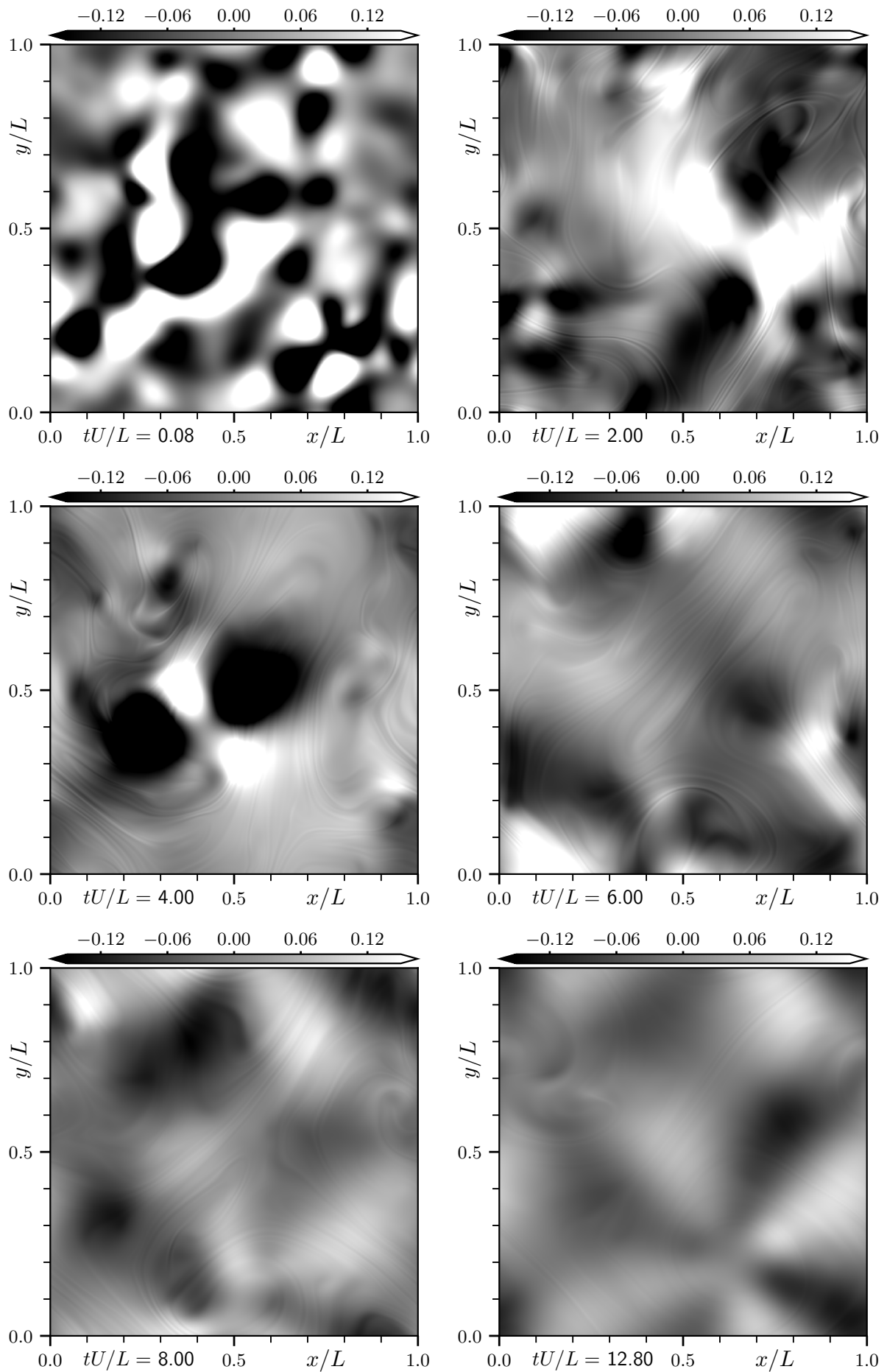
Figure 4.15: Divergence of velocity at advancing times. $\mathrm{Ma}_t = 0.8$, $\mathrm{Re}_L = 8 \times 10^4$, $\chi = 10^3$.

(a) Term (2). Min = -135, max = 157

(b) Term (3). Min=-194, max=163

(c) Term (4). Min=-3.5, max=16

(d) Term (5). Min=-0.0015, max= 0.00078

(e) Term (1). Min=-193, max=154

(f) Term (2)+(3). Min=-195, max=153
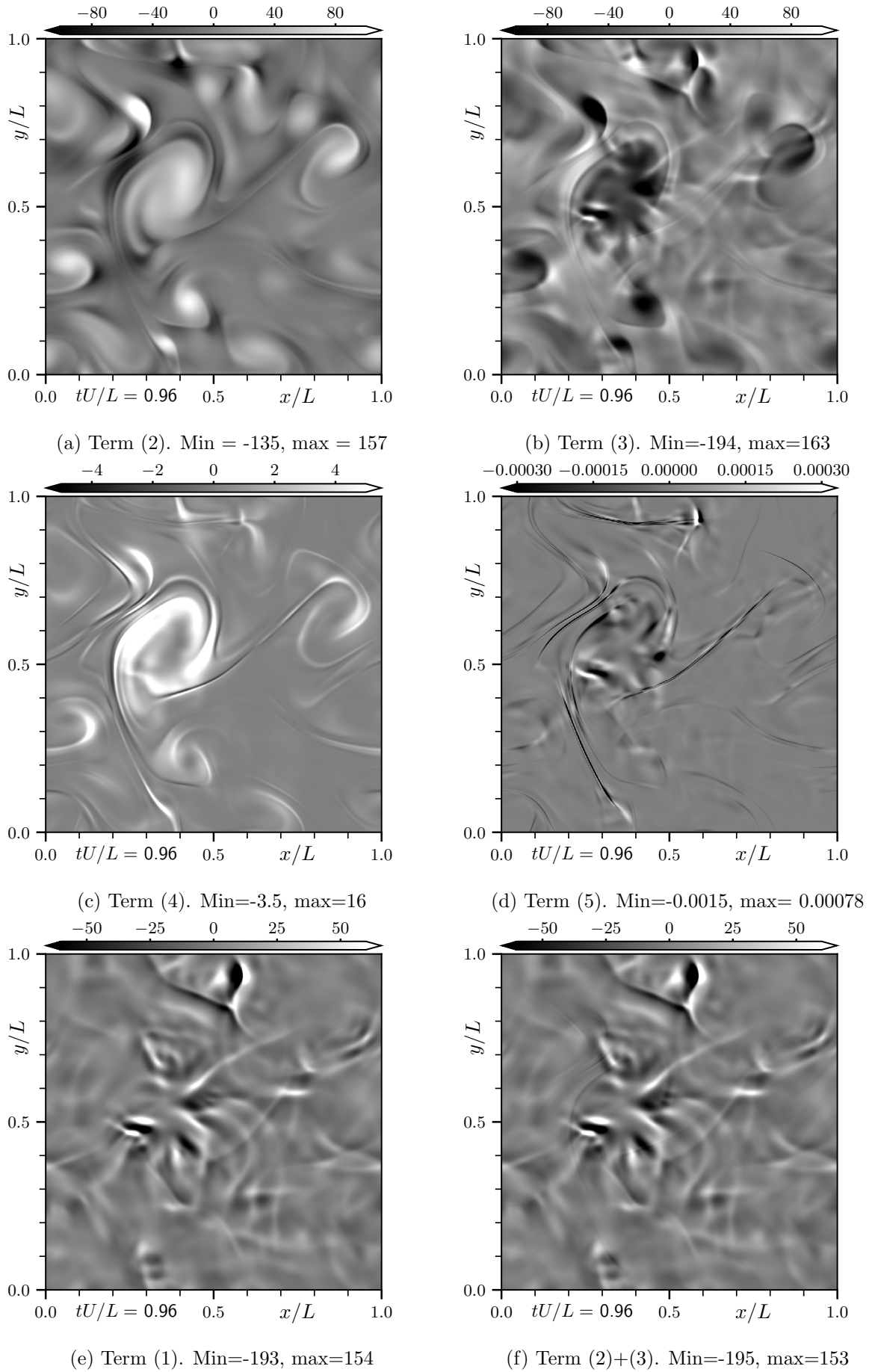
Figure 4.16: Theta budget terms at $tu_0/L = 0.96$. Numbers in brackets refer to the terms in equation 4.2.4. $\mathrm{Ma}_t = 0.8$, $\mathrm{Re}_L = 8 \times 10^4$. $\chi = 0$.

(a) Term (2). Min = -134, max = 156

(b) Term (3). Min=-160, max=255

(c) Term (4). Min=-3.5, max=16

(d) Term (5). Min=-4, max= 0.6

(e) Term (1). Min=-7, max=6

(f) Term (2)+(3). Min=-179, max=193
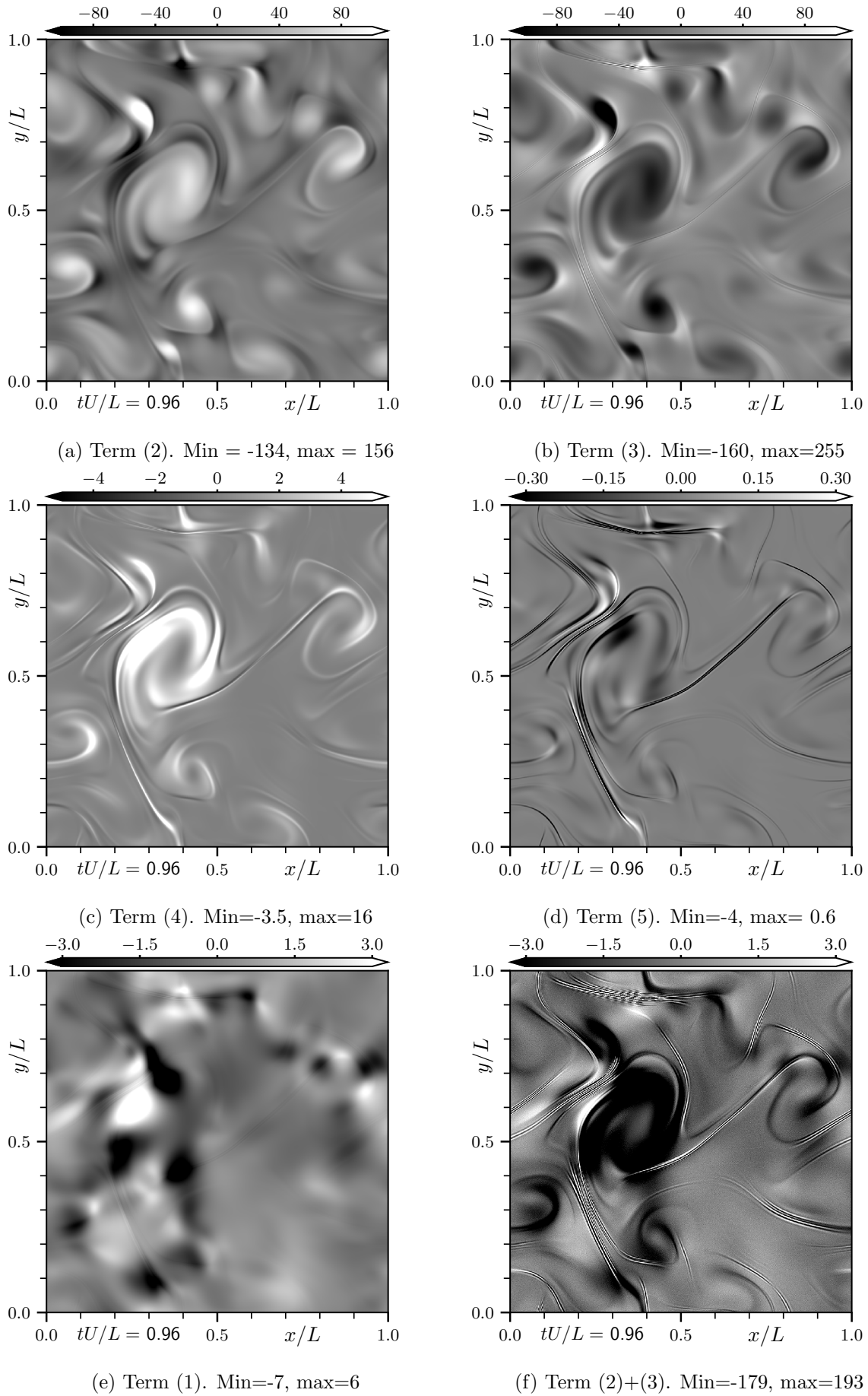
Figure 4.17: Theta budget terms at $tu_0/L = 0.96$. Numbers in brackets refer to the terms in equation 4.2.4. $\mathrm{Ma}_t = 0.8$, $\mathrm{Re}_L = 8 \times 10^4$. $\chi = 10^3$.

(a) Term (2)+(3). Min=-195, max=153. $\chi = 0$.

(b) Term (2)+(3). Min=-179, max=193. $\chi = 10^3$.

(c) Term (4)+(5). Min=-3.5, max=16. $\chi = 0$.

(d) Term (4)+(5). Min=-3.4, max= 16. $\chi = 10^3$.

(e) Term (1). Min=-193, max=154

(f) Term (1). Min=-7, max=6
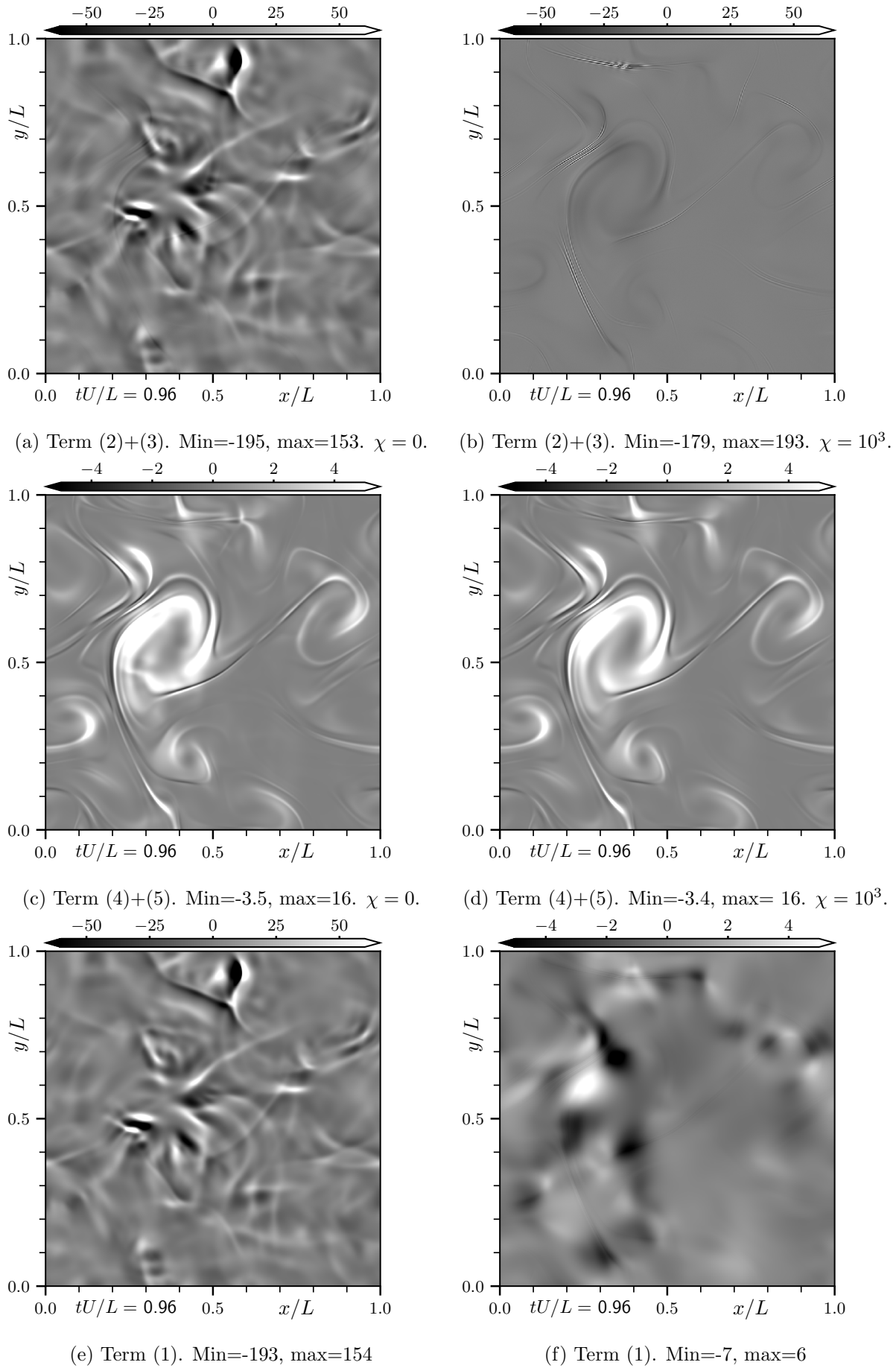
Figure 4.18: Theta budget terms (combined) at $tu_0/L = 0.96$. Numbers in brackets refer to the terms in equation 4.2.4. $\mathrm{Ma}_t = 0.8$, $\mathrm{Re}_L = 8 \times 10^4$. Left column: $\chi = 0$; right column $\chi = 10^3$.
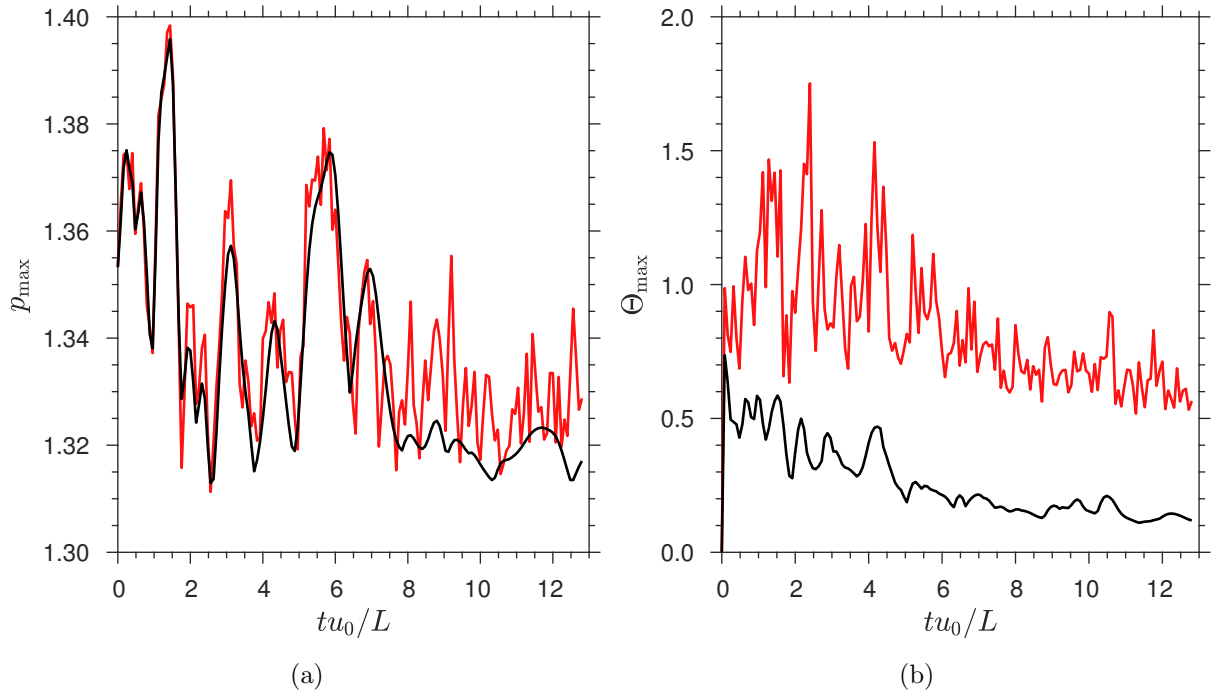
Figure 4.19: Global maximum of (a) pressure and (b) velocity dilatation versus time. $Ma_t = 0.8$, $Re_L = 8 \times 10^4$, $nx = ny = 1024$, $Pr = 0.7$, $\gamma = 1.29$. Red line is $\chi = 0$, black is $\chi = 10^3$.
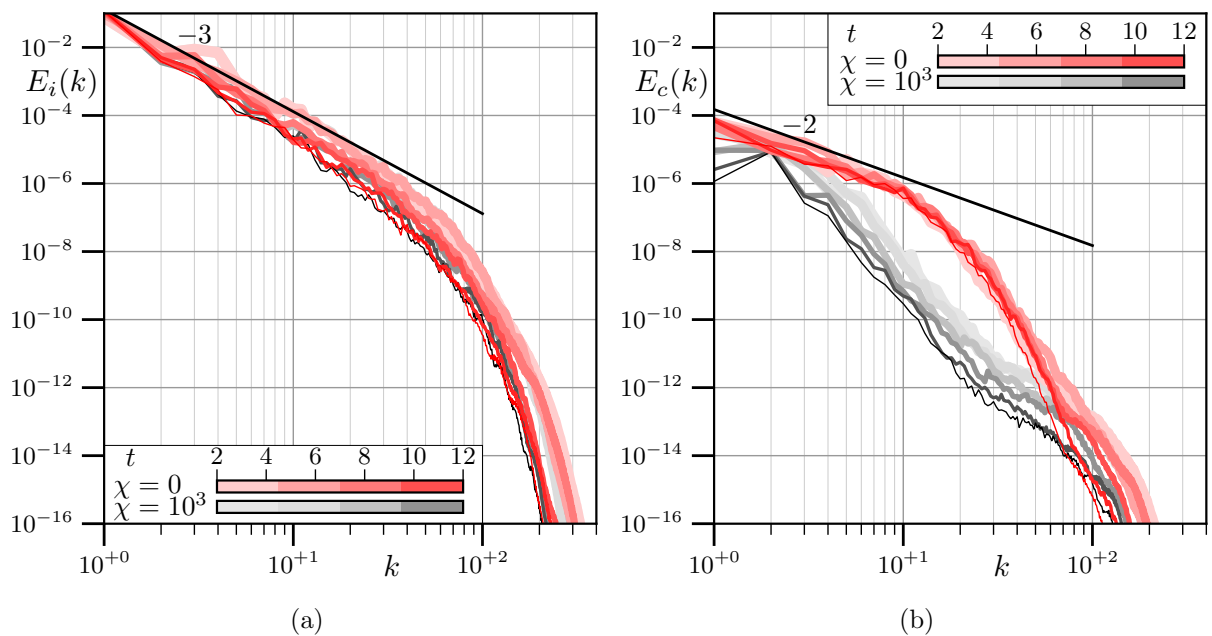
Figure 4.20: Energy spectra, $Ma_t = 0.8$, $Re_L = 8 \times 10^4$, $nx = ny = 1024$, $Pr = 0.7$, $\gamma = 1.29$. (a) solenoidal kinetic energy $E_i(k)$; (b) dilatational kinetic energy $E_c(k)$. Red line is $\chi = 0$, grey is $\chi = 10^3$. Colours darken as time advances.

Chapter 5

3D Couette flow

Presented in this chapter are the results of a DNS of compressible plane Couette flow used to study the effect of bulk viscosity on three dimensional wall–bounded turbulence. The initialisation, mean flow profiles, turbulence statistics are detailed along with Helmholtz decomposed velocity fields to observe the changes to the compressible velocity field.

5.1 Instantaneous fields

This section shows snapshots of the instantaneous flow fields of all five high Mach number cases (A, B, C, D, and E). Chapter 3 shows results for the low Mach number validation case. Table 5.1 summarises the configuration details. The aim is to convey the main turbulence features of the flow and to capture events that are particularly affected by bulk viscosity.

5.1.1 Large domain

Two supersonic cases at $Ma = 3.0$ were run to compare the effect of bulk viscosity at moderately high Reynolds number ($Re_\tau = 485$) when $\chi = 0$ and $\chi = 10$. The following figures are included to give a representation of the instantaneous flow field. A front view (normal to the $z-y$ plane) of the streamwise velocity for $\chi = 0$ is shown in the top panel of figure 5.1. Regions of slow moving fluid are seen to eject away from the either wall to a wall–normal height of approximately $y^+ = 100$. The domain's span in wall units is $L_z^+ \approx 2900$, which contains approximately twenty ejections, giving a spanwise spacing of approximately $145\nu/u_\tau$, which is similar to the widely accepted spanwise spacing Λ_e of $100\nu/u_\tau$ units (Kim *et al.*, 1971; Chernyshenko and Baig, 2005). Side views

of the ejections are shown in the top panel of figure 5.7, which exhibit the characteristic streak–lifting process caused by the motion of the wall, leaving the ejection in a region of slower moving fluid. It is difficult to count the number of ejections accurately, but given that they represent streak lifting (Pope, 2000), a better way to count is from a wall–normal view of streamwise velocity, as shown in the top panel of figure 5.3, which shows approximately twenty streaks at $y^+ \approx 13$. This agrees better with the experimental results of Smith and Metzler (1983) who measured $\Lambda_e \approx 120$ at $y^+ \approx 15$. At large wall normal distances (middle and lower panels of figure 5.3), the streamwise streaks become wider and more coherent. By the mid–plane there are three main regions of positive u, and two of negative u. These are associated with large–scale streamwise rollers characteristic of Couette flow (see section 3.4) which will be discussed further in section 5.6. All three wall–normal views of streamwise streaks show the emergence of the dominating scale set by the large streamwise rollers, the diameters of which are of the order of the domain height h. For $\chi = 10$, the main features of the ejections are very similar to the $\chi = 0$ case, although the coherence of streamwise streaks appears to be enhanced. This is visible from wall–normal views of u in figure 5.4. The second panel in figures 5.1 and 5.2 show wall-normal velocity for $\chi = 0$ and $\chi = 10$, respectively, in which there are two regions with structures of distinctly different length scales. The near–wall region ($y^+ = 100$ corresponds to $y/h \approx 0.1$) contains small scale patterns that match the ejections in the u field, many of which are moving away from the wall (white patches near the lower wall, for example). This agrees with the linear advection mechanism that states that fluctuations in v carrying fluid away from the wall are important for the sustainment of near–wall streaks, Kim and Lim (2000). In the outer layer the turbulent patterns have scales that are closer to h and show regions of the same signed v. These correspond to large streamwise rollers. In the third panel from top in figures 5.1 and 5.2 (for $\chi = 0$ and $\chi = 10$ cases) low pressure spots are visible throughout the domain, although they are mainly clustered in the near–wall region. These represent the centres of vortices driven by the bursting events at the walls, which, via the solenoidal production term derived in the context of an ideal vortex (4.2.4), produces velocity dilatation. This can be seen in the bottom plot of figure 5.1, where there are isocontours of Θ that represent the propagation of acoustic waves away from the wall. In the $\chi = 10$ figure, the near–wall region shows clearly defined acoustic fronts, but these appear more damped in the outer layer than in the $\chi = 0$ case. In the third panel from top in figures 5.7 and 5.8, the spanwise velocity shows coherent positive and negative regions that extend the full height of the channel at an inclination of close to $20°$

from the wall plane. The three panels in figures 5.5 and 5.6 present the temperature field at the same wall–normal locations as the top–view figures of streamwise velocity. There is a large similarity in the shape and scale of the patterns. Due to the constant Prandtl number close to unity (it is 0.7 for all cases), the simulations fall into the category to which the Reynolds analogy applies (Schlichting, 1979). As summarised by Huang *et al.* (1995), the strong Reynolds analogy (that relates temperature fluctuations to streamwise velocity fluctuations by the Mach number and ratio of specific heats) is applicable only to flows with adiabatic walls. More recently, Zhang *et al.* (2014) derived a generalised Reynolds analogy that includes a recovery factor to account for variations in the Prandtl number, wall temperature, and pressure gradient. The $\chi = 10$ case shows more coherent longitudinal streaks in T that correspond to the momentum transfer from the streamwise rollers.

5.1.2 Small domain

Three small domain ($3h \times h \times 1.5h$) cases were run at $\mathrm{Re}_\tau \approx 130$ and at $\chi = 0$ (case C), $\chi = 10^2$ (case D), and $\chi = 10^3$ (case E). Due to the lower Reynolds number, the near–wall features spread further from the wall, as seen by the shift in peak $u_{\mathrm{r.m.s.}}$ from $y/h \approx 0.02$ to $y/h \approx 0.08$ (figure 5.18). Ejections are seen in figures 5.9 and 5.13 (top panel) for the three χ cases. The bulk viscosity appears not to modify the spatial separation between streaks as shown by u at $y^+ \approx 0.2$ in figure 5.10. The domain span is $L_z^+ \approx 410$ for the $\chi = 0$ and $\chi = 10^2$ cases and all three figures have approximately four streaks in the span. The $\chi = 0$ case shows bands connecting the streaks that are not present in either the $\chi = 10^2$ case (middle plot) or $\chi = 10^3$ case (bottom plot). A side view of streamwise velocity (figure 5.11) shows eddies of similar size and spacing, and bursting events that almost reach the channel mid–plane. This is understandable as the bursting events occur in the region $0 < y^+ < 100$ and $L_y^+ \approx 270$. Figure 5.12 shows the divergence of velocity for the $\chi = 0$ and $\chi = 10^2$ cases and the lower panel of figure 5.13 shows the $\chi = 10^3$ case (note the reduction in greyscale range by a factor of five). In the zero bulk viscosity case there are large arcs of positive Θ that emerge ahead of the ejection.
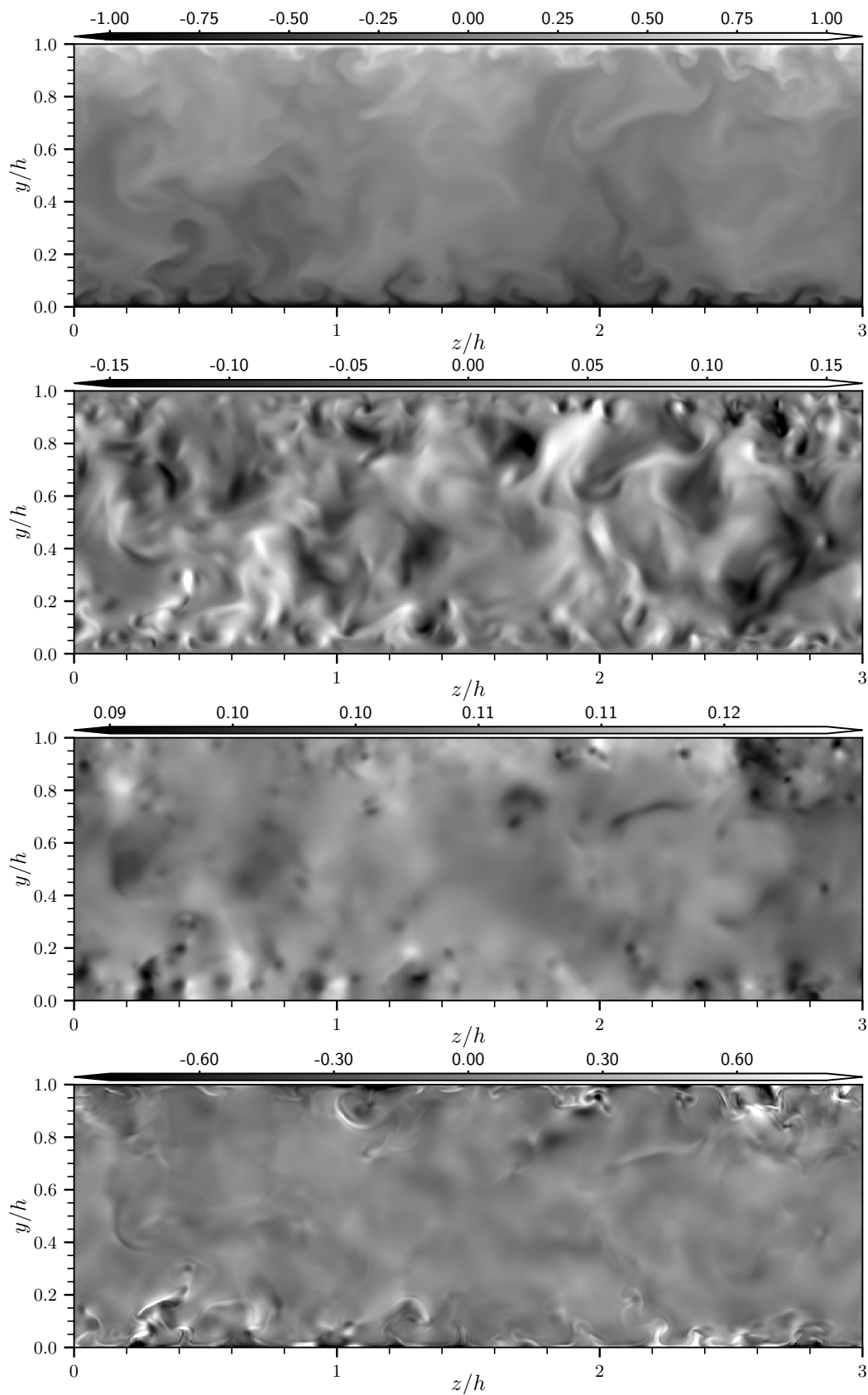
Figure 5.1: Case A, $\chi = 0$. From top to bottom: Streamwise velocity, wall–normal velocity, thermodynamic pressure, and divergence of velocity.
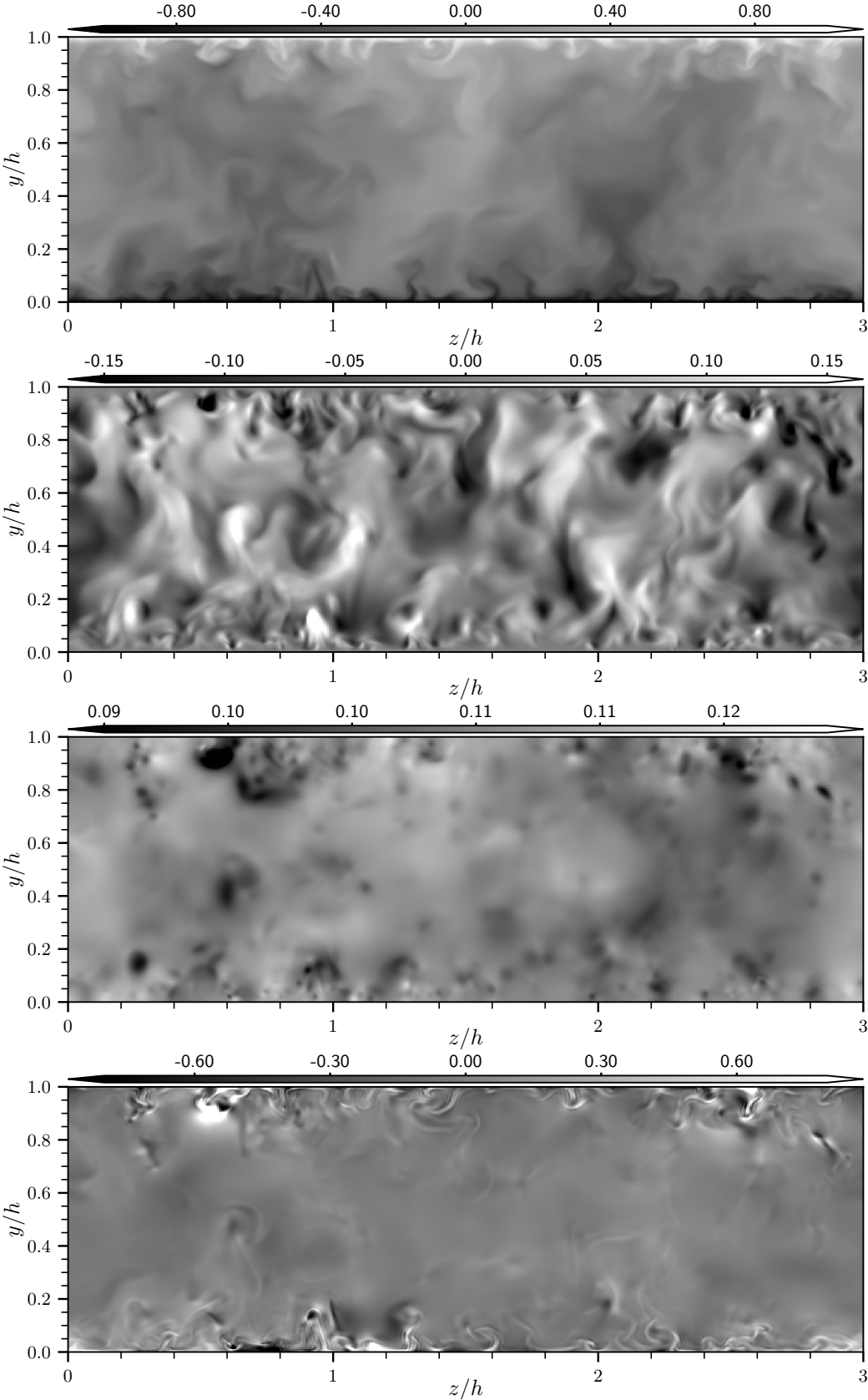
Figure 5.2: Case B, $\chi = 10$. From top to bottom: Streamwise velocity, wall–normal velocity, thermodynamic pressure, and divergence of velocity.
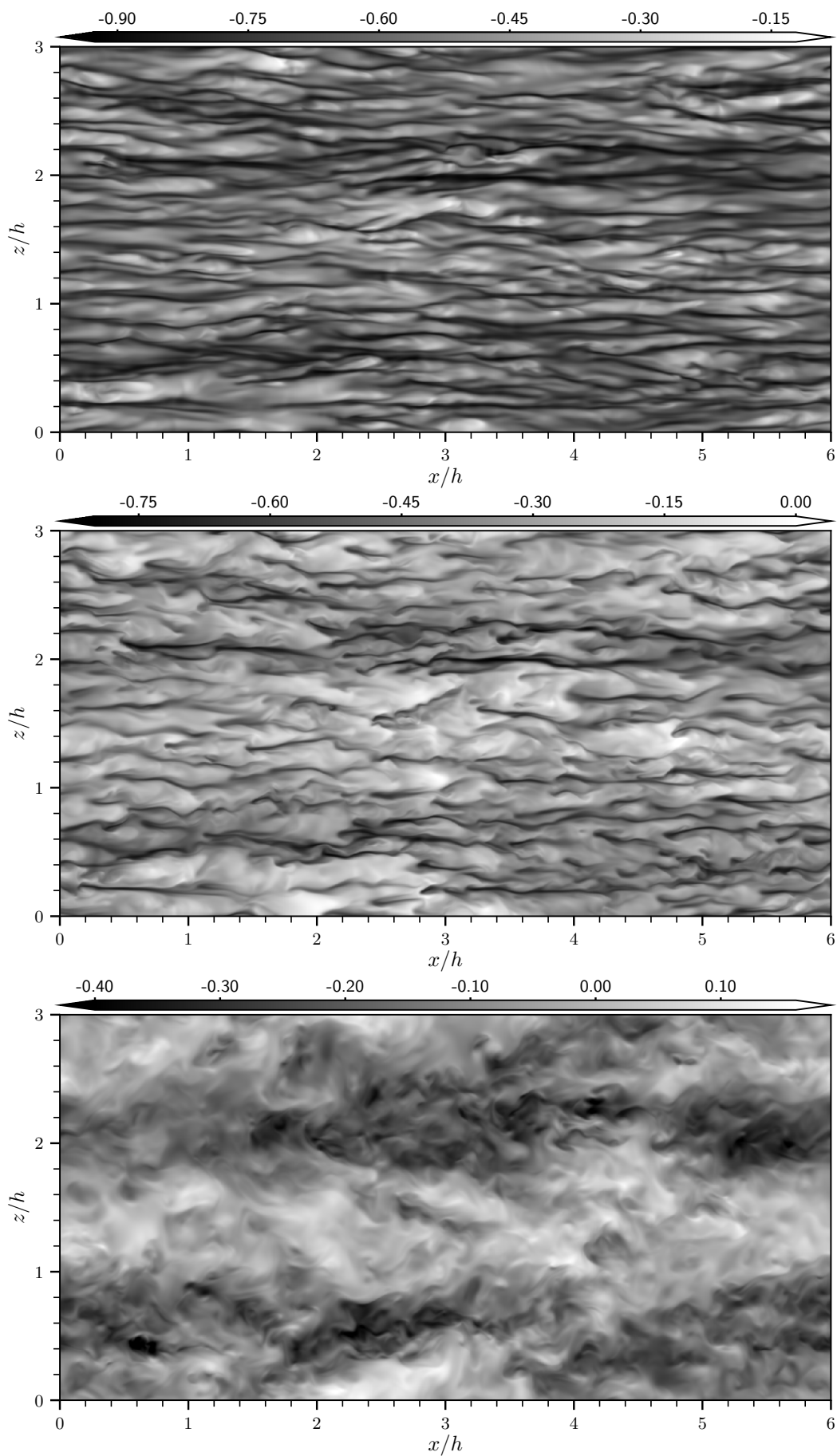
Figure 5.3: Streamwise velocity of $\chi = 0$ case A, top view. Top panel: $y^+ \approx 13$; middle panel: $y^+ \approx 39$, bottom panel: mid–plane, $y^+ \approx 481$.
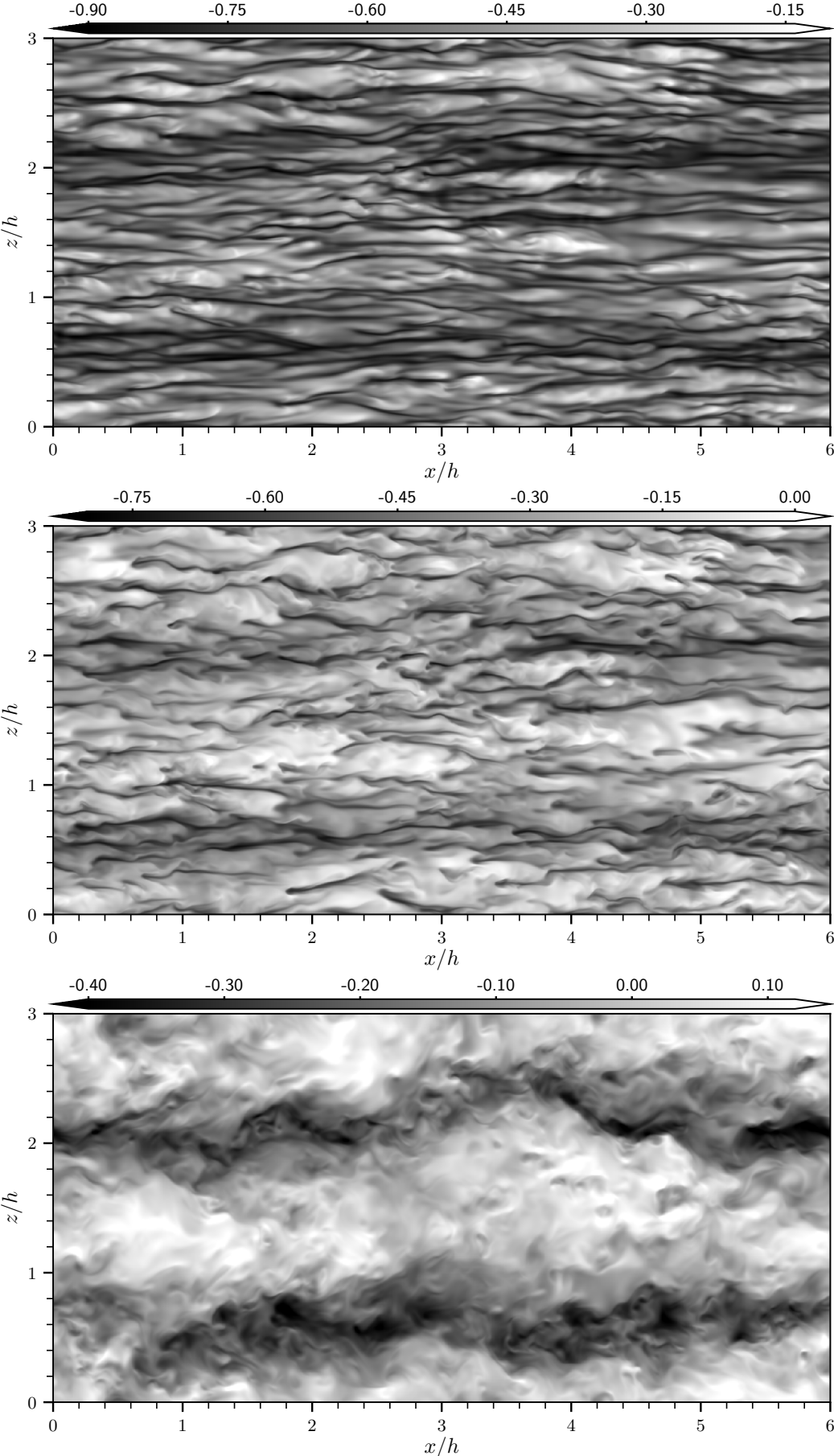
Figure 5.4: Streamwise velocity of $\chi = 0$ case B, top view. Top panel: $y^+ \approx 13$; middle panel: $y^+ \approx 39$, bottom panel: mid–plane, $y^+ \approx 488$.
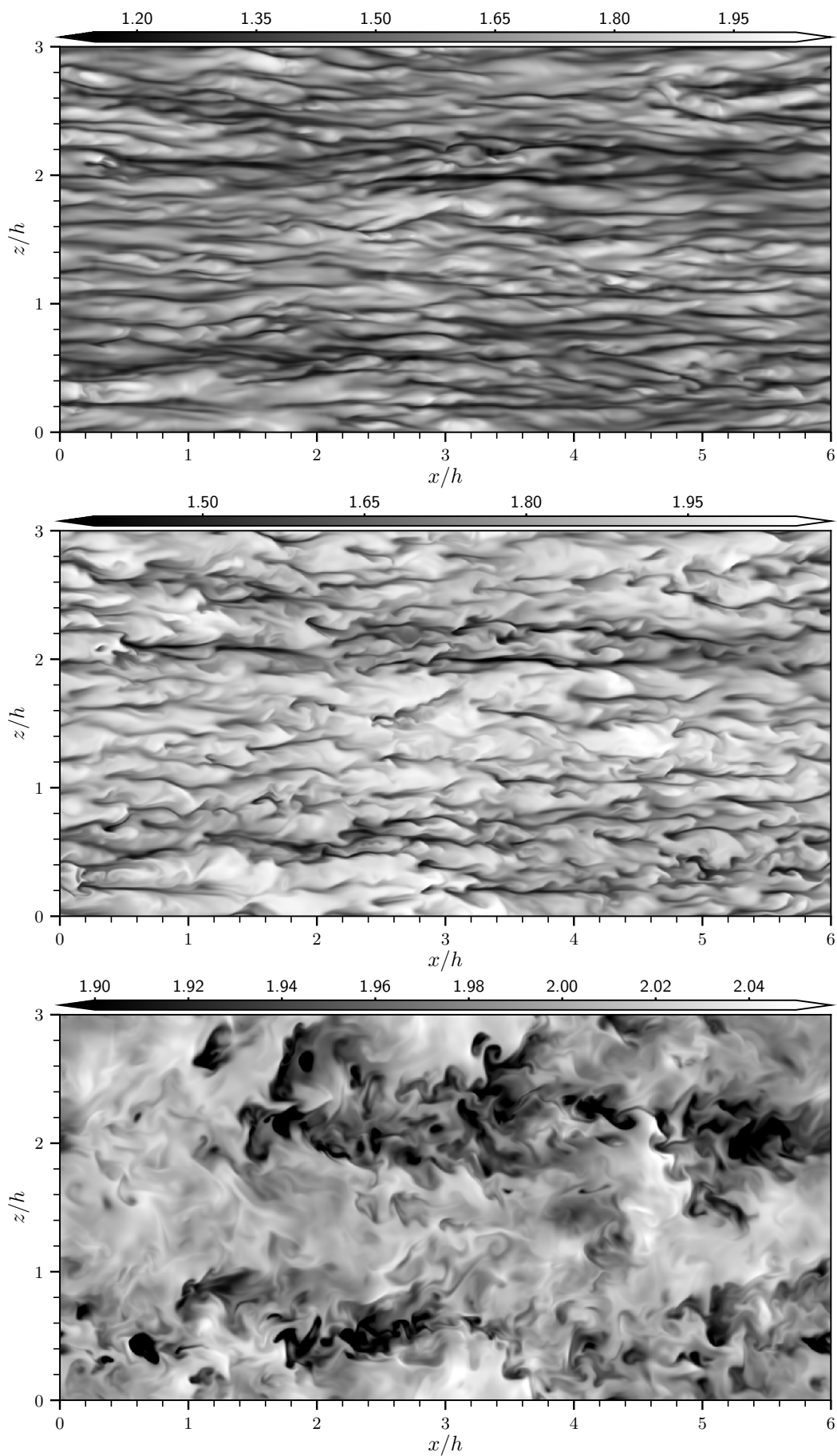
Figure 5.5: Temperature of $\chi = 0$ case A. Top panel: $y^+ \approx 13$; middle panel: $y^+ \approx 39$, bottom panel: mid–plane, $y^+ \approx 481$.
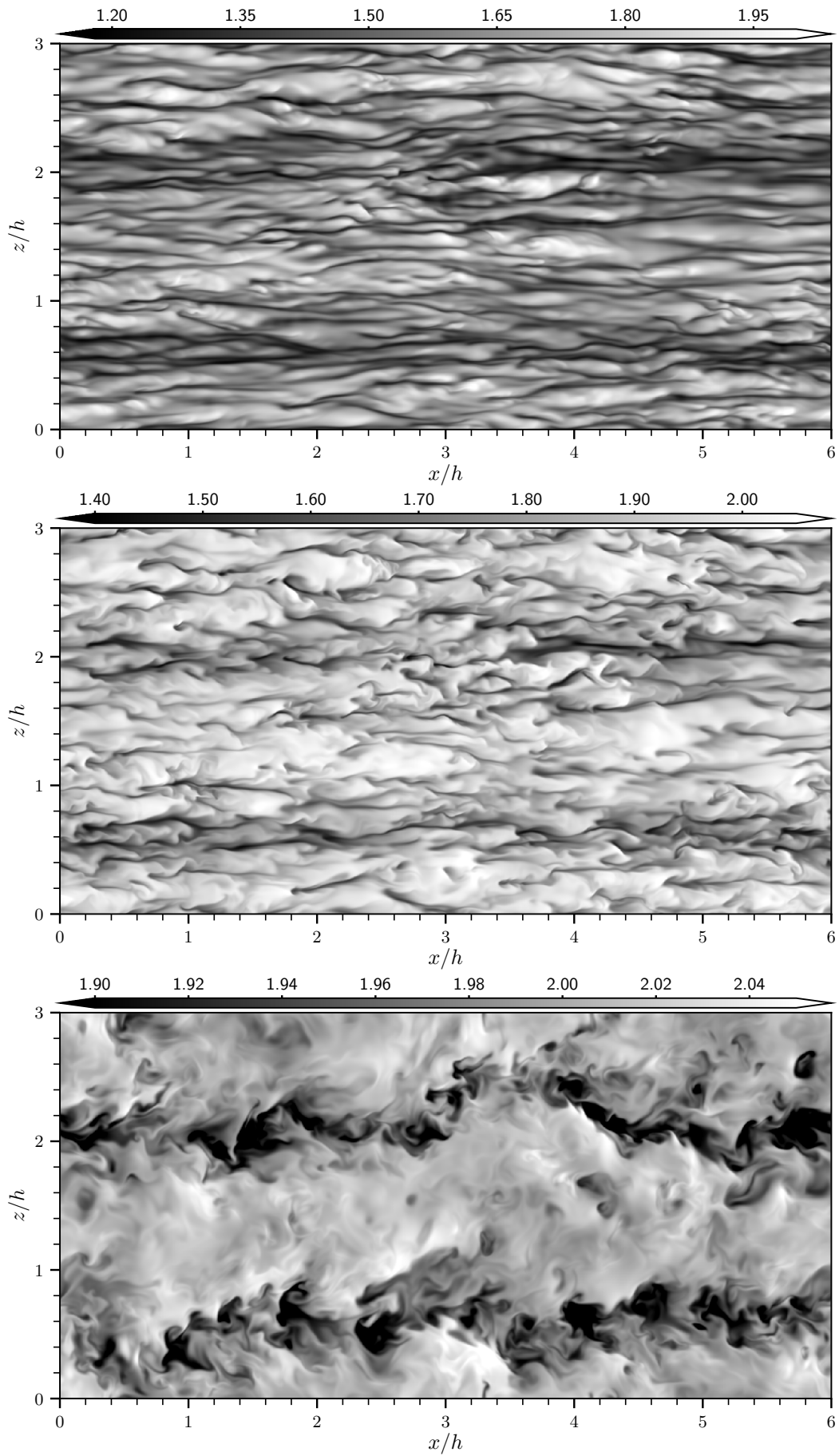
Figure 5.6: Temperature of $\chi = 10$ case B. Top panel: $y^+ \approx 13$; middle panel: $y^+ \approx 39$, bottom panel: mid–plane, $y^+ \approx 488$.
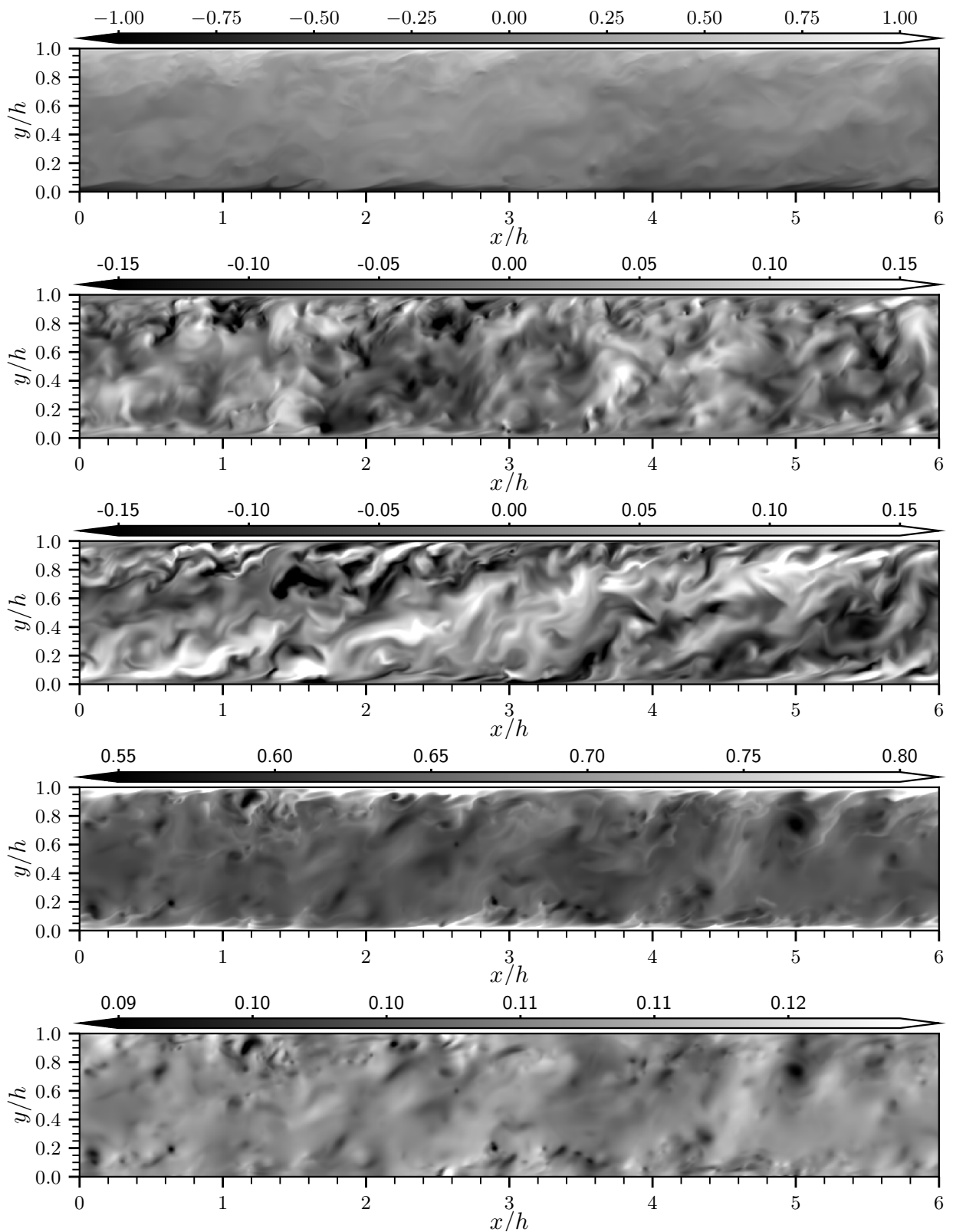
Figure 5.7: Side view of case A data, $\chi = 0$. From top to bottom: streamwise velocity, wall–normal velocity, spanwise velocity, density, and pressure.
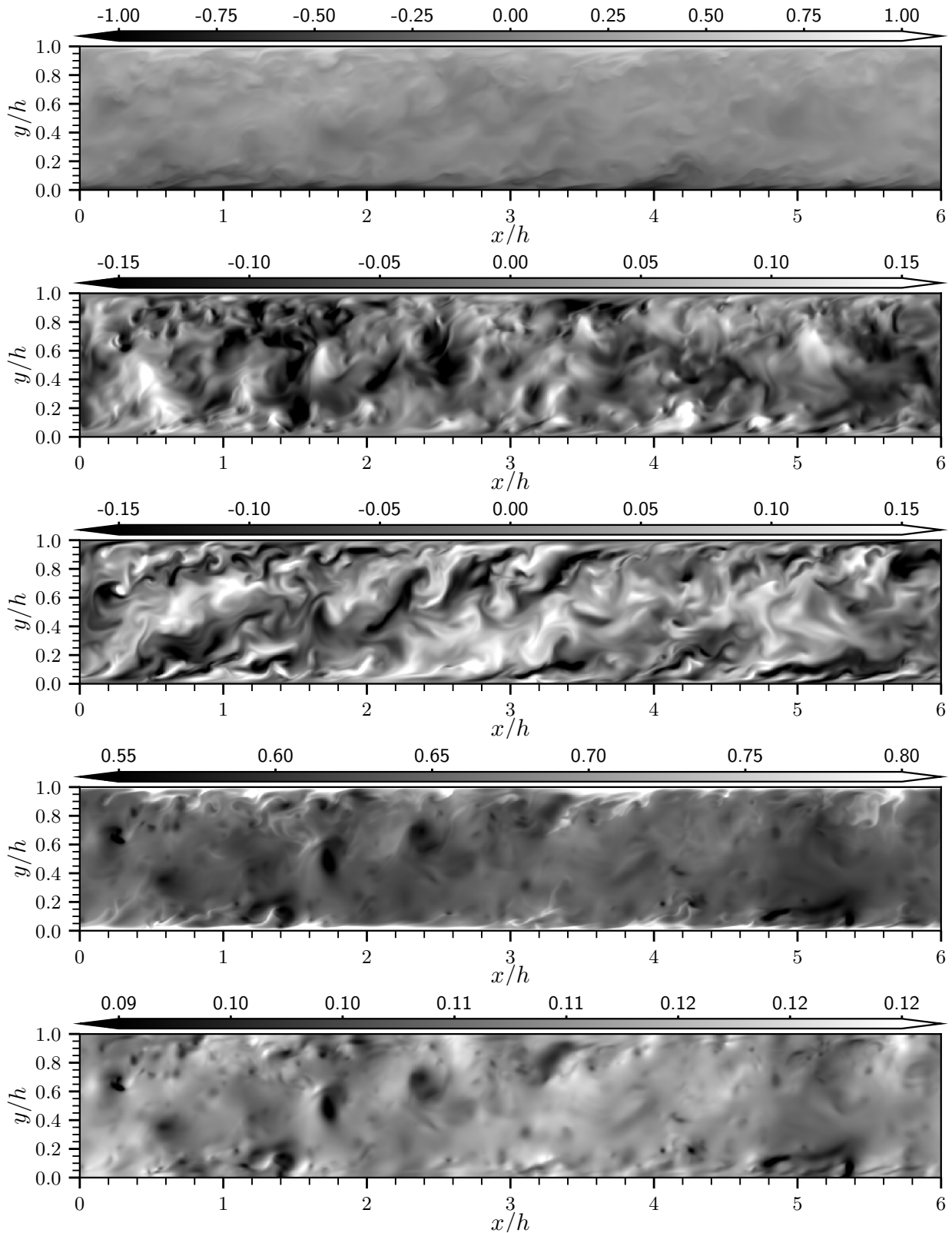
Figure 5.8: Side view of case B data, $\chi = 10$. From top to bottom: streamwise velocity, wall–normal velocity, spanwise velocity, density, and pressure.
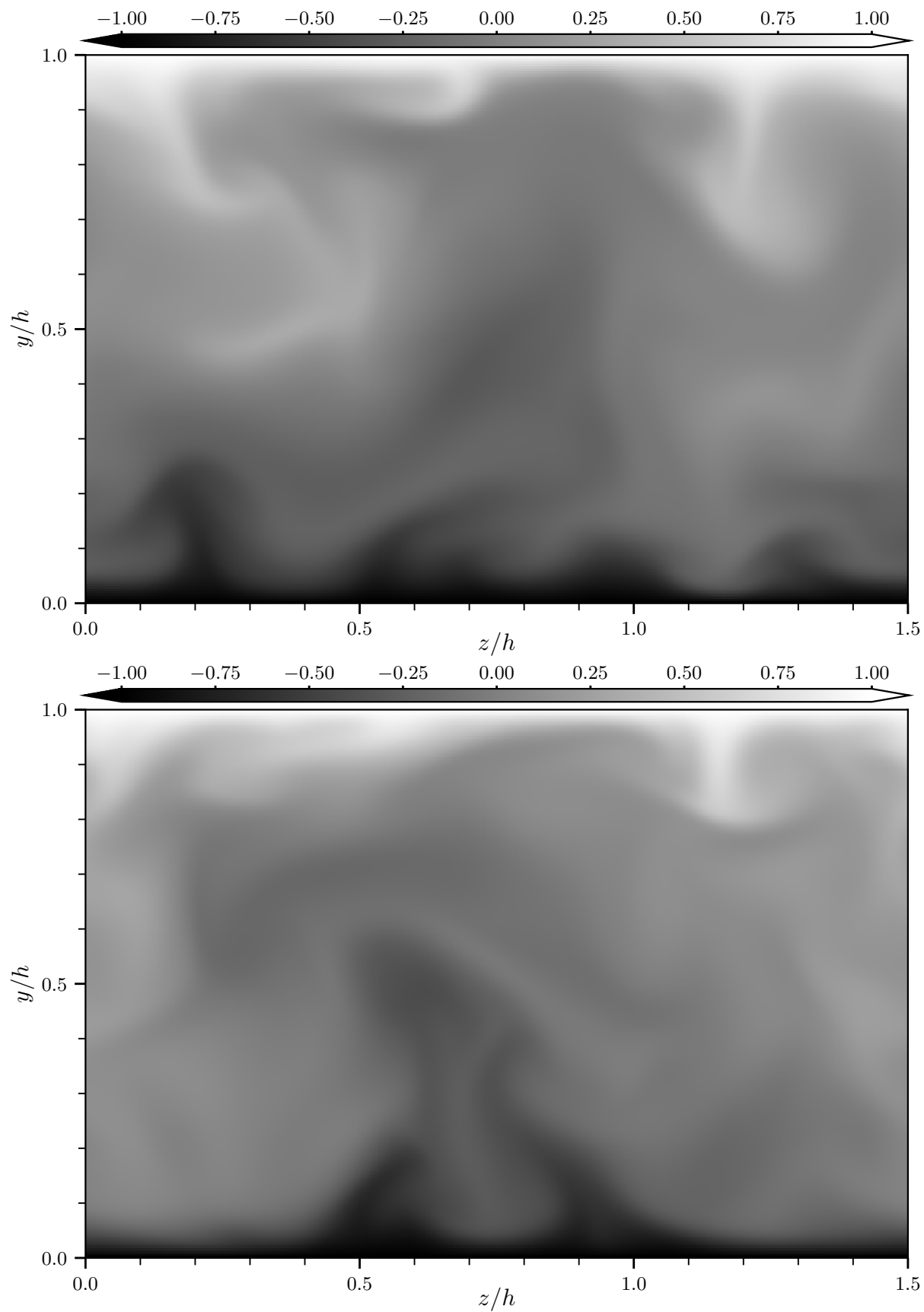
Figure 5.9: Streamwise velocity, front view. Top panel: case C, $\chi = 0$. Bottom panel: case D, $\chi = 10^2$.
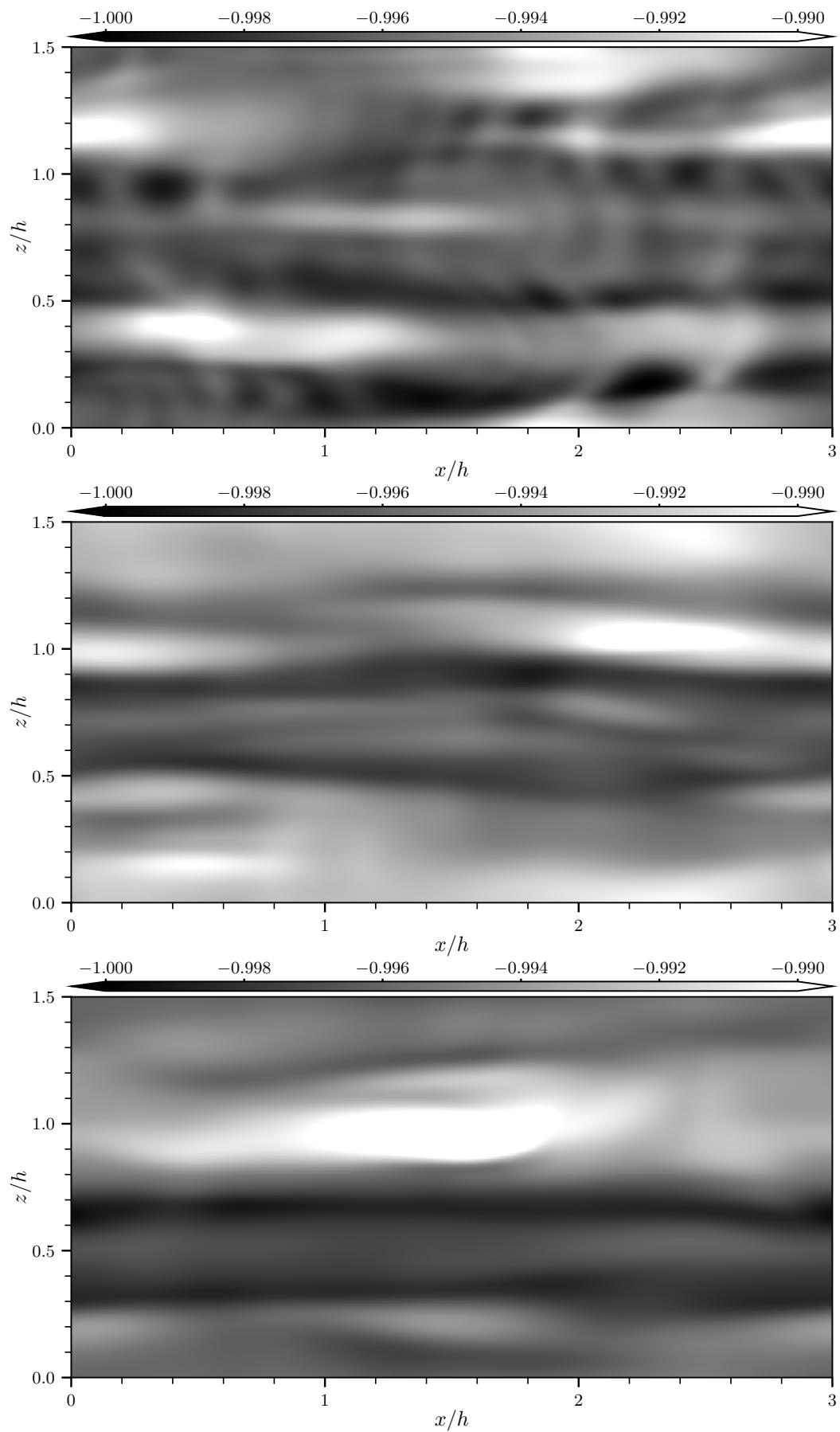
Figure 5.10: Streamwise velocity, top view at $y^+ \approx 0.2$. Top panel: case C, $\chi = 0$. Middle panel: case D, $\chi = 10^2$. Bottom panel: case E, $\chi = 10^3$.
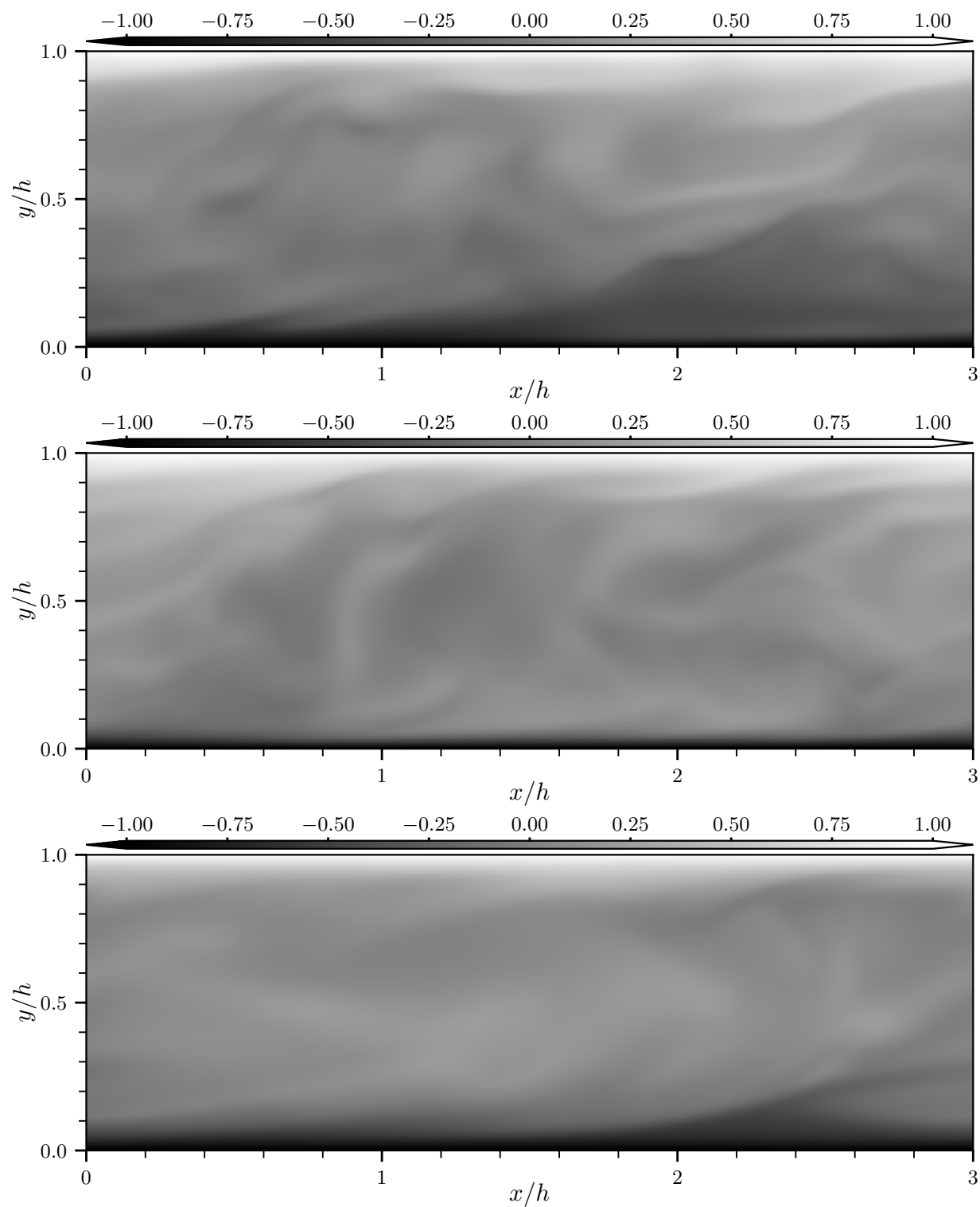
Figure 5.11: Streamwise velocity, side view. Top panel: case C, $\chi = 0$. Middle panel: case D, $\chi = 10^2$. Bottom panel: case E, $\chi = 10^3$.
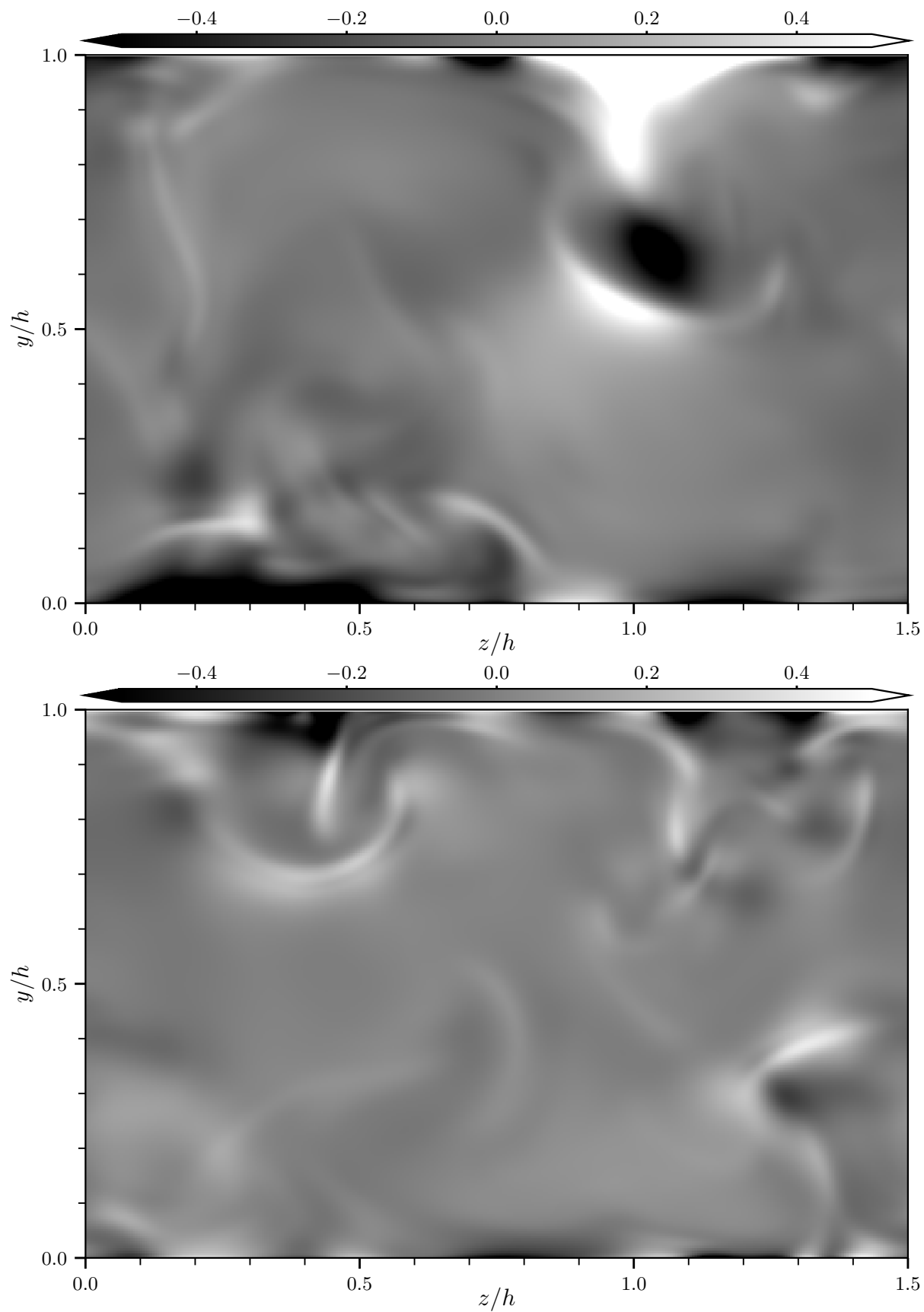
Figure 5.12: Velocity dilatation, front view. Top panel: case C, $\chi = 0$. Bottom panel: case D, $\chi = 10^2$.
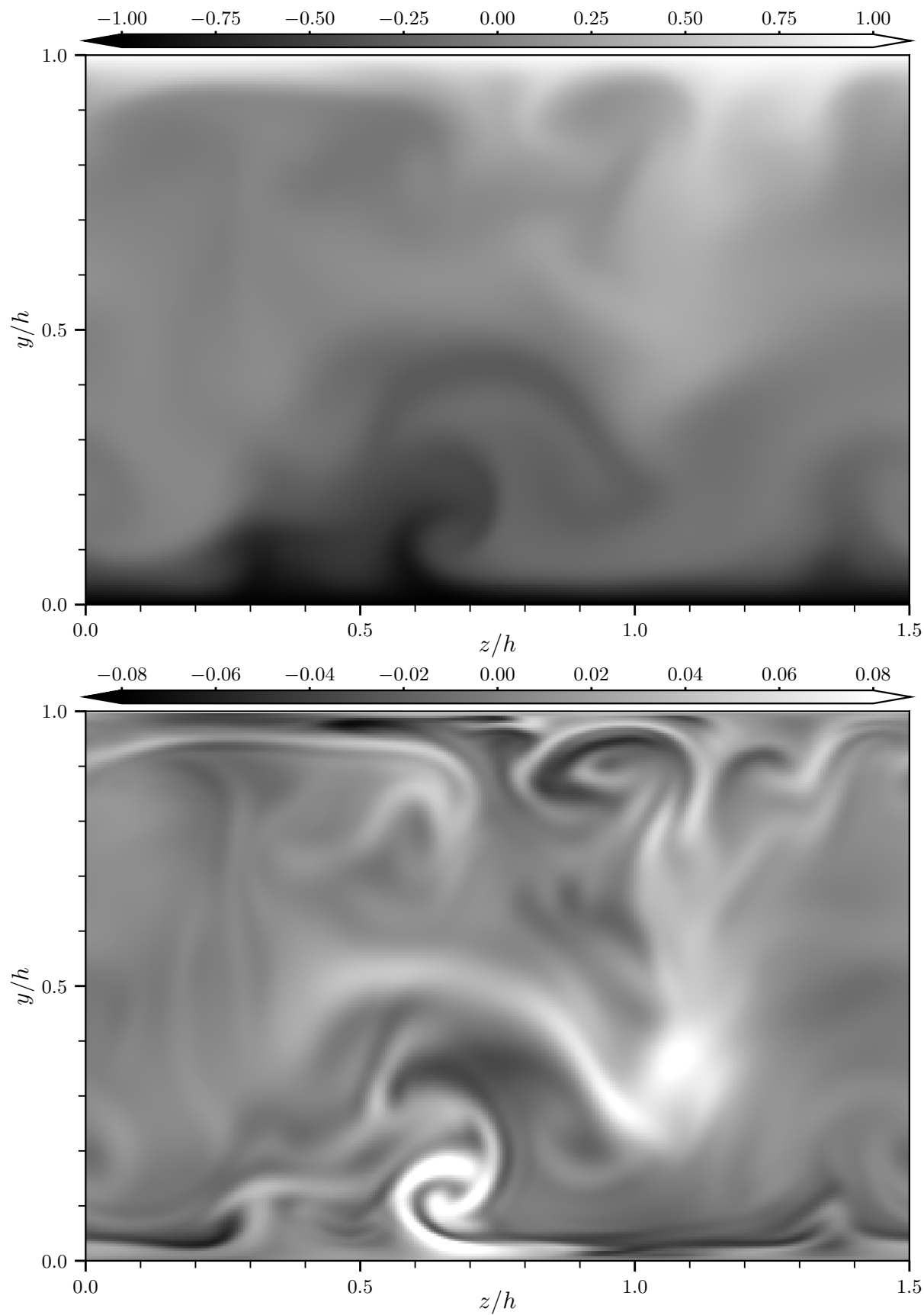
Figure 5.13: Case E, $\chi = 10^3$, only. Front view. Top panel: streamwise velocity. Bottom panel: velocity dilatation.

5.2 Time averaged statistics

There is little published data of the turbulence statistics of compressible Couette flow but its similarity to the incompressible case and channel flow allows certain comparisons to be made. One difference with channel flow is that the mean streamwise velocity gradient is non–zero in the centre of the channel, leading to turbulence production throughout the channel height. Both run–time volume statistics and slice–based statistics were collected. The former requires all quantities of interest to be selected before run–time and are based on the whole volume. The slice–based statistics require the slices locations of interest to be chosen.

5.2.1 Convergence

One of the only published studies of compressible Couette flow investigating its turbulence properties is by Buell (1991), which was conducted using temperature dependent viscosity $\mu = T^{0.7}$, $\gamma = 1.4$ and $\text{Pr} = 0.7$. His results showed large streamwise structures similar to those found in incompressible simulations (Avsarkisov *et al.*, 2014; Spalart *et al.*, 2014; Pirozzoli *et al.*, 2014; Komminaho *et al.*, 1996). These large structures meander in the spanwise direction and regenerate over long time periods, requiring long time series for converged statistics. However, including the bulk viscosity using a fully explicit numerical scheme requires the time step to be reduced in proportion with the value of χ. Given the computing resources available, a compromise had to be made between the Reynolds number, domain size, and χ value. The $\chi = 0$ case ran on Imperial College's CX2 high–performance–computing (HPC) facility and the $\chi = 10$ case on three thousand cores on the national supercomputer, Archer. Both cases took about six months to generate a time series of approximately $\Delta t u_w / h \approx 91$. The small domain cases were run on CX2 and case C, for which $\chi = 0$, generated approximately 214 time units of data. The shear stress as a function of time of this case is shown in figure 5.14. The increase and decrease in wall shear stress that occur at short time scales is likely due to bursting events at the wall. Longer time–scale variations are due to the presence and movement of large–scale structures (streamwise rollers) (Buell, 1991). It is due to these variations that converged statistics are difficult to achieve for Couette flow. Cases A and B were run with the same time step, limited by the diffusion CFL number $\mathrm{d}t\,\chi/(\rho\Delta x^2 \text{Re})$. However due to the large time–step penalty, each of the small domain cases (C, D, and E) were run at their maximum CFL number. A time series length of about 70 time units was achieved for case D ($\chi = 10^2$) and about 3 time units for case E ($\chi = 10^3$).
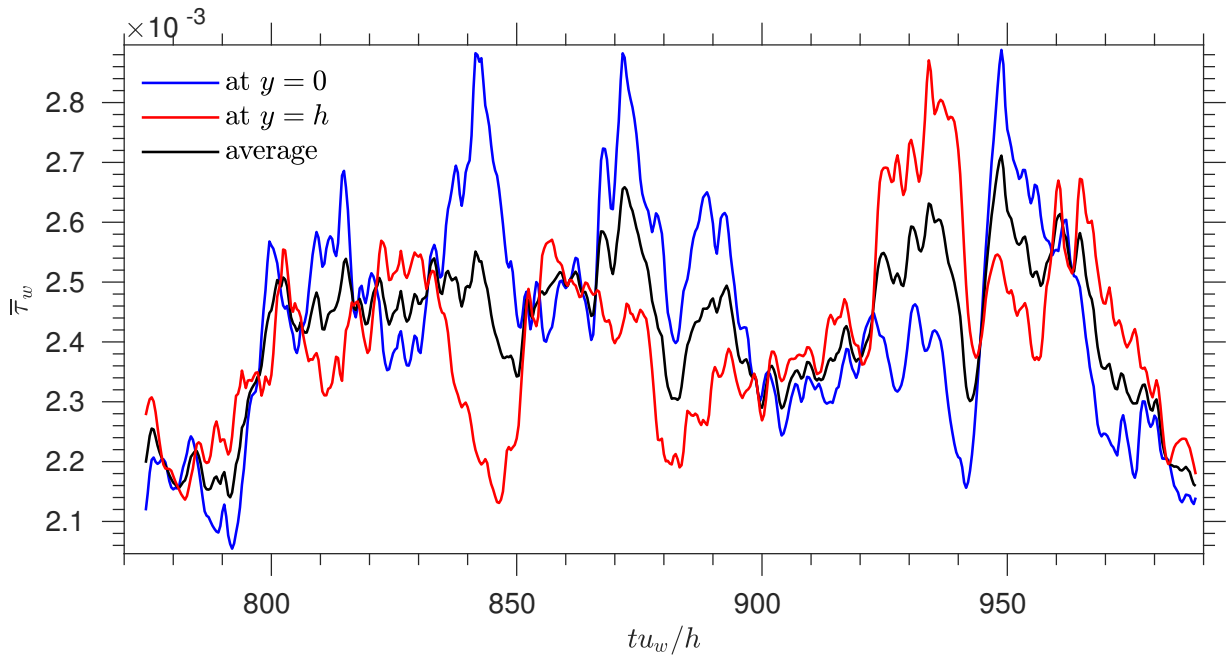
Figure 5.14: Time series of wall shear stress for case C, $\chi = 0$. Variations occur at all time scales, including the full time of the series. Lower wall: blue, upper wall: red, average: black.

The following section presents mean statistics and demonstrates their level of convergence as well as the ability of the selected grids to fully capture the smallest flow scales. Table 5.1 shows a summary of the Couette flow configurations used in this study.

5.2.2   Time average sensitivity of mean quantities

To check the sensitivity of the time averaging procedure, the mean quantities were averaged over three separate time–windows of the data. Figures 5.15 and 5.16 show the effect of averaging over different window lengths on the large domain datasets; cases A and B. Three curves correspond to an increasing window length (red, green and blue), and the last (magenta) is an average over only the last 30 time units of the dataset. The mean streamwise velocity for the $\chi = 0$ case (left column in figure) appears to be more affected than for the $\chi = 10$ case (right column in figure). The orthogonal velocity components show a large variation but this is expected due to the large streamwise rollers that meander in the spanwise direction. The specific total energy varies in a similar manner as the streamwise velocity, with the largest change at the shoulder of the profile ($y \approx 0.05$) at the edge of the viscous sublayer. The thermodynamic pressure shows larger variations and a small pressure drift can be seen at the walls (see section 5.3.1).

Case	l_x	l_z	nx	ny	nz	l_x^+	l_y^+	l_z^+	γ	χ	Re	Ma	Δx^+	Δy_{w}^+	Δy_{c}^+	Δz^+	Re_τ	u_τ	tu_{w}/h
A	$6h$	$3h$	960	480	672	5775	963	2888	1.29	0	2×10^4	3	6.0	0.20	4.6	4.3	481	0.037	91
B	$6h$	$3h$	960	480	672	5852	975	2926	1.29	10	2×10^4	3	6.1	0.20	4.6	4.4	488	0.038	91
C	$3h$	$3h/2$	480	240	336	823	274	411	1.29	0	5×10^3	3	1.7	0.12	2.6	1.2	137	0.044	214
D	$3h$	$3h/2$	480	240	336	799	266	399	1.29	10^2	5×10^3	3	1.7	0.11	2.5	1.2	133	0.044	71
E	$3h$	$3h/2$	480	240	336	-	-	-	1.29	10^3	5×10^3	3	-	-	-	-	-	-	3
V	$3h$	$3h/2$	480	240	336	1600	500	800	1.40	0	1×10^4	0.1	3	0.2	5	2	268	0.05	46

Table 5.1: Table of parameters for Couette results. Grid stretching is the same for all grids: $\beta = 4.5$. Pr $= 0.7$. Channel height is h.
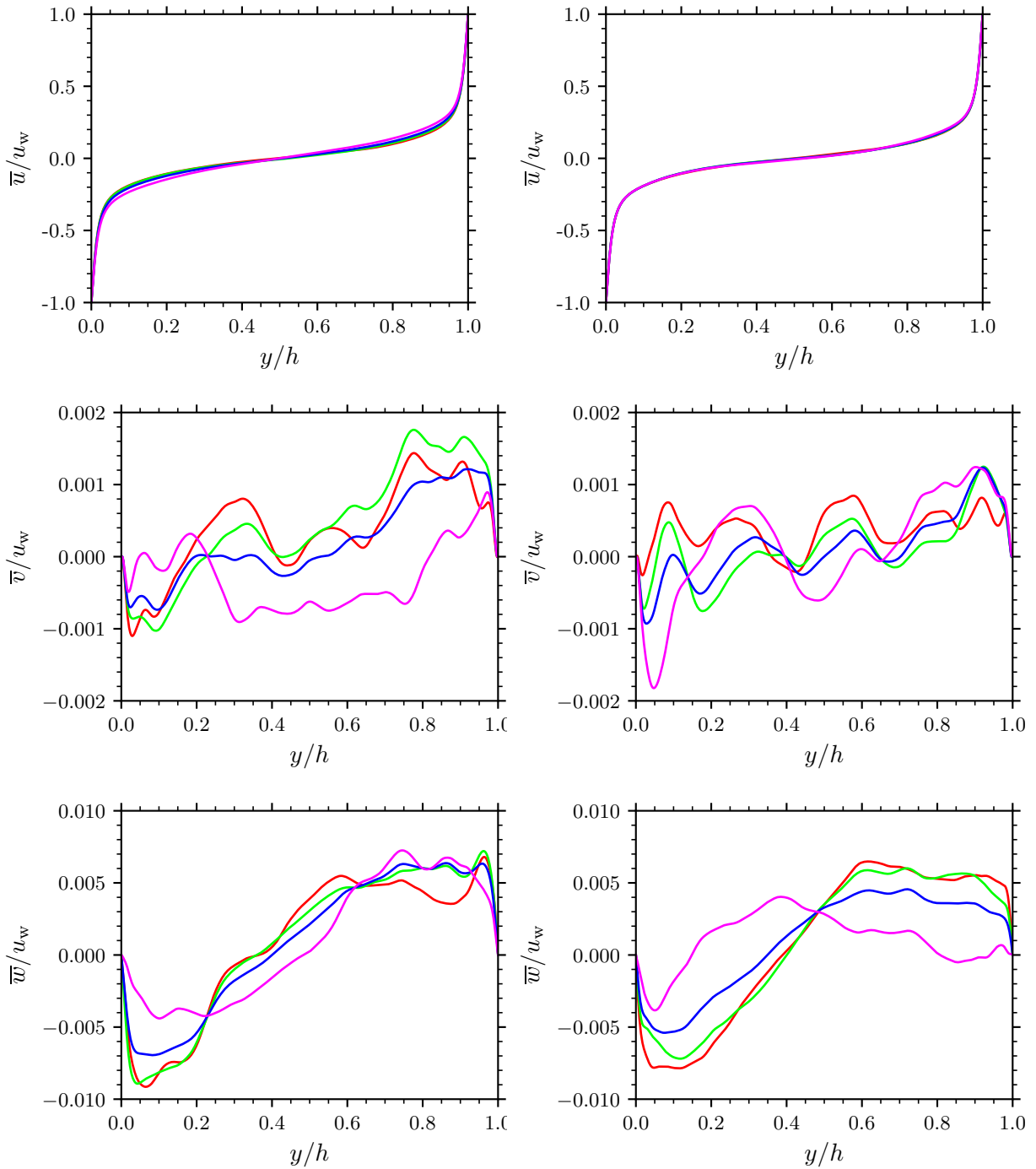
Figure 5.15: Sensitivity of mean profiles to time–averaging period. Cases A and B. Time units (tu_w/h) averaged over: 0-30 (red), 0-60 (green), 0-90 (blue), 60-90 (magenta). Left column: $\chi = 0$, right column: $\chi = 10$.

5.2.3   Shear stress and root–mean–square profiles

Time–averaging the Navier–Stokes equations simplified for Couette flow results in a relationship between laminar and turbulent shear stress. The sum can be shown to be constant across the channel and is a good measure of the level of convergence of a simulation. To form this equation,
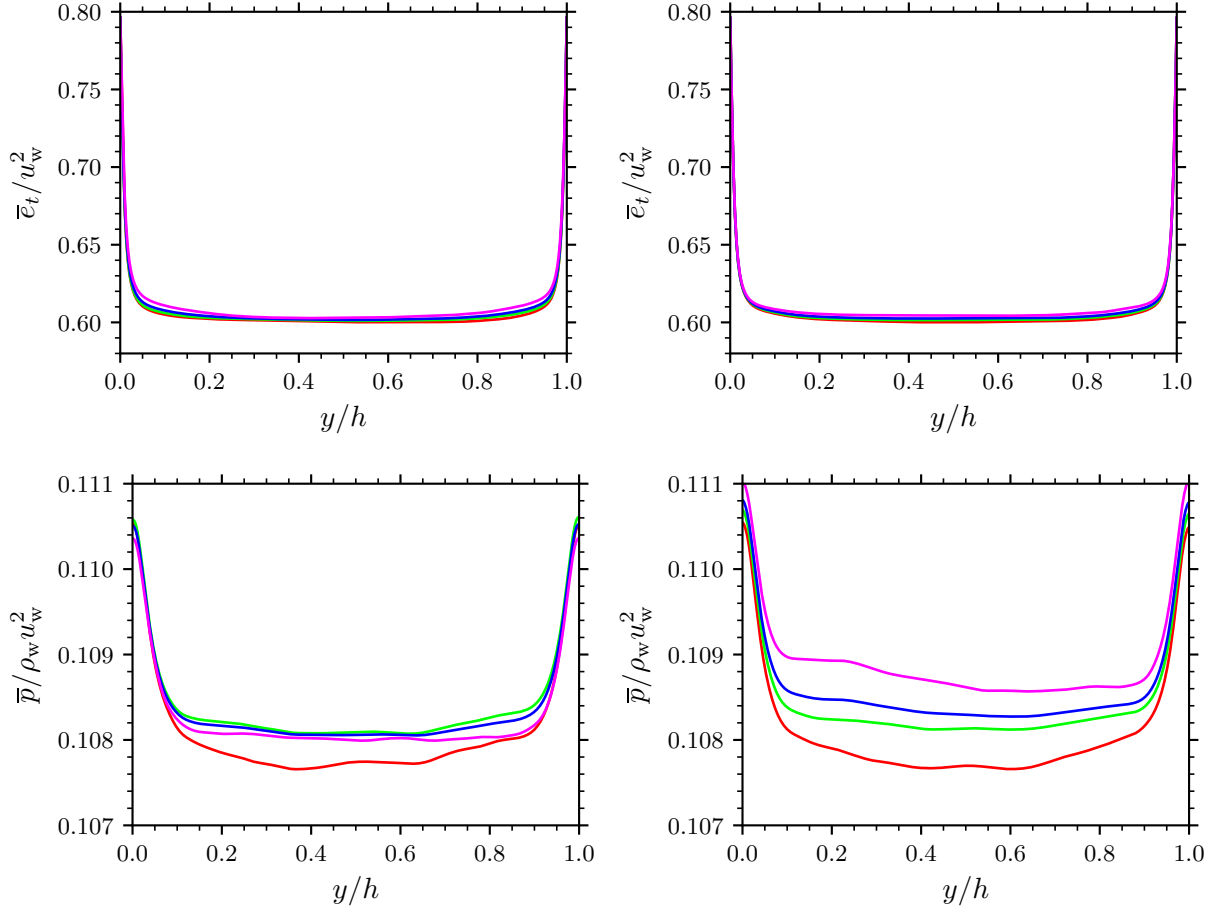
Figure 5.16: Sensitivity of mean profiles to time–averaging period. Cases A and B. Time units (tu_{w}/h) averaged over: 0-30 (red), 0-60 (green), 0-90 (blue), 60-90 (magenta). Left column: $\chi = 0$, right column: $\chi = 10$.

the momentum equation is written for each direction assuming a statistically stationary flow and recalling that derivatives in the homogeneous directions are zero:

$$\frac{\partial}{\partial t}(\overline{\rho}\,\widetilde{u}_i) + \frac{\partial}{\partial x_j}(\overline{\rho}\,\widetilde{u}_i\widetilde{u}_j) = -\frac{\partial \overline{p}_{\mathrm{m}}}{\partial x_i} + \frac{1}{\mathrm{Re}}\frac{\partial \overline{\Sigma}_{ij}}{\partial x_j} - \frac{\partial \overline{R}_{ij}}{\partial x_j}, \qquad (5.2.1)$$

where $\overline{R}_{ij} = \overline{\rho\,\widetilde{u_i''u_j''}}$. Terms are Reynolds decomposed (indicated by an over–bar) unless explicitly multiplied by ρ, in which case they are Favre–decomposed (indicated by a tilde). Appendix C.1.2 gives details on the Favre–decomposition. Applying the no–slip condition and noting that no pressure gradient is applied in the streamwise or spanwise directions, and that μ is constant, the momentum equations simplify to

$$0 = \frac{1}{\mathrm{Re}}\frac{\mathrm{d}^2\overline{u}}{\mathrm{d}y^2} - \frac{\mathrm{d}}{\mathrm{d}y}(\overline{\rho}\,\widetilde{u''v''})$$

$$0 = -\frac{\mathrm{d}\overline{p}_\mathrm{m}}{\mathrm{d}y} - \frac{\mathrm{d}}{\mathrm{d}y}(\overline{\rho}\,\widetilde{v''v''}) \qquad (5.2.2)$$

$$0 = -\frac{\mathrm{d}}{\mathrm{d}y}(\overline{\rho}\,\widetilde{w''v''}).$$

Integrating the x direction equation gives

$$\frac{1}{\mathrm{Re}}\frac{\mathrm{d}\overline{u}}{\mathrm{d}y} = \overline{\rho}\,\widetilde{u''v''} + \mathcal{C}_1 \qquad (5.2.3)$$

Writing (5.2.3) at the lower wall removes the Reynolds shear stress, due to the no slip boundary condition, and defines the wall shear stress as the constant $\mathcal{C}_1$:

$$\frac{1}{\mathrm{Re}}\frac{\mathrm{d}\overline{u}}{\mathrm{d}y}\bigg|_{y=0} = \mathcal{C}_1 = \overline{\tau}_\mathrm{w}. \qquad (5.2.4)$$

Hence the final expression for the simplified x momentum equation is

$$\frac{1}{\overline{\tau}_\mathrm{w}}\left(\frac{1}{\mathrm{Re}}\frac{\mathrm{d}\overline{u}}{\mathrm{d}y} - \overline{\rho}\,\widetilde{u''v''}\right) = 1. \qquad (5.2.5)$$

Figure 5.17 shows the total stress distribution for the large domain cases (A and B). Note that the profiles have been averaged about the centreline. Close to the wall the sum is close to unity for all cases and by the mid–plane, the largest deviation is 4% from the $\chi = 10$ case. Buell (1991) reports that a time series of $250u_\mathrm{w}/h$ time units is needed to maintain $\overline{\tau}_\mathrm{total}$ to within 2% of a constant value. Figure 5.18 compares the large domain cases with each other and the small domain cases (C and D) against the data Buell (1991), showing general agreement in the wall–normal location of peak $u_\mathrm{r.m.s.}$.
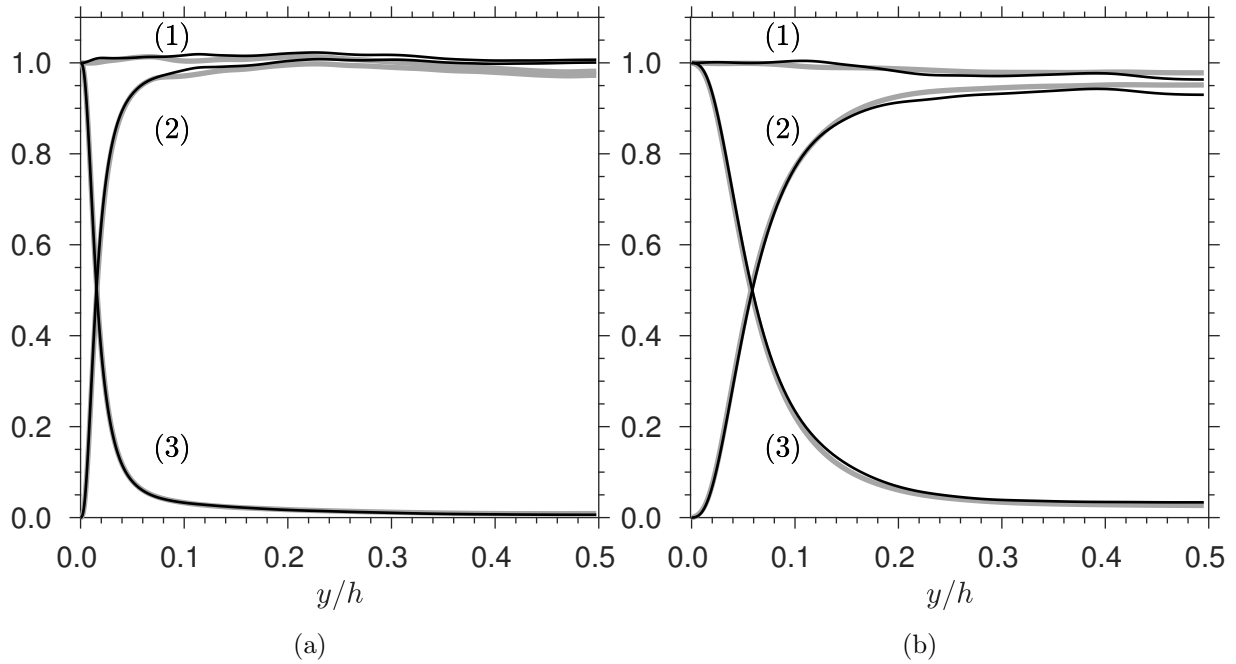
Figure 5.17: Shear stress decomposition where (1): $\overline{\tau}_{\text{total}}$, (2): $-\overline{\rho}\,\widetilde{u''v''}/\overline{\tau}_{\text{w}}$, (3): $(\mathrm{d}\overline{u}/\mathrm{d}y)/(\mathrm{Re}\,\overline{\tau}_{\text{w}})$. (a) $\chi = 0$ shown with a grey line (case A), $\chi = 10$ shown in black (case B); (b) $\chi = 0$ shown with a grey line (case C), $\chi = 10^2$ shown in black (case D). Both figures are averaged about centreline of channel at $y = h/2$.
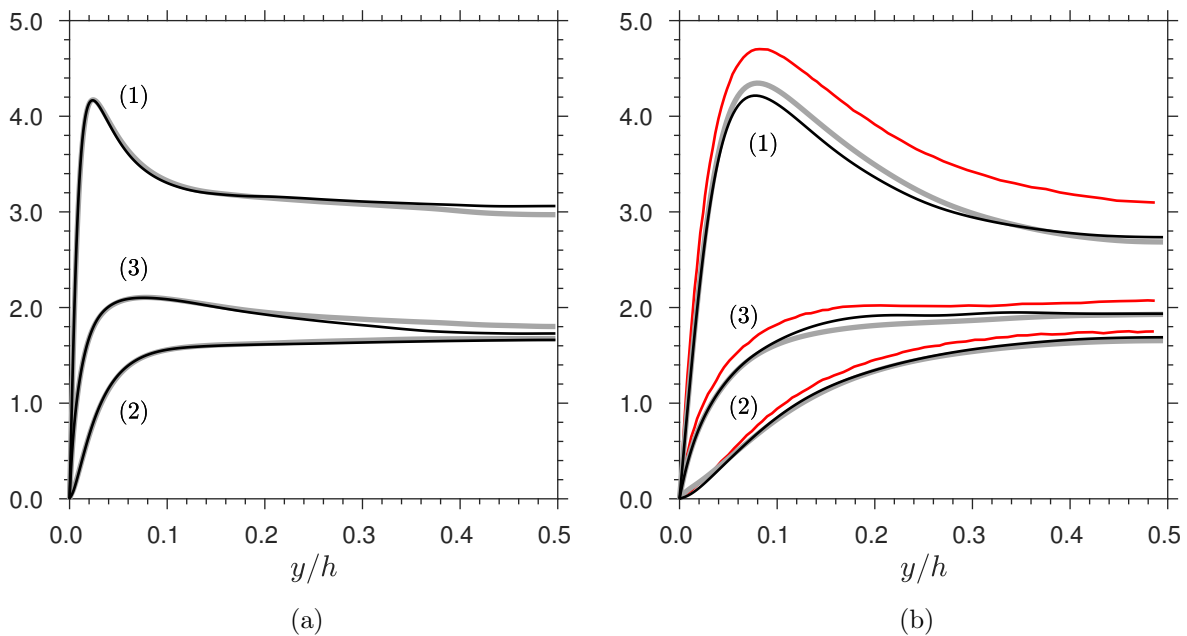
Figure 5.18: Root mean square velocity where (1): $u_{\text{r.m.s.}}/u_\tau$, (2): $v_{\text{r.m.s.}}/u_\tau$, (3): $w_{\text{r.m.s.}}/u_\tau$. Grey lines are for $\chi = 0$, black lines are for $\chi > 0$. (a) large domain case (A and B), (b) small domain case (C and D). Both figures are averaged about centreline of channel at $y = h/2$. Red lines show the $\mathrm{Ma} = 3.0$ data of Buell (1991). for which $\mathrm{Re} = 7500$, $\mathrm{Pr} = 0.7$, and $\gamma = 1.4$.

5.3   Mean profiles

The mean profiles of all five cases are presented in this section. Figure 5.19 shows the large domain data (cases A and B) in the left column, and the small domain data (cases C and D) in the right column. The large domain streamwise velocity, temperature, energy and pressure all show larger wall–normal gradients than the small domain data due to the increased Reynolds number in the large domain case. Figure 5.20 shows the log–law profiles for both large and small domain cases. The compressible channel flow case of Huang *et al.* (1995) is shown in magenta to give a comparison of a similar configuration at a similar Reynolds number. The lower panel shows the same data rescaled using the transformation of Trettel and Larsson (2016), which is equivalent to Patel *et al.* (2016), and accurately collapses variable density velocity profiles to the incompressible log–law profiles. Whilst the van Driest transform is accurate for adiabatic wall boundary conditions, this alternative scaling is accurate for isothermal walls as well. They not only include the change of density across the channel but also the relative change of density gradient and shear viscosity gradient in the wall–normal direction. The effect of χ on the value of mean pressure switches between the large and small domain cases. This can be partly explained by the difficulty to converge statistics but also by the pressure drift that results from using the filter to maintain numerical stability. Filtering is applied at every time step in all cases, but whilst the large domain cases (A and B) use the same time step, the small domain cases (C, D, and E) use a time step to maintain a constant CFL number. As a result, the pressure drift due to filtering is the same for the large domain cases but different for the small domain cases. Section 5.3.1 shows the effect of the filter on a two-dimensional laminar Couette case. Nevertheless, increasing χ to 10 shows minimal effect on the thermodynamic pressure. For the $\chi = 10^2$ case there appears to be a plateau at $y \approx 0.06$. All other quantities show minimal differences when χ is increased.

5.3.1   Pressure drift

Explicit filtering is required to remove excess energy at small scales which is generated when using centred finite–difference schemes. The filters used for this work (see section 2.5) are optimised in wavenumber space to remove energy most effectively at small scales (for waves with fewer than four points per wavelength). The pressure is not set by a boundary condition but calculated from the equation of state $p = \rho T/(\gamma \mathrm{Ma}^2)$. This process takes place after ρ and T have been filtered, which alters the thermodynamic state and hence the pressure. Figure 5.22 shows the effect of
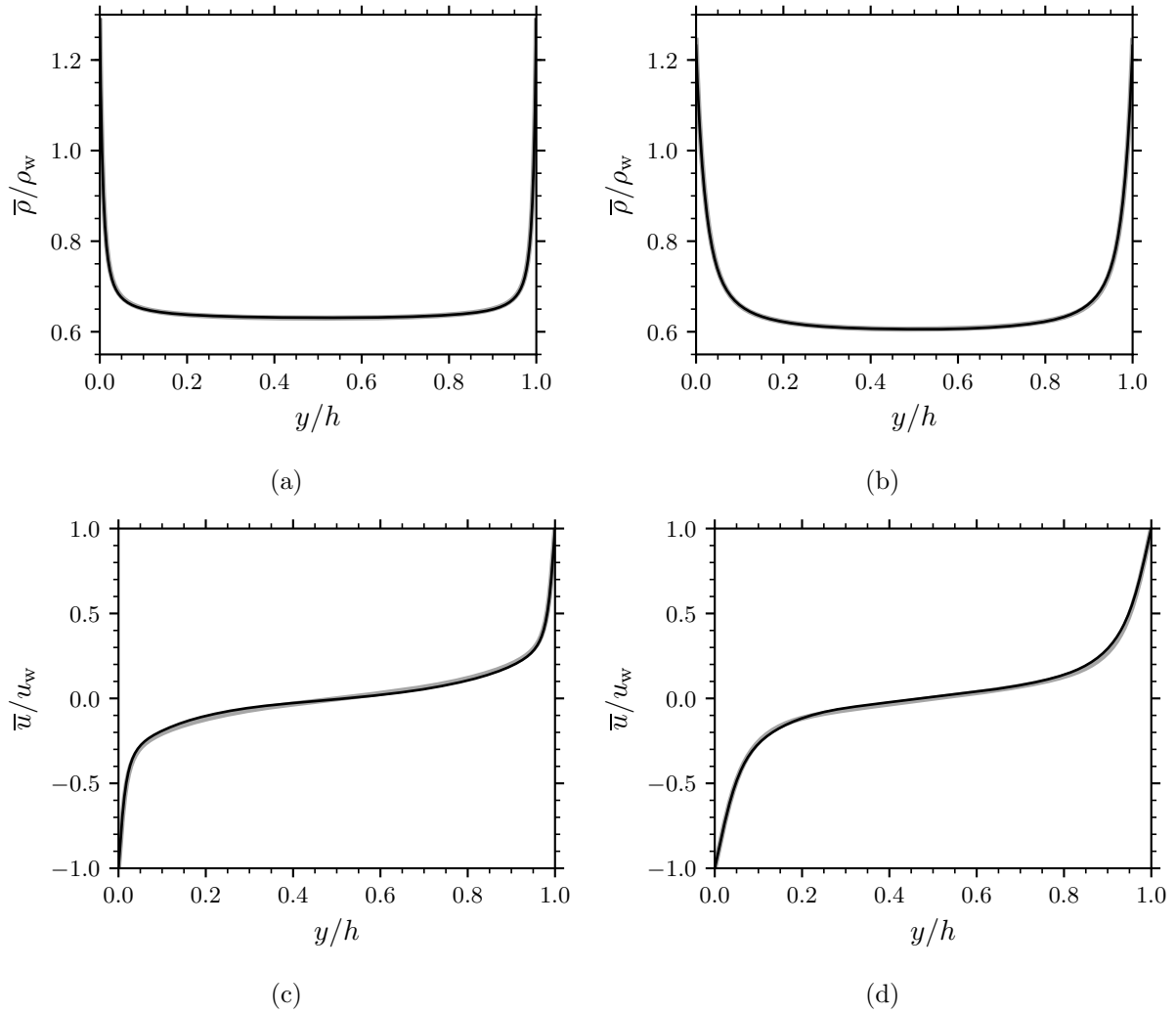
Figure 5.19: Top row: mean density; bottom row: mean streamwise velocity. Left column: large domain $\chi = 0$ (grey line) and $\chi = 10$ (black line) cases (A and B); right column: small domain $\chi = 0$ (grey line) and $\chi = 10^2$ (black line) cases (C and D).

(a)

(b)

(c)

(d)
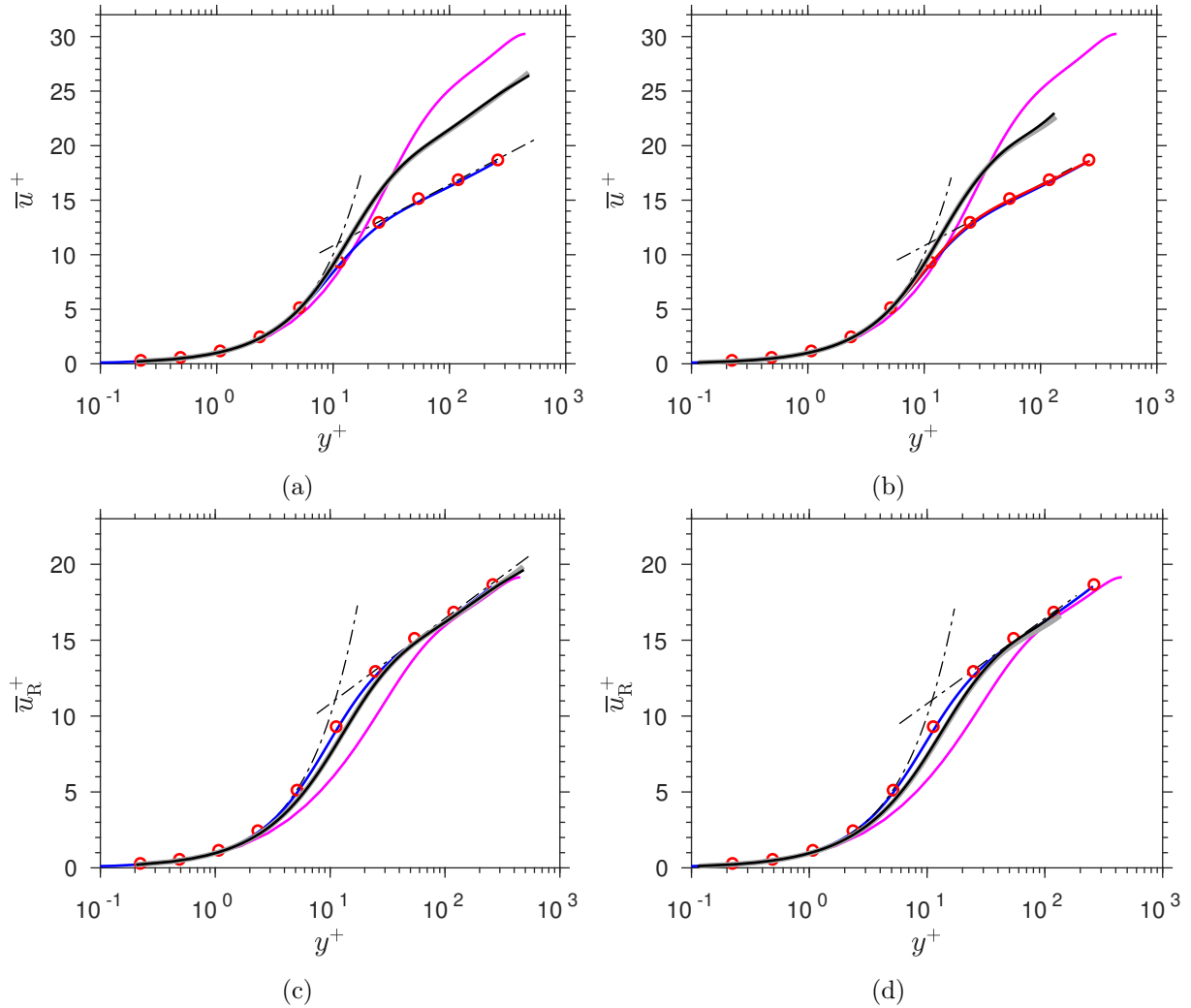
Figure 5.20: Mean streamwise velocity: in wall units (top row); in units rescaled using Trettel and Larsson (2016); Patel *et al.* (2016) (bottom row). The left column shows data for the large domain $\chi = 0$ (grey line) and $\chi = 10$ cases (black line). The right column shows data for the small domain $\chi = 0$ (grey line) and $\chi = 10^2$ (black line) cases. Also included is data from the compressible channel case of Huang *et al.* (1995) (magenta line), the incompressible Couette case of Pirozzoli *et al.* (2014) (blue line) and the low Mach number case V (red markers). Profiles have been averaged about the mid–channel. The chained lines show the viscous sublayer and log–law profile setting the von Kármán constant to 0.41 and the constant of integration to 5.
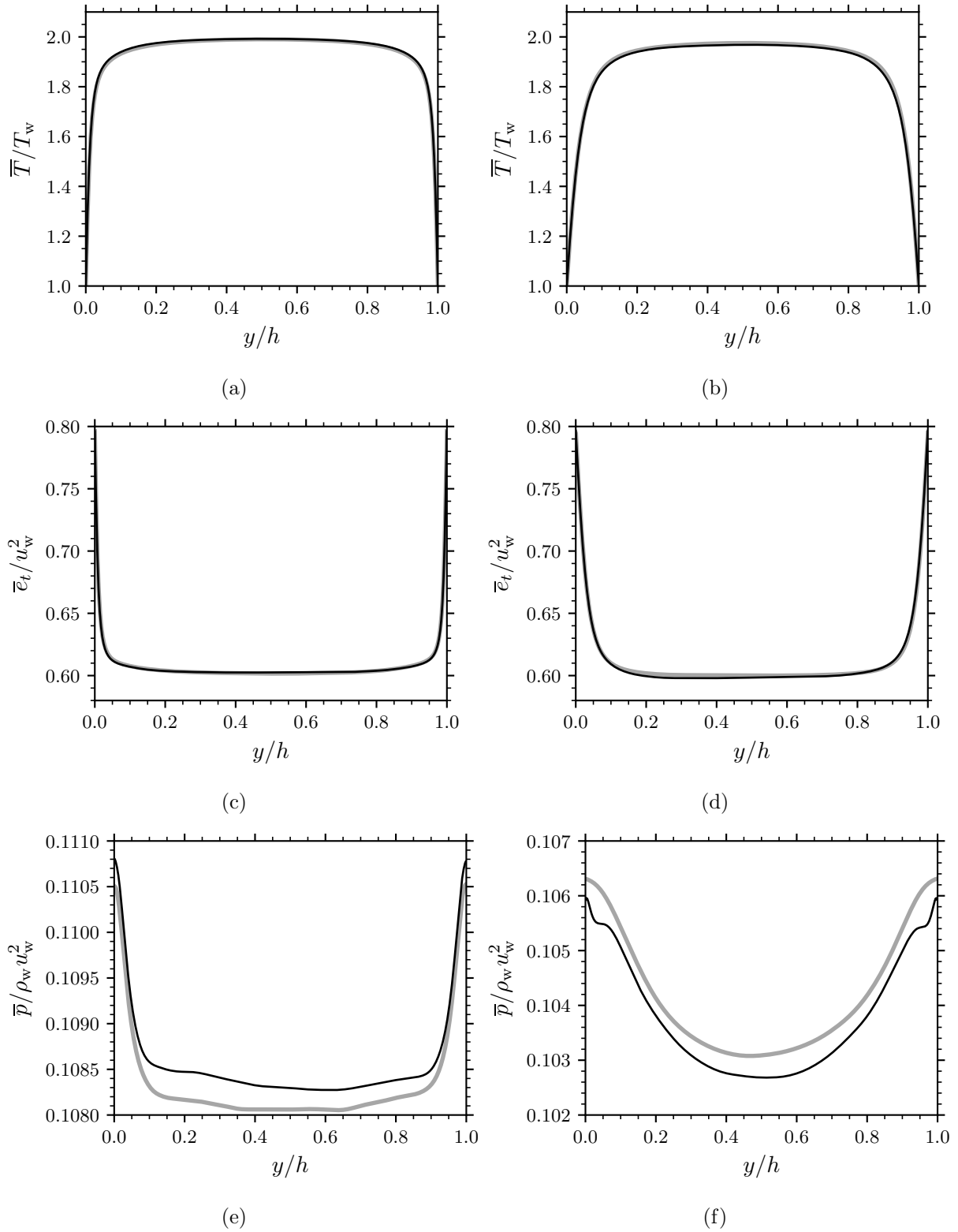
Figure 5.21: Top row: mean temperature; middle row: mean specific total energy; bottom row; mean pressure. The left column shows data for the large domain $\chi = 0$ (grey line) and $\chi = 10$ cases (black line). The right column shows data for the small domain $\chi = 0$ (grey line) and $\chi = 10^2$ (black line) cases.
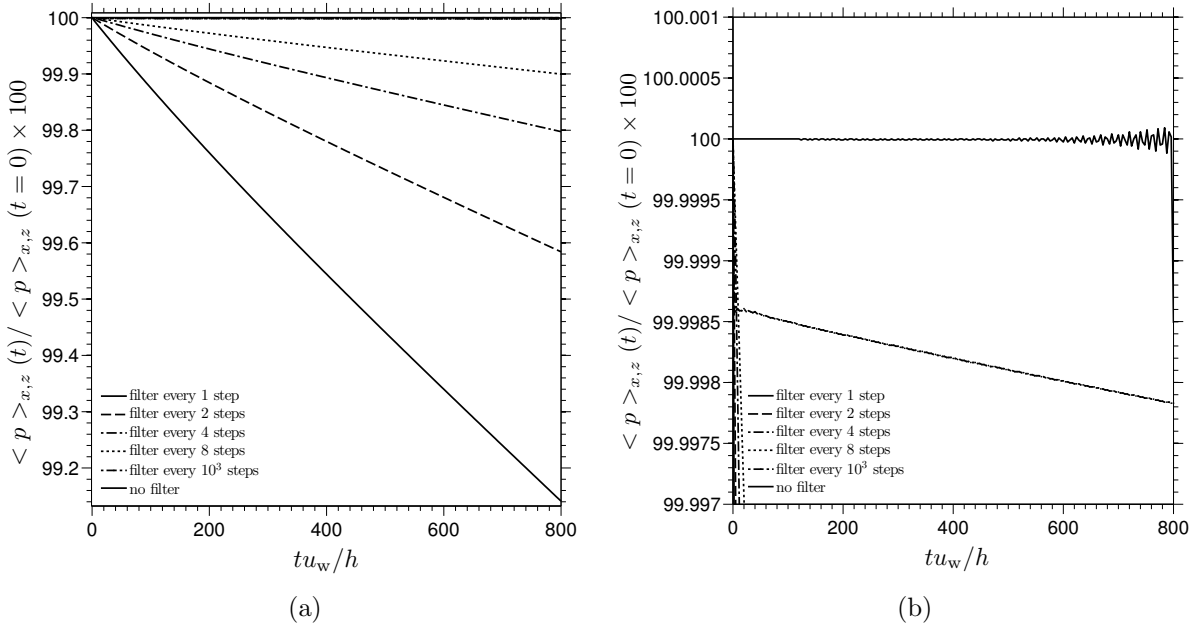
Figure 5.22: Change in thermodynamic pressure with time for the laminar 2D configuration. (a) ordinate clipped to show pressure drop when filtering every time step. (b) ordinate clipped to show zero filtering run in detail.

changing the filtering interval, from filtering every time step to not filtering at all. Figure 5.22a shows that as the filtering interval is reduced, the pressure drift reduces until it is zero when no filtering is applied. At late times there is a growing instability from the finite difference scheme (seen more clearly in the close–up view of figure 5.22b). Even when filtering every time step (as in the turbulent cases) the drift is slow, dropping by approximately 0.9% over $tu_\mathrm{w}/h = 800$. The longest time series of the turbulent runs is for the small domain, $\chi = 0$, case C, which is close to 200 time units and results in a pressure drift of approximately 0.25%.

5.3.2   Pressure plateau

Figure 5.21f shows a plateau in the thermodynamic pressure at approximately $y = 0.05$ and $y = 0.95$ for the $\chi = 10^2$ case not seen in the zero bulk viscosity case. To understand the reason for the plateau, the y momentum equation can be time averaged to give

$$\frac{\mathrm{d}\overline{\rho v v}}{\mathrm{d}y} = -\frac{\mathrm{d}\overline{p_\mathrm{m}}}{\mathrm{d}y} + \frac{1}{\mathrm{Re}}\frac{4}{3}\left(\frac{\mathrm{d}^2\overline{v}}{\mathrm{d}y^2}\right) \tag{5.3.1}$$

which can be integrated to give

$$\overline{p}_\mathrm{w} - \overline{p} = \overline{\rho v v} - \left(\frac{\chi}{\mathrm{Re}} + \frac{4}{3}\frac{1}{\mathrm{Re}}\right)\frac{\mathrm{d}\overline{v}}{\mathrm{d}y} \tag{5.3.2}$$
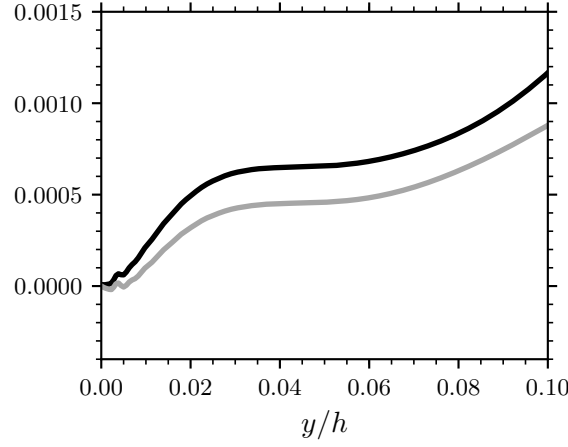
Figure 5.23: Terms from (5.3.2) for case D, $\chi = 10^2$. Grey line: $\overline{p}_\mathrm{w} - \overline{p}$; black line: $\overline{\rho v v} - (\chi/\mathrm{Re} + 4/(3\mathrm{Re}))\mathrm{d}\overline{v}/\mathrm{d}y$.

using the wall pressure as a boundary condition $p(y=0) = \overline{p}_\mathrm{w}$ and noting that $\overline{\Theta} = \mathrm{d}\overline{v}/\mathrm{d}y = -\mathrm{d}/\mathrm{d}y(\overline{\rho' v'}/\overline{\rho})$. Figure 5.23 shows the left-hand-side (in grey) and right-hand-side (in black) of equation 5.3.2 and indicates that the correlation of fluctuations in density and wall-normal velocity are responsible for the plateau as its magnitude varies according to χ/Re. A longer time series of case D would be required to further improve the agreement between the two curves, as the current database is approximately 25% of the length recommended for convergence (Buell, 1991).

5.4   Turbulence kinetic energy budget

To measure the influence of the bulk viscosity on the distribution of kinetic energy in the flow field, the balance of turbulence kinetic energy (TKE) can be plotted. The governing equation of TKE (see appendix B for a detailed derivation)

$$\underbrace{\frac{\partial}{\partial t}\left(\overline{\rho}\,\widetilde{k}\right)}_{(1)} + \underbrace{\frac{\partial}{\partial x_j}\left(\overline{\rho}\,\widetilde{k}\widetilde{u}_j\right)}_{(2)} = \underbrace{-\frac{\partial}{\partial x_j}\left(\overline{\rho}\,\widetilde{ku_j''}\right)}_{(3)} \underbrace{-\overline{\rho}\,\widetilde{u_i''u_j''}\frac{\partial \widetilde{u}_i}{\partial x_j}}_{(4)} \underbrace{-\overline{u_j''}\frac{\partial \overline{p}}{\partial x_j}}_{(5)} + \underbrace{\overline{p'\frac{\partial u_j''}{\partial x_j}}}_{(6)} - \underbrace{\frac{\partial \overline{(p'u_j'')}}{\partial x_j}}_{(7)}$$

$$+ \frac{1}{\mathrm{Re}}\left(\underbrace{\overline{u_i''}\frac{\partial \overline{\Sigma}_{ij}}{\partial x_j}}_{(8)} + \underbrace{\frac{\partial \overline{u_i''\Sigma_{ij}'}}{\partial x_j}}_{(9)} - \underbrace{\overline{\Sigma_{ij}'\frac{\partial u_i''}{\partial x_j}}}_{(10)}\right), \quad (5.4.1)$$

(1) unsteady turbulence kinetic energy,

(2) convective turbulent kinetic energy,

(3) turbulent transport,

(4) shear production,

(5) velocity mean–pressure–gradient interaction (compressible),

(6) pressure dilatation (compressible),

(7) velocity pressure interaction diffusion,

(8) velocity   mean–viscous–stress   gradient (compressible),

(9) laminar diffusion,

(10) energy dissipation,

shares common terms with the time evolution equations for mean kinetic energy (MKE) and mean internal energy (MIE); all three can be thought of as reservoirs of energy with a number of connecting (transfer) terms. Lele (1994); Huang *et al.* (1995) both show a map of the transfer terms. In Couette flow, the moving walls supply the flow with its only source of (kinetic) energy, which is distributed between the mean motion of the wall (MKE) and turbulent fluctuations near the wall (TKE). Due to constant energy supply, each reservoir and transfer term reaches equilibrium a long time after any transient behaviour, transitioning from the laminar solution in this case. The proportion transferred to each reservoir is in part controlled by the transport coefficients and hence the bulk viscosity. Due to the compressible nature of the flow, the turbulence kinetic energy budget is written using a density weighted average (see C.1.2 for details) in order to remove the density fluctuation terms and group terms in a similar way to the incompressible equivalent. The names of each term are taken from Huang *et al.* (1995); Chassaing *et al.* (2002). Terms (5), (6), and (8) are due to compressibility and are additional transfer terms. The first two exchange energy between MKE and TKE and the last exchanges energy with MIE. In addition to those directly affected by compressibility, the terms found in incompressible flows are also affected by changes in the transport coefficients.The budget can be plotted for different values of χ and its influenced assessed. The TKE budget can be simplified for Couette flow with constant transport properties based on its boundary conditions. Note that the unsteady term has been retained to measure the level of convergence of the budget. The terms are

(1) unsteady turbulence kinetic energy (retained for convergence check) =

$$\frac{\partial(\bar{\rho}\widetilde{k})}{\partial t} = \frac{1}{2}\frac{\partial}{\partial t}\left(\overline{\rho(u''^2 + v''^2 + w''^2)}\right) \qquad (5.4.2)$$

(2) convected turbulent kinetic energy =

$$\frac{\mathrm{d}}{\mathrm{d}y}\left(\bar{\rho}\,\widetilde{k}\,\widetilde{v}\right) \tag{5.4.3}$$

(3) turbulent transport =

$$-\frac{\mathrm{d}}{\mathrm{d}y}\left(\bar{\rho}\,\widetilde{kv''}\right) = -\frac{1}{2}\frac{\mathrm{d}}{\mathrm{d}y}\left(\overline{\rho(u''^2 + v''^2 + w''^2)v''}\right) \tag{5.4.4}$$

(4) shear production =

$$-\bar{\rho}\,\widetilde{u''v''}\frac{\mathrm{d}\widetilde{u}}{\mathrm{d}y} - \bar{\rho}\,\widetilde{w''v''}\frac{\mathrm{d}\widetilde{w}}{\mathrm{d}y} \tag{5.4.5}$$

(5) velocity mean–pressure-gradient interaction (compressible) =

$$-\overline{v''}\frac{\mathrm{d}\overline{p}}{\mathrm{d}y} \tag{5.4.6}$$

(6) pressure dilatation (compressible) =

$$\overline{p'\Theta''} \tag{5.4.7}$$

(7) velocity pressure interaction diffusion =

$$-\frac{\mathrm{d}\overline{p'v''}}{\mathrm{d}y} \tag{5.4.8}$$

(8) velocity mean–viscous–stress gradient (compressible) =

$$\frac{1}{\mathrm{Re}}\left[\overline{u''}\frac{\mathrm{d}\overline{\Sigma}_{12}}{\mathrm{d}y} + \overline{v''}\frac{\mathrm{d}\overline{\Sigma}_{22}}{\mathrm{d}y} + \overline{w''}\frac{\mathrm{d}\overline{\Sigma}_{32}}{\mathrm{d}y}\right] \tag{5.4.9}$$

where

$$\begin{aligned}
\overline{u''}\frac{\mathrm{d}\overline{\Sigma}_{12}}{\mathrm{d}y} &= \overline{u''}\frac{\mathrm{d}}{\mathrm{d}y}\left[\frac{\mathrm{d}\widetilde{u}}{\mathrm{d}y} + \frac{\mathrm{d}\overline{u''}}{\mathrm{d}y}\right] \\
\overline{v''}\frac{\mathrm{d}\overline{\Sigma}_{22}}{\mathrm{d}y} &= \overline{v''}\frac{\mathrm{d}}{\mathrm{d}y}\left(\left[2\frac{\mathrm{d}\overline{v''}}{\mathrm{d}y} - \frac{2}{3}\overline{\Theta''}\right] + \chi\overline{\Theta''}\right) \\
\overline{w''}\frac{\mathrm{d}\overline{\Sigma}_{32}}{\mathrm{d}y} &= \overline{w''}\frac{\mathrm{d}}{\mathrm{d}y}\left[\frac{\mathrm{d}\widetilde{w}}{\mathrm{d}y} + \frac{\mathrm{d}\overline{w''}}{\mathrm{d}y}\right]
\end{aligned} \tag{5.4.10}$$

(9) laminar diffusion =

$$\frac{1}{\mathrm{Re}}\left[\frac{\mathrm{d}\overline{u''\Sigma'_{12}}}{\mathrm{d}y} + \frac{\mathrm{d}\overline{v''\Sigma'_{22}}}{\mathrm{d}y} + \frac{\mathrm{d}\overline{w''\Sigma'_{32}}}{\mathrm{d}y}\right] \tag{5.4.11}$$

where

$$
\frac{\mathrm{d}\overline{u''\Sigma'_{12}}}{\mathrm{d}y} \;=\; \frac{\mathrm{d}}{\mathrm{d}y}\left[\overline{u''\frac{\partial u''}{\partial y}} + \overline{u''\frac{\partial v''}{\partial x}} - \overline{u''}\frac{\mathrm{d}\overline{u''}}{\mathrm{d}y}\right]
$$

$$
\frac{\mathrm{d}\overline{v''\Sigma'_{22}}}{\mathrm{d}y} \;=\; \frac{\mathrm{d}}{\mathrm{d}y}\Bigg(\left[\overline{2v''\frac{\partial v''}{\partial y}} - \frac{2}{3}\overline{v''\Theta''}\right] - \left[2\overline{v''}\frac{\mathrm{d}\overline{v''}}{\mathrm{d}y} - \frac{2}{3}\overline{v''}\,\overline{\Theta''}\right]
$$

$$
\qquad\qquad +\chi\left[\overline{v''\Theta''} - \overline{v''}\,\overline{\Theta''}\right]\Bigg)
$$

$$
\frac{\mathrm{d}\overline{w''\Sigma'_{32}}}{\mathrm{d}y} \;=\; \frac{\mathrm{d}}{\mathrm{d}y}\left[\overline{w''\frac{\partial w''}{\partial y}} + \overline{w''\frac{\partial v''}{\partial z}} - \overline{w''}\frac{\mathrm{d}\overline{w''}}{\mathrm{d}y}\right]
$$

$$(5.4.12)$$

(10) energy dissipation =

$$
-\frac{1}{\mathrm{Re}}\Bigg[\;\; \overline{\Sigma'_{11}\frac{\partial u''}{\partial x}} \;\;+\;\; \overline{\Sigma'_{12}\frac{\partial u''}{\partial y}} \;\;+\;\; \overline{\Sigma'_{13}\frac{\partial u''}{\partial z}}
$$

$$
+\;\; \overline{\Sigma'_{21}\frac{\partial v''}{\partial x}} \;\;+\;\; \overline{\Sigma'_{22}\frac{\partial v''}{\partial y}} \;\;+\;\; \overline{\Sigma'_{23}\frac{\partial v''}{\partial z}}
$$

$$
+\;\; \overline{\Sigma'_{31}\frac{\partial w''}{\partial x}} \;\;+\;\; \overline{\Sigma'_{32}\frac{\partial w''}{\partial y}} \;\;+\;\; \overline{\Sigma'_{33}\frac{\partial w''}{\partial z}} \;\;\Bigg]
$$

$$(5.4.13)$$

where

$$
\overline{\Sigma'_{11}\frac{\partial u''}{\partial x}} \;=\; 2\overline{\left(\frac{\partial u''}{\partial x}\right)^2} - \frac{2}{3}\overline{\frac{\partial u''}{\partial x}\Theta''} + \frac{2}{3}\overline{\frac{\partial \overline{u''}}{\partial x}\Theta''} + \chi\overline{\frac{\partial u''}{\partial x}\Theta''}
$$

$$
\overline{\Sigma'_{22}\frac{\partial v''}{\partial y}} \;=\; 2\overline{\left(\frac{\partial v''}{\partial y}\right)^2} - \frac{2}{3}\overline{\frac{\partial v''}{\partial y}\Theta''} - 2\left(\frac{\mathrm{d}\overline{v''}}{\mathrm{d}y}\right)^2 - \frac{2}{3}\frac{\mathrm{d}\overline{v''}}{\mathrm{d}y}\overline{\Theta''}
$$

$$
\qquad\qquad +\chi\left[\overline{\frac{\partial v''}{\partial y}\Theta''} - \frac{\partial \overline{v''}}{\partial y}\overline{\Theta''}\right]
$$

$$
\overline{\Sigma'_{33}\frac{\partial w''}{\partial z}} \;=\; 2\overline{\left(\frac{\partial w''}{\partial z}\right)^2} - \frac{2}{3}\overline{\frac{\partial w''}{\partial z}\Theta''} + \chi\overline{\frac{\partial w''}{\partial z}\Theta''}
$$

$$(5.4.14)$$

$$
\begin{aligned}
\overline{\Sigma'_{12}\frac{\partial u''}{\partial y}} &= \overline{\left(\frac{\partial u''}{\partial y}\right)^2} + \overline{\frac{\partial u''}{\partial y}\frac{\partial v''}{\partial x}} - \overline{\left(\frac{\mathrm{d}\overline{u''}}{\mathrm{d}y}\right)^2} \\[6pt]
\overline{\Sigma'_{21}\frac{\partial v''}{\partial x}} &= \overline{\left(\frac{\partial v''}{\partial x}\right)^2} + \overline{\frac{\partial u''}{\partial y}\frac{\partial v''}{\partial x}} \\[6pt]
\overline{\Sigma'_{13}\frac{\partial u''}{\partial z}} &= \overline{\left(\frac{\partial u''}{\partial z}\right)^2} + \overline{\frac{\partial w''}{\partial x}\frac{\partial u''}{\partial z}} \\[6pt]
\overline{\Sigma'_{31}\frac{\partial w''}{\partial x}} &= \overline{\left(\frac{\partial w''}{\partial x}\right)^2} + \overline{\frac{\partial w''}{\partial x}\frac{\partial u''}{\partial z}} \\[6pt]
\overline{\Sigma'_{23}\frac{\partial v''}{\partial z}} &= \overline{\left(\frac{\partial v''}{\partial z}\right)^2} + \overline{\frac{\partial w''}{\partial y}\frac{\partial v''}{\partial z}} \\[6pt]
\overline{\Sigma'_{32}\frac{\partial w''}{\partial y}} &= \overline{\left(\frac{\partial w''}{\partial y}\right)^2} + \overline{\frac{\partial w''}{\partial y}\frac{\partial v''}{\partial z}} - \overline{\left(\frac{\mathrm{d}\overline{w''}}{\mathrm{d}y}\right)^2}
\end{aligned}
\tag{5.4.15}
$$

Figure 5.24 shows the turbulence kinetic energy budget for the large domain $\chi = 0$ and $\chi = 10$ cases A and B (top row). On the bottom row are the small domain $\chi = 0$ and $\chi = 10^2$ cases C and D. Due to the restriction on the time step of the $\chi = 10^3$ case, it was not possible to achieve a time series long enough to produce converged statistics and has not been included. Both budgets are shown in normal and plus units. In red is shown the sum of right–hand–side, i.e. all terms in (5.4.1) except for the unsteady term. Figures 5.24a and 5.24b show that the effect of the bulk has little influence on the budget of terms. There is a slight increase in production, turbulent transport, dissipation and laminar diffusion and reduction in velocity–pressure interaction diffusion and compressibility terms. The same is true for the small domain cases shown in figures 5.24c and 5.24d although the $\chi = 10^2$ shows a slight decrease at the wall. Due to the subtle effect of the bulk viscosity, it is difficult to tell whether the changes seen are due to the convergence of the time series data or a physical effect. To measure the level of convergence, the sum of right–hand–side terms is plotted in figure 5.25a for the large domain cases, and figure 5.25b for the small domain cases. In blue is shown the time–averaged unsteady term, which is of the same order as the budget sum. The compressibility terms $(5 + 6 + 8)$ in equation (5.4.1) are shown separately in figure 5.26 and they are directly affected by the level of velocity dilatation and hence the bulk viscosity. The pressure dilatation $\overline{p\,\Theta''}$ (term 6) is a transfer term between TKE and MIE. The velocity–pressure interaction diffusion $-\mathrm{d}(\overline{p'v''})/\mathrm{d}y$ (term 7) is a measure of the power of pressure fluctuations in fluctuating motion (Chassaing *et al.*, 2002). A pressure gradient acts as a forcing term, in this case driven by the turbulence, and is influenced by the bulk viscosity. There is a clear decrease in pressure–dilatation for both small and large domain cases; by almost 50% for $\chi = 10$ case and by

more than an order of magnitude for the $\chi = 10^2$ case. From comparing the magnitudes of terms in the budget, the fact that the compressibility terms are an order of magnitude smaller than the terms found also in the incompressible budget gives an indication as to why the effect of the bulk viscosity is small in the TKE budget. The majority of the energy is contained in the solenoidal part of the velocity field and hence even large changes to the irrotational part are small. The coupling between the solenoidal and dilatational fields is of interest and is explored further in chapter 4. In figure 5.27, the root–mean–square velocity dilatation is shown for the two cases. The magnitude of $\sqrt{\overline{\Theta^2}}$ is large for the $\mathrm{Re}_\tau = 485$ (large domain) cases due to the high intensity fluctuating turbulent velocity field. Both figures reveal how significant the velocity dilatation in the proximity of the walls is and how quickly it decays, reaching almost zero at approximately $y^+ = 10$, similar to the crossing point of the pressure dilatation term in figure 5.26.
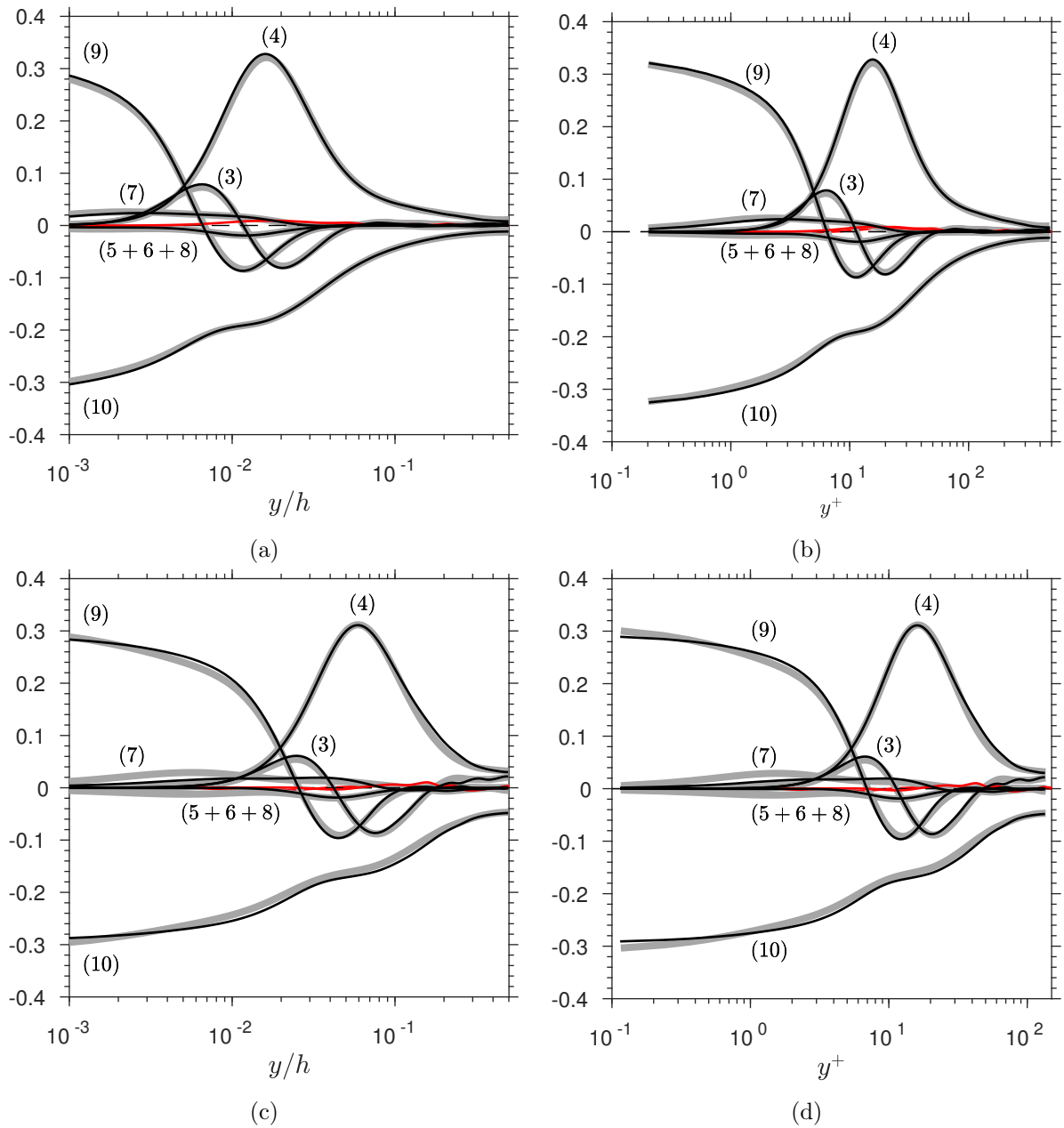
Figure 5.24: Turbulence kinetic energy budget for (a) large domain $\chi = 0$ (grey line) and $\chi = 10$ (black line) cases (A and B); (b) same as (a) but in wall units. (c) small domain $\chi = 0$ (grey line) and $\chi = 10^2$ (black line) cases (C and D). Numbers in brackets correspond to terms in TKE equation (5.4.1): (3) turbulent transport; (4) production; (5+6+8) sum of compressibility terms; (7) velocity pressure interaction diffusion; (9) laminar diffusion; (10) dissipation. All terms are scaled by ν_w/u_τ^4 and averaged about channel centreline $y = h/2$.
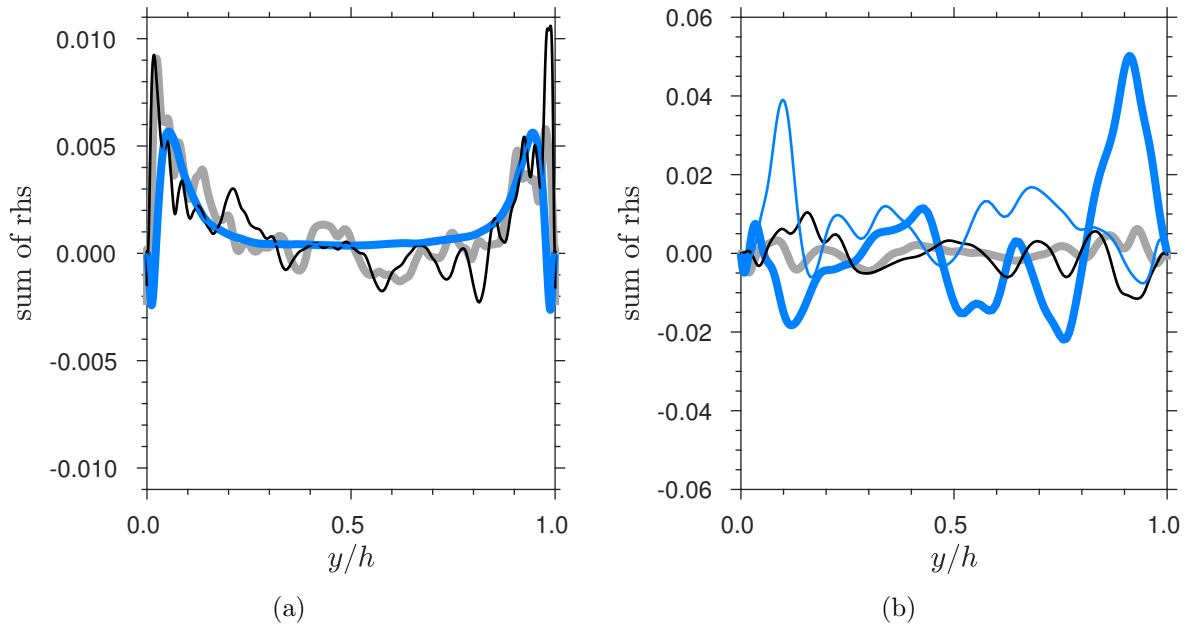
Figure 5.25: Sum of 'right–hand–side' terms in TKE equation (all terms except the time derivative): (a) large domain $\chi = 0$ (grey line) and $\chi = 10$ (black line) cases (A and B),; (b) small domain $\chi = 0$ (grey line) and $\chi = 10^2$ (black line) cases (C and D). Thick blue line in panel (a) is unsteady term (1) for $\chi = 0$, thin blue line (masked) is $\chi = 10$. Thick blue line in panel (b) is the same but for the $\chi = 0$ case, and the thin blue line is for the $\chi = 10^2$ case.

(a)   (b)
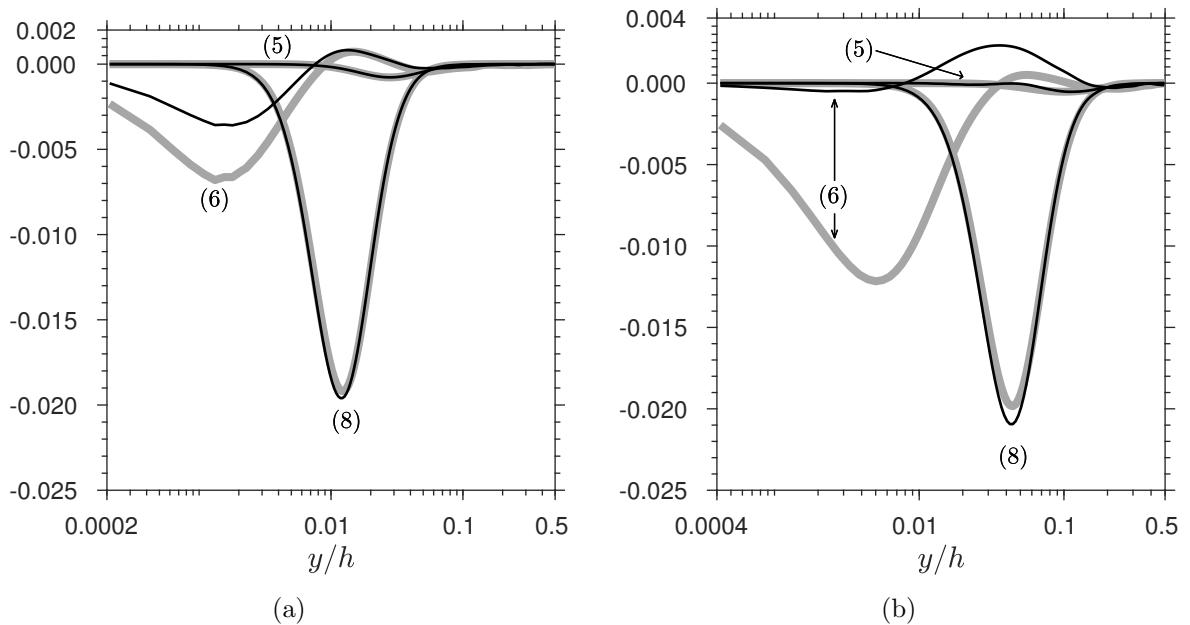
Figure 5.26: dilatational terms from TKE budget: (5) is velocity mean–pressure–gradient interaction; (6) is pressure dilatation; (8) is velocity mean–viscous–stress gradient. (a) large domain case (A and B); (b) small domain case (C and D). Grey is $\chi = 0$, black is $\chi > 0$.
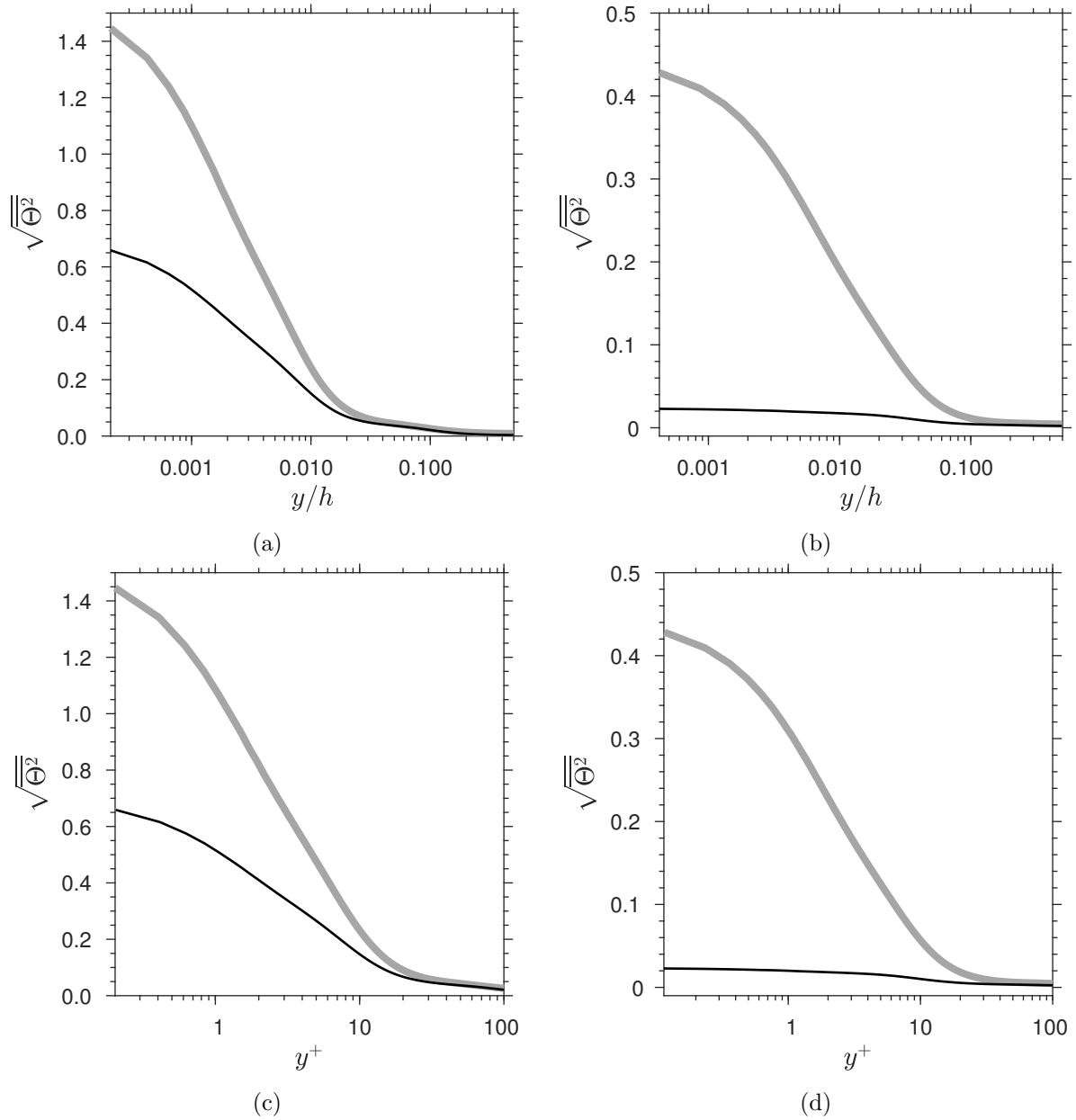
Figure 5.27: Root–mean–square velocity dilatation. (a) large domain for $\chi = 0$ (grey line) and $\chi = 10$ (black line) cases (A and B); (b) small domain for $\chi = 0$ (grey line) and $\chi = 10^2$ (black line) cases (C and D). (c) and (d) are the same as (a) and (b), respectively, but the y axis is in wall units.

5.5   Isentropic fluid particle

The sound absorption mechanism described by Landau and Lifshitz (1959) and explored in chapter 4 assumes the damping of a purely acoustic wave, i.e. one that is isentropic. To assess for how long a fluid particle is under isentropic conditions as it is convected in turbulent Couette flow, the thermodynamic pressure and "isentropic pressures" (defined below) of the fluid particle can be compared. To do so, the fluid particle is assumed to undergo an isentropic process, and the error this assumption has will be assessed as a function of the distance travelled along its trajectory. Assuming no change of entropy s, the fundamental equation of thermodynamics $\mathrm{d}e = -p\mathrm{d}v + T\mathrm{d}s$ simplifies to

$$\mathrm{d}e = -p\mathrm{d}v \qquad (5.5.1)$$

where e, v, T, and s are the specific internal energy, specific volume, temperature, and specific entropy, respectively. The total differential of the isentropic relation $pv^\gamma = \text{constant}$ is

$$\frac{\mathrm{d}p}{p} = -\gamma \frac{\mathrm{d}v}{v} \qquad (5.5.2)$$

which can be equated with continuity, and for a fluid particle is

$$\frac{1}{\rho}\frac{\mathrm{d}\rho}{\mathrm{d}t} = -\Theta = -\frac{1}{v}\frac{\mathrm{d}v}{\mathrm{d}t}. \qquad (5.5.3)$$

Combining (5.5.2) and (5.5.3) relates the change in pressure to the divergence of velocity

$$\frac{\mathrm{d}p}{p} = -\gamma\Theta\mathrm{d}t. \qquad (5.5.4)$$

A fluid particle, in a time $\mathrm{d}t$ and at a speed u_p moves a distance

$$\mathrm{d}\xi = u_p\mathrm{d}t, \qquad (5.5.5)$$

which when substituted into (5.5.4) gives

$$\frac{\mathrm{d}p}{p} = \underbrace{-\gamma\Theta\frac{\mathrm{d}x}{u_p}}_{\text{isentropic pressure}}. \qquad (5.5.6)$$

To test this assumption, each side of (5.5.6) is integrated along the particle's trajectory and the root–square difference P_{err} is computed, i.e.

$$P_{err} = \sqrt{\left(\int_{\xi_0}^{\xi_1} \frac{\mathrm{d}p}{p} - \int_{\xi_0}^{\xi_1} -\gamma \frac{\Theta}{u_p} \mathrm{d}\xi \right)^2} \qquad (5.5.7)$$

This difference is a measure of how much the path–integrated thermodynamic pressure and "isentropic pressure" $(-\gamma\Theta\mathrm{d}\xi/u_p)$ differ along the trajectory ξ of a fluid particle. Figure 5.28a shows the dependence of P_{err} on the distance travelled by the fluid particle and the distance from either wall. The orange line near either wall delineates the edge of the viscous sublayer at approximately $y^+ = 10$. To generate the map, each wall–normal plane of the $\chi = 0$, $\mathrm{Re}_\tau = 137$ case (C) is initially seeded with 4480 fluid particles, at every 5th grid point in the x and z directions. The required quantities are tracked and integrated in time, the methodology of which is outline in section 3.6. The paths of the 4480 particles at each wall–normal plane are then averaged to produce an ensemble. The error is largest just outside of the laminar region close to peak production, within the viscous sublayer the error reduces. For distances up to one h, P_{err} is less than approximately 6%. Figure 5.28 shows the integrated thermodynamic pressure compared with the integrated isentropic pressure for a single particle initially located at $y = h/12$ and $y = h/3$, respectively. Both particles are located at $x = nx/2$ and $z = nz/2$. Also shown is the P_{err} of the fluid particles.
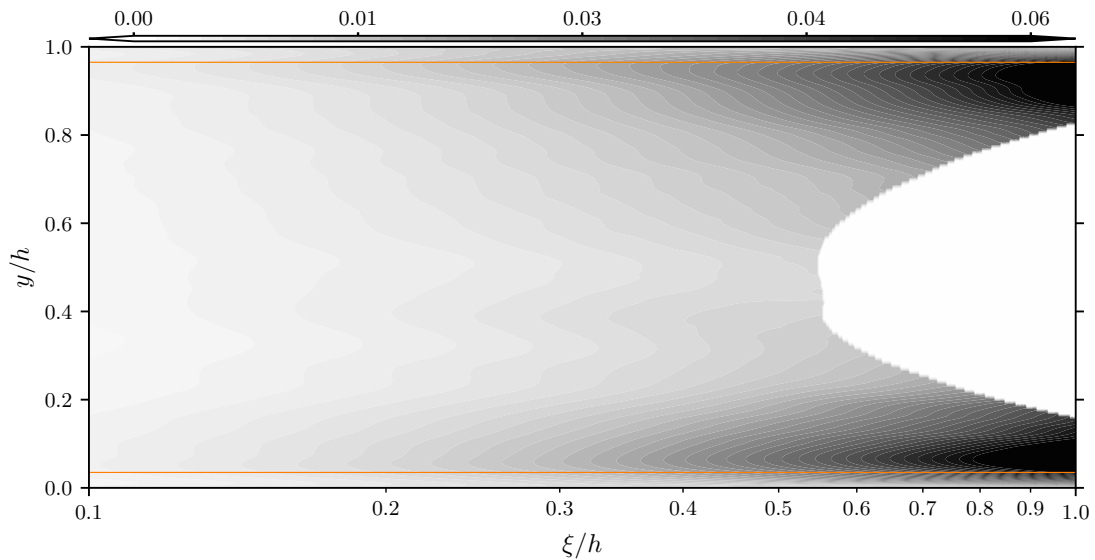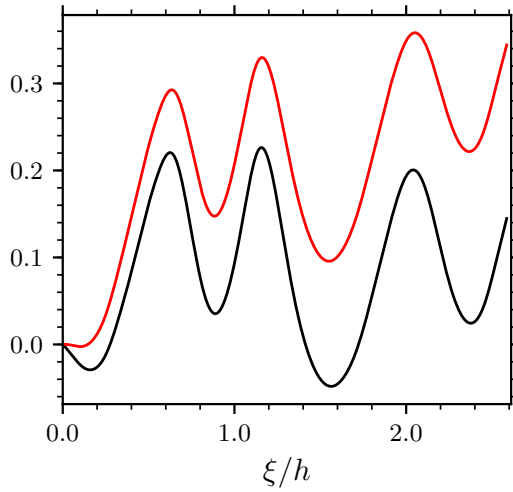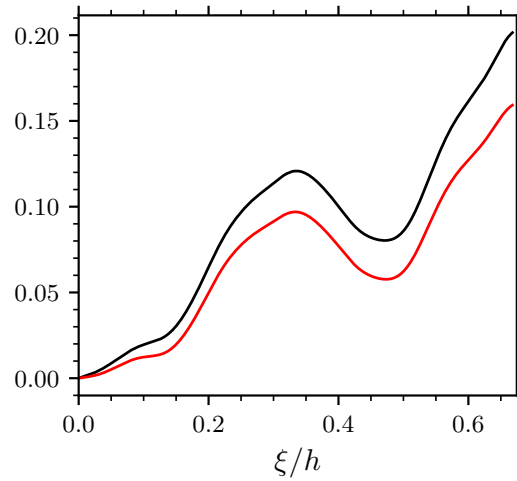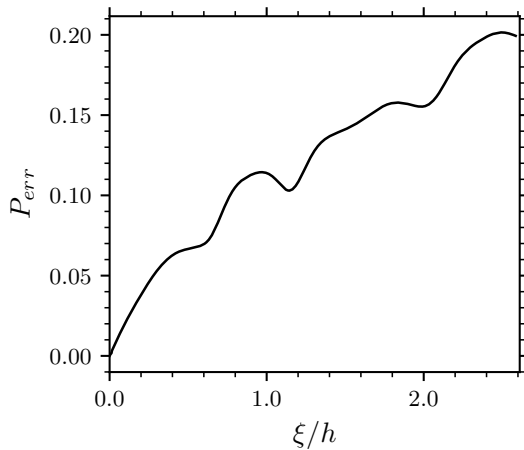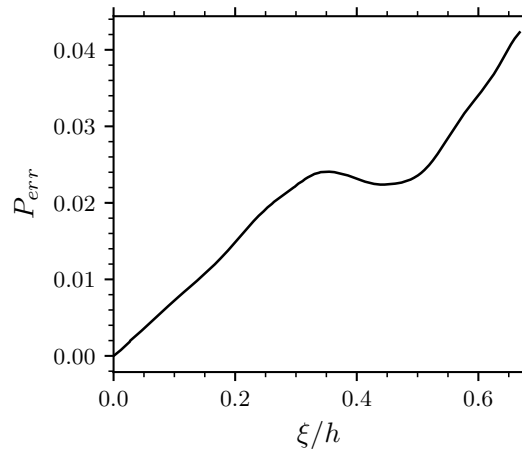
Figure 5.28: (a) contours of P_{err} for an ensemble of 4480 particles released from the same initial wall–normal plane. All planes between the two walls are shown. Orange line indicates approximately 10 wall units from either wall. Path–integrated thermodynamic pressures: thermal (black), isentropic (red) at (b) $y/h \approx 1/12$ and (c) $y/h \approx 1/3$; RMS error P_{err} between path–integrated pressures, see equation (5.5.7): (d) same location as (b); (e) same location as (c). Note the scale change between (b) and (c), and (d) and (e).

5.6 Velocity field projected onto solenoidal and dilatational components

The section presents the velocity field projected onto solenoidal and dilatation components for the large domain, $\chi = 0$ and $\chi = 10$ cases (A and B). Figure 5.29 and 5.30 show the streamwise velocity at the mid–plane for the $\chi = 0$ and $\chi = 10$ large domain cases, respectively. They show the streamwise alignment of large scale high- and low–speed streaks in the solenoidal flow field that are associated with the large streamwise rollers (Komminaho *et al.*, 1996). In the large domain case, there are four counter–rotating streamwise rollers (see figure 3.5); rollers two and three (counting from $z/h = y/h = 0$ rotate such that fluid from the top wall in the middle of the channel is drawn downwards. Between rollers one and two, and three and four, the same process happens but fluid from the bottom wall is drawn upward. The result is at the mid–plane, positive u is concentrated at the mid–span, and negative u is concentrated at the first and third-quarters of the span. (Indeed at the domain boundary is the interaction between rollers one and four producing another streak with positive u). The decomposition reveals that these structures are solenoidal. The lower panels in the figures show the presence of oblique acoustic waves (relative to the streamwise direction). The $\chi = 10$ case shows similar large–scale acoustic waves as for the zero bulk viscosity case, but a less broadband u field. At small scales there are features still sharply defined, indicating that an intermediate range of scales has been damped. Front views normal to the $y-z$ plane of u show the same effect on the dilatational velocity field, except that in the region $y < 0.2$ (and the same at the upper wall). In this region the intensity of the fluctuations remains high, indicating that the near–wall streaks are key to the generation of velocity fluctuations (see section 4.2.1) that contribute to velocity dilatation. In the region $0.2 < y < 0.8$, the $\chi = 0$ case shows small pockets of large positive and negative fluctuations, where in the $\chi = 10$ case these are rendered smooth at an intermediate range of scales. Features at the smallest scales are preserved and possibly represent a flow regime that is below the maximum damping predicted by the acoustic Reynolds number from the one–dimensional simulations. Applying the analysis to the $\chi = 0$ case $\Lambda_0/h = \text{MaRe}_{\Lambda_0}/\text{Re}$ which for the $\chi = 0$ case is of the order of 10^{-3}. This implies that 5×10^3 points would be needed in the y coordinate grid to ensure the wavelength experiencing maximum acoustic damping is above the filter cut–off. For this case, there are only 480 points in the y direction and hence maximum damping is not achieved. For the $\chi = 10$ case, $\Lambda_0/h \sim 10^{-2}$ and hence maximum damping occurs at waves with 100 points per wavelength. This

is more than well resolved by the grid and leaves a bandwith from 100 points per wavelength down to the filter cut–off of 4 points per wavelength that are below the scale for maximum damping. This explains why there are sharply resolved features in the dilatational velocity fields shown in figures. Figures 5.33a and 5.33b show the associated wall–normal velocity fluctuations. The top panel in both figures shows that in the near wall region there are small–scale, counter rotating vortices that burst away from the wall. In the dilatational field (lower panels), these correspond to a band of compression or expansion which is rapidly damped as it moves towards the centre of the channel. Figure 5.34 shows the overlay of fluctuating solenoidal (in colour) and compressible (in greyscale) streamwise velocity at a wall–normal distance of $y^+ \approx 0.2$. Slow moving solenoidal streaks (yellow and red) are visible. Compression fronts in the dilatational field (alternating black and white regions) appear at the upstream side of the streaks.
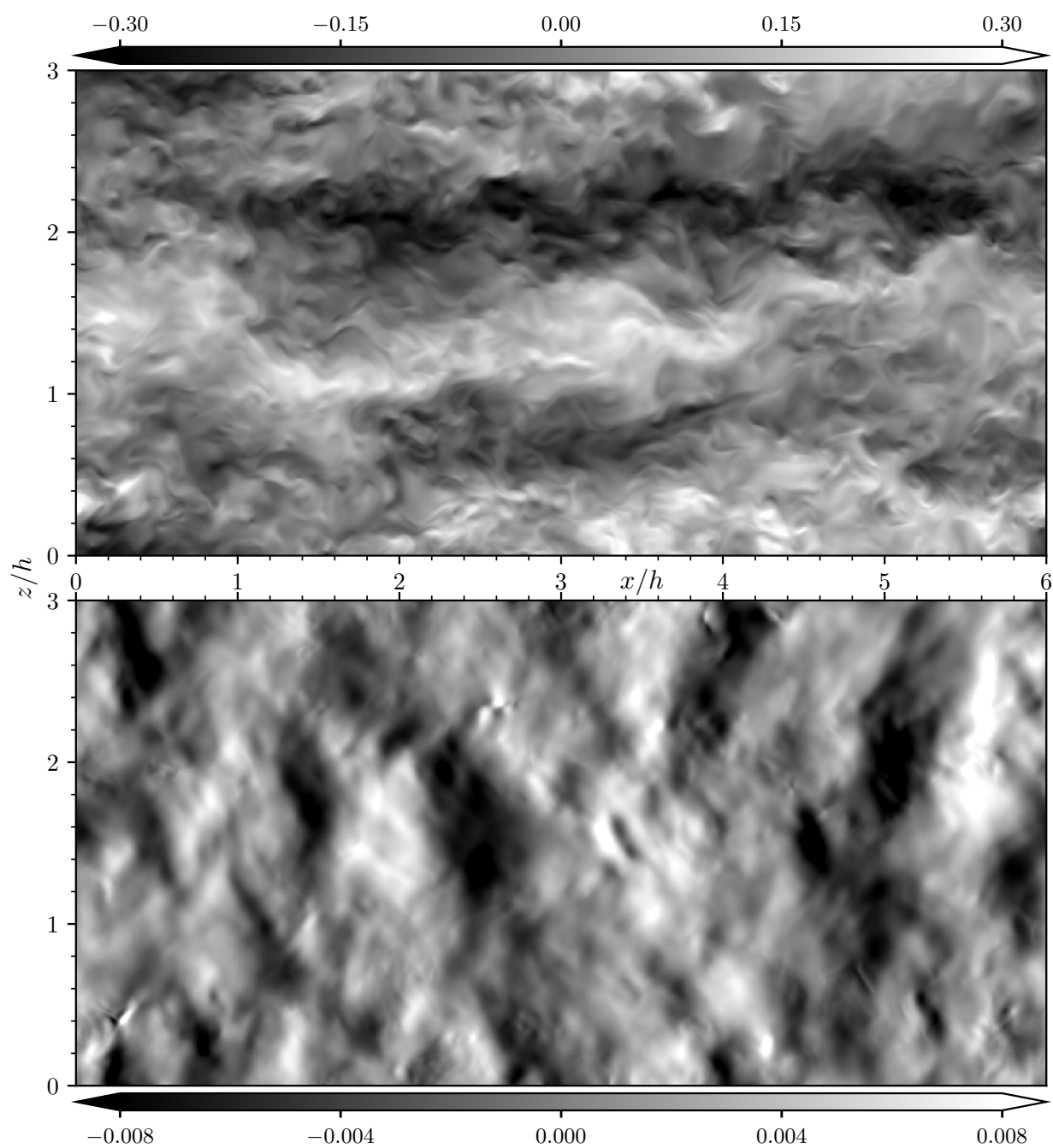
Figure 5.29: Streamwise velocity at the mid–plane, view is normal to the wall, case A, $\chi = 0$. Top panel: solenoidal field; bottom panel: dilatational field.
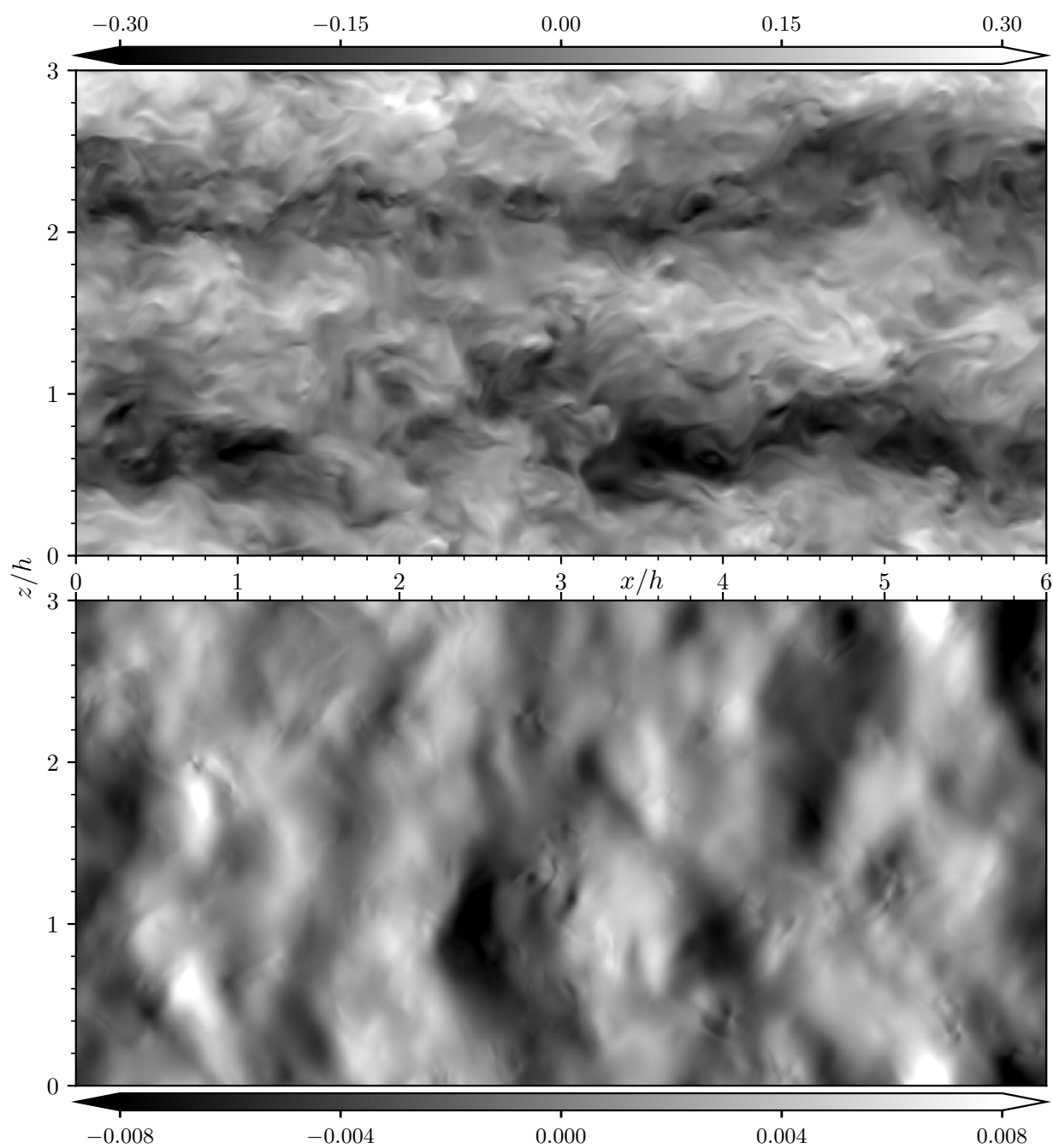
Figure 5.30: Streamwise velocity at the mid–plane, view is normal to the wall, case B, $\chi = 10$. Top panel: solenoidal field; bottom panel: dilatational field.

(a)

(b)
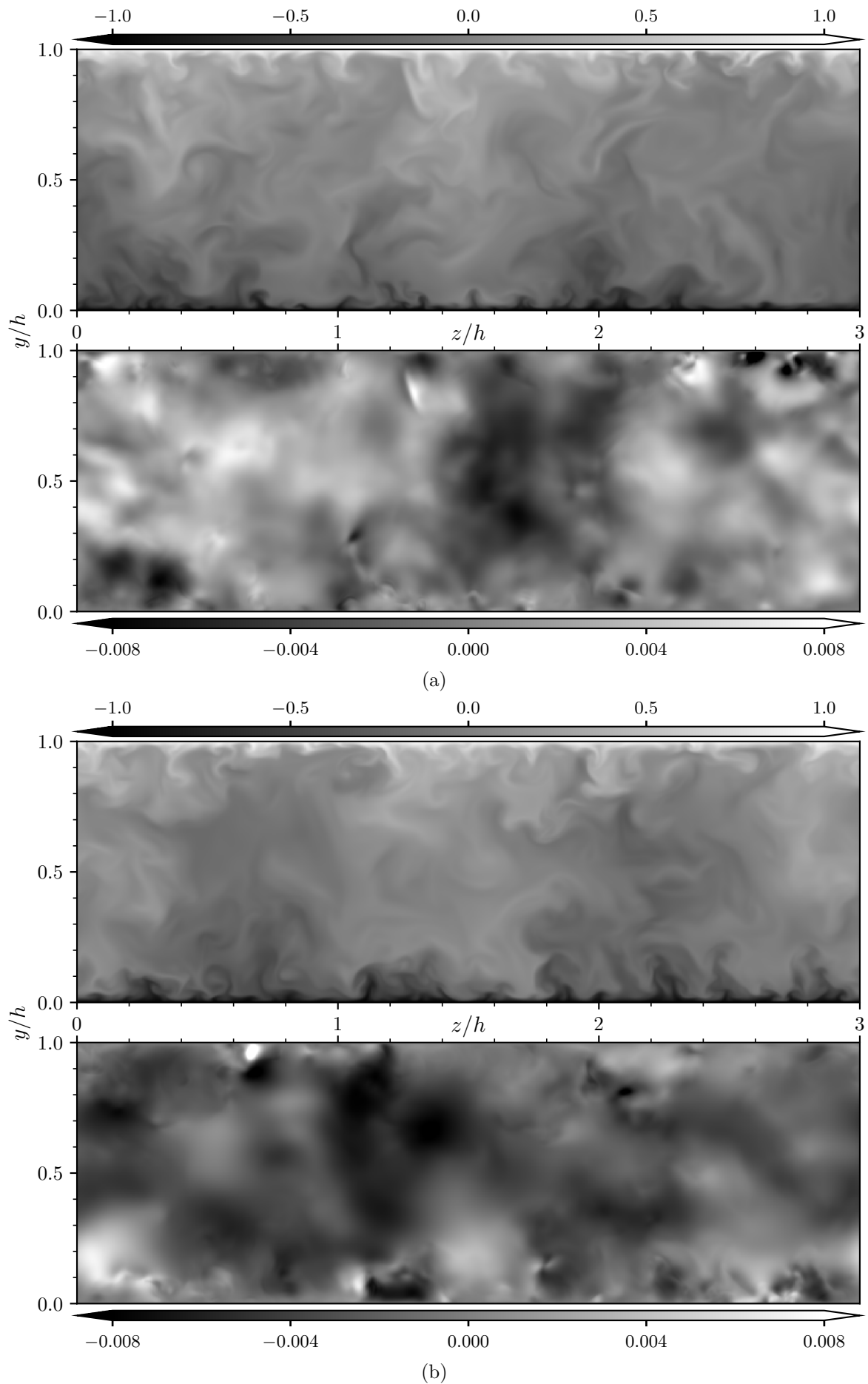
Figure 5.31: Streamwise velocity, front view is normal to the $z - y$ plane. Top panel: solenoidal field; bottom panel: dilatational field. (a) $\chi = 0$, case A; (b) $\chi = 10$, case B.

(a)

(b)
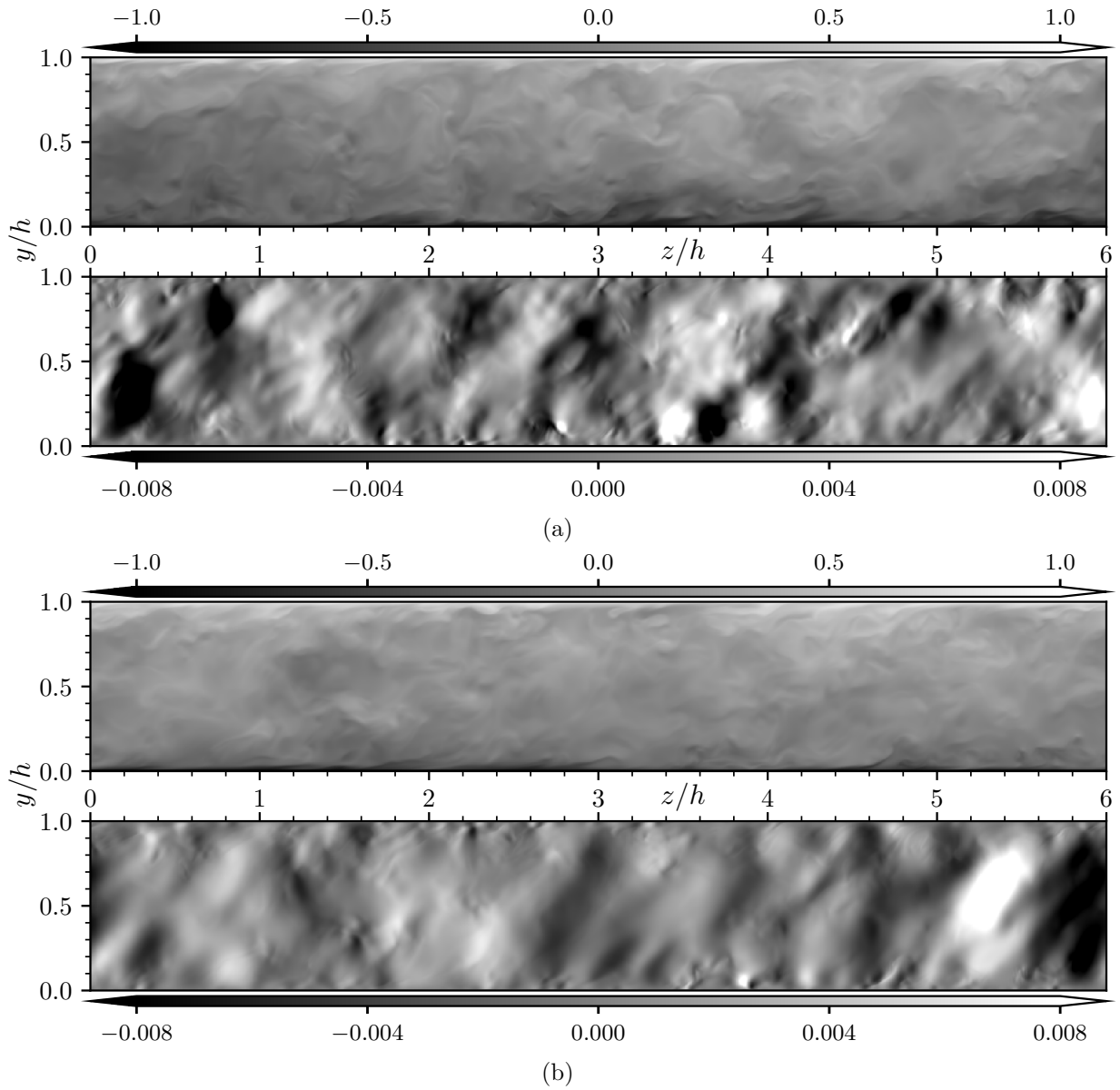
Figure 5.32: Streamwise velocity, side view is normal to the $x-y$ plane. Top panel: solenoidal field; bottom panel: dilatational field. (a) $\chi = 0$, case A; (b) $\chi = 10$, case B.

(a)

(b)
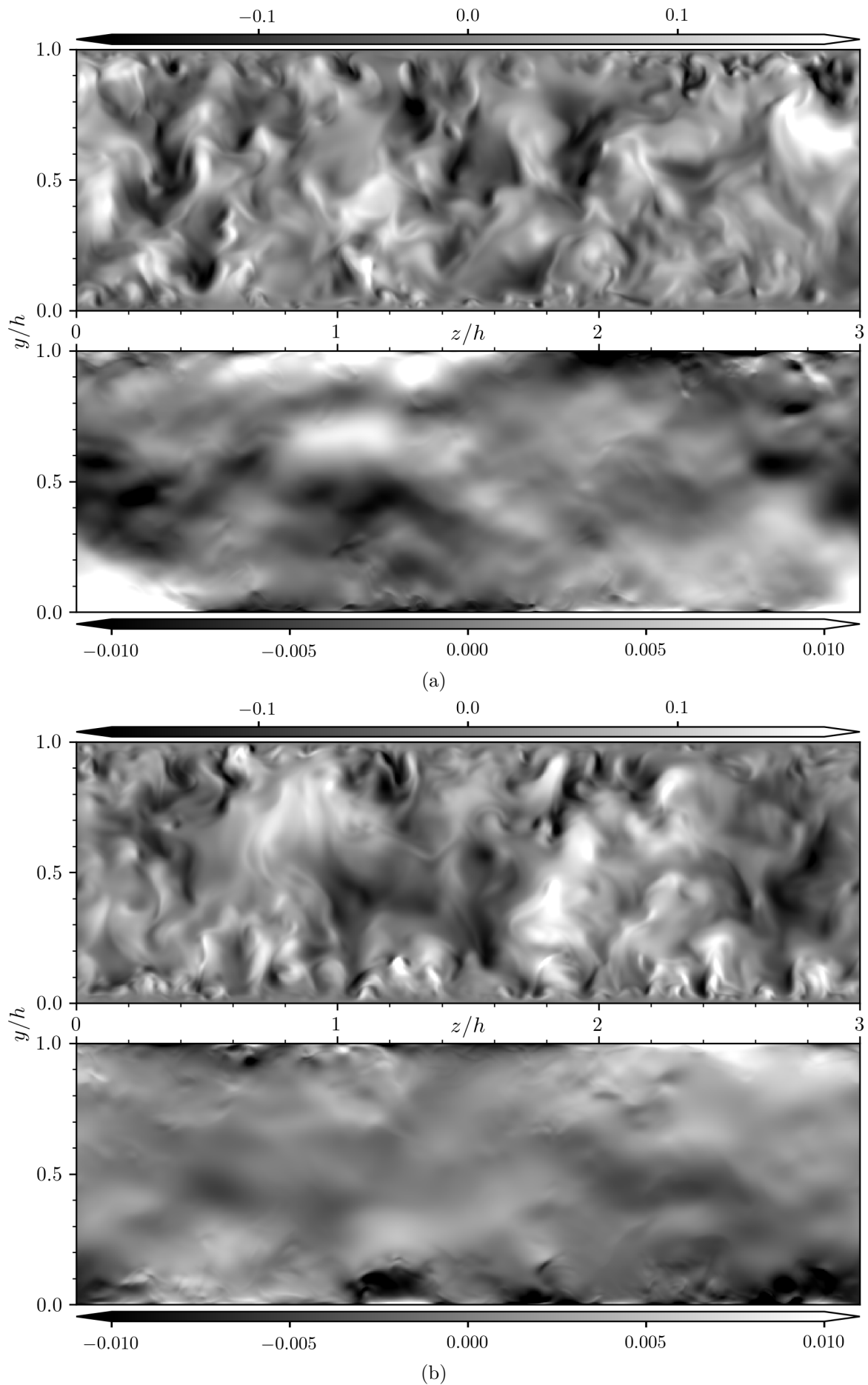
Figure 5.33: Wall-normal velocity fluctuations, front view is normal to the $z - y$ plane. Top panel: solenoidal field; bottom panel: dilatational field. (a) $\chi = 0$, case A; (b) $\chi = 10$, case B.
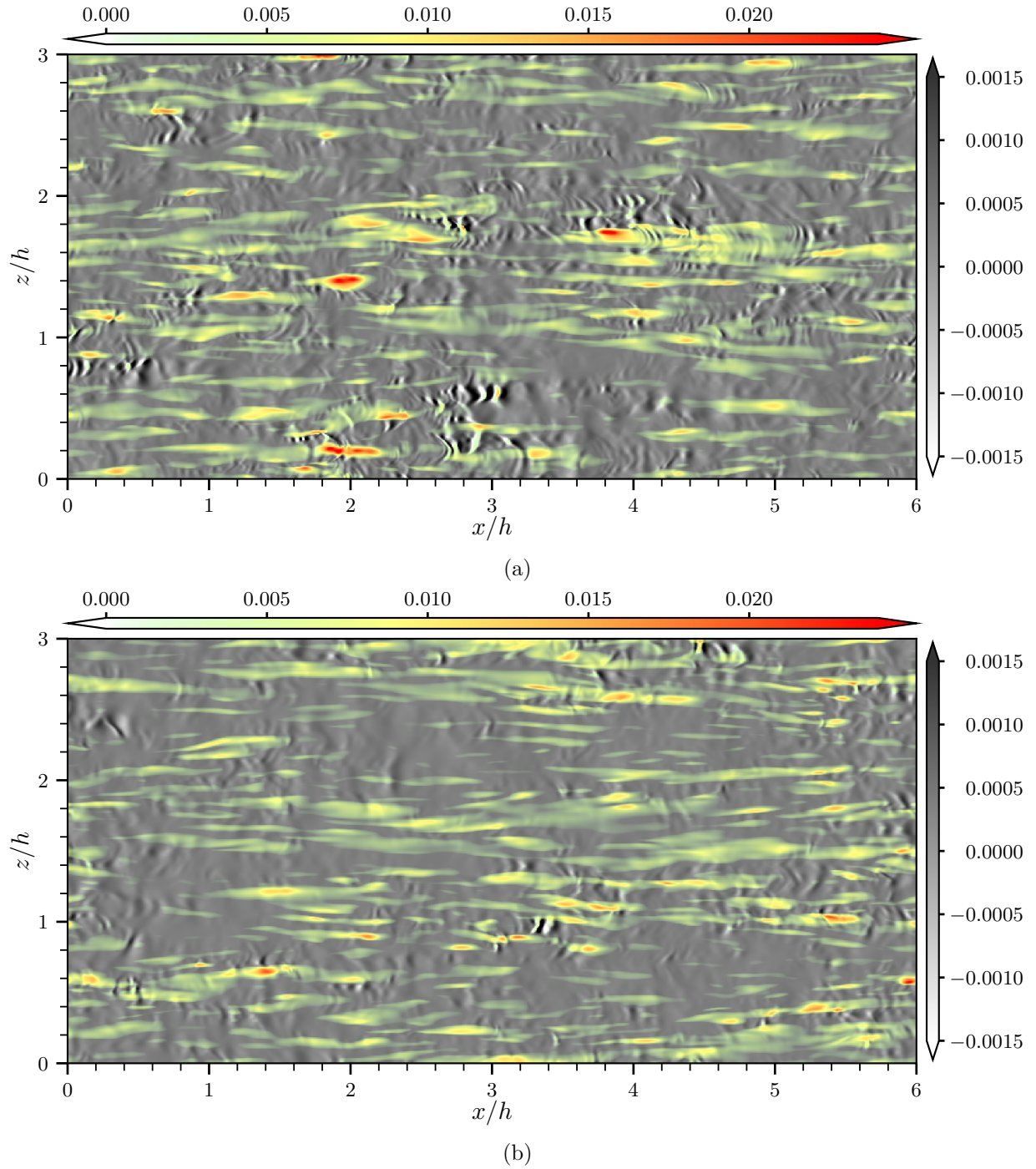
Figure 5.34: Top view at $y^+ \approx 0.2$ of streamwise velocity fluctuations decomposed into solenoidal (red) and dilatational (greyscale) contributions. (a) $\chi = 0$, case A; (b) $\chi = 10$, case B.

Chapter 6

Conclusions

This thesis assessed the effect of the bulk viscosity in compressible flows by performing one-two- and three–dimensional direct numerical simulations. In the one–dimensional framework, the acoustic absorption theory of Landau and Lifshitz (1959) is compared to simulation results of the damping characteristics of a perturbation to velocity. Landau's retention of all three transport coefficients (μ, μ_{b} and κ) extended the work of (Stokes, 1845) (who considered only the shear viscosity). The damping factor derived by Landau is dependent on the square of the frequency of the acoustic wave and on the linear combination of the transport coefficients. The perturbation simulations show how the amplitude of ρ, u and p vary with Re_{Λ_0} in the range 10^{-1} to 10^4 for $\chi = 0$ and $\chi = 10$. Landau's damping coefficient matches the simulation results as Re_{Λ_0} is reduced from 10^4 to 10, covering flows in which the convective forces dominate. As the Reynolds number is reduced from $\mathrm{Re}_{\Lambda_0} = 10^4$, the damping effectiveness increases, until the simulation results show maximum damping at $\mathrm{Re}_{\Lambda_0} \sim 10$ for $\chi = 0$. Landau's acoustic damping theory does not show a maximum due to the assumption of considering a purely acoustic wave, an assumption that becomes progressively less accurate as the viscous forces begin to dominate. Instead, the prediction continues to increase the damping effectiveness from $\mathrm{Re}_{\Lambda_0} \sim 10$ to 10^{-1}. From the simulation results, as Re_{Λ_0} is further reduced from 10 to 10^{-1}, a different mechanism to Landau's acoustic absorption reduces the damping. As χ increases, the Reynolds number at which maximum damping occurs increases by the same order of magnitude: $\mathrm{Re}_{\Lambda_0} \sim 10^2$ for $\chi = 10$. Landau's damping theory matches the trend of the simulation results when approaching the point of maximum damping from $\mathrm{Re}_{\Lambda_0} \sim 10^2$ (although not below) provoking the definition of an acoustic Reynolds number $\mathrm{Re}_{\mathrm{ac.}} \equiv \rho_0 c_0 \Lambda_0 / (\mu_0 [4/3 + \chi + (\gamma - 1)/\mathrm{Pr}])$ which is order unity for

maximum acoustic damping. The acoustic Reynolds number can be used to predict the optimal value of Re_{Λ_0} for different values of χ. This prediction was used in the context of two- and three–dimensional flows to explain the differences in instantaneous flow fields.

The relevance of acoustic absorption to turbulence is due to the energy transfer between solenoidal and dilatation kinetic energy is via acoustic waves (Miura and Kida, 1995). The bulk viscosity introduces a new transfer mechanism from dilatational kinetic energy to internal energy. To explore the generation of velocity dilatation from a solenoidal initial condition, a two–dimensional ideal vortex case was examined. A ring of Θ propagated in the radial direction with respect to the initial solenoidal vortex. Increasing χ to 10^3 reduced the magnitude of Θ, indicating a lack of production.

Given finite computational resources and the linear increase in computational cost as χ is increased (when using explicit schemes), three–dimensional DNS simulations at $Re_L = 2 \times 10^4$ were only possible up to $\chi = 10$. In two dimensions, however, the lower computational cost allowed runs of $\chi = 10^3$, representative of CO_2, to be performed. Decaying homogeneous turbulence was initialised with a solenoidal velocity field and runs of $\chi = 0$ and $\chi = 10^3$ were compared. For $\chi = 10^3$, the velocity dilatation field reduced in magnitude and had fewer small scale structures than the $\chi = 0$ case. However, thin thread–like structures in the velocity dilatation field below the wavelength for maximum Landau acoustic damping were not damped, whilst an intermediate bandwidth of large scales were damped. The terms in the budget of Θ showed dilatational production $((1/3 + \chi)(\boldsymbol{\nabla} v \cdot \boldsymbol{\nabla} \Theta)/Re_L)$ for $\chi = 10^3$ to be three orders of magnitude larger than for $\chi = 0$, expected due to the factor $(1/3 + \chi)/Re_L$ multiplying the dilatational production term. The time evolution equation of Θ can be written in such a way to isolate two production terms, one that is solenoidal and dominated by the scalar product of v with $-\boldsymbol{\nabla} p$, and a second that is dilatational. The sum of these two terms represents the overall production of Θ and remained unchanged when $\chi = 10^3$. The extended Poisson equation term, however, is better balanced except for localised areas that correspond to strong dilatational production. Energy spectra show that the solenoidal kinetic energy is largely unchanged when χ is increased. However, a bandwidth exists at $5 < k < 100$ in which the dilatational kinetic energy reduces; by as much as two orders of magnitude at $k = 20$. This demonstrates that a range of scales are damped by the presence of bulk viscosity. From taking the ratio of Re_L to Re_{Λ_0}, the wavelength at which maximum Landau acoustic damping occurs can be computed for a given simulation. For the $nx = ny = 1024$, $\chi = 0$ case, $\Lambda_0 = 10^{-4}L$, which corresponds to 1 point–per–wavelength, a scale not resolved due to the

filter cut–off at four points–per–wavelength. For $\chi = 10^3$ however, the same calculation yields the maximum Landau acoustic damping to occur at scales of 100 point–per–wavelength, far above the filter cut off. The range of scales below this value are less damped, possibly corresponding to the well defined thread–like structures observed in the velocity dilatation field.

To test the effect of bulk viscosity in three–dimensional, wall bounded turbulence, compressible Couette flows at Ma = 3.0 were simulated at Re_τ approximately 485 for both $\chi = 0$ and $\chi = 10$ in a domain of size $6h \times h \times 3h$. Smaller domain runs ($3h \times h \times 1.5h$) at Re_τ approximately 135 were run for three χ values: 0, 10^2 and 10^3. Couette flow has zero mean velocity dilatation and the instantaneous divergence of velocity is due to turbulent fluctuations. Couette flow has the advantage of no mean pressure gradient and instead feeds the flow with kinetic energy from the constant motion of the driving walls. The balance of turbulence kinetic energy showed little change, except for compressibility terms such as $\overline{p'\Theta''}$ that are an order χ/Re smaller than other terms. Landau's acoustic damping regime assumes the presence of purely acoustic waves. To check whether this is the case for the Couette cases, the thermodynamic and "isentropic" pressures were integrated along fluid particles' trajectories. The error between the two integrated pressures was less than 6% for trajectory distances of $\xi/h \sim 1$, which quantified the uncertainty when applying the Landau acoustic damping analysis to Couette flow. For the large domain, $\chi = 0$ case, the grid was unable to resolve the scale of maximum Landau damping; it would require 5×10^3 points in the wall–normal direction to ensure that scales undergoing the maximum acoustic damping had five points per wavelength. The large domain $\chi = 10$ case required 10^2 points and was sufficiently resolved for maximum damping, and in fact left a bandwidth of small scales (limited by the filter cut–off) which underwent less than maximum damping. Helmholtz decomposed views of the instantaneous velocity field confirmed that some small scale regions remain sharply visible and not damped.

To conclude, the bulk viscosity plays an important role in the production of the divergence of velocity. The majority of the kinetic energy of turbulent flows is contained in the solenoidal velocity field, causing only a minimal effect on turbulence statistics. However, the assumption that the bulk viscosity acts with increasing effectiveness as the wavelength on which it acts reduces is not accurate. It instead acts within a bandwidth that shifts, relative to the characteristic length scale of the flow, by changing the value of the bulk–to–shear viscosity ratio.

The relevance of the findings in this thesis to the applications mentioned in the introduction

depends on the accuracy that is required from the predictive simulations. For both carbon-capture and storage and concentrated solar power, despite the compressors operating at supersonic conditions, the majority of the energy is contained in the solenoidal velocity field and hence from this work (assuming ideal gas and constant transport properties), invoking Stokes's hypothesis is unlikely to result in significantly large errors. However, of greater concern is the proximity of the operating conditions to the thermodynamic critical point. In this region the sound speed drops considerably (increasing compressibility) and the transport coefficients show large variation. Hence the importance of bulk viscosity may become significant. It would be an interesting next step to investigate the role of bulk viscosity in non-ideal gases. Considering aeroshell design for descent into the Martian atmosphere, there is a long list of physics phenomena that must be accurately modelled. As an example, the radiative heating behind the bow shock that occurs in the upper atmosphere is the largest contributor to the heat flux into the aeroshell. Therefore efforts to improve modelling accuracy would be better placed in that area as they would have a larger impact on the accuracy of the predicted flow environment experienced by the aeroshell. However, it is the hope of this author that the current work will provide useful information on the validity of Stokes's hypothesis once the leading inaccuracy is from setting $\mu_\mathrm{b} = 0$.

Bibliography

M. R. Abu Zahra, E. S. Fernandez, and E. L. Goetheer. Guidelines for process development and future cost reduction of CO2 post-combustion capture. *Energy Procedia*, 4:1051–1057, jan 2011.

H. Alsmeyer. Density Profile in Argon and Nitrogen Shock Waves Measured by the Absorption of an Electron Beam. *J. Fluid Mech.*, 74:497–513, 1976.

W. H. Andersen and D. F. Hornig. Shock Front Thickness and Bulk Viscosity in Polyatomic Gases. *The Journal of Chemical Physics*, 24(4):767, 1956.

E. N. D. C. Andrade. Review of discussion. *Proceedings of the Royal Society A: Mathematical, Physical and Engineering Sciences*, 226(1164):65–69, 1954.

R. Aris. *Vectors, Tensors, and the Basic Equations of Fluid Mechanics*. Dover Publications, 1989.

V. Avsarkisov, S. Hoyas, M. Oberlack, and J. P. García-Galache. Turbulent plane Couette flow at moderately high Reynolds number. *Journal of Fluid Mechanics*, 751(V):R1, 2014.

R. Baierlein. Representing a Vector Field - Helmholtz Theorem Derived From a Fourier Identity. *American Journal of Physics*, 63(2):180–182, 1995.

R. A. S. Beck, D. M. Driver, M. J. Wright, H. H. Hwang, K. T. Edquist, and S. A. Sepka. Development of the Mars Science Laboratory Heatshield Thermal Protection System. *Journal of Spacecraft and Rockets*, 51(4):1139–1150, 2014.

J. Berland, C. Bogey, O. Marsden, and C. Bailly. High-order, low dispersive and low dissipative explicit schemes for multiple-scale and boundary problems. *Journal of Computational Physics*, 224(2):637–662, jun 2007.

H. Bhatia, V. Pascucci, and P. Bremer. The Natural Helmholtz-Hodge Decomposition for Open-Boundary Flow Analysis. *IEEE Transactions on Visualization and Computer Graphics*, 20(11):1566–1578, 2014.

C. Bogey and C. Bailly. A family of low dispersive and low dissipative explicit schemes for flow and noise computations. *Journal of Computational Physics*, 194(1):194–214, feb 2004.

D. Bose, M. Olson, B. Laub, T. White, J. Feldman, J. Santos, M. Mahzari, M. MacLean, A. Dufrene, and M. Holden. Initial Assessment of Mars Science Laboratory Heatshield Instrumentation and Flight Data. *51st AIAA Aerospace Sciences Meeting including the New Horizons Forum and Aerospace Exposition*, (January), 2013.

G. E. P. Box and M. E. Muller. A Note on the Generation of Random Normal Deviates. *The Annals of Mathematical Statistics*, 29(2):610–611, 1958.

J. C. Buell. Direct simulations of compressible wall-bounded turbulence. Technical report, Center for Turbulence Research, Stanford Univ./ NASA-Ames, 1991.

G. Buresti. A note on Stokes' hypothesis. *Acta Mechanica*, 226(10):3555–3559, 2015.

G. D. Chagelishvili, A. D. Rogava, and I. N. Segal. Hydrodynamic stability of compressible plane Couette flow. *Physical Review E*, 50(6):4283–4285, 1994.

P. Chassaing, R. A. Antonia, F. Anselmet, L. Joly, and S. Sarkar. *Variable Density Fluid Turbulence*. Kluwer Academic Publishers, 2002.

S. I. Chernyshenko and M. F. Baig. The mechanism of streak formation in near-wall turbulence. *Journal of Fluid Mechanics*, 544:99–131, 2005.

A. V. Chikitkin, B. V. Rogov, G. A. Tirsky, and S. V. Utyuzhnikov. Effect of bulk viscosity in supersonic flow past spacecraft. *Applied Numerical Mathematics*, 93:47–60, 2015.

M. S. Cramer. Numerical estimates for the bulk viscosity of ideal gases. *Physics of Fluids*, 24, 2012.

O. Dauchot and F. Daviaud. Streamwise vortices in plane Couette flow. *Physics of Fluids*, 7(5):901–903, 1995.

J. DeBonis. Solutions of the Taylor-Green Vortex Problem Using High-Resolution Explicit Finite Difference Methods. *51st AIAA Aerospace Sciences Meeting including the New Horizons Forum and Aerospace Exposition*, (January):1–20, 2013.

P. W. Duck, G. Erlebacher, and M. Y. Hussaini. On the linear stability of compressible plane Couette flow. *Journal of Fluid*, 258:131–165, 1994.

A. S. Dukhin and P. J. Goetz. Bulk viscosity and compressibility measurement using acoustic spectroscopy. *Journal of Chemical Physics*, 130(12), 2009.

K. T. Edquist, B. R. Hollis, C. O. Johnston, D. Bose, T. R. White, and M. Mahzari. Mars Science Laboratory Heat Shield Aerothermodynamics: Design and Reconstruction. *Journal of Spacecraft and Rockets*, 51(4):1106–1124, 2014.

G. Emanuel and B. M. Argrow. Linear dependence of the bulk viscosity on shock wave thickness. *Physics of Fluids*, 6(9):3203–3205, sep 1994.

G. Emanuel. Effect of bulk viscosity on a hypersonic boundary layer. *Physics of Fluids A: Fluid Dynamics*, 4(3):491, 1992.

B. C. Eu and Y. G. Ohr. Generalized hydrodynamics, bulk viscosity, and sound wave absorption and dispersion in dilute rigid molecular gases. *Physics of Fluids*, 13(3):744, 2001.

P. A. Fischer and A. T. Patera. Parallel Simulation of Viscous Incompressible Flows. *Annual Review of Fluid Mechanics*, 26:483–527, 1994.

T. B. Gatski and J.-P. Bonnet. *Compressibility, Turbulence and High Speed Flow.* Number 1. Elsevier, 2014.

X. Gloerfelt. *Bruit Rayonne par un ecoulement affleurant une cavite: simulation aeroacoustique directe et application de methodes integrales.* Phd, L'Ecole Centrale de Lyon, 2001.

H. Gonzalez and G. Emanuel. Effect of bulk viscosity on Couette flow. *Physics of Fluids A: Fluid Dynamics*, 5(5):1267–1268, 1993.

K. Goto, K. Yogo, and T. Higashii. A review of efficiency penalty in a coal-fired power plant with post-combustion CO_2 capture. *Applied Energy*, 111, 2013.

D. J. Griffiths. *Introduction To Electrodynamics.* Prentice Hall, 3rd edition, 1999.

J. M. Hamilton, J. Kim, and F. Waleffe. Regeneration mechanisms of near-wall turbulence structures. *Journal of Fluid Mechanics*, 287:317, 1995.

W. G. Hoover, A. J. C. Ladd, R. B. Hickman, and B. L. Holian. Bulk viscosity via nonequilibrium and equilibrium molecular dynamics. *Phyisical Review A*, 21(5), 1980.

P. Huang, G. N. Coleman, and P. Bradshaw. Compressible turbulent channel flows: DNS results and modelling. *Journal of Fluid Mechanics*, 305:185–218, 1995.

W. F. Hughes and J. F. Osterle. On the adiabatic Couette flow of a compressible fluid. *Zeitschrift fur angewandte Mathematik und Physik ZAMP*, 8(2):89–96, 1957.

S. M. Karim and L. Rosenhead. The Second Coefficient of Viscosity of Liquids and Gases. *Review of Modern Physics*, 24(2):108–116, 1952.

J. Kim and J. Lim. A linear process in wall-bounded turbulent shear flows. *Physics of Fluids*, 12(8):1885–1888, 2000.

H. T. Kim, S. J. Kline, and W. C. Reynolds. The production of turbulence near a smooth wall in a turbulent boundary layer. *Journal of Fluid Mechanics*, 50(1):133–160, 1971.

S. G. Kim, J. Lee, Y. Ahn, J. I. Lee, Y. Addad, and B. Ko. CFD investigation of a centrifugal compressor derived from pump technology for supercritical carbon dioxide as a working fluid. *Journal of Supercritical Fluids*, 86:160–171, 2014.

O. Kitoh and M. Umeki. Experimental study on large-scale streak structure in the core region of turbulent plane Couette flow. *Physics of Fluids*, 20(2), 2008.

H. O. Kneser. Schallabsorption in mehratomigen Gasen. *Annalen der Physik*, 1933.

J. Komminaho, A. Lundbladh, and A. V. Johansson. Very large structures in plane turbulent Couette flow. *Journal of Fluid Mechanics*, 320:259, 1996.

R. H. Korkegi and R. A. Briggs. Compressible Turbulent Plane Couette Flow. *Aerospace Research Laboratories*, ARL 67-022(November), 1967.

R. H. Kraichnan. Inertial Ranges in Two Dimensional Turbulence. *Physics of Fluids (1958-1988)*, 10(7):1417–1423, 1967.

L. D. Landau and E. M. Lifshitz. *Course of Theoretical Physics: Fluid Mechanics*. Pergamon, 1 edition, 1959.

M. J. Lee. Direct numerical simulation of turbulent Couette flow. Technical report, Center for Turbulence Research, Stanford Univ./ NASA-Ames, 1991.

S. K. Lele. Compressibility Effects on Turbulence. *Annual Review of Fluid Mechanics*, 26:211–254, 1994.

R. J. Leveque. *Finite Difference Methods for Ordinary and Partial Differential Equations*. Society for Industrial and Applied Mathematics, 1st edition, 2007.

A. Lundbladh and A. V. Johansson. Direct simulation of turbulent spots in plane Couette flow. *Journal of Fluid Mechanics*, 229:499, 1991.

M. Malik, J. Dey, and M. Alam. Linear stability, transient energy growth, and the role of viscosity stratification in compressible plane Couette flow. *Physical Review E - Statistical, Nonlinear, and Soft Matter Physics*, 77(3):036322, mar 2008.

G. R. Miller and G. W. Lewis. CASE FILE COPY Shock Losses in Transonic Compressor. 1961.

H. Miura and S. Kida. Acoustic energy exchange in compressible turbulence. *Physics of Fluids*, 7(7):1732–1742, 1995.

P. Orlandi, M. Bernardini, and S. Pirozzoli. Poiseuille and Couette flows in the transitional and fully turbulent regime. *Journal of Fluid Mechanics*, 770:424–441, 2015.

S. A. Orszag and M. Israeli. Numerical Simulations of Viscous Incompressible Flows. *Annual Review of Fluid Mechanics*, 6:281–318, 1974.

S. Pan and E. Johnsen. The role of bulk viscosity on the decay of compressible, homogeneous, isotropic turbulence. *Journal of Fluid Mechanics*, 833:717–744, 2017.

C. Y. Pan. How Bad Are Vandermonde Matrices? *SIAM Journal on Matrix Analysis and Applications*, 37(2):676–694, 2016.

A. Patel, B. J. Boersma, and R. Pecnik. The influence of near-wall density and viscosity gradients on turbulence in channel flows. (2016):793–820, 2016.

S. Pirozzoli, M. Bernardini, and P. Orlandi. Turbulence statistics in Couette flow at high Reynolds number. *Journal of Fluid Mechanics*, 758:327–343, 2014.

S. B. Pope. *Turbulent Flows*. Cambridge University Press, 2000.

G. J. Prangsma, A. H. Alberga, and J. J. M. Beenakker. Ultrasonic determination of the volume viscosity of N2, CO, CH4 and CD4 between 77 and 300 K. *Physica*, 64(2):278–288, 1973.

M. Pugh. *Introductory numerical methods for PDE (lecture notes)*. University of Toronto, Department of Mathematics, 2009.

W. T. Richards. Supersonic phenomena. *Reviews of Modern Physics*, 11(1):36–64, 1939.

P. J. Roache. *Computational Fluid Dynamics*. Hermosa Publishers, 1982.

H. Schlichting. *Boundary Layer Theory*. McGraw-Hill, 7 edition, 1979.

F. S. Sherman. A Low-Density Wind-Tunnel Study of Schock-Wave Structures. Technical Report NACA TN 3298, 1955.

C. R. Smith and S. P. Metzler. The characteristics of low-speed streaks in the near-wall region of a turbulent boundary layer. *Journal of Fluid Mechanics*, 129:27–54, 1983.

P. R. Spalart, a. Garbaruk, and M. Strelets. RANS Solutions in Couette flow with streamwise vortices. *International Journal of Heat and Fluid Flow*, 49:128–134, 2014.

G. G. Stokes. On the Theories of the Internal Friction of Fluids in Motion, and of the Equilibrium and Motion of Elastic Solids. *Transactions of the Cambridge Philosophical Society*, 8:287–319, 1845.

W. A. Strauss. *Partial Differential Equations: An Introduction*. Wiley, 2nd edition, 2007.

C. K. W. Tam and Z. Dong. Wall boundary conditions for high-order finite-difference schemes in computational aeroacoustics. *Theoretical and Computational Fluid Dynamics*, 6(5-6):303–322, 1994.

C. K. W. Tam and J. C. Webb. Dispersion-Relation-Preserving Finite Difference Schemes for Computational Acoustics. *Journal of Computational Physics*, 107:262–281, 1993.

J. C. Tannehill, D. A. Anderson, and R. H. Pletcher. *Computational fluid mechanics and heat transfer*, volume Second Edi. 1997.

P. A. Thompson. *Compressible-Fluid Dynamics*. McGraw-Hill Book Company, 1972.

L. Tisza. Supersonic Absorption and Stokes' Viscosity Relation. *Physical Reviews*, 61:531–536, 1942.

A. Trettel and J. Larsson. Mean velocity scaling for compressible wall turbulence with heat transfer. *Physics of Fluids*, 28:1—-18, 2016.

C. Truesdell. The Mechanical Foundations of Elasticity and Fluid Dynamics. *Journal of Rational Mechanics and Analysis*, 1(1):125–300, 1952.

C. Truesdell. The Present Status of the Controversy Regarding the Bulk Viscosity of Fluids. *Proceedings of the Royal Society A: Mathematical, Physical and Engineering Sciences*, 226(1164):59–65, oct 1954.

W. M. van Rees, A. Leonard, D. Pullin, and P. Koumoutsakos. A comparison of vortex and pseudo-spectral methods for the simulation of periodic vortical flows at high Reynolds numbers. *Journal of Computational Physics*, 230(8):2794–2805, apr 2011.

M. J. Wright, C. Y. Tang, K. T. Edquist, B. R. Hollis, P. Krasa, and C. H. Campbell. A Review of Aerothermal Modeling for Mars Entry Missions. *AIAA Paper 2010-443*, (January):1–39, 2010.

S. A. Wright, R. F. Radel, M. E. Vernon, G. E. Rochau, and P. S. Pickard. Operation and Analysis of a Supercritical CO 2 Brayton Cycle. Technical Report September, 2010.

Y. S. Zhang, W. T. Bi, F. Hussain, and Z. S. She. A generalized Reynolds analogy for compressible wall-bounded turbulent flows. *Journal of Fluid Mechanics*, 739:392–420, 2014.

Appendix A

Governing equations

The governing equations for mass conservation, momentum balance and energy conservation in a compressible fluid are summarised below in conservative form:

A.1 Nondimensionalisation

$$\frac{\partial \rho^\star}{\partial t^\star} + \nabla^\star \cdot (\rho^\star \boldsymbol{u}^\star) = 0$$

$$\frac{\partial \rho^\star \boldsymbol{u}^\star}{\partial t^\star} + \boldsymbol{\nabla}^\star \cdot (\rho^\star \boldsymbol{u}^\star \otimes \boldsymbol{u}^\star) = -\boldsymbol{\nabla}^\star p^\star + \boldsymbol{\nabla}^\star \cdot \boldsymbol{\Sigma}^\star \tag{A.1.1}$$

$$\frac{\partial \rho^\star e_t^\star}{\partial t^\star} + \nabla^\star \cdot (\rho^\star e_t^\star \boldsymbol{u}^\star) = -\nabla^\star \cdot (p^\star \boldsymbol{u}^\star) + \nabla^\star \cdot (\boldsymbol{\Sigma}^\star \boldsymbol{u}^\star) - \nabla^\star \cdot \boldsymbol{q}^\star.$$

Dimensioned quantities are indicated by a star ("$\star$"). The specific total energy and heat flux vector are

$$e_t^\star = e^\star + \frac{1}{2}(u^{\star 2} + v^{\star 2})$$

$$\boldsymbol{q}^\star = -\kappa^\star \boldsymbol{\nabla}^\star (T^\star). \tag{A.1.2}$$

The viscous stress tensor $\boldsymbol{\Sigma}^\star$ can be written in terms of the deviatoric part of the strain-rate tensor $\mathbf{D}^{\bullet\star}$:

$$\boldsymbol{\Sigma}^\star = 2\mu^\star \mathbf{D}^{\bullet\star} + \mu_{\mathrm{b}}^\star (\nabla^\star \cdot \boldsymbol{u}^\star)\mathbf{I}, \tag{A.1.3}$$

where

$$\mathbf{D}^{\bullet\star} \equiv \mathbf{D}^{\star} - \frac{1}{3}\nabla^{\star}\cdot\boldsymbol{u}^{\star}\mathbf{I} \tag{A.1.4}$$

and

$$\mathbf{D}^{\star} \equiv \frac{1}{2}\left(\boldsymbol{\nabla}^{\star}\boldsymbol{u}^{\star} + (\boldsymbol{\nabla}^{\star}\boldsymbol{u}^{\star})^{\mathrm{t}}\right). \tag{A.1.5}$$

The bulk viscosity is defined as

$$\mu_{\mathrm{b}}^{\star} \equiv \frac{2}{3}\mu^{\star} + \lambda^{\star}. \tag{A.1.6}$$

The density, velocity and temperature are non-dimensionalised by their wall (at $y = 0$) values, and space coordinates by the gap between the walls $h^{\star}$ as follows

$$\rho^{\star} = \rho\rho_{\mathrm{w}}^{\star}, \quad \boldsymbol{x}^{\star} = \boldsymbol{x}h^{\star}, \quad \boldsymbol{u}^{\star} = \boldsymbol{u}U_{\mathrm{w}}^{\star}, \quad T^{\star} = TT_{\mathrm{w}},$$

$$\mu^{\star} = \mu\mu_{\mathrm{w}}^{\star}, \quad \mu_{\mathrm{b}}^{\star} = \mu_{\mathrm{b}}\mu_{\mathrm{w}}^{\star}, \quad \lambda^{\star} = \lambda\mu_{\mathrm{w}}^{\star}, \quad \kappa^{\star} = \kappa\kappa_{\mathrm{w}}^{\star} \tag{A.1.7}$$

Non-dimensionalising continuity leads to

$$\frac{h^{\star}}{U_{\mathrm{w}}^{\star}t_{\mathrm{ref}}^{\star}}\frac{\partial\rho}{\partial t} + \mathrm{div}(\rho\boldsymbol{u}) = 0 \tag{A.1.8}$$

and assuming unity Strouhal number $\mathrm{St} \equiv h^{\star}/(t_{\mathrm{ref}}^{\star}U_{\mathrm{w}}^{\star}) = 1$ results in a timescale $t_{\mathrm{ref}}^{\star} = h^{\star}/U_{\mathrm{w}}^{\star}$. The momentum equation becomes

$$\frac{\partial\rho\boldsymbol{u}}{\partial t} + \boldsymbol{\nabla}\cdot(\rho\boldsymbol{u}\otimes\boldsymbol{u}) = -\frac{p_{\mathrm{ref}}^{\star}}{\rho_{\mathrm{w}}^{\star}U_{\mathrm{w}}^{\star 2}}\boldsymbol{\nabla}p + \underbrace{\frac{\mu_{\mathrm{w}}^{\star}}{\rho_{\mathrm{w}}^{\star}U_{\mathrm{w}}^{\star}h^{\star}}}_{\mathcal{A}}\boldsymbol{\nabla}\cdot\left(2\mu\left(\mathbf{D}^{\bullet} + \chi(\nabla\cdot\boldsymbol{u})\mathbf{I}\right)\right) \tag{A.1.9}$$

which leads to a scale for the pressure gradient if unity Euler number $\mathrm{Eu} \equiv p_{\mathrm{ref}}^{\star}/(\rho_{\mathrm{w}}^{\star}U_{\mathrm{w}}^{\star 2}) = 1$ is assumed. Term $\mathcal{A}$ is the Reynolds number based on the wall separation and wall speed is $\mathrm{Re} = \rho_{\mathrm{w}}^{\star}U_{\mathrm{w}}^{\star}h^{\star}/\mu_{\mathrm{w}}^{\star}$. The specific total energy equation becomes

$$\frac{e_{t,ref}^{\star}}{U_{\mathrm{w}}^{\star 2}}\frac{\partial\rho e_{\mathrm{t}}}{\partial t} + \frac{e_{t,ref}^{\star}}{U_{\mathrm{w}}^{\star 2}}\nabla\cdot(\rho e_{\mathrm{t}}\boldsymbol{u}) = -\nabla\cdot(p\boldsymbol{u}) + \frac{1}{\mathrm{Re}}\nabla\cdot\left(2\mu\left(\mathbf{D}^{\bullet} + \chi(\nabla\cdot\boldsymbol{u})\mathbf{I}\right)\right)$$
$$+ \underbrace{\frac{T_{\mathrm{w}}\kappa^{\star}}{\rho_{\mathrm{w}}^{\star}U_{\mathrm{w}}^{\star 3}h^{\star}}}_{\mathcal{B}}\nabla\cdot(\kappa\boldsymbol{\nabla}(T)). \tag{A.1.10}$$

The specific total energy scale is therefore $e_{t,ref}^\star = U_w^{\star 2}$. Term $\mathcal{B}$ can be transformed by using the speed equation at the wall $c_w = \sqrt{\gamma R^\star T_w}$, the Mach number $\mathrm{Ma} = U_w^\star/c_w$, the Prandtl number $\mathrm{Pr} \equiv \mu^\star c_p^\star / \kappa^\star$ and $(\gamma - 1)c_p^\star = \gamma R^\star$ to form the heat term scale:

$$\frac{T_w \kappa^\star}{\rho_w^\star U_w^{\star 3} h^\star} = \frac{1}{\mathrm{ReMaPr}(\gamma - 1)}. \tag{A.1.11}$$

A.2   Laminar solution

Applying these boundary conditions leads to an analytic solution for the wall-normal velocity v:

$$\frac{\mathrm{d}(\rho v)}{\mathrm{d}y} = 0 \tag{A.2.1}$$

which results in

$$\rho v = \mathrm{constant}. \tag{A.2.2}$$

From the no-penetration boundary condition, $v(y = 0) = 0$ and hence $v = 0$ for all y.

$$v(y = 0) = 0, \tag{A.2.3}$$

the velocity is identically equal to zero throughout the domain:

Introducing this result into the momentum equations simplifies them to

$$
\begin{aligned}
0 &= \frac{\mathrm{d}^2 u}{\mathrm{d}y^2} \\
0 &= \frac{\mathrm{d}p}{\mathrm{d}y}.
\end{aligned}
\tag{A.2.4}
$$

For the x-momentum equation, the walls move at constant speed u_w but in opposite senses, leading to the boundary conditions

$$
\begin{aligned}
u(y = 0) &= -u_w \\
u(y = h) &= +u_w
\end{aligned}
\tag{A.2.5}
$$

which leads to the well known linear velocity profile

$$u = u_w(2y - 1). \tag{A.2.6}$$

Integrating the y-momentum equation leads to constant pressure in the flow ($p = $ constant). The equation of state

$$p = \frac{\rho T}{\gamma \mathrm{Ma}^2} \tag{A.2.7}$$

can be evaluated at the top wall where the density is its reference value $\rho(y = h) = \rho_w$ and the wall temperature is fixed and in general, different from the lower wall temperature ($T_1^\star$ is taken as the reference)

$$T(y = 0) = T_0$$
$$\tag{A.2.8}$$
$$T(y = h) = T_1.$$

This leads to

$$p = \frac{\rho_w T_w}{\gamma \mathrm{Ma}^2}. \tag{A.2.9}$$

The energy equation simplifies to

$$0 = \frac{\mathrm{d}}{\mathrm{d}y}\left(u\frac{\mathrm{d}u}{\mathrm{d}y}\right) + \frac{1}{\mathrm{PrMa}^2(\gamma - 1)}\frac{\mathrm{d}}{\mathrm{d}y}\left(\frac{\mathrm{d}T}{\mathrm{d}y}\right). \tag{A.2.10}$$

Substituting the velocity profile (whose second derivative is equal to one) and applying the boundary conditions (A.2.8) leads to

$$\begin{aligned} T(y) &= -\frac{\mathrm{PrMa}^2(\gamma - 1)}{2}y^2 + \left(1 - T_0 + \frac{\mathrm{Pr}_1\mathrm{Ma}_1^2(\gamma - 1)}{2}\right)y + T_0 \\ &= \frac{\mathrm{PrMa}^2(\gamma - 1)}{2}(y - y^2) + (1 - T_0)y + T_0. \end{aligned} \tag{A.2.11}$$

and temperature profile

$$T(y) = 2u_w^2\mathrm{PrMa}^2(\gamma - 1)y(1 - y) + (T_1 - T_0)y + T_0. \tag{A.2.12}$$

Appendix B

Turbulence kinetic energy equation

B.1 Mean flow equations

The first step is to establish the mean flow equations of mass, momentum, specific total energy and specific internal energy, using the Favre decomposition defined in section C.

B.1.1 Mean continuity equation

Instantaneous continuity can be written in material derivative form

$$\frac{D\rho}{Dt} + \rho \frac{\partial u_j}{\partial x_j} = 0 \tag{B.1.1}$$

where

$$\frac{D}{Dt} = \frac{\partial}{\partial t} + u_j \frac{\partial}{\partial x_j}. \tag{B.1.2}$$

(B.1.1) can be written in conservative form

$$
\begin{aligned}
\frac{\partial \rho}{\partial t} + u_j \frac{\partial \rho}{\partial x_j} + \rho \frac{\partial u_j}{\partial x_j} &= 0 \\
\frac{\partial \rho}{\partial t} + \frac{\partial \rho u_j}{\partial x_j} &= 0.
\end{aligned}
\tag{B.1.3}
$$

Applying the above decompositions to the continuity equation and time averaging gives the mean continuity equation with density weighted convective terms.

$$\frac{\partial \rho}{\partial t} \quad + \quad \frac{\partial(\rho u_j)}{\partial x_j} \qquad\qquad\qquad = \quad 0$$

$$\frac{\partial}{\partial t}(\overline{\rho} + \rho') \quad + \quad \frac{\partial}{\partial x_j}\left(\overline{(\overline{\rho} + \rho')(\widetilde{u}_j + u_j'')}\right) \qquad = \quad 0$$

$$\frac{\partial}{\partial t}(\overline{\rho} + \rho') \quad + \quad \frac{\partial}{\partial x_j}\left(\overline{\rho}\,\widetilde{u}_j + \overline{\rho}\,\overline{u_j''} + \overline{\rho'\widetilde{u}_j}^{\,0} + \overline{\rho'u_j''}\right) \quad = \quad 0 \qquad\text{(B.1.4)}$$

$$\frac{\partial}{\partial t}(\overline{\rho} + \rho') \quad + \quad \frac{\partial}{\partial x_j}\left(\overline{\rho}\,\widetilde{u}_j - \overline{\rho}\,\frac{\overline{\rho'u_j'}}{\overline{\rho}} + \overline{\rho'u_j'}\right) \qquad = \quad 0$$

$$\frac{\partial \overline{\rho}}{\partial t} \quad + \quad \frac{\partial}{\partial x_j}(\overline{\rho}\,\widetilde{u}_j) \qquad\qquad\qquad = \quad 0.$$

It can be seen that whenever there is the product of density and one or more variable to be Favre decomposed, i.e. ρf or $\rho f g$, it is not necessary to expand the density into mean and fluctuating component as the resulting terms cancel (using P.1 and P.3).

B.1.2   Mean momentum equation

The mean momentum equation can be written by time averaging the instantaneous equation using Favre decomposition for the unsteady and convective terms and Reynolds decomposition for the pressure and viscous terms (although the velocity in the strain rate tensor are Favre decomposed)

$$\frac{\partial(\rho u_i)}{\partial t} \quad + \quad \frac{\partial}{\partial x_j}(\rho u_i u_j) \qquad\qquad = \quad -\frac{\partial p}{\partial x_i} + \frac{1}{\mathrm{Re}}\frac{\partial \Sigma_{ij}}{\partial x_j}$$

$$\frac{\partial}{\partial t}(\overline{\rho(\widetilde{u}_i + u_i'')}) \quad + \quad \frac{\partial}{\partial x_j}(\overline{\rho(\widetilde{u}_i + u_i'')(\widetilde{u}_j + u_j'')}) \quad = \quad -\frac{\partial}{\partial x_i}(\overline{p} + p') + \frac{1}{\mathrm{Re}}\frac{\partial}{\partial x_j}(\overline{\Sigma}_{ij} + \Sigma_{ij}')$$

$$\frac{\partial(\overline{\rho}\,\widetilde{u}_i)}{\partial t} \quad + \quad \frac{\partial}{\partial x_j}(\overline{\rho(\widetilde{u}_i\widetilde{u}_j + \widetilde{u}_i u_j'' + u_i''\widetilde{u}_j + u_i''u_j'')}) \quad = \quad -\frac{\partial \overline{p}}{\partial x_i} + \frac{1}{\mathrm{Re}}\frac{\partial \overline{\Sigma}_{ij}}{\partial x_j}$$

$$\frac{\partial(\overline{\rho}\,\widetilde{u}_i)}{\partial t} \quad + \quad \frac{\partial}{\partial x_j}(\overline{\rho}\,\widetilde{u}_i\widetilde{u}_j + \overline{\rho\,u_i''u_j''}) \qquad = \quad -\frac{\partial \overline{p}}{\partial x_i} + \frac{1}{\mathrm{Re}}\frac{\partial \overline{\Sigma}_{ij}}{\partial x_j}$$

$$\frac{\partial}{\partial t}(\overline{\rho}\,\widetilde{u}_i) \quad + \quad \frac{\partial}{\partial x_j}(\overline{\rho}\,\widetilde{u}_i\widetilde{u}_j) \qquad\qquad = \quad -\frac{\partial \overline{p}}{\partial x_i} + \frac{1}{\mathrm{Re}}\frac{\partial \overline{\Sigma}_{ij}}{\partial x_j} - \frac{\partial \overline{R}_{ij}}{\partial x_j}.$$

$$\text{(B.1.5)}$$

where

$$\overline{R}_{ij} \equiv \overline{\rho\,u_i''u_j''} = \overline{\rho u_i u_j} - \overline{\rho}\,\widetilde{u}_i\widetilde{u}_j. \qquad\qquad\text{(B.1.6)}$$

The viscous stress tensor Σ_{ij} can be decomposed into a mean and fluctuating term, applying a Favre decomposition to the velocity terms

$$
\begin{aligned}
\Sigma_{ij} = \overline{\Sigma}_{ij} + \Sigma'_{ij} \quad = \quad & (\overline{\mu} + \mu') \left[\left(\frac{\partial \widetilde{u}_i}{\partial x_j} + \frac{\partial \widetilde{u}_j}{\partial x_i} \right) + \left(\frac{\partial u''_i}{\partial x_j} + \frac{\partial u''_j}{\partial x_i} \right) - \frac{2}{3} \widetilde{\Theta} \delta_{ij} - \frac{2}{3} \Theta'' \delta_{ij} \right] \\
+ \quad & (\overline{\mu}_b + \mu'_b) \left(\widetilde{\Theta} + \Theta'' \right) \delta_{ij}
\end{aligned}
\tag{B.1.7}
$$

where $\Theta = \partial u_k / \partial x_k$ is the instantaneous dilatation, and is decomposed into mean and fluctuating parts

$$
\Theta = \widetilde{\Theta} + \Theta'' = \frac{\partial \widetilde{u}_k}{\partial x_k} + \frac{\partial u''_k}{\partial x_k}
\tag{B.1.8}
$$

The time averaged stress tensor $\overline{\Sigma}_{ij}$ is found by taking the time average of (B.1.7), noting that the fluctuating viscous stress tensor is centred about zero, i.e. $\overline{\Sigma'_{ij}} = 0$

$$
\begin{aligned}
\overline{\Sigma}_{ij} \quad = \quad & \overline{\mu} \left[\left(\frac{\partial \widetilde{u}_i}{\partial x_j} + \frac{\partial \widetilde{u}_j}{\partial x_i} \right) + \left(\frac{\partial \overline{u''}_i}{\partial x_j} + \frac{\partial \overline{u''}_j}{\partial x_i} \right) - \frac{2}{3} \widetilde{\Theta} \delta_{ij} - \frac{2}{3} \overline{\Theta''} \delta_{ij} \right] \\
+ \quad & \overline{\mu' \left[\left(\frac{\partial u''_i}{\partial x_j} + \frac{\partial u''_j}{\partial x_i} \right) - \frac{2}{3} \Theta'' \delta_{ij} \right]} \\
+ \quad & \overline{\mu}_b \left(\widetilde{\Theta} + \overline{\Theta''} \right) \delta_{ij} + \overline{\mu'_b \Theta''} \delta_{ij}.
\end{aligned}
\tag{B.1.9}
$$

The fluctuating stress tensor Σ'_{ij} is the difference between (B.1.7) and (B.1.9)

$$\Sigma'_{ij} = \Sigma_{ij} - \overline{\Sigma}_{ij} \quad = \quad \overline{\mu} \left[\left(\frac{\partial u''_i}{\partial x_j} + \frac{\partial u''_j}{\partial x_i} \right) - \left(\frac{\partial \overline{u''_i}}{\partial x_j} + \frac{\partial \overline{u''_j}}{\partial x_i} \right) - \frac{2}{3} \Theta'' \delta_{ij} + \frac{2}{3} \overline{\Theta''} \delta_{ij} \right]$$

$$+ \quad \mu' \left[\left(\frac{\partial \widetilde{u}_i}{\partial x_j} + \frac{\partial \widetilde{u}_j}{\partial x_i} \right) + \left(\frac{\partial u''_i}{\partial x_j} + \frac{\partial u''_j}{\partial x_i} \right) - \frac{2}{3} \widetilde{\Theta} \delta_{ij} - \frac{2}{3} \Theta'' \delta_{ij} \right] \tag{B.1.10}$$

$$- \quad \overline{\mu' \left[\left(\frac{\partial u''_i}{\partial x_j} + \frac{\partial u''_j}{\partial x_i} \right) - \frac{2}{3} \Theta'' \delta_{ij} \right]}$$

$$+ \quad \overline{\mu}_b \left(\Theta'' - \overline{\Theta''} \right) \delta_{ij} + \mu'_b \left(\widetilde{\Theta} + \Theta'' \right) \delta_{ij} - \overline{\mu'_b \Theta''} \delta_{ij}$$

B.1.3   Mean total energy

The governing equation for the mean total energy is derived from the instantaneous equation

$$\rho \frac{D e_t}{D t} = -\frac{\partial (p u_j)}{\partial x_j} + \frac{1}{\mathrm{Re}} \frac{\partial (u_i \Sigma_{ij})}{\partial x_j} - \frac{1}{\mathrm{Pr Re Ma}^2 (\gamma - 1)} \frac{\partial q_j}{\partial x_j}, \tag{B.1.11}$$

and follows a similar logic to the mean momentum equation. It is first convenient to collect the pressure term with the total energy, resulting in a convection of total enthalpy ρH:

$$\frac{\partial (\rho e_t)}{\partial t} \quad + \quad \frac{\partial}{\partial x_j} (\rho u_j e_t) \quad = \quad -\frac{\partial (p u_j)}{\partial x_j} \quad + \quad \frac{1}{\mathrm{Re}} \frac{\partial (u_i \Sigma_{ij})}{\partial x_j} \quad - \quad \frac{1}{\mathrm{Pr Re Ma}^2 (\gamma - 1)} \frac{\partial q_j}{\partial x_j},$$

$$\frac{\partial (\rho e_t)}{\partial t} \quad + \quad \frac{\partial}{\partial x_j} (\rho u_j H) \quad = \qquad\qquad \frac{1}{\mathrm{Re}} \frac{\partial}{\partial x_j} (u_i \Sigma_{ij}) \quad - \quad \frac{1}{\mathrm{Pr Re Ma}^2 (\gamma - 1)} \frac{\partial q_j}{\partial x_j},$$
$$\tag{B.1.12}$$

where

$$H = e_t + \frac{p}{\rho}$$

$$q_j = -\kappa \frac{\partial T}{\partial x_j}$$

(B.1.13)

are the specific total enthalpy and heat flux, respectively. Applying the Favre averaging to the unsteady and convective terms and the Reynolds averaging to the remaining terms results in

$$\frac{\partial}{\partial t}\overline{(\rho(\widetilde{e}_t + e_t''))} + \frac{\partial}{\partial x_j}\overline{(\rho(\widetilde{u}_j + u_j'')(\widetilde{H} + H''))} = \frac{1}{\mathrm{Re}}\frac{\partial}{\partial x_j}\overline{((\widetilde{u}_i + u_i'')(\overline{\Sigma}_{ij} + \Sigma_{ij}'))}$$

$$- \frac{1}{\mathrm{PrReMa}^2(\gamma-1)}\frac{\partial}{\partial x_j}\overline{(\overline{q}_j + q_j')},$$

$$\frac{\partial}{\partial t}(\overline{\rho}\widetilde{e}_t + \overline{\rho e_t''}) + \frac{\partial}{\partial x_j}(\overline{\rho\widetilde{u}_j\widetilde{H}} + \overline{\rho\widetilde{u}_j H''} + \overline{\rho u_j''\widetilde{H}} + \overline{\rho u_j'' H''}) = \frac{1}{\mathrm{Re}}\frac{\partial}{\partial x_j}(\overline{\widetilde{u}_i\overline{\Sigma}_{ij}} + \overline{\widetilde{u}_i\Sigma_{ij}'} + \overline{u_i''\overline{\Sigma}_{ij}} + \overline{u_i''\Sigma_{ij}'})$$

$$- \frac{1}{\mathrm{PrReMa}^2(\gamma-1)}\frac{\partial\overline{q}_j}{\partial x_j},$$

$$\frac{\partial(\overline{\rho}\widetilde{e}_t)}{\partial t} + \frac{\partial}{\partial x_j}(\overline{\rho}\widetilde{u}_j\widetilde{H}) = \frac{1}{\mathrm{Re}}\frac{\partial}{\partial x_j}(\widetilde{u}_i\overline{\Sigma}_{ij} + \overline{u_i''\Sigma_{ij}'} + \overline{u_i''}\,\Sigma_{ij}')$$

$$- \frac{1}{\mathrm{PrReMa}^2(\gamma-1)}\frac{\partial\overline{q}_j}{\partial x_j} - \frac{\partial}{\partial x_j}(\widetilde{\overline{\rho}u_j''H''}).$$

(B.1.14)

Both the mean total enthalpy can be written in terms of their definitions including Favre-averaging the energy and velocity terms. The definition of the mean total energy relates the mean internal energy, mean kinetic energy and turbulent kinetic energy

$$\overline{\rho H} = \overline{\rho\left(e_t + \frac{p}{\rho}\right)} = \overline{\rho\left(\widetilde{e}_t + e_t'' + \frac{\overline{p}+p'}{\rho}\right)} = \overline{\rho}\left(\widetilde{e}_t + \frac{\overline{p}}{\overline{\rho}}\right)$$

(B.1.15)

$$\overline{\rho}\widetilde{e}_t = \overline{\rho e_t} = \overline{\rho e} + \overline{\rho\frac{u_i u_i}{2}} = \overline{\rho(\widetilde{e} + e'')} + \overline{\rho\frac{(\widetilde{u}_i + u_i'')(\widetilde{u}_i + u_i'')}{2}} = \overline{\rho}\widetilde{e} + \overline{\rho}\underbrace{\frac{\widetilde{u}_i\widetilde{u}_i}{2}}_{K} + \overline{\rho}\underbrace{\frac{\widetilde{u_i'' u_i''}}{2}}_{k}$$

B.1.4   Mean internal energy

The internal energy equation can be found by subtracting the instantaneous kinetic energy $(u_i u_i)/2$ from the total energy equation (B.1.11). It is useful to write the left hand side of the momentum equation in material derivative form:

$$\frac{\partial(\rho u_i)}{\partial t} + \frac{\partial}{\partial x_j}(\rho u_i u_j) \;=\; -\frac{\partial p}{\partial x_i} + \frac{1}{\mathrm{Re}}\frac{\partial \Sigma_{ij}}{\partial x_j}$$

$$\rho\frac{\partial u_i}{\partial t} + \rho u_j\frac{\partial u_i}{\partial x_j} + u_i\underbrace{\left[\frac{\partial\rho}{\partial t} + \frac{\partial(\rho u_j)}{\partial x_j}\right]}_{=\,0\ \text{from continuity}} \;=\; \tag{B.1.16}$$

$$\rho\frac{D u_i}{D t} \;=\;$$

Multiplying the momentum equation for u_i by u_i:

$$\rho u_i\frac{D u_i}{D t} \;=\; -u_i\frac{\partial p}{\partial x_i} + \frac{1}{\mathrm{Re}}u_i\frac{\partial \Sigma_{ij}}{\partial x_j}$$
$$\tag{B.1.17}$$

$$\rho\frac{\partial}{\partial t}\left(\frac{1}{2}u_i u_i\right) + \rho u_j\frac{\partial}{\partial x_j}\left(\frac{1}{2}u_i u_i\right) \;=\; -\frac{\partial(p u_i)}{\partial x_i} + p\frac{\partial u_i}{\partial x_i} + \frac{1}{\mathrm{Re}}\frac{\partial u_i\Sigma_{ij}}{\partial x_j} - \frac{1}{\mathrm{Re}}\Sigma_{ij}\frac{\partial u_i}{\partial x_j}$$

and rearranging gives the governing equation for the instantaneous kinetic energy

$$\rho\frac{D}{D t}\left(\frac{1}{2}u_i u_i\right) \;=\; -\frac{\partial(p u_i)}{\partial x_i} + p\frac{\partial u_i}{\partial x_i} + \frac{1}{\mathrm{Re}}\frac{\partial u_i\Sigma_{ij}}{\partial x_j} - \frac{1}{\mathrm{Re}}\Sigma_{ij}\frac{\partial u_i}{\partial x_j}. \tag{B.1.18}$$

The specific total energy equation can be written in terms of internal energy e and kinetic energy

$$\frac{\partial(\rho e_t)}{\partial t} + \frac{\partial}{\partial x_j}(\rho u_j e_t) = -\frac{\partial(p u_j)}{\partial x_j} + \frac{1}{\text{Re}}\frac{\partial(u_i \Sigma_{ij})}{\partial x_j} - \frac{1}{\text{PrReMa}^2(\gamma-1)}\frac{\partial q_j}{\partial x_j}$$

$$\rho\frac{D}{Dt}\left(e + \frac{1}{2}u_i u_i\right) = -\frac{\partial(p u_j)}{\partial x_j} + \frac{1}{\text{Re}}\frac{\partial(u_i \Sigma_{ij})}{\partial x_j} - \frac{1}{\text{PrReMa}^2(\gamma-1)}\frac{\partial q_j}{\partial x_j}.$$

$$(\text{B.1.19})$$

Subtracting (B.1.18) from (B.1.19) gives the instantaneous specific internal energy equation

$$\rho\frac{De}{Dt} = -p\frac{\partial u_j}{\partial x_j} + \frac{1}{\text{Re}}\Sigma_{ij}\frac{\partial u_i}{\partial x_j} - \frac{1}{\text{PrReMa}^2(\gamma-1)}\frac{\partial q_j}{\partial x_j}. \tag{B.1.20}$$

As for the total energy, the internal energy uses Favre decomposition. Applying this and time averaging gives

$$\frac{\partial}{\partial t}(\overline{\rho(\widetilde{e}+e'')}) + \frac{\partial}{\partial x_j}(\overline{\rho(\widetilde{u}_j+u''_j)(\widetilde{e}+e'')}) = -\overline{(\overline{p}+p')\frac{\partial(\widetilde{u}_j+u''_j)}{\partial x_j}} + \frac{1}{\text{Re}}\overline{\overline{\Sigma}_{ij}+\Sigma'_{ij}\frac{\partial(\widetilde{u}_i+u''_i)}{\partial x_j}}$$

$$- \frac{1}{\text{PrReMa}^2(\gamma-1)}\frac{\partial\overline{(\overline{q}_j+q')}}{\partial x_j}. \tag{B.1.21}$$

Cancelling and combining the stress tensor and pressure into their instantaneous form gives the mean internal energy equations with the right-hand-side terms as given in Chassaing *et al.* (2002, p.130).

$$\rho\frac{\widetilde{D}\widetilde{e}}{\widetilde{Dt}} = -\overline{p}\frac{\partial\widetilde{u}_j}{\partial x_j} \underbrace{-\overline{p\frac{\partial u''_j}{\partial x_j}}}_{\mathcal{A}} + \frac{1}{\text{Re}}\overline{\Sigma}_{ij}\frac{\partial\widetilde{u}_i}{\partial x_j} + \frac{1}{\text{Re}}\overline{\Sigma_{ij}\frac{\partial u''_i}{\partial x_j}} - \frac{1}{\text{PrReMa}^2(\gamma-1)}\frac{\partial\overline{q}_j}{\partial x_j} \underbrace{-\frac{\partial\overline{\rho}\,\widetilde{e''u''_j}}{\partial x_j}}_{\mathcal{B}} \tag{B.1.22}$$

where

$$\frac{\widetilde{D}}{\widetilde{Dt}} = \frac{\partial}{\partial t} + \widetilde{u}_j\frac{\partial}{\partial x_j} \tag{B.1.23}$$

To compare with Lele (1994) the turbulent diffusion ($\mathcal{B}$) is written in terms of fluctuating enthalpy. To do so, the relationship between enthalpy and internal energy is averaged, applying the identities for Favre averaging:

$$\rho h u_j = \rho e u_j + p u_j$$

$$(\text{B.1.24})$$

$$\overline{\rho}\,\widetilde{h}\widetilde{u}_j + \overline{\rho h''u''_j} = \overline{\rho}\,\widetilde{e}\widetilde{u}_j + \overline{\rho e''u''_j} + \overline{p}\widetilde{u}_j + \overline{p}u''_j + \overline{p'u''_j}$$

In the absence of turbulent flow, the terms that remain for the laminar flow solution are

$$\overline{\rho}\,\widetilde{h}\widetilde{u}_j \;=\; \overline{\rho}\,\widetilde{e}\widetilde{u}_j + \overline{p}\widetilde{u}_j. \tag{B.1.25}$$

Subtracting this from the averaged equation gives an identity relating the enthalpy to the internal energy in the turbulent contribution.

$$\overline{\rho h'' u_j''} \;=\; \overline{\rho e'' u_j''} + \overline{p} u_j'' + \overline{p' u_j''}. \tag{B.1.26}$$

Using this identity, $\mathcal{B}$ can be rewritten

$$-\frac{\partial(\overline{\rho}\,\widetilde{e'' u_j''})}{\partial x_j} = -\frac{\partial(\overline{\rho}\,\widetilde{h'' u_j''})}{\partial x_j} + \frac{\partial \overline{p' u_j''}}{\partial x_j} + \overline{p}\frac{\partial \overline{u_j''}}{\partial x_j} + \overline{u_j''}\frac{\partial \overline{p}}{\partial x_j}. \tag{B.1.27}$$

The pressure fluctuation-dilatation correlation ($\mathcal{B}$) is expanded in order to cancel repeating terms in $\mathcal{A}$

$$-\overline{p\frac{\partial u_j''}{\partial x_j}} = -\overline{p}\frac{\partial \overline{u_j''}}{\partial x_j} - \overline{p'\frac{\partial u_j''}{\partial x_j}}. \tag{B.1.28}$$

Summing $\mathcal{A}$ and $\mathcal{B}$ and cancelling terms leaves

$$\mathcal{A} + \mathcal{B} = \frac{\partial \overline{p' u_j''}}{\partial x_j} + \overline{u_j''}\frac{\partial \overline{p}}{\partial x_j} - \overline{p'\frac{\partial u_j''}{\partial x_j}}. \tag{B.1.29}$$

Substituting this result into the mean internal energy equation (B.1.22) leaves

$$\rho\frac{\widetilde{D}\widetilde{e}}{\widetilde{Dt}} = -\frac{\partial \overline{\rho}\,\widetilde{h'' u_j''}}{\partial x_j} + \frac{\partial \overline{p' u_j''}}{\partial x_j} + \overline{u_j''}\frac{\partial \overline{p}}{\partial x_j} - \overline{p'\frac{\partial u_j''}{\partial x_j}} - \overline{p}\frac{\partial \widetilde{u}_j}{\partial x_j}$$
$$+ \frac{1}{\mathrm{Re}}\overline{\Sigma}_{ij}\frac{\partial \widetilde{u}_i}{\partial x_j} + \underbrace{\frac{1}{\mathrm{Re}}\overline{\Sigma_{ij}\frac{\partial u_i''}{\partial x_j}}}_{\mathcal{C}} - \frac{1}{\mathrm{PrReMa}^2(\gamma-1)}\frac{\partial \overline{q}_j}{\partial x_j}. \tag{B.1.30}$$

The last term to expand is the "viscous heat production due to mechanical dissipation in the fluctuating motion" (Chassaing *et al.*, 2002) ($\mathcal{C}$)

$$\frac{1}{\mathrm{Re}}\overline{\Sigma_{ij}\frac{\partial u_i''}{\partial x_j}} = \frac{1}{\mathrm{Re}}\left(\overline{\Sigma}_{ij}\overline{\frac{\partial u_i''}{\partial x_j}} + \overline{\Sigma_{ij}'\frac{\partial u_i''}{\partial x_j}}\right)$$
$$= \frac{1}{\mathrm{Re}}\left(\frac{\partial}{\partial x_j}\left(\overline{\Sigma}_{ij}\overline{u_i''}\right) - \overline{u_j''}\frac{\partial \overline{\Sigma}_{ij}}{\partial x_j} - \frac{1}{\mathrm{Re}}\overline{\Sigma_{ij}'\frac{\partial u_i''}{\partial x_j}}\right). \tag{B.1.31}$$

Substituting $\mathcal{C}$ into (B.1.30) and writing the equation in conservative form gives the mean internal energy in the same form as Lele (1994).

$$\frac{\partial(\overline{\rho}\,\widetilde{e})}{\partial t} = -\frac{\partial(\overline{\rho}\,\widetilde{e}\,\widetilde{u}_j)}{\partial x_j} - \frac{\partial(\overline{\rho\,\widetilde{h''u''_j}})}{\partial x_j} + \frac{\partial(\overline{p'u''_j})}{\partial x_j} + \overline{u''_j}\frac{\partial\overline{p}}{\partial x_j} - \overline{p'\frac{\partial u''_j}{\partial x_j}} - \overline{p}\frac{\partial\widetilde{u}_j}{\partial x_j}$$

$$+ \frac{1}{\mathrm{Re}}\overline{\Sigma}_{ij}\frac{\partial\widetilde{u}_i}{\partial x_j} + \frac{1}{\mathrm{Re}}\left(\frac{\partial}{\partial x_j}\left(\overline{\Sigma_{ij}u''_i}\right) - \overline{u''_j\frac{\partial\overline{\Sigma}_{ij}}{\partial x_j}} + \overline{\Sigma'_{ij}\frac{\partial u''_i}{\partial x_j}}\right) + \frac{1}{\mathrm{PrReMa}^2(\gamma-1)}\frac{\partial\overline{q}_j}{\partial x_j}. \quad \text{(B.1.32)}$$

B.1.5 Mean kinetic energy equations

The mean kinetic energy can be formed by taking the scalar product of the mean momentum equation and the Favre averaged velocity $\widetilde{u}_i$. First, note that

$$\overline{\rho}\,\widetilde{u}_i\frac{\widetilde{D}\widetilde{u}_i}{\widetilde{D}t} = \overline{\rho}\left[\widetilde{u}_i\frac{\partial\widetilde{u}_i}{\partial t} + \widetilde{u}_k\widetilde{u}_i\frac{\partial\widetilde{u}_i}{\partial x_k}\right]$$

$$= \overline{\rho}\left[\frac{\partial}{\partial t}\left(\frac{1}{2}\widetilde{u}_i\widetilde{u}_i\right) + \widetilde{u}_k\frac{\partial}{\partial x_k}\left(\frac{1}{2}\widetilde{u}_i\widetilde{u}_i\right)\right]$$

$$= \overline{\rho}\frac{\widetilde{D}}{\widetilde{D}t}\left(\frac{1}{2}\widetilde{u}_i\widetilde{u}_i\right) \qquad\qquad\qquad\text{(B.1.33)}$$

$$= \overline{\rho}\left[\frac{\partial}{\partial t}\left(\frac{1}{2}\widetilde{u}_i\widetilde{u}_i\right) + \frac{\partial}{\partial x_k}\left[\left(\frac{1}{2}\widetilde{u}_i\widetilde{u}_i\right)\widetilde{u}_k\right] - \frac{1}{2}\widetilde{u}_i\widetilde{u}_i\underbrace{\frac{\partial\widetilde{u}_k}{\partial x_k}}_{0}\right]$$

$$= \frac{\partial}{\partial t}\left[\left(\overline{\rho}\frac{1}{2}\widetilde{u}_i\widetilde{u}_i\right)\right] + \frac{\partial}{\partial x_k}\left[\overline{\rho}\left(\frac{1}{2}\widetilde{u}_i\widetilde{u}_i\right)\widetilde{u}_k\right] - \frac{1}{2}\widetilde{u}_i\widetilde{u}_i\underbrace{\left(\frac{\partial\overline{\rho}}{\partial t} + \frac{\partial(\overline{\rho}\,\widetilde{u}_k)}{\partial x_k}\right)}_{=\,0\text{ from continuity}}$$

and so

$$\overline{\rho}\frac{\widetilde{D}}{\widetilde{D}t}\left(\frac{1}{2}\widetilde{u}_i\widetilde{u}_i\right) = \frac{\partial}{\partial t}\left[\left(\overline{\rho}\frac{1}{2}\widetilde{u}_i\widetilde{u}_i\right)\right] + \frac{\partial}{\partial x_k}\left[\overline{\rho}\left(\frac{1}{2}\widetilde{u}_i\widetilde{u}_i\right)\widetilde{u}_k\right]. \qquad\text{(B.1.34)}$$

Now applying the mean material derivative to the momentum equation:

$$\frac{\partial}{\partial t}(\overline{\rho}\widetilde{u}_i) + \frac{\partial}{\partial x_j}(\overline{\rho}\widetilde{u}_i\widetilde{u}_j) = -\frac{\partial \overline{p}}{\partial x_i} + \frac{1}{\text{Re}}\frac{\partial \overline{\Sigma}_{ij}}{\partial x_j} - \frac{\partial \overline{R}_{ij}}{\partial x_j}$$

$$\overline{\rho}\frac{\widetilde{D}\widetilde{u}_i}{\widetilde{D}t} = -\frac{\partial \overline{p}}{\partial x_i} + \frac{1}{\text{Re}}\frac{\partial \overline{\Sigma}_{ij}}{\partial x_j} - \frac{\partial \overline{R}_{ij}}{\partial x_j} \tag{B.1.35}$$

Multiplying by $\widetilde{u}_i$ and rearranging:

$$\overline{\rho}\frac{\widetilde{D}\widetilde{u}_i}{\widetilde{D}t} = -\frac{\partial \overline{p}}{\partial x_i} + \frac{1}{\text{Re}}\frac{\partial \overline{\Sigma}_{ij}}{\partial x_j} - \frac{\partial \overline{R}_{ij}}{\partial x_j}$$

$$\widetilde{u}_i\overline{\rho}\frac{\widetilde{D}\widetilde{u}_i}{\widetilde{D}t} = -\widetilde{u}_i\frac{\partial \overline{p}}{\partial x_i} + \frac{1}{\text{Re}}\widetilde{u}_i\frac{\partial \overline{\Sigma}_{ij}}{\partial x_j} - \widetilde{u}_i\frac{\partial \overline{R}_{ij}}{\partial x_j}$$

$$\overline{\rho}\frac{\widetilde{D}}{\widetilde{D}t}\left(\frac{1}{2}\widetilde{u}_i\widetilde{u}_i\right) = -\widetilde{u}_i\frac{\partial \overline{p}}{\partial x_i} + \frac{1}{\text{Re}}\widetilde{u}_i\frac{\partial \overline{\Sigma}_{ij}}{\partial x_j} - \widetilde{u}_i\frac{\partial \overline{R}_{ij}}{\partial x_j}$$

$$\frac{\partial}{\partial t}\left(\frac{1}{2}\overline{\rho}\widetilde{u}_i\widetilde{u}_i\right) + \frac{\partial}{\partial x_j}\left(\left[\frac{1}{2}\overline{\rho}\widetilde{u}_i\widetilde{u}_i\right]\widetilde{u}_j\right) = -\frac{\partial(\overline{p}\widetilde{u}_i)}{\partial x_i} + \overline{p}\frac{\partial \widetilde{u}_i}{\partial x_i} + \frac{1}{\text{Re}}\left[\frac{\partial(\widetilde{u}_i\overline{\Sigma}_{ij})}{\partial x_j} - \overline{\Sigma}_{ij}\frac{\partial \widetilde{u}_i}{\partial x_j}\right]$$

$$-\frac{\partial \widetilde{u}_i\overline{R}_{ij}}{\partial x_j} + \overline{R}_{ij}\frac{\partial \widetilde{u}_i}{\partial x_j}$$

$$\tag{B.1.36}$$

Finally, defining the mean kinetic energy as $K = 1/2\,\widetilde{u}_i\widetilde{u}_i$, the governing equation can be written in non-conservative form (using mean continuity) in the same form as Chassaing *et al.* (2002) and has the same grouping of terms on the right-hand-side as Lele (1994).

$$\overline{\rho}\frac{\widetilde{D}K}{\widetilde{D}t} = -\frac{\partial(\overline{p}\widetilde{u}_i)}{\partial x_i} + \overline{p}\frac{\partial \widetilde{u}_i}{\partial x_i} + \frac{1}{\text{Re}}\left[\frac{\partial(\widetilde{u}_i\overline{\Sigma}_{ij})}{\partial x_j} - \overline{\Sigma}_{ij}\frac{\partial \widetilde{u}_i}{\partial x_j}\right] - \frac{\partial \widetilde{u}_i\overline{R}_{ij}}{\partial x_j} + \overline{R}_{ij}\frac{\partial \widetilde{u}_i}{\partial x_j} \tag{B.1.37}$$

B.2 Fluctuating equations

The fluctuating flow equations can be derived by subtracting the mean flow equations from the instantaneous equations.

B.2.1 Fluctuating continuity

The instantaneous continuity equation can be written

$$
\begin{aligned}
\frac{\partial \rho}{\partial t} \quad + \quad \frac{\partial}{\partial x_j}(\rho \widetilde{u}_j + \rho u_j'') \quad &= \quad 0, \\
\frac{\partial \rho}{\partial t} \quad + \quad \rho \frac{\partial \widetilde{u}_j}{\partial x_j} + \widetilde{u}_j \frac{\partial \rho}{\partial x_j} \quad &= \quad -\frac{\partial}{\partial x_j}(\rho u_j''),
\end{aligned}
\tag{B.2.1}
$$

and the mean continuity equation (B.1.4) can be written

$$
\frac{\partial \overline{\rho}}{\partial t} \quad + \quad \overline{\rho} \frac{\partial \widetilde{u}_j}{\partial x_j} + \widetilde{u}_j \frac{\partial \overline{\rho}}{\partial x_j} \quad = \quad 0.
\tag{B.2.2}
$$

Subtracting (B.2.2) from (B.2.1) gives the fluctuating continuity equation.

$$
\frac{\partial \rho'}{\partial t} + \widetilde{u}_j \frac{\partial \rho'}{\partial x_j} + \rho' \frac{\partial \widetilde{u}_j}{\partial x_j} = -\frac{\partial}{\partial x_j}(\rho u_j'').
\tag{B.2.3}
$$

B.2.2 Fluctuating momentum equation

The instantaneous momentum equation is

$$
\frac{\partial (\rho u_i)}{\partial t} + \frac{\partial}{\partial x_j}(\rho u_i u_j) = -\frac{\partial p}{\partial x_i} + \frac{1}{\mathrm{Re}} \frac{\partial \Sigma_{ij}}{\partial x_j}
\tag{B.2.4}
$$

which can be expanded to

$$
\rho \frac{\partial u_i}{\partial t} + \underbrace{u_i \frac{\partial \rho}{\partial t} + u_i \frac{\partial (\rho u_j)}{\partial x_j}}_{= \,0 \text{ from instantaneous continuity (B.1.4)}} + \rho u_j \frac{\partial u_i}{\partial x_j} = -\frac{\partial p}{\partial x_i} + \frac{1}{\mathrm{Re}} \frac{\partial \Sigma_{ij}}{\partial x_j}.
\tag{B.2.5}
$$

Applying a Favre decomposition gives

$$
\rho \frac{\partial \widetilde{u}_i}{\partial t} + \rho \frac{\partial u_i''}{\partial t} + \rho \widetilde{u}_j \frac{\partial \widetilde{u}_i}{\partial x_j} + \rho u_j'' \frac{\partial \widetilde{u}_i}{\partial x_j} + \rho \widetilde{u}_j \frac{\partial u_i''}{\partial x_j} + \rho u_j'' \frac{\partial u_i''}{\partial x_j} = -\frac{\partial (\overline{p} + p')}{\partial x_i} + \frac{1}{\mathrm{Re}} \frac{\partial (\overline{\Sigma}_{ij} + \Sigma_{ij}')}{\partial x_j}.
\tag{B.2.6}
$$

The mean momentum equation was derived earlier (B.1.5) and can be expanded to

$$\bar{\rho}\frac{\partial \widetilde{u}_i}{\partial t} + \underbrace{\widetilde{u}_i\frac{\partial \bar{\rho}}{\partial t} + \widetilde{u}_i\frac{\partial}{\partial x_j}(\bar{\rho}\,\widetilde{u}_j)}_{=\,0\text{ from mean continuity (B.1.4)}} + \bar{\rho}\,\widetilde{u}_j\frac{\partial \widetilde{u}_i}{\partial x_j} = -\frac{\partial \bar{p}}{\partial x_i} + \frac{1}{\mathrm{Re}}\frac{\partial \overline{\Sigma}_{ij}}{\partial x_j} - \frac{\partial \overline{R}_{ij}}{\partial x_j} \qquad (\text{B.2.7})$$

and multiplied by $\rho/\bar{\rho}$

$$\rho\frac{\partial \widetilde{u}_i}{\partial t} + \rho\widetilde{u}_j\frac{\partial \widetilde{u}_i}{\partial x_j} = \frac{\rho}{\bar{\rho}}\left[-\frac{\partial \bar{p}}{\partial x_i} + \frac{1}{\mathrm{Re}}\frac{\partial \overline{\Sigma}_{ij}}{\partial x_j} - \frac{\partial \overline{R}_{ij}}{\partial x_j}\right]. \qquad (\text{B.2.8})$$

Subtracting (B.2.8) from (B.2.6) leaves the fluctuating momentum equation

$$\rho\frac{\partial u_i''}{\partial t} + \rho u_j''\frac{\partial \widetilde{u}_i}{\partial x_j} + \rho\widetilde{u}_j\frac{\partial u_i''}{\partial x_j} + \rho u_j''\frac{\partial u_i''}{\partial x_j} =$$
$$-\frac{\partial(\bar{p}+p')}{\partial x_i} + \frac{1}{\mathrm{Re}}\frac{\partial(\overline{\Sigma}_{ij}+\Sigma_{ij}')}{\partial x_j} - \frac{\rho}{\bar{\rho}}\left[-\frac{\partial \bar{p}}{\partial x_i} + \frac{1}{\mathrm{Re}}\frac{\partial \overline{\Sigma}_{ij}}{\partial x_j} - \frac{\partial \overline{R}_{ij}}{\partial x_j}\right]. \quad (\text{B.2.9})$$

B.3   Turbulence kinetic energy

B.3.1   Reynolds stress equation

The governing equation of the Reynolds stress $\overline{R}_{ij} = \bar{\rho}\,\widetilde{u_i''u_j''}$ is found by taking the u_i'' momentum equation and multiplying by u_j'', and summing it with the u_j'' momentum equation multiplied by u_i''. The unsteady and convective terms can be combined into one material derivative. First note that

$$\rho\overline{\frac{Du_i''u_j''}{Dt}} = \underbrace{\overline{\rho u_j''\frac{Du_i''}{Dt}}}_{\mathcal{A}} + \underbrace{\overline{\rho u_i''\frac{Du_j''}{Dt}}}_{\mathcal{B}}. \qquad (\text{B.3.1})$$

Expanding $\mathcal{A}$ (note that the convective velocity is the instantaneous one)

$$\overline{\rho u_j''\frac{Du_i''}{Dt}} = \overline{\rho u_j''\frac{\partial u_i''}{\partial t}} + \overline{\rho u_j''u_k\frac{\partial u_i''}{\partial x_k}} \qquad (\text{B.3.2})$$

Expanding $\mathcal{B}$ and using product rule

$$
\begin{aligned}
\overline{\rho u_i'' \frac{Du_j''}{Dt}} &= \overline{\rho \left[u_i'' \frac{\partial u_j''}{\partial t} + u_i'' u_k \frac{\partial u_j''}{\partial x_k} \right]} \\
&= \overline{\frac{\partial \rho u_i'' u_j''}{\partial t}} - \overline{u_j'' \frac{\partial \rho u_i''}{\partial t}} + \overline{\frac{\partial}{\partial x_k} (\rho u_i'' u_j'' u_k)} - \overline{u_j'' \frac{\partial}{\partial x_k} (\rho u_i'' u_k)} \\
&= \overline{\frac{\partial \rho u_i'' u_j''}{\partial t}} + \overline{\frac{\partial \rho u_i'' u_j'' \widetilde{u}_k}{\partial x_k}} + \overline{\frac{\partial \rho u_i'' u_j'' u_k''}{\partial x_k}} - \overline{\rho u_j'' \frac{\partial u_i''}{\partial t}} - \overline{\rho u_j'' \widetilde{u}_k \frac{\partial u_i''}{\partial x_k}} - \underbrace{\overline{u_i'' u_j'' \frac{\partial \rho}{\partial t}} - \overline{u_i'' u_j'' \frac{\partial \rho u_k}{\partial x_k}}}_{=\,0 \text{ from continuity}}.
\end{aligned}
$$

$$(B.3.3)$$

Finally summing with $\mathcal{A}$ leaves

$$
\rho \overline{\frac{D\widetilde{u_i'' u_j''}}{Dt}} = \frac{\partial \overline{\rho} \, \widetilde{u_i'' u_j''}}{\partial t} + \frac{\partial \overline{\rho} \, \widetilde{u_i'' u_j''} \widetilde{u}_k}{\partial x_k} + \frac{\partial \overline{\rho} \, \widetilde{u_i'' u_j'' u_k''}}{\partial x_k}
\tag{B.3.4}
$$

This result simplifies the combination of the unsteady and convective terms when building the Reynolds stress equation. Only one momentum equation needs to be manipulated; the second is found simply by replacing i for j. The dummy index used for summation is changed from j to k. Equation (B.2.9) is first written in material derivative form:

$$
\rho \frac{\partial u_i''}{\partial t} + \rho u_k \frac{\partial u_i''}{\partial x_k} + \rho u_k'' \frac{\partial \widetilde{u}_i}{\partial x_k} = -\frac{\partial p}{\partial x_i} + \frac{1}{\text{Re}} \frac{\partial \Sigma_{ik}}{\partial x_k} - \frac{\rho}{\overline{\rho}} \left[-\frac{\partial \overline{p}}{\partial x_i} + \frac{1}{\text{Re}} \frac{\partial \overline{\Sigma}_{ik}}{\partial x_k} - \frac{\partial \overline{R}_{ik}}{\partial x_k} \right]
$$

$$
\frac{\partial \rho u_i''}{\partial t} + \frac{\partial \rho u_i'' u_k}{\partial x_k} - u_i'' \underbrace{\left[\frac{\partial \rho}{\partial t} + \frac{\partial (\rho u_k)}{\partial x_k} \right]}_{=\,0 \text{ from continuity}} + \rho u_k'' \frac{\partial \widetilde{u}_i}{\partial x_k} =
$$

$$
\rho \frac{Du_i''}{Dt} + \rho u_k'' \frac{\partial \widetilde{u}_i}{\partial x_k} =
$$

$$(B.3.5)$$

Multiplying by u_j'' and time averaging gives

$$
\overline{\rho u_j'' \frac{Du_i''}{Dt}} + \overline{\rho u_j'' u_k'' \frac{\partial \widetilde{u}_i}{\partial x_k}} = -\overline{u_j'' \frac{\partial p}{\partial x_i}} + \frac{1}{\text{Re}} \overline{u_j'' \frac{\partial \Sigma_{ik}}{\partial x_k}} - \overline{\frac{\rho u_j''}{\overline{\rho}} \left[-\frac{\partial \overline{p}}{\partial x_i} + \frac{1}{\text{Re}} \frac{\partial \overline{\Sigma}_{ik}}{\partial x_k} - \frac{\partial \overline{R}_{ij}}{\partial x_j} \right]}^{\,0}.
\tag{B.3.6}
$$

Using product rule on the work and friction terms gives

$$
\overline{\rho u_j'' \frac{Du_i''}{Dt}} = -\overline{\rho} \, \widetilde{u_j'' u_k''} \frac{\partial \widetilde{u}_i}{\partial x_k} - \frac{\partial (\overline{p} \, \overline{u_j''})}{\partial x_i} - \frac{\partial (\overline{p' u_j''})}{\partial x_i} + \overline{p \frac{\partial u_j''}{\partial x_i}} + \frac{1}{\text{Re}} \frac{\partial \overline{u_j'' \Sigma_{ik}}}{\partial x_k} - \frac{1}{\text{Re}} \overline{\Sigma_{ik} \frac{\partial u_j''}{\partial x_k}}.
\tag{B.3.7}
$$

The same can be written for the u_j'' momentum equation multiplied by u_i''. Summing this with

(B.3.7) and using the result from (B.3.4) gives the governing equation for the Reynolds stress tensor

$$
\bar{\rho}\frac{\widetilde{D u_i'' u_j''}}{\widetilde{Dt}} = -\underbrace{\frac{\partial}{\partial x_k}(\bar{\rho}\,\widetilde{u_i'' u_j'' u_k''})}_{(i)} - \underbrace{\bar{\rho}\,(\widetilde{u_i'' u_k''}\frac{\partial \widetilde{u}_j}{\partial x_k} + \widetilde{u_j'' u_k''}\frac{\partial \widetilde{u}_i}{\partial x_k})}_{(ii)}
$$

$$
\underbrace{-\frac{\partial(\bar{p}\,\overline{u_j''})}{\partial x_i} - \frac{\partial(\bar{p}\,\overline{u_i''})}{\partial x_j}}_{(iii)} \underbrace{-\frac{\partial \overline{(p' u_j'')}}{\partial x_i} - \frac{\partial \overline{(p' u_i'')}}{\partial x_j}}_{(iv)} + \underbrace{\overline{p\left[\frac{\partial u_j''}{\partial x_i} + \frac{\partial u_i''}{\partial x_j}\right]}}_{(v)}
$$

$$
+ \underbrace{\frac{1}{\mathrm{Re}}\left[\frac{\partial \overline{u_j'' \Sigma_{ik}}}{\partial x_k} + \frac{\partial \overline{u_i'' \Sigma_{jk}}}{\partial x_k}\right]}_{(vi)} - \underbrace{\frac{1}{\mathrm{Re}}\left[\overline{\Sigma_{ik}\frac{\partial u_j''}{\partial x_k}} + \overline{\Sigma_{jk}\frac{\partial u_i''}{\partial x_k}}\right]}_{(vii)} \quad (\mathrm{B.3.8})
$$

The terms on the right-hand-side of (B.3.8) are labelled as follows according to Chassaing *et al.* (2002)

(i)   turbulent diffusion,

(ii) mean motion "shear" coupling,

(iii) mean motion pressure coupling,

(iv) pressure action in the fluctuation motion,

(v) pressure (instantaneous value) strain correlation,

(vi) viscous action in the fluctuating motion,

(vii) dissipation.

B.3.2   Turbulence kinetic energy (TKE)

The governing equation for the turbulent kinetic energy $\widetilde{k} \equiv 1/2\,\widetilde{u_i'' u_i''} = 1/2\,\overline{\rho u_i'' u_i''}/\bar{\rho}$ is the trace of the Reynolds transport equation, i.e. by setting $i = j$.

$$
\frac{\partial}{\partial t}(\bar{\rho}\,\widetilde{u_i'' u_i''}) + \frac{\partial}{\partial x_k}(\bar{\rho}\,\widetilde{u_i'' u_i''}\,\widetilde{u}_k) = -\frac{\partial}{\partial x_k}(\bar{\rho}\,\widetilde{u_i'' u_i'' u_k''}) - 2\bar{\rho}\,\widetilde{u_i'' u_k''}\frac{\partial \widetilde{u}_i}{\partial x_k} - 2\frac{\partial(\bar{p}\,\overline{u_j''})}{\partial x_j} - 2\frac{\partial \overline{(p' u_j'')}}{\partial x_j}
$$

$$
+ 2\overline{p\frac{\partial u_j''}{\partial x_j}} + \frac{2}{\mathrm{Re}}\frac{\partial \overline{u_i'' \Sigma_{ik}}}{\partial x_k} - \frac{2}{\mathrm{Re}}\overline{\Sigma_{ik}\frac{\partial u_i''}{\partial x_k}} \quad (\mathrm{B.3.9})
$$

Substituting for $\widetilde{k}$ gives and changing the dummy variable k back to j gives the final form of the TKE:

$$\frac{\partial}{\partial t}(\bar{\rho}\widetilde{k}) + \frac{\partial}{\partial x_j}(\bar{\rho}\widetilde{k}\widetilde{u}_j) = -\frac{\partial}{\partial x_j}(\bar{\rho}\widetilde{ku_j''}) - \bar{\rho}\widetilde{u_i''u_j''}\frac{\partial\widetilde{u}_i}{\partial x_j} - \frac{\partial(\bar{p}\overline{u_j''})}{\partial x_j} - \frac{\partial\overline{(p'u_j'')}}{\partial x_j}$$
$$+ \overline{p\frac{\partial u_j''}{\partial x_j}} + \frac{1}{\text{Re}}\frac{\partial\overline{u_i''\Sigma_{ij}}}{\partial x_j} - \frac{1}{\text{Re}}\overline{\Sigma_{ij}\frac{\partial u_i''}{\partial x_j}} \quad \text{(B.3.10)}$$

which in non-conservative form is written

$$\bar{\rho}\underbrace{\frac{\widetilde{D}\widetilde{k}}{\widetilde{D}t}}_{(C.i)} = \underbrace{-\frac{\partial}{\partial x_j}(\bar{\rho}\widetilde{ku_j''})}_{(C.ii)} \underbrace{- \bar{\rho}\widetilde{u_i''u_j''}\frac{\partial\widetilde{u}_i}{\partial x_j}}_{(C.iii)} \underbrace{- \frac{\partial(\bar{p}\overline{u_j''})}{\partial x_j}}_{(C.iv)} \underbrace{- \frac{\partial\overline{(p'u_j'')}}{\partial x_j}}_{(C.v)} \underbrace{+ \overline{p\frac{\partial u_j''}{\partial x_j}}}_{(C.vi)} \underbrace{+ \frac{1}{\text{Re}}\frac{\partial\overline{u_i''\Sigma_{ij}}}{\partial x_j}}_{(C.vii)} \underbrace{- \frac{1}{\text{Re}}\overline{\Sigma_{ij}\frac{\partial u_i''}{\partial x_j}}}_{(C.viii)}.$$
$$\text{(B.3.11)}$$

The terms can be described as follows (Chassaing *et al.*, 2002) (except $(C.i)$):

(C.i) turbulent kinetic energy of a fluid particle,

(C.ii) turbulent diffusion,

(C.iii) shear production,

(C.iv) external power of mean pressure forces acting through fluctuating motion,

(C.v) external power of pressure fluctuations in the fluctuating motion,

(C.vi) pressure correlation with dilatation fluctuation,

(C.vii) external power of fluctuating viscous forces in the fluctuating motion,

(C.viii) turbulent dissipation.

For the same form as Lele (1994) terms $(C.iv)$ and $(C.vi)$ are expanded and when summed, cancel to a simpler form

$$(C.iv) + (C.vi) = -\bar{p}\frac{\partial\overline{u_j''}}{\partial x_j} - \overline{u_j''}\frac{\partial\bar{p}}{\partial x_j} + \bar{p}\frac{\partial\overline{u_j''}}{\partial x_j} + \overline{p'\frac{\partial u_j''}{\partial x_j}}. \quad \text{(B.3.12)}$$

Terms $(C.vii)$ and $(C.viii)$ are expanded and summed

$$(C.vii) + (C.viii) = \frac{1}{\mathrm{Re}} \left(\overline{u_i'' \frac{\partial \overline{\Sigma}_{ij}}{\partial x_j}} + \frac{\partial \overline{u_i'' \Sigma_{ij}'}}{\partial x_j} + \overline{\Sigma}_{ij} \frac{\partial \overline{u_i''}}{\partial x_j} - \overline{\Sigma}_{ij} \frac{\partial \overline{u_i''}}{\partial x_j} - \overline{\Sigma_{ij}' \frac{\partial u_i''}{\partial x_j}} \right) \tag{B.3.13}$$

Substituting the results into (B.3.10) gives

$$\underbrace{\frac{\partial}{\partial t}(\overline{\rho}\widetilde{k})}_{(L.i)} + \underbrace{\frac{\partial}{\partial x_j}(\overline{\rho}\,\widetilde{k}\widetilde{u}_j)}_{(L.ii)} = \underbrace{-\frac{\partial}{\partial x_j}(\overline{\rho\,ku_j''})}_{(L.iii)} \underbrace{-\overline{\rho}\,\widetilde{u_i''u_j''}\frac{\partial \widetilde{u}_i}{\partial x_j}}_{(L.iv)} \underbrace{-\overline{u_j''}\frac{\partial \overline{p}}{\partial x_j}}_{(L.v)} + \underbrace{\overline{p'\frac{\partial u_j''}{\partial x_j}}}_{(L.vi)} \underbrace{-\frac{\partial \overline{(p'u_j'')}}{\partial x_j}}_{(L.vii)}$$

$$+ \frac{1}{\mathrm{Re}}\left(\underbrace{\overline{u_i''}\frac{\partial \overline{\Sigma}_{ij}}{\partial x_j}}_{(L.viii)} + \underbrace{\frac{\partial \overline{u_i''\Sigma_{ij}'}}{\partial x_j}}_{(L.ix)} \underbrace{-\overline{\Sigma_{ij}'\frac{\partial u_i''}{\partial x_j}}}_{(L.x)} \right), \quad (B.3.14)$$

which is the same form as Lele (1994) with the following names (from Huang *et al.* (1995))

(L.i) unsteady turbulent kinetic energy,

(L.ii) convective turbulent kinetic energy,

(L.iii) turbulent diffusion,

(L.iv) shear production,

(L.v) velocity-mean pressure gradient,

(L.vi) pressure dilatation,

(L.vii) diffusion from velocity pressure interaction,

(L.viii) velocity-mean viscous stress gradient,

(L.ix) viscous diffusion,

(L.x) energy dissipation.

B.4   Equations simplified for Couette flow

A number of assumptions can be made about the mean flow and Reynolds stresses to simplify the TKE for the turbulent Couette flow. Note that the indices 1,2,3 have been converted to x,y,z coordinates, respectively, and represent the streamwise, wall-normal, and spanwise directions.

B.4.1 Simplifying assumptions

A.1 No mean flow in the span (z), i.e. $\overline{w} = 0$.

A.2 The turbulent mean flow is homogeneous in the streamwise and spanwise directions. I.e.

$$\frac{\partial \widetilde{u}}{\partial x} = \frac{\partial \widetilde{v}}{\partial x} = \frac{\partial \widetilde{w}}{\partial x} = 0$$

$$\frac{\partial \widetilde{u}}{\partial z} = \frac{\partial \widetilde{v}}{\partial z} = \frac{\partial \widetilde{w}}{\partial z} = 0 \tag{B.4.1}$$

A.3 The Reynolds stresses $\overline{R}_{ij} = \overline{\rho} \, \widetilde{u_i'' u_j''}$ are independent of the streamwise or spanwise locations

$$\frac{\partial \overline{R}_{ij}}{\partial x} = \frac{\partial \overline{R}_{ij}}{\partial z} = 0. \tag{B.4.2}$$

A.4 The Favre averaged wall normal velocity is zero: From mean continuity (B.1.4)

$$\frac{\mathrm{d}(\overline{\rho}\,\widetilde{v})}{\mathrm{d}y} = \frac{\mathrm{d}}{\mathrm{d}y}\left(\frac{\overline{\rho}\,\overline{\rho v}}{\overline{\rho}}\right) = 0 \tag{B.4.3}$$

which implies that the integrand must be everywhere constant

$$\overline{\rho v} = C_1. \tag{B.4.4}$$

At the walls $(y = 0$ and $y = 1)$ the no penetration condition enforces

$$\overline{\rho v}\big|_{y=0} = \overline{\rho v}\big|_{y=1} = 0. \tag{B.4.5}$$

Therefore

$$\widetilde{v} = 0 \tag{B.4.6}$$

everywhere.

A.5 Note that Favre averaged spanwise velocity is not zero: c.f. (C.1.11)

$$\widetilde{w} - \overset{0}{\cancel{\overline{w}}} = -\overline{w''} = -\frac{\overline{\rho' w'}}{\overline{\rho}} \neq 0 \tag{B.4.7}$$

B.4.2   Simplified stress tensor

The components of the deviatoric stress tensor that remain after simplifying terms $(L.viii)$, $(L.ix)$ and $(L.x)$ are written for reference

Mean deviatoric stress (dilatational components)

$$
\begin{aligned}
\overline{\Sigma}_{11} &= -\overline{\mu}\left[\frac{2}{3}\overline{\Theta''}\right] + \overline{\mu'\left[2\frac{\partial u''}{\partial x} - \frac{2}{3}\Theta''\right]} + \overline{\mu}_b\overline{\Theta''} + \overline{\mu'_b\Theta''} \\
\overline{\Sigma}_{22} &= \overline{\mu}\left[2\frac{\mathrm{d}\overline{v''}}{\mathrm{d}y} - \frac{2}{3}\overline{\Theta''}\right] + \overline{\mu'\left[2\frac{\partial v''}{\partial y} - \frac{2}{3}\Theta''\right]} + \overline{\mu}_b\overline{\Theta''} + \overline{\mu'_b\Theta''} \\
\overline{\Sigma}_{33} &= -\overline{\mu}\left[\frac{2}{3}\overline{\Theta''}\right] + \overline{\mu'\left[2\frac{\partial w''}{\partial z} - \frac{2}{3}\Theta''\right]} + \overline{\mu}_b\overline{\Theta''} + \overline{\mu'_b\Theta''}
\end{aligned}
\tag{B.4.8}
$$

Mean deviatoric stress (shear components)

$$
\begin{aligned}
\overline{\Sigma}_{12} = \overline{\Sigma}_{21} &= \overline{\mu}\left[\frac{\mathrm{d}\widetilde{u}}{\mathrm{d}y}\right] + \overline{\mu}\left[\frac{\mathrm{d}\overline{u''}}{\mathrm{d}y}\right] + \overline{\mu'\left[\frac{\partial u''}{\partial y} + \frac{\partial v''}{\partial x}\right]} \\
\overline{\Sigma}_{13} = \overline{\Sigma}_{31} &= \overline{\mu'\left[\frac{\partial u''}{\partial z} + \frac{\partial w''}{\partial x}\right]} \\
\overline{\Sigma}_{23} = \overline{\Sigma}_{32} &= \overline{\mu}\left[\frac{\mathrm{d}\widetilde{w}}{\mathrm{d}y}\right] + \overline{\mu}\left[\frac{\mathrm{d}\overline{w''}}{\mathrm{d}y}\right] + \overline{\mu'\left[\frac{\partial v''}{\partial z} + \frac{\partial w''}{\partial y}\right]}
\end{aligned}
\tag{B.4.9}
$$

Fluctuating deviatoric stress (dilatational components)

$$
\begin{aligned}
\Sigma'_{11} &= \overline{\mu}\left[2\frac{\partial u''}{\partial x} - \frac{2}{3}\Theta''\right] + \overline{\mu}\left[\frac{2}{3}\overline{\Theta''}\right] + \mu'\left[2\frac{\partial u''}{\partial x} - \frac{2}{3}\Theta''\right] - \overline{\mu'\left[2\frac{\partial u''}{\partial x} - \frac{2}{3}\Theta''\right]} \\
&+ \overline{\mu}_b\Theta'' - \overline{\mu}_b\overline{\Theta''} + \mu'_b\Theta'' - \overline{\mu'_b\Theta''} \\[4pt]
\Sigma'_{22} &= \overline{\mu}\left[2\frac{\partial v''}{\partial y} - \frac{2}{3}\Theta''\right] - \overline{\mu}\left[2\frac{\mathrm{d}\overline{v''}}{\mathrm{d}y} - \frac{2}{3}\overline{\Theta''}\right] + \mu'\left[2\frac{\partial v''}{\partial y} - \frac{2}{3}\Theta''\right] - \overline{\mu'\left[2\frac{\partial v''}{\partial y} - \frac{2}{3}\Theta''\right]} \\
&+ \overline{\mu}_b\Theta'' + \overline{\mu}_b\overline{\Theta''} + \mu'_b\Theta'' - \overline{\mu'_b\Theta''} \\[4pt]
\Sigma'_{33} &= \overline{\mu}\left[2\frac{\partial w''}{\partial z} - \frac{2}{3}\Theta''\right] + \overline{\mu}\left[\frac{2}{3}\overline{\Theta''}\right] + \mu'\left[2\frac{\partial w''}{\partial z} - \frac{2}{3}\Theta''\right] - \overline{\mu'\left[2\frac{\partial w''}{\partial z} - \frac{2}{3}\Theta''\right]} \\
&+ \overline{\mu}_b\Theta'' - \overline{\mu}_b\overline{\Theta''} + \mu'_b\Theta'' - \overline{\mu'_b\Theta''}
\end{aligned}
$$

$$
\tag{B.4.10}
$$

Fluctuating deviatoric stress (shear components)

$$\Sigma'_{12} = \Sigma'_{21} \;\; = \;\; \overline{\mu}\left[\frac{\partial u''}{\partial y} + \frac{\partial v''}{\partial x}\right] - \overline{\mu}\left[\frac{\mathrm{d}\overline{u''}}{\mathrm{d}y}\right] + \mu'\left[\frac{\mathrm{d}\widetilde{u}}{\mathrm{d}y}\right] + \mu'\left[\frac{\partial u''}{\partial y} + \frac{\partial v''}{\partial x}\right] - \overline{\mu'\left[\frac{\partial u''}{\partial y} + \frac{\partial v''}{\partial x}\right]}$$

$$\Sigma'_{13} = \Sigma'_{31} \;\; = \;\; \overline{\mu}\left[\frac{\partial u''}{\partial z} + \frac{\partial w''}{\partial x}\right] + \mu'\left[\frac{\partial u''}{\partial z} + \frac{\partial w''}{\partial x}\right] - \overline{\mu'\left[\frac{\partial u''}{\partial z} + \frac{\partial w''}{\partial x}\right]}$$

$$\Sigma'_{23} = \Sigma'_{32} \;\; = \;\; \overline{\mu}\left[\frac{\partial v''}{\partial z} + \frac{\partial w''}{\partial y}\right] - \overline{\mu}\left[\frac{\mathrm{d}\overline{w''}}{\mathrm{d}y}\right] + \mu'\left[\frac{\mathrm{d}\widetilde{w}}{\mathrm{d}y}\right] + \mu'\left[\frac{\partial v''}{\partial z} + \frac{\partial w''}{\partial y}\right] - \overline{\mu'\left[\frac{\partial v''}{\partial z} + \frac{\partial w''}{\partial y}\right]}$$

$$(\text{B.4.11})$$

B.4.3 Mean momentum equations

The above simplifications can be applied to the mean momentum equation (B.1.5)

$$\frac{\partial}{\partial t}(\overline{\rho}\widetilde{u}_i) \;\; + \;\; \frac{\partial}{\partial x_j}(\overline{\rho}\widetilde{u}_i\widetilde{u}_j) \;\; = \;\; -\frac{\partial\overline{p}}{\partial x_i} + \frac{1}{\mathrm{Re}}\frac{\partial\overline{\Sigma}_{ij}}{\partial x_j} - \frac{\partial\overline{R}_{ij}}{\partial x_j}. \qquad (\text{B.4.12})$$

in the streamwise (x-momentum)

$$\cancelto{0}{\frac{\partial}{\partial t}(\overline{\rho}\widetilde{u})} + \cancelto{0}{\frac{\partial}{\partial x}(\overline{\rho}\widetilde{u}\widetilde{u})} + \frac{\partial}{\partial y}(\overline{\rho}\widetilde{u}\cancelto{0}{\widetilde{v}}) + \cancelto{0}{\frac{\partial}{\partial z}(\overline{\rho}\widetilde{u}\widetilde{w})} \;\; = \;\; -\cancelto{0}{\frac{\partial\overline{p}}{\partial x}} + \frac{1}{\mathrm{Re}}\cancelto{0}{\frac{\partial\overline{\Sigma}_{11}}{\partial x}} + \frac{1}{\mathrm{Re}}\frac{\partial\overline{\Sigma}_{12}}{\partial y} + \frac{1}{\mathrm{Re}}\cancelto{0}{\frac{\partial\overline{\Sigma}_{13}}{\partial z}}$$

$$-\cancelto{0}{\frac{\partial}{\partial x}(\overline{\rho\widetilde{u''u''}})} - \frac{\partial}{\partial y}(\overline{\rho\widetilde{u''v''}}) - \cancelto{0}{\frac{\partial}{\partial z}(\overline{\rho\widetilde{u''w''}})}$$

$$0 \;\; = \;\; \frac{1}{\mathrm{Re}}\frac{\mathrm{d}\overline{\Sigma}_{12}}{\mathrm{d}y} - \frac{\mathrm{d}}{\mathrm{d}y}(\overline{\rho\widetilde{u''v''}})$$

$$(\text{B.4.13})$$

wall-normal (y-momentum)

$$\cancel{\frac{\partial}{\partial t}(\overline{\rho}\widetilde{v})}^{0} + \cancel{\frac{\partial}{\partial x}(\overline{\rho}\widetilde{v}\widetilde{u})}^{0} + \frac{\partial}{\partial y}(\overline{\rho}\widetilde{v}\widetilde{v}) + \cancel{\frac{\partial}{\partial z}(\overline{\rho}\widetilde{v}\widetilde{w})}^{0} \;=\; -\frac{\partial \overline{p}}{\partial y} + \frac{1}{\mathrm{Re}}\cancel{\frac{\partial \overline{\Sigma}_{21}}{\partial x}}^{0} + \frac{1}{\mathrm{Re}}\frac{\partial \overline{\Sigma}_{22}}{\partial y} + \frac{1}{\mathrm{Re}}\cancel{\frac{\partial \overline{\Sigma}_{23}}{\partial z}}^{0}$$

$$-\;\cancel{\frac{\partial}{\partial x}(\overline{\rho}\,\widetilde{v''u''})}^{0} - \frac{\partial}{\partial y}(\overline{\rho}\,\widetilde{v''v''}) - \cancel{\frac{\partial}{\partial z}(\overline{\rho}\,\widetilde{v''w''})}^{0}$$

$$0 \;=\; -\frac{\mathrm{d}\overline{p}}{\mathrm{d}y} + \frac{1}{\mathrm{Re}}\frac{\mathrm{d}\overline{\Sigma}_{22}}{\mathrm{d}y} - \frac{\mathrm{d}}{\mathrm{d}y}(\overline{\rho}\,\widetilde{v''v''})$$

$$(\text{B.4.14})$$

and spanwise (z-momentum) directions

$$\cancel{\frac{\partial}{\partial t}(\overline{\rho}\widetilde{w})}^{0} + \cancel{\frac{\partial}{\partial x}(\overline{\rho}\widetilde{w}\widetilde{u})}^{0} + \frac{\partial}{\partial y}(\overline{\rho}\widetilde{w}\widetilde{v}) + \cancel{\frac{\partial}{\partial z}(\overline{\rho}\widetilde{w}\widetilde{w})}^{0} \;=\; -\cancel{\frac{\partial \overline{p}}{\partial z}}^{0} + \frac{1}{\mathrm{Re}}\cancel{\frac{\partial \overline{\Sigma}_{31}}{\partial x}}^{0} + \frac{1}{\mathrm{Re}}\frac{\partial \overline{\Sigma}_{32}}{\partial y} + \frac{1}{\mathrm{Re}}\cancel{\frac{\partial \overline{\Sigma}_{33}}{\partial z}}^{0}$$

$$-\;\cancel{\frac{\partial}{\partial x}(\overline{\rho}\,\widetilde{w''u''})}^{0} - \frac{\partial}{\partial y}(\overline{\rho}\,\widetilde{w''v''}) - \cancel{\frac{\partial}{\partial z}(\overline{\rho}\,\widetilde{w''w''})}^{0}$$

$$0 \;=\; \frac{1}{\mathrm{Re}}\frac{\mathrm{d}\overline{\Sigma}_{32}}{\mathrm{d}y} - \frac{\mathrm{d}}{\mathrm{d}y}(\overline{\rho}\,\widetilde{w''v''}).$$

$$(\text{B.4.15})$$

B.5　Turbulence kinetic energy budget

The assumptions from § B.4.1 can be used to simplify (B.3.11) for plane Couette flow. Taking each term in turn:

(L.i) rate of change of kinetic energy of a fluid particle: from A.1

$$(L.i) = \frac{\partial(\overline{\rho}\,\widetilde{k})}{\partial t} = \frac{1}{2}\frac{\partial}{\partial t}(\overline{\rho(u''^2 + v''^2 + w''^2)}) \tag{B.5.1}$$

(L.ii) convected turbulent kinetic energy

$$(L.ii) = \frac{\mathrm{d}}{\mathrm{d}y}(\overline{\rho}\,\widetilde{k}\widetilde{v}) \tag{B.5.2}$$

(L.iii) turbulent diffusion

$$(L.iii) = -\frac{\mathrm{d}}{\mathrm{d}y}(\overline{\rho}\,\widetilde{kv''}) = -\frac{1}{2}\frac{\mathrm{d}}{\mathrm{d}y}(\overline{\rho(u''^2 + v''^2 + w''^2)v''}) \tag{B.5.3}$$

(L.iv) energy production

$$(L.iv) = -\overline{\rho}\,\widetilde{u''v''}\frac{\mathrm{d}\widetilde{u}}{\mathrm{d}y} - \overline{\rho}\,\widetilde{w''v''}\frac{\mathrm{d}\widetilde{w}}{\mathrm{d}y} \tag{B.5.4}$$

(L.v) velocity mean pressure gradient interaction

$$(L.v) = -\overline{v''}\frac{\mathrm{d}\overline{p}}{\mathrm{d}y}, \tag{B.5.5}$$

(L.vi) pressure dilatation,

$$(L.vi) = \overline{p'\Theta''} \tag{B.5.6}$$

(L.vii) diffusion from velocity pressure interaction,

$$(L.vii) = -\frac{\mathrm{d}\overline{p'v''}}{\mathrm{d}y} \tag{B.5.7}$$

(L.viii) velocity mean viscous stress gradient

$$(L.viii) \;=\; \frac{1}{\mathrm{Re}}\left[\overline{u''}\frac{\mathrm{d}\overline{\Sigma}_{12}}{\mathrm{d}y} + \overline{v''}\frac{\mathrm{d}\overline{\Sigma}_{22}}{\mathrm{d}y} + \overline{w''}\frac{\mathrm{d}\overline{\Sigma}_{32}}{\mathrm{d}y}\right] \tag{B.5.8}$$

where

$$
\begin{aligned}
\overline{u''}\frac{\mathrm{d}\overline{\Sigma}_{12}}{\mathrm{d}y} &= \overline{u''}\frac{\mathrm{d}}{\mathrm{d}y}\left(\overline{\mu}\left[\frac{\mathrm{d}\widetilde{u}}{\mathrm{d}y}\right] + \overline{\mu}\left[\frac{\mathrm{d}\overline{u''}}{\mathrm{d}y}\right] + \overline{\mu'\left[\frac{\partial u''}{\partial y} + \frac{\partial v''}{\partial x}\right]}\right) \\
\overline{v''}\frac{\mathrm{d}\overline{\Sigma}_{22}}{\mathrm{d}y} &= \overline{v''}\frac{\mathrm{d}}{\mathrm{d}y}\left(\overline{\mu}\left[2\frac{\mathrm{d}\overline{v''}}{\mathrm{d}y} - \frac{2}{3}\overline{\Theta''}\right] + \overline{\mu'\left[2\frac{\partial v''}{\partial y} - \frac{2}{3}\Theta''\right]} + \overline{\mu_b\Theta''} + \overline{\mu_b'\Theta''}\right) \\
\overline{w''}\frac{\mathrm{d}\overline{\Sigma}_{32}}{\mathrm{d}y} &= \overline{w''}\frac{\mathrm{d}}{\mathrm{d}y}\left(\overline{\mu}\left[\frac{\mathrm{d}\widetilde{w}}{\mathrm{d}y}\right] + \overline{\mu}\left[\frac{\mathrm{d}\overline{w''}}{\mathrm{d}y}\right] + \overline{\mu'\left[\frac{\partial v''}{\partial z} + \frac{\partial w''}{\partial y}\right]}\right)
\end{aligned}
\tag{B.5.9}
$$

(L.ix) viscous (laminar) diffusion

$$(L.ix) \;=\; \frac{1}{\mathrm{Re}}\left[\frac{\mathrm{d}\overline{u''\Sigma'_{12}}}{\mathrm{d}y} + \frac{\mathrm{d}\overline{v''\Sigma'_{22}}}{\mathrm{d}y} + \frac{\mathrm{d}\overline{w''\Sigma'_{32}}}{\mathrm{d}y}\right] \tag{B.5.10}$$

where

$$\frac{\mathrm{d}\overline{u''\Sigma'_{12}}}{\mathrm{d}y} = \frac{\mathrm{d}}{\mathrm{d}y}\left(\overline{\mu}\left[\overline{u''\frac{\partial u''}{\partial y} + u''\frac{\partial v''}{\partial x}} \right] - \overline{\mu}\left[\overline{u''\frac{\mathrm{d}\overline{u''}}{\mathrm{d}y}} \right]\right.$$

$$+ \quad \overline{\mu'u''}\frac{\mathrm{d}\widetilde{u}}{\mathrm{d}y} + \overline{\mu'\left[u''\frac{\partial u''}{\partial y} + u''\frac{\partial v''}{\partial x}\right]} - \overline{u''}\overline{\mu'\left[\frac{\partial u''}{\partial y} + \frac{\partial v''}{\partial x}\right]}\right)$$

$$\frac{\mathrm{d}\overline{v''\Sigma'_{22}}}{\mathrm{d}y} = \frac{\mathrm{d}}{\mathrm{d}y}\left(\overline{\mu}\left[\overline{2v''\frac{\partial v''}{\partial y} - \frac{2}{3}v''\Theta''} \right] - \overline{\mu}\left[2\overline{v''\frac{\mathrm{d}\overline{v''}}{\mathrm{d}y}} - \frac{2}{3}\overline{v''}\,\overline{\Theta''} \right]\right.$$

$$+ \quad \overline{\mu'\left[2v''\frac{\partial v''}{\partial y} - \frac{2}{3}v''\Theta''\right]} - \overline{v''}\overline{\mu'\left[2\frac{\partial v''}{\partial y} - \frac{2}{3}\Theta''\right]} \qquad\qquad \text{(B.5.11)}$$

$$+ \quad \overline{\mu}_b\overline{v''\Theta''} - \overline{\mu}_b\overline{v''}\,\overline{\Theta''} + \overline{\mu'_b v''\Theta''} - \overline{\mu'_b\Theta''}\,\overline{v''}\Big)$$

$$\frac{\mathrm{d}\overline{w''\Sigma'_{32}}}{\mathrm{d}y} = \frac{\mathrm{d}}{\mathrm{d}y}\left(\overline{\mu}\left[\overline{w''\frac{\partial w''}{\partial y} + w''\frac{\partial v''}{\partial z}} \right] - \overline{\mu}\left[\overline{w''\frac{\mathrm{d}\overline{w''}}{\mathrm{d}y}} \right]\right.$$

$$+ \quad \overline{\mu'w''}\frac{\mathrm{d}\widetilde{w}}{\mathrm{d}y} + \overline{\mu'\left[w''\frac{\partial w''}{\partial y} + w''\frac{\partial v''}{\partial z}\right]} - \overline{w''}\overline{\mu'\left[\frac{\partial w''}{\partial y} + \frac{\partial v''}{\partial z}\right]}\right)$$

(L.x) turbulent dissipation.

$$(L.x) = - \overline{\Sigma'_{11}\frac{\partial u''}{\partial x}} - \overline{\Sigma'_{12}\frac{\partial u''}{\partial y}} - \overline{\Sigma'_{13}\frac{\partial u''}{\partial z}}$$

$$- \overline{\Sigma'_{21}\frac{\partial v''}{\partial x}} - \overline{\Sigma'_{22}\frac{\partial v''}{\partial y}} - \overline{\Sigma'_{23}\frac{\partial v''}{\partial z}} \qquad\qquad \text{(B.5.12)}$$

$$- \overline{\Sigma'_{31}\frac{\partial w''}{\partial x}} - \overline{\Sigma'_{32}\frac{\partial w''}{\partial y}} - \overline{\Sigma'_{33}\frac{\partial w''}{\partial z}}$$

where

$$
\overline{\Sigma'_{11}\frac{\partial u''}{\partial x}} = \overline{\mu}\left[2\overline{\left(\frac{\partial u''}{\partial x}\right)^2} - \frac{2}{3}\overline{\frac{\partial u''}{\partial x}\Theta''}\right] + \overline{\mu}\frac{2}{3}\frac{\partial \overline{u''}}{\partial x}\overline{\Theta''} + \overline{\mu'\left[2\left(\frac{\partial u''}{\partial x}\right)^2 - \frac{2}{3}\frac{\partial u''}{\partial x}\Theta''\right]}
$$

$$
+ \ \overline{\mu}_b\overline{\frac{\partial u''}{\partial x}\Theta''} + \overline{\mu'_b\frac{\partial u''}{\partial x}\Theta''}
$$

$$
\overline{\Sigma'_{22}\frac{\partial v''}{\partial y}} = \overline{\mu}\left[2\overline{\left(\frac{\partial v''}{\partial y}\right)^2} - \frac{2}{3}\overline{\frac{\partial v''}{\partial y}\Theta''}\right] - \overline{\mu}\left[2\left(\frac{\mathrm{d}\overline{v''}}{\mathrm{d}y}\right)^2 - \frac{2}{3}\frac{\mathrm{d}\overline{v''}}{\mathrm{d}y}\overline{\Theta''}\right]
$$

$$
+ \ \overline{\mu'\left[2\left(\frac{\partial v''}{\partial y}\right)^2 - \frac{2}{3}\frac{\partial v''}{\partial y}\Theta''\right]} - \overline{\mu'\left[2\frac{\partial v''}{\partial y} - \frac{2}{3}\Theta''\right]\frac{\mathrm{d}\overline{v''}}{\mathrm{d}y}}
$$

$$
+ \ \overline{\mu}_b\overline{\frac{\partial v''}{\partial y}\Theta''} - \overline{\mu}_b\frac{\partial \overline{v''}}{\partial y}\overline{\Theta''} + \overline{\mu'_b\Theta''\frac{\partial v''}{\partial y}} - \overline{\mu'_b\Theta''}\frac{\mathrm{d}\overline{v''}}{\mathrm{d}y}
$$

$$
\overline{\Sigma'_{33}\frac{\partial w''}{\partial z}} = \overline{\mu}\left[2\overline{\left(\frac{\partial w''}{\partial z}\right)^2} - \frac{2}{3}\overline{\frac{\partial w''}{\partial z}\Theta''}\right] + \overline{\mu'\left[2\left(\frac{\partial w''}{\partial z}\right)^2 - \frac{2}{3}\frac{\partial w''}{\partial z}\Theta''\right]}
$$

$$
+ \ \overline{\mu}_b\overline{\frac{\partial w''}{\partial z}\Theta''} + \overline{\mu'_b\frac{\partial w''}{\partial z}\Theta''}
$$

$$
\text{(B.5.13)}
$$

$$\overline{\Sigma'_{12}\frac{\partial u''}{\partial y}} = \overline{\mu}\left[\overline{\left(\frac{\partial u''}{\partial y}\right)^2} + \overline{\frac{\partial u''}{\partial y}\frac{\partial v''}{\partial x}}\right] - \overline{\mu}\left[\overline{\left(\frac{\mathrm{d}u''}{\mathrm{d}y}\right)^2}\right] + \overline{\mu'\frac{\partial u''}{\partial y}\frac{\mathrm{d}\widetilde{u}}{\mathrm{d}y}}$$

$$+ \overline{\mu'\left(\frac{\partial u''}{\partial y}\right)^2 + \frac{\partial u''}{\partial y}\frac{\partial v''}{\partial x}} - \overline{\mu'\left[\frac{\partial u''}{\partial y} + \frac{\partial v''}{\partial x}\right]\frac{\mathrm{d}\overline{u''}}{\mathrm{d}y}}$$

$$\overline{\Sigma'_{21}\frac{\partial v''}{\partial x}} = \overline{\mu}\left[\overline{\left(\frac{\partial v''}{\partial x}\right)^2} + \overline{\frac{\partial u''}{\partial y}\frac{\partial v''}{\partial x}}\right] + \overline{\mu'\frac{\partial v''}{\partial x}\frac{\mathrm{d}\widetilde{u}}{\mathrm{d}y}} + \overline{\mu'\left[\left(\frac{\partial v''}{\partial x}\right)^2 + \frac{\partial u''}{\partial y}\frac{\partial v''}{\partial x}\right]}$$

$$\overline{\Sigma'_{13}\frac{\partial u''}{\partial z}} = \overline{\mu}\left[\overline{\left(\frac{\partial u''}{\partial z}\right)^2} + \overline{\frac{\partial w''}{\partial x}\frac{\partial u''}{\partial z}}\right] + \overline{\mu'\left[\left(\frac{\partial u''}{\partial z}\right)^2 + \frac{\partial w''}{\partial x}\frac{\partial u''}{\partial z}\right]}$$

$$\text{(B.5.14)}$$

$$\overline{\Sigma'_{31}\frac{\partial w''}{\partial x}} = \overline{\mu}\left[\overline{\left(\frac{\partial w''}{\partial x}\right)^2} + \overline{\frac{\partial w''}{\partial x}\frac{\partial u''}{\partial z}}\right] + \overline{\mu'\left[\left(\frac{\partial w''}{\partial x}\right)^2 + \frac{\partial w''}{\partial x}\frac{\partial u''}{\partial z}\right]}$$

$$\overline{\Sigma'_{23}\frac{\partial v''}{\partial z}} = \overline{\mu}\left[\overline{\left(\frac{\partial v''}{\partial z}\right)^2} + \overline{\frac{\partial w''}{\partial y}\frac{\partial v''}{\partial z}}\right] + \overline{\mu'\left[\left(\frac{\partial v''}{\partial z}\right)^2 + \frac{\partial w''}{\partial y}\frac{\partial v''}{\partial z}\right]}$$

$$\overline{\Sigma'_{32}\frac{\partial w''}{\partial y}} = \overline{\mu}\left[\overline{\left(\frac{\partial w''}{\partial y}\right)^2} + \overline{\frac{\partial w''}{\partial y}\frac{\partial v''}{\partial z}}\right] - \overline{\mu}\left[\overline{\left(\frac{\mathrm{d}\overline{w''}}{\mathrm{d}y}\right)^2}\right] + \overline{\mu'\frac{\partial w''}{\partial y}\frac{\mathrm{d}\widetilde{w}}{\mathrm{d}y}}$$

$$+ \overline{\mu'\left[\left(\frac{\partial w''}{\partial y}\right)^2 + \frac{\partial w''}{\partial y}\frac{\partial v''}{\partial z}\right]} - \overline{\mu'\left[\frac{\partial v''}{\partial z} + \frac{\partial w''}{\partial y}\right]\frac{\mathrm{d}\overline{w''}}{\mathrm{d}y}}$$

B.6   Time-evolution equation of velocity dilatation

The time-evolution equation of the divergence of velocity $\boldsymbol{\nabla}\cdot\boldsymbol{u} \equiv \partial u_j/\partial x_j \equiv \Theta$ is found by taking the divergence of the compressible Navier–Stokes equation in non-conservative form, i.e.

$$\frac{\partial}{\partial x_i}\left(\frac{\partial u_i}{\partial t}\right) + \frac{\partial}{\partial x_i}\left(u_j\frac{\partial u_i}{\partial x_j}\right) = -\frac{\partial}{\partial x_i}\left(\frac{1}{\rho}\frac{\partial p_m}{\partial x_i}\right) + \frac{1}{\mathrm{Re}}\frac{\partial}{\partial x_i}\left(\frac{1}{\rho}\frac{\partial \Sigma_{ij}}{\partial x_j}\right) \tag{B.6.1}$$

Assuming that the velocity is $\mathcal{C}_2$, the time and space derivatives can be switched. Collecting terms in Θ gives

$$\frac{\partial \Theta}{\partial t} + u_j\frac{\partial^2 u_i}{\partial x_i \partial x_j} + \frac{\partial u_i}{\partial x_j}\frac{\partial u_j}{\partial x_i} = -\frac{\partial}{\partial x_i}\left(\frac{1}{\rho}\right)\frac{\partial p_m}{\partial x_i} - \frac{1}{\rho}\frac{\partial^2 p_m}{\partial x_i \partial x_i} + \frac{1}{\mathrm{Re}}\frac{\partial}{\partial x_i}\left(\frac{1}{\rho}\frac{\partial \Sigma_{ij}}{\partial x_j}\right). \tag{B.6.2}$$

Combining unsteady and convective term into the material derivative and switching to non-index notation gives

$$\frac{D\Theta}{Dt} + \boldsymbol{\nabla}\boldsymbol{u}^{\mathrm{t}} : \boldsymbol{\nabla}\boldsymbol{u} = -\boldsymbol{\nabla}\left(\frac{1}{\rho}\right) \cdot \boldsymbol{\nabla}p_m - \frac{1}{\rho}\nabla^2 p_m + \frac{1}{\mathrm{Re}}\boldsymbol{\nabla}\left(\frac{1}{\rho}\boldsymbol{\nabla}\cdot\boldsymbol{\Sigma}\right). \tag{B.6.3}$$

Appendix C

Favre decomposition

C.1 Decomposition of field quantities

C.1.1 Reynolds decomposition

Turbulent flows of a compressible fluid lead to (spatial and temporal) changes in both velocity and thermodynamic quantities. The governing equations of mass, momentum and energy can be separated into mean and fluctuating components, producing a governing equation for each. It is common to apply the Reynolds decomposition

$$f(\vec{x}, t) = \overline{f}(\vec{x}, t) + f'(\vec{x}, t) \tag{C.1.1}$$

(where f is the instantaneous value of a scalar quantity and a $(\bar{\ })$ represents its averaged value) to an incompressible fluid. As an example, consider the time average of a convective term

$$\overline{uv} = \overline{(\overline{u} + u')(\overline{v} + v')}$$

$$\overline{uv} = \overline{u}\,\overline{v} + \overline{u'v'}. \tag{C.1.2}$$

Two quantities result: a product of mean flow quantities and a Reynolds stress term. If the same is done to the corresponding term in the compressible set of governing equations, two extra terms emerge; correlations with density are shown explicitly

$$\overline{\rho u v} = \overline{(\overline{\rho} + \rho')(\overline{u} + u')(\overline{v} + v')}$$

(C.1.3)

$$= \underbrace{\overline{\rho}\,\overline{u}\,\overline{v}}_{\text{mean flow quantities}} + \underbrace{\overline{\rho}\,\overline{u'v'}}_{\text{Reynolds stresses}} + \underbrace{\overline{u}\,\overline{\rho' v'} + \overline{v}\,\overline{\rho' u'}}_{\text{mass transport}} + \underbrace{\overline{\rho' u'v'}}_{\text{triple correlation}} .$$

One way of removing the density correlations (that are present for all terms that contain density) is to introduce a density weighting to all terms except the density and pressure. Introduced by Reynolds and developed by Favre (see Gatski and Bonnet (2014) for an in depth history), the decomposition retains the same form as the Reynolds decomposition for an incompressible flow.

C.1.2   Favre decomposition

The Favre decomposition

$$f(\vec{x},t) = \widetilde{f}(\vec{x},t) + f''(\vec{x},t)$$

(C.1.4)

labels the density weighted average with a tilde (˜)

$$\widetilde{f} = \frac{\overline{\rho f}}{\overline{\rho}}$$

(C.1.5)

and the fluctuation with a double prime (″)

$$f'' = f - \widetilde{f}.$$

(C.1.6)

The Favre average properties are different from the Reynolds average:

P.1 The time average of the Favre fluctuation is, in general, not equal to zero:

$$\overline{f''} = \overline{f - \widetilde{f}} = \overline{\widetilde{f} + f' - \frac{\overline{\rho f}}{\overline{\rho}}} = \overline{f} - \frac{\overline{(\overline{\rho} + \rho')(\overline{f} + f')}}{\overline{\rho}}$$

$$= \overline{f} - \frac{\overline{\rho}\,\overline{f}}{\overline{\rho}} - \frac{\overline{\rho' f'}}{\overline{\rho}} = -\frac{\overline{\rho' f'}}{\overline{\rho}} \neq 0.$$

(C.1.7)

P.2 The Favre average of a Favre fluctuation is zero

$$\widetilde{f''} = \frac{\overline{\rho f''}}{\overline{\rho}} = \frac{\overline{\rho(f - \widetilde{f})}}{\overline{\rho}} = \frac{\overline{\rho f}}{\overline{\rho}} - \frac{\overline{\rho \widetilde{f}}}{\overline{\rho}} = \widetilde{f} - \widetilde{f} = 0$$

(C.1.8)

P.3 The average of a Reynolds fluctuation multiplied by a Favre fluctuation is the average of a product of Reynolds fluctuations: Consider f and g as generic scalars

$$\overline{f'g''} = \overline{f'(g - \widetilde{g})} = \overline{f'(\overline{g} + g')} - \overline{f'\widetilde{g}}^{\,0} = \overline{f'\overline{g}}^{\,0} + \overline{f'g'} = \overline{f'g'} \qquad \text{(C.1.9)}$$

P.4 The Favre average can be related to Reynolds average quantities by

$$\overline{f} = \overline{\widetilde{f}} + \overline{f''} = \widetilde{f} + \overline{f''} \qquad \text{(C.1.10)}$$

so that

$$\widetilde{f} = \overline{f} - \overline{f''} \qquad \text{(C.1.11)}$$

C.1.2.1   Simplified averaged

Applying the Favre decomposition to the convective term (C.1.3) gives

$$
\begin{aligned}
\overline{\rho u v} &= \overline{\rho(\widetilde{u} + u'')(\widetilde{v} + v'')} \\[2mm]
&= \overline{\rho(\widetilde{u}\widetilde{v} + \widetilde{u}v'' + u''\widetilde{v} + u''v'')} \\[2mm]
&= \overline{\rho}\,\widetilde{u}\widetilde{v} + \overline{\rho u''}\widetilde{v} + \overline{\rho v''}\widetilde{u} + \overline{\rho u''v''} \\[2mm]
&= \overline{\rho}\,\widetilde{u}\widetilde{v} + \overline{\rho}\,\widetilde{u''}^{\,0}\widetilde{v} + \overline{\rho}\,\widetilde{v''}^{\,0}\widetilde{u} + \overline{\rho}\,\widetilde{u''v''} \\[2mm]
&= \overline{\rho}\,\widetilde{u}\widetilde{v} + \overline{\rho}\,\widetilde{u''v''}
\end{aligned}
\qquad \text{(C.1.12)}
$$

which hides the explicit correlations of density fluctuations with other variables, simplifying the convective terms of the governing equations. It should be noted that there is not a unique combination of terms once the Favre averaging has been applied (compare Lele (1994) and Huang *et al.* (1995) for example).

Appendix D

DRP coefficient calculation

```
!—————————————————————————————————!
! Objective(s): This is a Compreal module to compute DRP weights      !
!                  (first derivative, to be updated for higher order...)!
! Author(s)    : N. Alferez                                   Jan 2015  !
!—————————————————————————————————!
! Code Sections:                                                        !
! (1) Read parameters                                                   !
! (2) Fill first part of A matrix, Taylor constraints for targeted      !
!     order                                                             !
! (3) Fill second part of A matrix, Optimization of the dispertion      !
!     error                                                             !
!     for waves with at least 4 point/wavelength                        !
! (4) Inverse the linear system Ax=b                                    !
!—————————————————————————————————!


  module mod_weights


  use mod_param


  implicit none
```

```fortran
contains


subroutine weights(N,M,Order,Res)


! declaration section ———————————————————————————


  implicit none
  integer, intent(IN) :: N,M,Order
  integer(dp) :: i,j,Factorial
  real(qp):: pi_qp
  real(qp),allocatable :: A(:,:),X(:),B(:),Temp(:)
  real(dp) :: Res(N+M+1)
  logical :: Sym
! instructions start here ——————————————————————————


  pi_qp=4.0_qp*atan(1.0_qp)


!(1) Input parameters


  if((N-M).eq.0)then
  Sym=.true.
  Allocate(A(N,N))
  Allocate(B(N))
  Allocate(X(N))
  Allocate(Temp(N))
  else
  Sym=.false.
  Allocate(A(N+M+1,N+M+1))
  Allocate(B(N+M+1))
  Allocate(X(N+M+1))
  Allocate(Temp(N+M+1))
  endif
```

```
!(2) Taylor constraints to match the convergency order

  If (Sym) then

    Do i = 1,Order/2
      Do j=1,N
        call Fact(2*i-1,Factorial)
        A(i,j)=1.0_qp/real(Factorial,qp)*j**(2*i-1)
      enddo
      B=0.0_qp
  ! Seeking first order derivative weights, otherwise 2 -> Order + 1...
      B(1)=1.0_qp/2.0_qp
    enddo

  else

    Do i = 1,Order+1
      Do j=-N,M
        call Fact(i-1,Factorial)
        A(i,j+N+1)=1.0_qp/real(Factorial,qp)*j**(i-1)
      enddo
    enddo
    B=0.0_qp
  ! Seeking first order derivative weights, otherwise 2 -> Order + 1...
    B(2)=1.0_qp
  endif

!(3) DRP optimization using the other degrees of freedom
!    provided by the stencil

  If (Sym) then
```

```fortran
Do i = Order/2+1,N

  Do j=1,i-1

    A(i,j)= sin(real(j-i,qp)*pi_qp/2.0_qp)/real(j-i,qp) &
            -sin(real(j+i,qp)*pi_qp/2.0_qp)/real(j+i,qp)

  enddo

  A(i,i)=pi_qp/2.0_qp


  Do j=i+1,N

  A(i,j)= sin(real(j-i,qp)*pi_qp/2.0_qp)/real(j-i,qp) &
          -sin(real(j+i,qp)*pi_qp/2.0_qp)/real(j+i,qp)

  enddo


  B(i)= 1.0_qp/real(i,qp)**2*sin(real(i,qp)*pi_qp/2.0_qp)&
        -pi_qp/(2.0_qp*real(i,qp))*cos(real(i,qp)*pi_qp/2.0_qp)


enddo


else


Do i = Order+2,N+M+1

  Do j=-N,i-N-2

    A(i,j+N+1)=2.0_qp*sin(real(j-(i-N-1),qp)&
                *pi_qp/2.0_qp)/real(j-(i-N-1),qp)

  enddo

  A(i,i)=pi_qp

  Do j=i-N,M

    A(i,j+N+1)=2.0_qp*sin(real(j-(i-N-1),qp)&
                *pi_qp/2.0_qp)/real(j-(i-N-1),qp)

  enddo


  if((i-N-1).ne.0)then
```

```
          B(i)=2.0_qp/real(i−N−1,qp)**2*sin(real(i−N−1,qp)&
                *pi_qp/2.0_qp)−pi_qp/real(i−N−1,qp)&
                *cos(real(i−N−1,qp)*pi_qp/2.0_qp)
      else
        B(i)=0.0_qp
      endif
    enddo
  endif


!(4) Solve the linear system
   If (Sym)then
      call Gauss(N,A,B,X)
   else
      call Gauss(N+M+1,A,B,X)
   endif


   If(Sym)then
      Do i=1,N
         Res(i)=−real(X(N−i+1),dp)
      enddo
      Res(N+1)=0.0_wp
      Do i=N+2,2*N+1
         Res(i)=real(X(i−N−1),dp)
      enddo
   else
      Res=real(X,dp)
   endif


   deallocate(A)
   deallocate(B)
   deallocate(X)
   deallocate(Temp)
```

```fortran
  end subroutine weights


!_____

  subroutine Fact(n,f)


  implicit none
  integer(dp), INTENT(IN) :: n
  integer(dp) :: i,f
  f=1


  if(n.ne.0)then


  do i = 1,n
     f=f*i
  enddo


  else
  f=1
  endif


  end subroutine Fact


!_____

  subroutine Gauss(n,A,B,X)


  implicit none


  integer :: i,j,k,n,Pk
  integer,DIMENSION(n) :: P
  real(qp),DIMENSION(n,n)   :: A
```

```fortran
   real(qp),DIMENSION(n)  ::  B,X,Scale
   real(qp)  ::  scmax,qmax,q,Temp


! (1)
   Do  i = 1,n
       P(i)=i
       scmax=0.0_qp
       Do  j= 1,n
           scmax = max(abs(A(i,j)),scmax)
       enddo
       Scale(i)=scmax
   enddo


   j=0


! (2)
   Do k = 1,n-1    ! N-1 Elimination
       qmax = 0.0_qp
       Do i = k,n   ! N-K line not "pivoted" yet
           q = abs(A(P(i),k)/Scale(P(i)))
           if (q .gt. qmax) then
               j = i
               qmax = q
           endif
       enddo


       Pk   = P(j)
       P(j)= P(k)
       P(k)= Pk


       Do i = k+1,n
           Temp = A(P(i),k)/A(P(k),k)
```

```fortran
            A(P( i ) , k)= Temp
            Do  j  =  k+1,n
                A(P( i ) , j ) = A(P( i ) , j ) − Temp∗A(P(k) , j )
            enddo
        enddo
    enddo


! Permute B vector in accordance
    Do k =  1 ,n−1
        Do  i=k+1,n
            B(P( i )) = B(P( i )) − A(P( i ) ,k)∗B(P(k))
        enddo
    enddo


! (3)
    Do  i  =  n,1 ,−1
        Temp= B(P( i ))
        Do  j  =  i+1,n
            Temp =  Temp − A(P( i ) , j )∗X( j )
        enddo
        X( i)=Temp/(A(P( i ) , i ))
    enddo


    end subroutine Gauss


    end module mod_weights ! _____
```